FLOW AND HEAT TRANSFER IN TUBES WITH OBSTACLES

by

Aurelian Tanase

A thesis submitted

in partial fulfilment of the requirements for the degree of

Doctor of Philosophy in Mechanical Engineering

Ottawa-Carleton Institute for Mechanical and Aerospace Engineering

Department of Mechanical Engineering

University of Ottawa

July 2017

ABSTRACT

The objective of this research work is to enhance the understanding of heat transfer and pressure loss in heated tubes equipped with flow obstacles by experimentally investigating the axial and circumferential distributions of convective heat transfer in a heated tube, complemented by pressure loss and velocity measurements in an adiabatic pipe flow. The heat transfer experiments employed refrigerant R-134a as the working fluid with a Reynolds number range of 14,000 to 97,000. Three types of flow obstructions were investigated: eccentric cylinders with flat and rounded ends and annular obstacles, each having a flow blockage of either 0.15 or 0.3. The axial distribution of heat transfer coefficient was measured downstream from the downstream end of the obstruction over a distance of 3 to 70 tube diameters. The experimental data indicate that heat transfer augmentation downstream from the flow obstructions depends on the obstructed area, the flow Reynolds number, the distance from the flow blockage and, to a lesser extent, the shape and the circumferential location of the obstruction. Our experiments confirm the previous findings that heat transfer augmentation (compared to the bare tube heat transfer case) decreases with an increase of flow Reynolds number. It was found that heat transfer augmentation typically extends up to 30 diameters downstream of a flow obstacle. An improved prediction method that correlates the obstructed flow area, Re number and the distance from the trailing edge of the obstacle has been derived.

Pressure loss and velocity measurements were also collected for a flow Reynolds number range from 11,000 to 65,000, for flat ended (blunt) and rounded cylinders with a flow blockage ratio of 0.3 and a blunt cylinder with a flow blockage ratio of 0.15. The results showed that blockage ratio and shape of flow obstacle affect the obstacle pressure loss coefficient significantly and they confirm previous research findings that obstacle pressure loss coefficient decreases with an increase of bulk Reynolds number. Measurements of the reattachment length downstream from flow obstacles indicated that the reattachment length for three-dimensional turbulent flow around square-shaped cylinders was significantly shorter than two-dimensional flow over a backward-facing step. An important finding of the current

investigation is that, for the flow range investigated, heat transfer augmentation could not be correlated with the local pressure loss coefficient of the obstruction, which differs from the smooth heated channel case where the Reynolds analogy usually applies. Additionally, to assess the capabilities of the widely used k-ω turbulence model, some CFD simulations were performed. The CFD results were generally in satisfactory agreement with the experimental data; however, near the obstacle, close to the separation and recirculation areas, the agreement with the experimental data was less satisfactory.

The current research can be applied to the design and optimization of spacers and appendages of nuclear fuel elements, as well as serve for the improvement of state of the art computer codes employed in the safety assessment of nuclear reactors.

ACKNOWLEDGEMENTS

I would like to express my sincere gratitude and thankfulness to my advisors and mentors Dr. Stavros Tavoularis and Dr. Dé Groeneveld for their continuous support of my Ph.D study and related research, and for their knowledge, wisdom, patience, motivation and kindness. Their guidance helped me in my research and in writing this thesis.

Special thanks to all of my colleagues for their help and friendship during my studies, especially to Hassan Shaban, Christina Vanderwel, George Choueiri, Laura Haya, Ahmad Ether and Hussam Zahlan. Their support and willingness to help and share their knowledge are highly appreciated.

I also would like to thank my family and friends for their patience, love and their support during my studies.

Finally, I gratefully acknowledge the support of the University of Ottawa Mechanical Engineering Machine Shop, especially Stan Weedmark, Leo Denner and John Perrins, as well as the kind support of Susan Rennie for issues related to administrative assistance.

Table of Contents

ABSTRACT .... **ii**

ACKNOWLEDGEMENTS .... **iv**

TABLE OF CONTENTS .... **v**

LIST OF FIGURES .... **vi**

LIST OF TABLES .... **ix**

NOMENCLATURE .... **x**

CHAPTER 1 INTRODUCTION **1**

1.1 MOTIVATION 1
1.2 OBJECTIVES 2
1.3 OUTLINE OF THE THESIS 3

CHAPTER 2 LITERATURE REVIEW **5**

2.1 EXPERIMENTS 5
2.2 NUMERICAL SIMULATIONS 23

CHAPTER 3 EXPERIMENTAL FACILITIES AND PROCEDURES **30**

3.1 HEAT TRANSFER EXPERIMENTAL LOOP 31
3.2 HEAT TRANSFER UNCERTAINTIES 33
3.2.1 Thermocouple Calibration *33*
3.2.2 Heat Balance Test *34*
3.2.3 Repeatability *35*
3.3 ISOTHERMAL FLOW LOOP 37
3.4 FLOW RATE AND PRESSURE LOSS MEASUREMENTS 38
3.5 PARTICLE IMAGE VELOCIMETRY 40
3.6 PIV AND PRESSURE LOSS UNCERTAINTIES 42
3.6.1 Voltage calibration of data acquisition system *42*
3.6.2 Differential pressure calibration *43*
3.6.3 Flow rate calibration *44*
3.6.4 PIV measurement uncertainty *46*
3.6.5 Seeding *47*
3.7 FLOW VISUALIZATION AROUND OBSTACLES USING HYDROGEN BUBBLE TECHNIQUE 51

CHAPTER 4 COMPUTATIONAL PROCEDURES **59**

4.1 THEORETICAL FOUNDATIONS 59
4.1.1 Conservation equations *59*
4.1.2 Reynolds Averaged Navier-Stokes (RANS) Equations *61*
4.1.3 Reynolds stress equations *66*
4.1.4 Turbulent kinetic energy equation *67*
4.2 TURBULENCE MODELLING 67
4.2.1 Spalart-Allmaras (S-A) model *68*
4.2.2 Standard k-ε model *68*
4.2.3 RNG k-ε model *69*
4.2.4 Realizable k-ε model *69*

4.2.5 Heat transfer in k-ε turbulence models ... *70*
4.2.6 Standard k-ω model ... *71*
4.2.7 Shear-Stress Transport (SST) k−ω model ... *71*
4.2.8 Reynolds Stress Model ... *73*

CHAPTER 5 AN EXPERIMENTAL INVESTIGATION OF THE EFFECT OF FLOW OBSTACLES ON SINGLE PHASE HEAT TRANSFER ... 75

CHAPTER 6 EXPERIMENTAL INVESTIGATION OF TURBULENT PIPE FLOWS WITH OBSTRUCTIONS ... 112

CHAPTER 7 CONCLUSIONS ... 139

7.1 SUMMARY OF RESULTS ... 139
7.2 MAIN CONTRIBUTIONS OF THIS WORK ... 141
7.3 RECOMMENDATIONS FOR FUTURE WORK ... 143

REFERENCES ... 145

APPENDIX A: LIST OF PUBLICATIONS BY A. TANASE ... 149

APPENDIX B: ANALYSIS OF WALL THICKNESS ECCENTRICITY ... 151

APPENDIX C: PRELIMINARY INVESTIGATION OF THE EFFECT OF FLOW OBSTACLES ON SINGLE PHASE HEAT TRANSFER ... 166

APPENDIX D: CFD SIMULATIONS SST K-ω TURBULENCE MODEL ... 176

MESH PROPERTIES ... 182
RESULTS OF NUMERICAL SIMULATIONS ... 183
Pressure loss ... *183*
Pressure loss coefficient ... *184*
Computed center plane streamwise velocity profiles ... *186*
Computed center plane turbulent kinetic energy ... *187*
Flow reattachment length ... *188*
Mesh convergence issues and inconsistency with the experimental data ... *204*

APPENDIX E: ANALYSIS OF OPTICAL DISTORTIONS ... 205

APPENDIX F: ANALYSIS OF PIV CONVERGENCE ... 212

List of Figures

FIGURE 2 - 1 DISTRIBUTION OF LOCAL NU NUMBER FOR FULLY DEVELOPED CONDITIONS AT RE=10,500 (YAO ET AL., 1995). ... 10
FIGURE 2 - 2 ARRANGEMENT OF TWO CYLINDERS AND THE COORDINATE SYSTEM (DALOGU AND UNAL, 2000). ... 11
FIGURE 2 - 3 COMPARISON OF AVERAGE NU NUMBER OBTAINED USING SQUARE AND CIRCULAR CROSS SECTION OBSTACLES A) $D=d$ B) $D=2d$ C) $D=3d$ (DALOGU AND UNAL, 2000). ... 12
FIGURE 2 - 4 MEASURED LOCAL HEAT TRANSFER COEFFICIENT IN BETWEEN THE ROUGHNESS ELEMENTS AT TWO DIFFERENT STEPS (SLANCIAUKAS, 2001). ... 13
FIGURE 2 - 5 TYPICAL VORTEX STRUCTURE AROUND A CUBE (MEINDERS AND HANJALIC, 2002). ... 15

FIGURE 2 - 6 DISTRIBUTION OF MEASURED LOCAL HEAT TRANSFER COEFFICIENT FOR THE FRONT CUBE (MEINDERS AND HANJALIC, 2002). 15
FIGURE 2 - 7 DISTRIBUTION OF MEASURED LOCAL HEAT TRANSFER COEFFICIENT FOR THE SECOND CUBE (MEINDERS AND HANJALIC, 2002). 16
FIGURE 2 - 8 AVERAGED HEAT TRANSFER COEFFICIENT FOR THE SIDES OF THE SECOND CUBE FOR IN-LINE TANDEM AS FUNCTION OF THE NORMALIZED AXIAL DISTANCE (MEINDERS AND HANJALIC, 2002). 16
FIGURE 2 - 9 SEPARATED FLOW OVER A BACKWARD FACING STEP AND A RIB (TEREKHOV ET AL., 2002) 17
FIGURE 2 - 10 LOCAL NORMALIZED NU NUMBER FOR SMOOTH CHANNEL (LEFT) AND RIBBED CHANNEL (RIGHT) (SOURCE: KHAN ET AL (2000)) 18
FIGURE 2 - 11 NUSSELT NUMBER NORMALIZED BY HYDRODYNAMICALLY FULLY DEVELOPED NUSSELT NUMBER FOR STANDARD GRIDS A AND G AND COMPARISON WITH YAO PREDICTIONS (HOLLOWAY ET AL., 2004). 20
FIGURE 2 - 12 AZIMUTHAL VARIATION IN NU NUMBER FOR STANDARD GRID AT RE=28,000 (HOLLOWAY ET AL., 2005) 21
FIGURE 2 - 13 CONTOUR PLOTS OF TEMPERATURE DIFFERENCE (T-T_B) AT RE=28,000 FOR (A) STANDARD GRID, (B) DISC GRID AND (C) SPLIT-VANE PAIR GRID (HOLLOWAY ET AL., 2005). 22
FIGURE 2 - 14 CHANNEL GEOMETRY AND A CLOSE-UP OF THE MESH AROUND THE OBSTACLE (YOUN AND VAFAI, 1998). 24
FIGURE 2 - 15 STREAMLINES OF FLOW AROUND THE OBSTACLE AT RE=2,000 (YOUN AND VAFAI, 1998). 25
FIGURE 2 - 16 BOTTOM WALL SKIN FRICTION COEFFICIENT AND NUSSELT NUMBER (LABBE ET AL., 2002). 26
FIGURE 2 - 17 CHANNEL WITH SQUARE CROSS SECTION RING (TOP) AND SEMICIRCULAR CROSS SECTION RING (BOTTOM) (CHANDRA ET AL., 2009). 28
FIGURE 2 - 18 HEAT TRANSFER ENHANCEMENT DECAY WITH DOWNSTREAM DISTANCE FOR DIFFERENT BLOCKAGE RATIOS, q=698 KW/M^2 (ZHANG ET AL., 2009). 29

FIGURE 3 - 1 UNIVERSITY OF OTTAWA MULTI-FLUID LOOP (VERTICAL TEST SECTION). 32
FIGURE 3 - 2 THE SCHEMATIC OF THE TEST SECTION, THERMOCOUPLE LAYOUT AND THE OBSTACLE TYPES (FROM LEFT TO RIGHT: ANNULAR, BLUNT AND ROUNDED). 33
FIGURE 3 - 3 HEAT BALANCE ERROR VERSUS MASS FLUX. 35
FIGURE 3 - 4 REPEAT TESTS FOR THE ROUNDED OBSTACLE HAVING 0.15 OBSTRUCTED RATIO AT RE=28,000 36
FIGURE 3 - 5 EXPERIMENTAL WATER LOOP, CONSISTING OF THE HEAD TANK (1), FEED PIPE (2), INLET TANK (3), FLOW DEVELOPMENT SECTION (4), TEST SECTION (5), RETURN PIPE (6), PUMP (7), COLLECTION TANK (8), FLOW CONTROL VALVES (9), FLOW METER (10), AND OVERFLOW RETURN PIPE (11) 38
FIGURE 3 - 6 SKETCHES OF THE THREE FLOW OBSTACLES; DIMENSIONS IN MM; CROSSHATCHED AREAS INDICATE FERROMAGNETIC CORES. 39
FIGURE 3 - 7 SKETCH OF THE EXPERIMENTAL SETUP FOR PRESSURE LOSS MEASUREMENT. 40
FIGURE 3 - 8 SKETCH OF THE PIV SETUP. 42
FIGURE 3 - 9 CALIBRATION CURVE OF THE ULTRASONIC FLOW METER. 45
FIGURE 3 - 10 EXAMPLE OF TYPICAL PIV IMAGE WITH ZOOMED-IN AREA SHOWING DETAILED SEEDING. AN INTERROGATION WINDOW OF 32X32 PIXELS IS EXEMPLIFIED BY THE RED SQUARE. 51
FIGURE 3 - 11 EXPERIMENTAL WATER LOOP FOR HYDROGEN BUBBLE VISUALIZATION. 53
FIGURE 3 - 12 FLOW VISUALIZATION BY HYDROGEN BUBBLES AROUND 30B OBSTACLE, RE=350. 54
FIGURE 3 - 13 FLOW VISUALIZATION BY HYDROGEN BUBBLES AROUND 30B OBSTACLE, RE=700. 55
FIGURE 3 - 14 FLOW VISUALIZATION BY HYDROGEN BUBBLES AROUND 30B OBSTACLE, RE=1400. 55
FIGURE 3 - 15 FLOW VISUALIZATION BY HYDROGEN BUBBLES AROUND 30B AND 30R OBSTACLES, RE=1400. 56
FIGURE 3 - 16 FLOW VISUALIZATION BY HYDROGEN BUBBLES AROUND 30B AND 30R OBSTACLES, RE=2200. 57
FIGURE 3 - 17 FLOW VISUALIZATION BY HYDROGEN BUBBLES AROUND 30B OBSTACLE, RE=3000. 58
FIGURE 3 - 18 FLOW VISUALIZATION BY HYDROGEN BUBBLES AROUND 30B OBSTACLE, RE=3500 58

Figure D - 1 Example of a region of the computational mesh developed for the square-ended cylinder (30B). 177
Figure D - 2 Example of a mid-plane section of average mesh for 30B, with upstream structured section visible on the left. 178
Figure D - 3 Example of structured mesh cross section at the inlet of the computational domain. 178
Figure D - 4 Details of the mid-plane section of unstructured mesh in the proximity of the 30B obstacle, coarse (top), average (middle) and fine (bottom). 179
Figure D - 5 Example of a region of the computational mesh developed for the rounded-ended cylinder (30R). 180
Figure D - 6 Example of a mid-plane section of the average mesh for 30R, with upstream structured section visible on the left (top) and detail in the proximity of the obstacle (bottom). 182
Figure D - 7 Comparison between the results of numerical simulations (coarse, average, fine meshes) and experiments for normalized ΔP between pressure taps (30B). 185
Figure D - 8 Comparison between the results of numerical simulations (coarse, average, fine meshes) and experiments for normalized ΔP between pressure taps (30R). 185
Figure D - 9 Identification of flow reattachment location from streamwise velocity and wall shear stress; 30R, fine mesh, Re=35,000. 189
Figure D - 10 Computed normalized streamwise centerplane velocity, fully developed flow bare test section, Re=35,000. 190
Figure D - 11 Computed normalized streamwise centerplane velocity, at 1D upstream the 30B obstacle, Re=35,000. 190
Figure D - 12 Computed normalized streamwise centerplane velocity, at mid of 30B obstacle, Re=35,000. 191
Figure D - 13 Computed normalized streamwise centerplane velocity, at 1/2D downstream 30B obstacle, Re=35,000. 191
Figure D - 14 Computed normalized streamwise centerplane velocity, at 1D downstream 30B obstacle, Re=35,000. 192
Figure D - 15 Computed normalized streamwise centerplane velocity, at 3D downstream 30B obstacle, Re=35,000. 192
Figure D - 16 Computed normalized streamwise centerplane velocity, at 9D downstream 30B obstacle, Re=35,000. 193
Figure D - 17 Computed normalized streamwise centerplane velocity, fully developed flow bare test section, Re=35,000. 193
Figure D - 18 Computed normalized streamwise centerplane velocity, at 1D upstream 30R obstacle, Re=35,000. 194
Figure D - 19 Computed normalized streamwise centerplane velocity, at mid 30R obstacle, Re=35,000. 194
Figure D - 20 Computed normalized streamwise centerplane velocity, at 1/2D downstream 30R obstacle, Re=35,000. 195
Figure D - 21 Computed normalized streamwise centerplane velocity, at 1D downstream 30R obstacle, Re=35,000. 195
Figure D - 22 Computed normalized streamwise centerplane velocity, at 3D downstream 30R obstacle, Re=35,000. 196
Figure D - 23 Computed normalized streamwise centerplane velocity, at 9D downstream 30R obstacle, Re=35,000. 196
Figure D - 24 Computed normalized TKE at centerplane, fully developed flow bare test section, Re=35,000. 197
Figure D - 25 Computed normalized TKE at centerplane, at 1D upstream 30R obstacle, Re=35,000. 197

FIGURE D - 26 COMPUTED NORMALIZED TKE AT CENTERPLANE, MID 30B OBSTACLE, RE=35,000. 198
FIGURE D - 27 COMPUTED NORMALIZED TKE AT CENTERPLANE, AT 1/2D DOWNSTREAM 30B OBSTACLE, RE=35,000. 198
FIGURE D - 28 COMPUTED NORMALIZED TKE AT CENTERPLANE, AT 1D DOWNSTREAM 30B OBSTACLE, RE=35,000. 199
FIGURE D - 29 COMPUTED NORMALIZED TKE AT CENTERPLANE, AT 3D DOWNSTREAM 30B OBSTACLE, RE=35,000. 199
FIGURE D - 30 COMPUTED NORMALIZED TKE AT CENTERPLANE, AT 9D DOWNSTREAM 30B OBSTACLE, RE=35,000. 200
FIGURE D - 31 COMPUTED NORMALIZED TKE AT CENTERPLANE, FULLY DEVELOPED FLOW BARE TEST SECTION, RE=35,000. 200
FIGURE D - 32 COMPUTED NORMALIZED TKE AT CENTERPLANE, AT 1D UPSTREAM 30R OBSTACLE, RE=35,000. 201
FIGURE D - 33 COMPUTED NORMALIZED TKE AT CENTERPLANE, MID 30R OBSTACLE, RE=35,000. 201
FIGURE D - 34 COMPUTED NORMALIZED TKE AT CENTERPLANE, AT 1/2D DOWNSTREAM 30R OBSTACLE, RE=35,000. 202
FIGURE D - 35 COMPUTED NORMALIZED TKE AT CENTERPLANE, AT 1D DOWNSTREAM 30R OBSTACLE, RE=35,000. 202
FIGURE D - 36 COMPUTED NORMALIZED TKE AT CENTERPLANE, AT 3D DOWNSTREAM 30R OBSTACLE, RE=35,000. 203
FIGURE D - 37 COMPUTED NORMALIZED TKE AT CENTERPLANE, AT 9D DOWNSTREAM 30R OBSTACLE, RE=35,000. 203

FIGURE E - 1 SCHEMATIC OF TOP VIEW OF THE MEASUREMENT TANK. 210
FIGURE E - 2 SCHEMATIC OF THE SIDE VIEW OF THE MEASUREMENT TEST SECTION AND THE WATER TANK. 211

FIGURE F - 1 NORMALIZED TIME AVERAGED STREAMWISE PLANAR VELOCITY COMPONENT, CASE A. 213
FIGURE F - 2 NORMALIZED RMS OF STREAMWISE VELOCITY FLUCTUATIONS, CASE A. 213
FIGURE F - 3 NORMALIZED RMS OF SPANWISE VELOCITY FLUCTUATIONS, CASE A. 214
FIGURE F - 4 NORMALIZED REYNOLDS STRESS, CASE A. 214
FIGURE F - 5 NORMALIZED TIME AVERAGED STREAMWISE PLANAR VELOCITY COMPONENT, CASE B. 216
FIGURE F - 6 NORMALIZED STREAMWISE RMS OF VELOCITY FLUCTUATIONS, CASE B. 216
FIGURE F - 7 NORMALIZED RMS OF SPANWISE VELOCITY FLUCTUATIONS, CASE A. 217
FIGURE F - 8 NORMALIZED REYNOLDS STRESS, CASE B. 217
FIGURE F - 9 STANDARD DEVIATIONS OF ERRORS VS THE SIZE OF SAMPLES, CASE A. 219
FIGURE F - 10 STANDARD DEVIATIONS OF ERRORS VS THE SIZE OF SAMPLES, CASE B. 220

List of Tables

TABLE 3 - 1 COMPARISON BETWEEN VARIOUS TYPES OF SEEDING PARTICLES AND CONTAMINANTS 48

TABLE D - 1 TYPES AND VALUES OF INITIAL CONDITIONS 181
TABLE D - 2 NUMBER OF CELLS FOR 30B AND 30R, COARSE, MEDIUM AND FINE MESHES 183
TABLE D - 3 MESH MAIN FEATURES 183

TABLE D - 4 OBSTACLE PRESSURE LOSS COEFFICIENT (*K*) FOR 30B AND 30R, RE=35,000.................................. 186

TABLE E- 2 ESTIMATES OF ERRORS CAUSED BY TEST SECTION CURVATURE.. 209

Nomenclature

A	annular obstacle
B	blunt obstacle
C_v	modified pressure loss coefficient
D_h	hydraulic diameter
D, Di	inside tube diameter (mm)
Do	outside tube diameter (mm)
G	mass flux($kgm^{-2}s^{-1}$)
H	obstacle height (mm)
h	enthalpy ($J\ kg^{-1}$)
I	electric current (A)
K	pressure loss coefficient
k	thermal conductivity ($W \cdot m^{-1} \cdot K^{-1}$) or absolute wall roughness (mm)
L_h	heated length (m)
$\dot{m}$	mass flow rate ($kg \cdot s^{-1}$)
Nu	Nusselt number
P	pressure (kPa)
Pr	Prandtl number
R	tube outside radius (mm)
R	rounded obstacle
Re	Reynolds number
r	tube inside radius (mm)

q_s	surface heat flux (kW·m^{-2})
q_v	Joule volumetric heat source (kW m^{-3})
q_{xy}	Planar velocity magnitudes on the x-y plane (m/s)
RS	turbulent (Reynolds) stress (kg/(ms^2) or Pa)
T	temperature (°C)
t	time (s)
T_f	bulk fluid temperature (°C)
T_{WI}	inside wall temperature (°C)
T_{WO}	outside wall temperature (°C)
U, V, W	Components of the velocity vector (m/s)
u, v, w	Velocity fluctuation components (m/s)
u', v', w'	Components of the r.m.s. velocity fluctuation (m/s)
U	electric voltage (V)
U_b	bulk (average) fluid velocity (m/s)
x	distance downstream the obstacle trailing edge (m)

Acronyms

2D	Two-dimensional
3D	Three-dimensional
AC	Alternate Current
ADC	Analog to Digital Convertor
DAS	Data Acquisition System
DC	Direct Current
HTC	Heat Transfer Coefficient
LHS	Left Hand Side

NB	Nucleate Boiling
ONB	Onset of Nucleate Boiling
PDO	Post Dryout
PDF	Probability density function
PIV	Particle image velocimetry
PWR	Pressurized Water Reactor
RBHT	Rod Bundle Heat Transfer
r.m.s.	Root mean square
RHS	Right Hand Side
RTD	Resistance Temperature Detector
TC	Thermocouple
TS	Test Section

Greek symbols

α	Magnification factor (dimensionless)
ΔT	Temperature difference = T_{WO}-T_{WI} (°C)
ΔX	Particle displacement (pixels)
δ	Wall thickness (mm)
ε	Blockage ratio - the ratio between the obstructed cross section area and the area of the unobstructed tube
ν	Kinematic viscosity (m^2 s^{-1})

Subscripts

avg	Average
i	Inside

in	Inlet
max	Maximum
o	Outside
out	Outlet
ref	Reference
sat	Saturation
0	Reference

CHAPTER 1

Introduction

1.1 Motivation

Convective heat transfer is the dominant heat transfer mechanism within the vast majority of heat transfer systems in conventional and nuclear power plants. Efficient, safe and reliable operation of heat transfer equipment (such as boilers, heat exchangers, and fuel bundles) significantly contributes to the overall improvement of plant safety and performance indicators. However, these major benefits are achieved upon proper understanding and adequate control of heat transfer regimes and mechanisms that occur in heat transfer systems and a detailed knowledge of equipment features. Flow obstructions are essential and very common features of heat transfer systems. Even if designed only for improvement of mechanical rigidity or specifically for the heat transfer or critical heat flux enhancement, any flow obstruction would modify the flow field around it. The current experimental studies and numerical simulations indicate that, in general, flow obstacles improve the heat transfer coefficient downstream, at the expense of increased pressure drop. Proper design and optimization of heat transfer equipment requires understanding of complex mechanisms that govern the overall flow behavior, boundary layers, pressure drop and heat transfer around flow obstructions.

The complexity of flow around obstacles or relatively complicated geometries gives rise to insurmountable difficulties for a purely analytical approach; however, experimental and numerical methods are available that have given promising results. The study of flows of practical interest requires extensive investigation and understanding of turbulence, vortices formation and dynamics, boundary layers, as well as the impact of turbulent flow structures on heat transfer and pressure drop. Few investigators have examined the effect of flow blockages on heat transfer in the turbulent flow region. Those who did, usually employed rod bundle geometries equipped with grid spacers, examined the obstacle effect during film-boiling heat transfer instead of single-phase heat transfer, or studied the hydrodynamic and heat transfer at relatively low flows, with little practical interest. Moreover, contradictory conclusions between different researchers have been found.

A significant part of the research literature on flow obstacle effects on heat transfer deals with cooling of electronics components and usually involves studies of heated obstacles cooled by natural or forced convection, but very few papers involve a study of heated channels equipped with ribs or other types of flow obstructions.

The present research work is intended to fill the knowledge gaps of complex phenomena of turbulent flow in channels with obstacles through a systematic experimental investigation and numerical simulations of flow in geometries and flow conditions relevant to practical applications. It is also expected that the current results will be useful in optimizing the design of convective heat transfer systems.

1.2 Objectives

The general objective of this research work is to enhance understanding of heat transfer and pressure loss in tubes equipped with flow obstacles by experimentally investigating axial and circumferential distribution of convective heat transfer in heated tubes, complemented by adiabatic Particle Image Velocimetry (PIV) and pressure loss measurements. Additionally, a complementary general objective is to assist industry in designing and optimizing spacers and appendages of nuclear fuel elements, as well as for the improvement of state of the art computer codes (e.g. best estimate system codes) employed in the safety assessment of nuclear reactors.

The specific objectives of this research are:

(i) To provide an experimental data base for heat transfer enhancement in single phase turbulent flow downstream of flow obstacles of various shapes.

(ii) To derive an improved prediction methodology for heat transfer enhancement near obstacles, capable of accounting for various geometric and flow effects that have not been considered previously.

(iii) To recommend an optimum flow obstacle shape, designed to maximize heat transfer enhancement while minimizing the pressure drop penalty.

(iv) To perform some numerical simulations of single phase flow around selected flow obstacles and provide an assessment of the overall performance of some widely-used turbulence models, particularly the k-ω model.

1.3 Outline of the thesis

A literature survey of experiments and simulations of isothermal and heated channels equipped with various types of flow obstacles is presented in Chapter 2. The literature review includes discussions of heat transfer augmentation and its presumed mechanisms, flow visualization, coherent structures around flow obstacles, flow reattachment, two-dimensional versus three-dimensional flows. This survey also includes a review of papers addressing pressure drop due to flow obstacles and its relationship with heat transfer augmentation.

Experimental facilities and procedures are described in Chapter 3. The description includes the geometry and dimensions of the heat transfer and isothermal water loops, their principles of operation, test sections, materials, and working fluids. A discussion on the loop instrumentation and data acquisition system, calibration and estimation of experimental uncertainties is also included. Chapter 3 includes description of the experimental setup for flow visualization by hydrogen bubbles method, and several representative images of the flow distribution around flow obstacles at various Reynolds numbers.

Chapter 4 contains a description of the computational procedures, which includes a theoretical background and an overview of the most common turbulence models.

The results of heat transfer experiments are summarized and discussed in Chapter 5. Chapter 6 includes a discussion of the results from pressure distribution and Particle Image Velocimetry experiments. The conclusions, the main contributions of the current work and recommendations for future work are presented in Chapter 7.

Appendix A contains a list of articles authored or co-authored by A. Tanase. A paper describing several methods for determination of wall thickness eccentricity (e.g. direct measurement, Joule heating and forced convection heat transfer) is reproduced in Appendix B. This information is important to assess the circumferential variation in heat flux of the heat transfer tests described in Chapter 3. Appendix C contains a paper which describes a preliminary investigation on the effect of flow obstacle on single phase heat transfer, which used blunt and rounded obstacles having an obstruction ratio of 0.24. Appendix D contains a description of the computational domain, meshes, convergence criteria and simulation options. The results of numerical simulations and comparison against experiments are summarized, as well. Analyses of optical distortions and PIV convergence are presented in Appendices E and F, respectively.

CHAPTER 2

Literature review

2.1 Experimental studies

Most experimental studies of the effect of flow obstacles on heat transfer have been performed on bundle geometries, e.g. Yao et al., (1980), Rehme (1977) Kidd and Hoffman (1968), Marek and Rehme, (1979), Hassan and Rehme, (1981), Hudina and Nothigen (1972), Yoder et al., (1982). Stosic et al. (1999) discussed the analogy between the increased pressure drop at the flow obstacle such as a grid spacer, and the enhancement in wall heat transfer. Immediately downstream of the blockage, the flow decelerates and turbulent wakes are generated. The wakes agitate the wall boundary layer and enhance the heat transfer from the wall. Using Equation (2.1), Marek and Rehme (1979) correlated the heat transfer augmentation[1] at the blockages on smooth rods in single-phase flow as:

$$\frac{Nu}{Nu_0} = 1 + 5.55 \cdot \varepsilon^2 \quad , \qquad (2.1)$$

where ε is the flow blockage ratio (the ratio of flow blockage area and bare tube cross section area) and Nu_o is the Nusselt number for a bare channel (that is, without flow blockage). It is worth noting that in a previous paper, which describes the experimental work performed in fuel bundle geometry for the pressure drop measurement on smooth and roughened fuel surfaces, Rehme (1977) found that the local (obstacle) pressure loss coefficient is also proportional to the square of flow blockage ratio, as indicated by Equation (2.2):

$$K = C_v \cdot \varepsilon^2 , \qquad (2.2)$$

where C_v is the modified pressure loss coefficient for the flow blockage and was determined experimentally. These results suggest that phenomena that govern the heat transfer enhancement are analogous to those that control the pressure drop. The experimental fuel

[1] In this work and the vast majority of papers we reviewed, heat transfer augmentation is defined as the ratio of the Nusselt numbers of the obstacle-equipped test section and the unobstructed test section (i.e., the bare test section, which provides the reference or baseline values).

bundle consisted of 12 rods arranged in a triangular array with a pitch of 11.1 mm (see Figure 2-1). The length of the bundle was 900 mm and the tubes were supported by five spacer grids. The length of the spacer was 14 mm. The overall blockage factors of the grids (defined as the ratio of the flow blockage area of the spacer and the flow cross-sectional area of the bundle

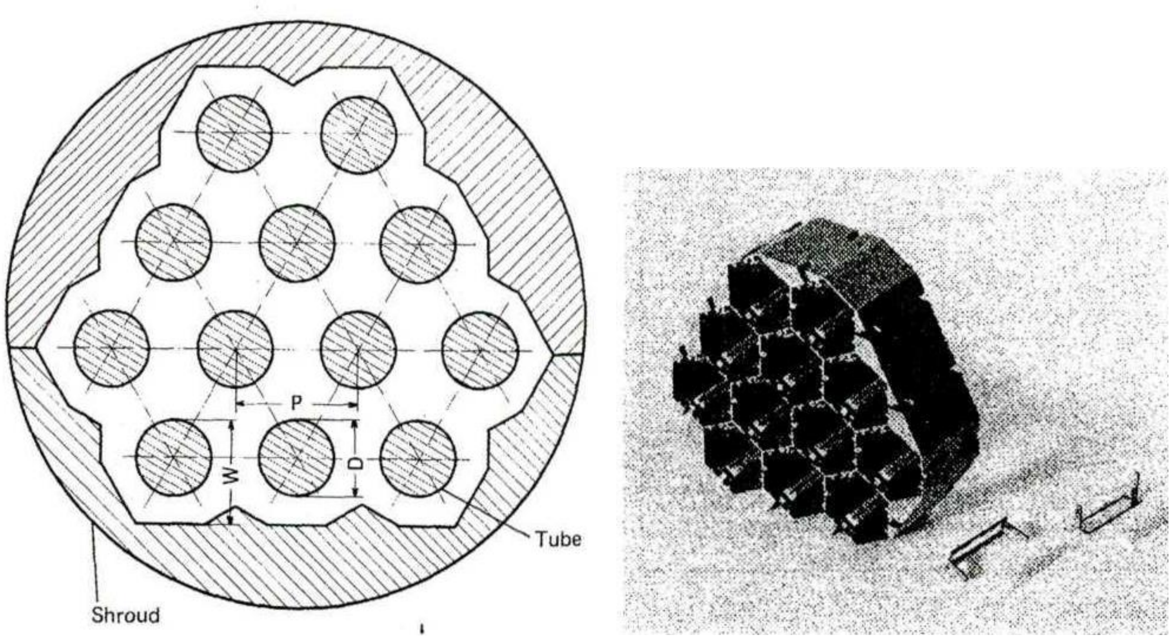

Figure 2- 1 Cross section of the tube bundle (LHS) and spacer grid (RHS) (Rehme, 1977)

away from the spacer) were 0.348 for the smooth bundle and 0.338 for the bundle with a roughened surface. The Reynolds number investigated varied between $7x10^3$ and $4x10^4$. It was also observed that, for the smooth fuel bundle, the friction factor decreased as Re increased, for both cases - with and without spacer. The fuel bundle with a roughened surface showed less sensitivity of friction factor to Re. The authors reported that the modified loss coefficient C_v decreased with an increase of flow Re number. At low Reynolds numbers ($\sim 10^3$) C_v was around 15 for the smooth bundle and 18 for the rough bundle. In the high Re range ($\sim 10^5$) C_v decreased to 7.9 for the smooth test section and 11 for the roughened one. Moreover, for Re > 10^4, the modified loss coefficient was practically constant.

Yao et al (1982) performed a study of heat transfer enhancement in rod bundles near grid spacers, for single phase and post critical heat flux flow regimes. Referring to the work performed by Rehme (1977), Yao et al. (1982) recommends a value of 10.5 for the modified pressure loss coefficient. It was observed that the Nu number reaches a maximum at, or slightly behind the flow obstacle (Yao et al., 1980). Downstream of the spacer, the hydrodynamic and thermal boundary layers begin to re-establish their fully developed profiles. The boundary layer re-establishment is similar to the entry length effect of turbulent tube flow. According to the authors, the main mechanism of heat transfer augmentation at the spacer location is flow acceleration due to flow area contraction. For relatively large obstacles, the fin effect (i.e. conduction effect) can be another effective cooling mechanism. In the wake region, it seemed that heat transfer is enhanced by the turbulent wakes created downstream of an obstacle as the flow decelerates. For simplicity, Yao et al. (1980) assumed that the wake-induced heat-transfer-augmentation was linearly dependent upon the blockage-induced pressure drop. Assuming that this assumption is valid, the equation for heat transfer augmentation due to the flow blockage will be of a similar form as that for the pressure drop increase due to the blockage. Upstream of the blockage, the data show that the heat transfer is affected only over a short distance (~2*D*) with the augmentation varying linearly from the bare test section fully developed value to the higher heat transfer within the blockage region. This increase in heat transfer can be explained by the gradual contraction of the flow upstream of the blockage. Downstream of the obstacle the augmentation of heat transfer has been observed to be an exponentially decaying function of *x/D* where *x* is the distance downstream of the blockage:

$$\frac{Nu}{Nu_0} = 1 + 5.55\varepsilon^2 \exp\left(-0.13\frac{x}{D}\right) \quad , \qquad (2.3)$$

where Nu_o is the Nusselt number of the bare tube and *Nu* refers the obstacle equipped tube. The authors recommend Equation (2.3) for Reynolds numbers higher than 10^4. The above mentioned equation shows a typical variation of heat transfer enhancement downstream of a bundle spacer for various flow blockage ratios. The results of Yao et al. clearly show that there is an influence of the Reynolds number on the maximum and on the axial distribution of the Nusselt numbers for different blockage factors. The improvement of heat transfer due to the blockage decreases with increasing Reynolds numbers above 3000. For the same Reynolds number, the improvement in heat transfer is higher for higher blockage ratios as was shown by Equation 2.3. The reason is that higher blockages produce higher flow velocities and turbulent eddies resulting in greater improvements in heat transfer (Hassan and Rehme, 1981).

The experimentally observed, exponentially decaying trend has been matched fairly well by the predictions. Similar results were obtained by Hassan and Rehme (1981), who performed tests with air in a three-rod subassembly, equipped with honeycomb-type spacer grids. Three sizes of the spacers were used, obstructing the flow by 25.3%, 30.2% and 34.8%. The Reynolds number was varied between 600 and $2 \cdot 10^5$, to simulate gas-cooled reactor conditions. They found a significant improvement in heat transfer caused by the spacer grid. In particular: (i) the highest increase (from 50% to 100%) was observed at the downstream end of the grid, and this improvement decayed exponentially with length, (ii) the higher flow obstruction area of the grid resulted in a larger heat transfer improvement, and (iii) with increasing Reynolds number the improvement decreased, and the axial extent of the influence was reduced. Hassan and Rehme (1981) also developed and recommended a correlation accounting for the spacer grid effect on heat transfer. The Doerffer et al (1996) results show a similar trend as was observed by Hassan and Rehme (1981). But for the same flow blockage, the Nu/Nu_0 values are about 25% higher, possibly because of the differences in flow channel and obstruction geometries.

The experimental investigation conducted by Yao et al. (1995) used two methods of flow visualization - hydrogen bubble and dye injection - to study the vortex dynamics and heat transfer enhancement mechanisms in the presence of flow obstructions[2]. The obstruction had a square cross section, with an estimated obstruction ratio of 20%. The flow Re number, based on the mean stream velocity and channel width, was 10,500. The experiment revealed that the Karman vortices are shed from the wake of the obstacle, with a velocity close to the mainstream velocity and they tend to move in a criss-cross motion along the channel. When the obstacle was mounted in the middle of the channel, the vortices were shed symmetrically, but when the obstacle was located at relatively small distances from the wall, the vortices were shed only from the side of the obstacle further from the wall. It appears that the heat transfer is directly influenced by the vortices. The heat transfer coefficients were measured in a wind tunnel with heated walls, for a Re number range of 9,900 to 27,700.The experiments showed that the streamwise distribution of Nu number is similar in shape regardless of the flow Re number; for the investigated range of Re numbers, the Nu number reaches a maximum just downstream of the flow obstacle. It was reported that, when the cylinder

[2] In the present thesis investigation a similar approach was used to visualize the flow disturbance caused by flow obstructions – see Appendix D.

touches the heated wall, Nu numbers downstream of flow obstacle (Re = 10,500) increase from ~40 to almost 75 (see Figure 2-1). On the opposite wall, Nu numbers decrease slightly, from ~45 (undisturbed value upstream of the obstacle) to 40. The paper concluded that the "washing" action exerted by discrete vorticity islands is the main mechanism of heat transfer enhancement. Strong enhancement of heat transfer coefficient was observed in regions with high vorticity near the walls. The regions of high vorticity are formed by interaction between the Karman vortices shed by the obstacle and the vorticity in the near-wall region.

A relevant experimental investigation that studied enhancement of both single phase heat transfer and critical heat flux has been conducted by Doerffer et al. (1996) with refrigerant R134a as the working fluid, in a test section with D_i = 8 mm and D_o =10 mm. The obstacles were of an annular ring shape with obstruction ratios of 17.8% and 30%. The temperatures were measured with six fixed thermocouples and the obstacles were relocated inside of the test section (using an external magnets) to change the axial distance from the thermocouple planes. The results showed that, for the obstacle with obstruction ratio of 17.8%, the maximum heat transfer augmentation (vs. the bare tube) occurred just downstream of the obstacle and was 38% for Re=$3.9 \cdot 10^4$ and decreased to 14% for Re=$2.3 \cdot 10^5$. For the ring having 30% obstruction ratio, the heat transfer enhancement was 61% at the low Re number ($3.9 \cdot 10^4$) and 34% at higher Re number ($2.3 \cdot 10^5$). The heat transfer augmentation decreased exponentially with an increase in distance downstream from the flow obstacle. It has been found that for the lowest obstruction ratio obstacle the effect was significant up to ~ 5 *D* downstream and for the highest obstruction ratio the effect extended to about 15 *D*. The authors explained the enhancement effect of obstacle by two mechanisms: flow acceleration at the obstruction plane and increased turbulence (or turbulent mixing) downstream of the obstacle. The work confirmed also the previous findings that for the same obstruction ratio, the highest heat transfer augmentation was observed at lower Re numbers and decreased as the Re number increased.

Dalogu and Unal (2000) performed an experimental investigation of heat transfer from a heated cylinder located in the wake of another cylinder or a prism, for Re numbers ranging between 1,100 and 19,500. The copper test cylinder had d=12.5mm diameter and the length L=103.5mm (see Figure 2-2). Due to a relatively low temperature (max 100 °C) and the insulation at the ends, radiation and conduction heat transfer effects were negligible. In determining the average heat transfer coefficient, a lumped capacitance analysis (i.e. uniform temperature of the cylinder) was employed. Three sizes of front obstacle were used, as follows *D*=1*d*, 2*d* and 3*d* respectively (see Figure 2-2). Also, the dimensionless distance between the centres of cylinders (the ratio between axial distance between obstacles and diameter of the first cylinder, *P*= *L*/ *D*) was varied between 0.8 and 9. Re numbers were calculated based on the characteristic length of the flow being equal to the diameter of the heated (second) cylinder. The experimental results revealed that the convective heat transfer from a cylinder located in the wake of an obstacle depends on the obstacle geometry, dimensionless pitch ratio and flow Reynolds number. The comparison of Nu number for single cylinder and two cylinders versus the normalized distance between cylinders (see Figure 2-3) have shown that at lower Re numbers and small obstacle sizes (*d*) the first cylinder has no significant effect on the heat transfer from the second cylinder.

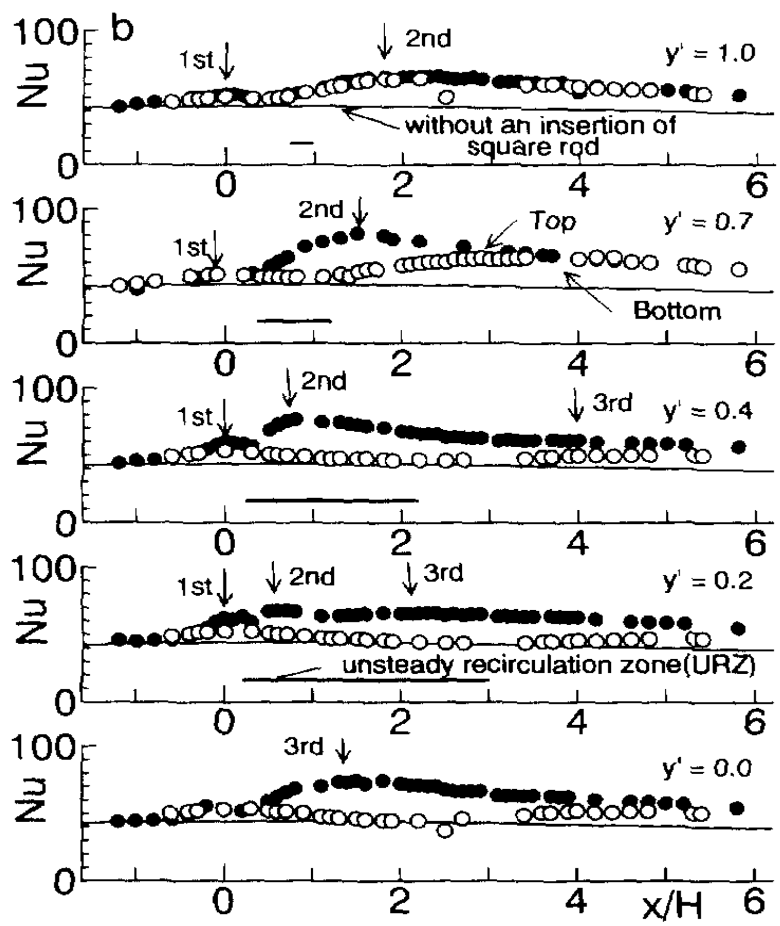

Figure 2 - 1 Distribution of local Nusselt number for fully developed conditions at Re=10,500 (Yao et al., 1995).

However as Re number increases, heat transfer is enhanced in average by 14% for small size cylinder and by 35% for the largest cylinder ($3D_o$). Also, at high Re numbers (~19,500) in the wake of the front obstacle (0.8 D_o) heat transfer coefficient is lower than the free stream case (single cylinder) but increases and remains relatively constant at distances larger than 2 D_o. These observations are confirmed by the experiments performed by Meinders and Hanjalic (2002) that showed that in the wake vortex the local heat transfer coefficient is relatively low. An interesting observation is that unlike internal flows, where a quasi-exponential decay of heat transfer enhancement was observed, for free stream flows, the enhancement shows a much weaker dependence on the distance downstream.

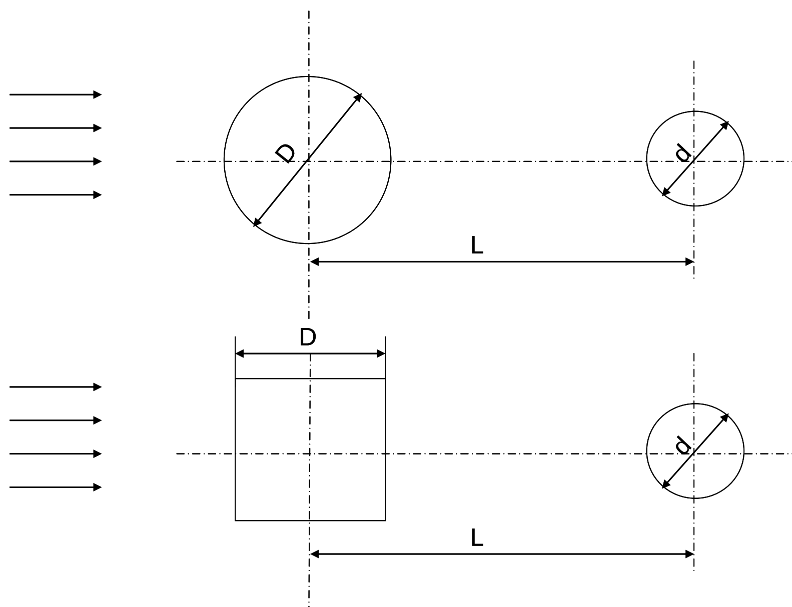

Figure 2 - 2 Arrangement of two cylinders and the coordinate system (Dalogu and Unal, 2000).

Slanciaukas (2001) pointed out the difference of wall roughness effects on convective heat transfer for liquids and gases, due to differences of thermal resistance of the viscous sublayer. For liquids, a Prandtl number range from 0.71 to 100 was investigated. The paper states that the main resistance to heat exchange in the turbulent boundary layer of many common liquids (such as water, glycerol, oil) is in the viscous sublayer. As an example, it is mentioned that for a fluid with Pr = 5, it causes about 60% of the temperature drop between the surface temperature and the bulk temperature; the proportion increases as Pr increases, such that at Pr = 100, in the viscous sublayer the temperature drop is 95%. The roughness elements create eddies that disturb the viscous sublayer and reduce its thickness, thus enhancing the local heat transfer.

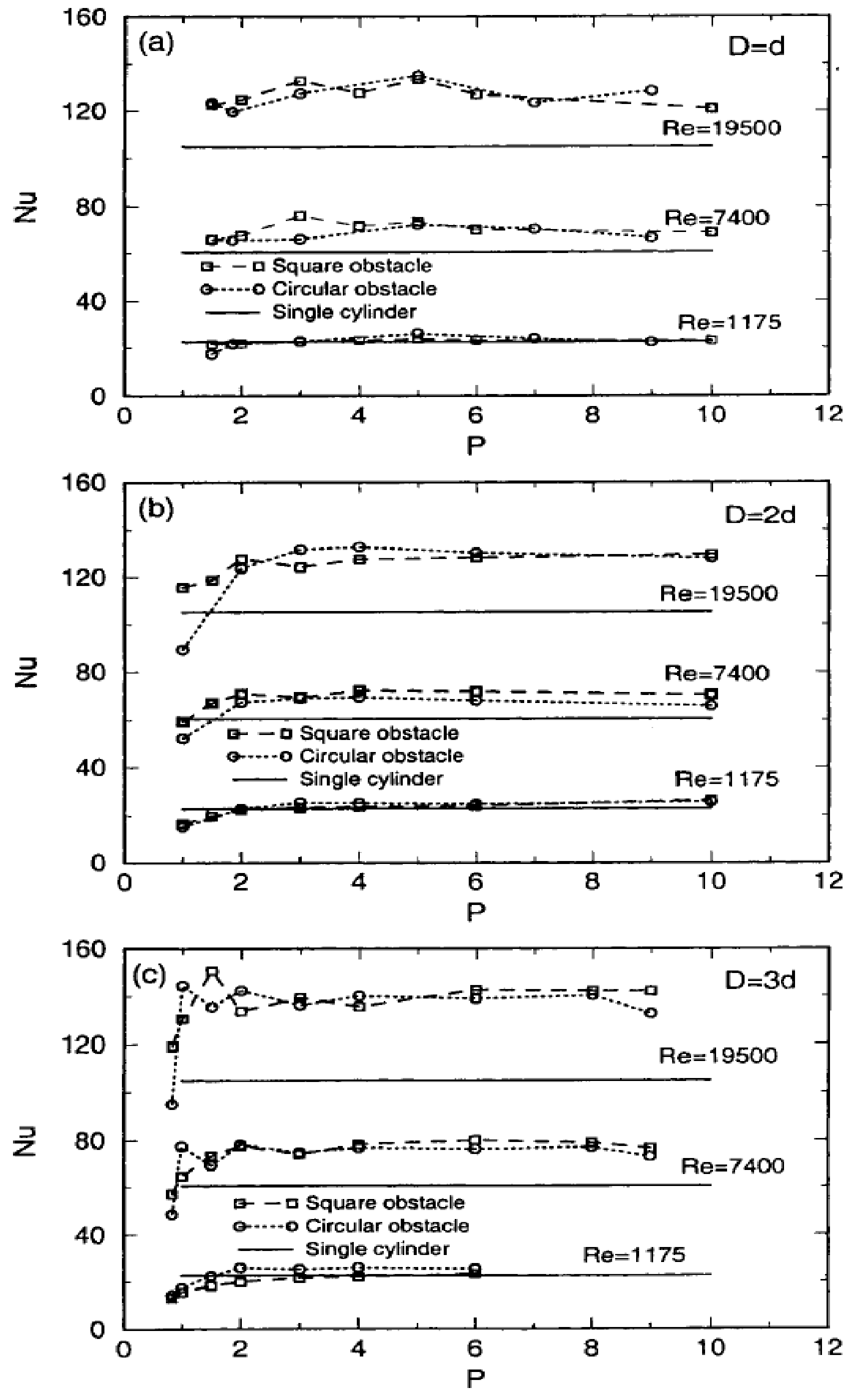

Figure 2 - 3 Comparison of average Nusselt number obtained using square and circular cross section obstacles a) *D*=*d* b) *D*=2*d* c) *D*=3*d* (Dalogu and Unal, 2000).

The increase of turbulence intensity within the viscous sublayer becomes noticeable when the roughness Re number (y^+) is greater than 10. The roughness Re number is defined as $y^+=u^*{\cdot}k/\nu$, where u^* is the friction velocity $(\tau_w/\rho)^{0.5}$, k is the height of the roughness element and ν is the kinematic viscosity. For gases it has been found that just behind the obstacle the local heat transfer coefficient reaches a minimum and increases rapidly as the streamlines reattach to the heated wall. Figure 2-4 (from Slanciaukas, 2001) shows that, for co-linear obstacles located at 14 obstacle heights the maximum enhancement is about 1.7 (compared with the bare heated channel), while at a pitch of 8 obstacle heights, the maximum enhancement is about 1.55. No explicit information about flow velocity or Re number was provided.

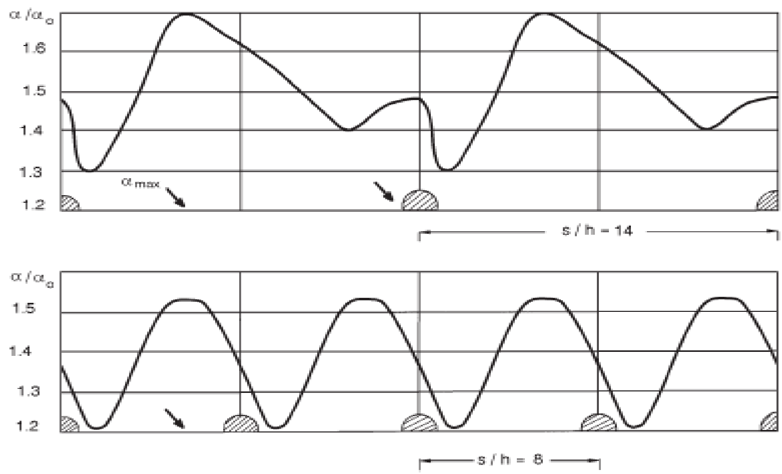

Figure 2 - 4 Measured local heat transfer coefficient in between the roughness elements at two different steps (Slanciaukas, 2001).

Meinders and Hanjalic (2002) investigated experimentally the convective heat transfer for in-line and staggered configuration of two wall-mounted cubes, located in a fully developed turbulent channel flow. Only the cubes were heated (the channel walls were unheated). The heat transfer coefficient was calculated from infrared thermography and local convective heat flux analysis. In order to study the vortex formation and flow around the obstacles, laser Doppler anemometry and flow visualisations were performed, as well. Although the research was focused on forced convective cooling of electronic components on printed circuit boards, the results and conclusions of this research can be applied to similar configurations of various thermal systems. The experimental setup consisted of two cubes of H=15 mm located on a wall of a rectangular channel with a height of 51 mm. The Reynolds number of the flow was calculated based on the bulk velocity of the air in the channel (3.9

m/s) and the characteristic length the size of the cube (15mm) resulting in a value of 3,900. The main method for flow visualization (performed at Re ~7000) was the oil-film technique. A laser Doppler anemometer was employed to provide quantitative information on the mean velocity, local velocity and turbulence fields. The overall accuracy of velocity measured by the anemometer was 5% and for second-order moments 10%. After careful calibration, the accuracy of the infrared thermography system was found to be 0.4 °C. The cubes were made of copper and covered with an epoxy liner. The measurement of the copper core and the epoxy surface temperatures provided data for calculating the conductive heat flux at the surface of the cubes. Their investigation found that for both in-line and staggered arrangements, the most important parameter that influences the flow pattern and the distribution of heat transfer coefficient is the axial distance between the cubes. The flow visualization revealed that complex vortex systems were formed around the cubes, consisting typically of a front horseshoe vortex, top, side and wake vortices. Schematically, the structure of flow pattern is shown in Figure 2-5 and the typical profile of measured heat transfer coefficient in vertical and horizontal planes that divide the flow obstacle symmetrically is shown in Figures 2-6 and 2-7, for the front cube and second cube, respectively, at various relative distances between the cubes. It can be observed that the local heat transfer coefficient strongly depends on the local flow structure. As expected, flow structure and distribution of heat transfer coefficient of the front cube is practically not dependent on the geometrical configuration of the two cubes. Also, the flow detachment and recirculation vortices reduce locally the heat transfer coefficient. In the authors' opinion this effect can be due to the heat removed from the hot faces and re-trapped by the vortex. The experiments conducted at various axial distances between obstacles (S_x/H=2, 4 and 8) have shown that for S_x/H=2, there is no re-attachment of streamlines to the channel wall between the flow obstacles and a stable recirculation vortex is formed in the space between the flow obstacles. At S_x/H=4 and 8, the flow re-attaches to the channel floor at about 2.5 S_x/H in the wake of the first obstacle. In all cases for the in-line arrangement, the symmetry of the averaged flow field and heat transfer distribution was maintained. However, for the staggered layout, and a relatively small longitudinal spacing, a strong flow deflection and asymmetrical flow pattern and heat transfer coefficient was observed. Similar to the in-line configuration, in the staggered layout, the flow pattern around the first cube was not affected by the system geometry. The wake of the upstream cube was subject to periodic vortex shedding, that were measured and plotted as non-dimensional Strouhal number. This behaviour created periodic variations in measured heat transfer coefficient of the downstream cube. In spite of the uneven distribution of local heat transfer coefficient and its dependence on the system geometry, it was found that the downstream cube-averaged heat transfer coefficient is not very sensitive to the streamwise and spanwise distances between the cubes, which suggests that the bulk flow through the channel controls the overall heat convection from the cubes (at Re_H=3900) (see Figure 2-5). A similar observation was made for the upstream cube.

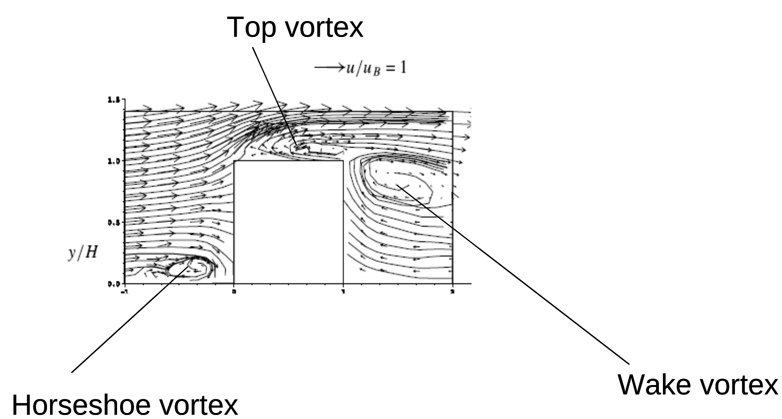

Figure 2 - 5 Typical vortex structure around a cube (Meinders and Hanjalic, 2002).

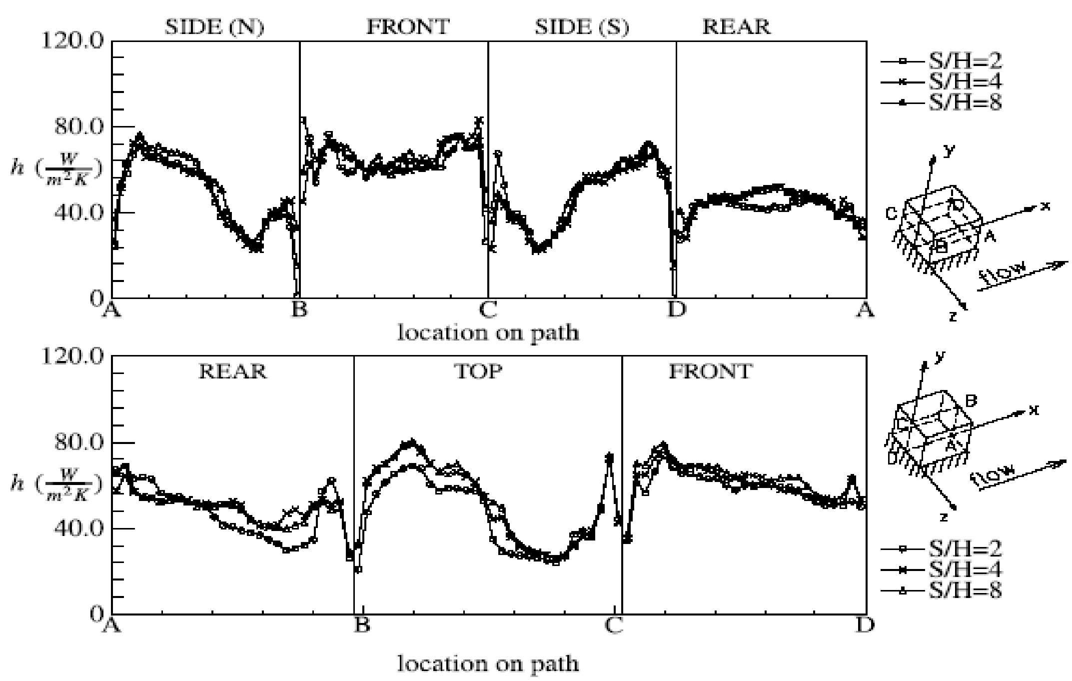

Figure 2 - 6 Distribution of measured local heat transfer coefficient for the front cube (Meinders and Hanjalic, 2002).

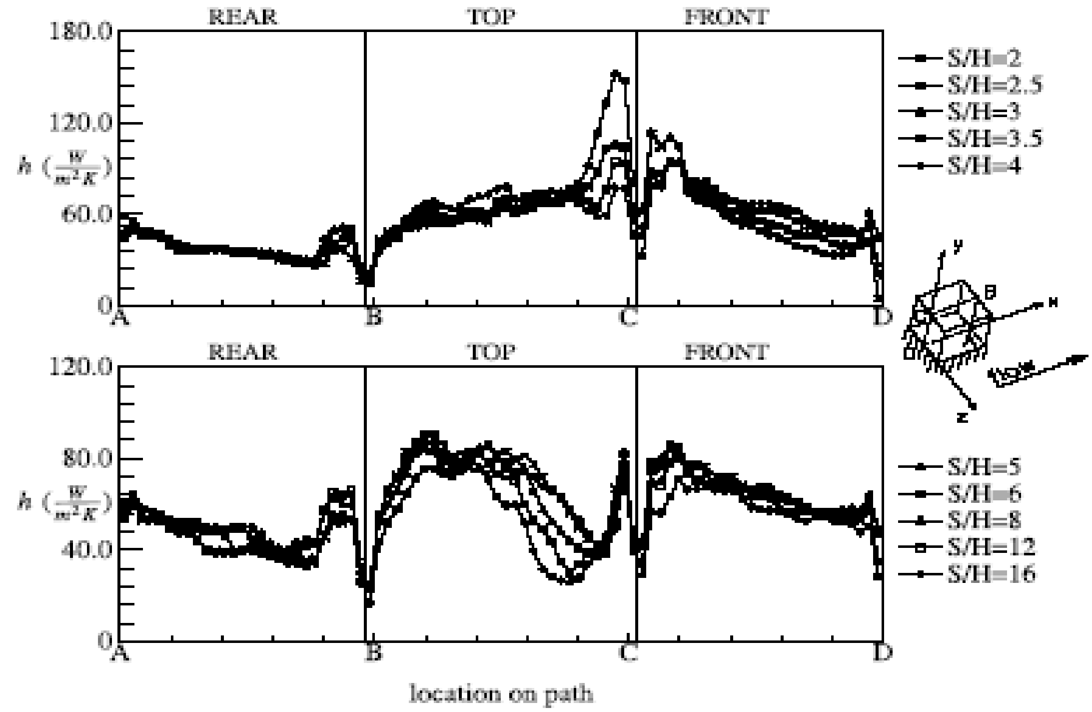

Figure 2 - 7 Distribution of measured local heat transfer coefficient for the second cube (Meinders and Hanjalic, 2002).

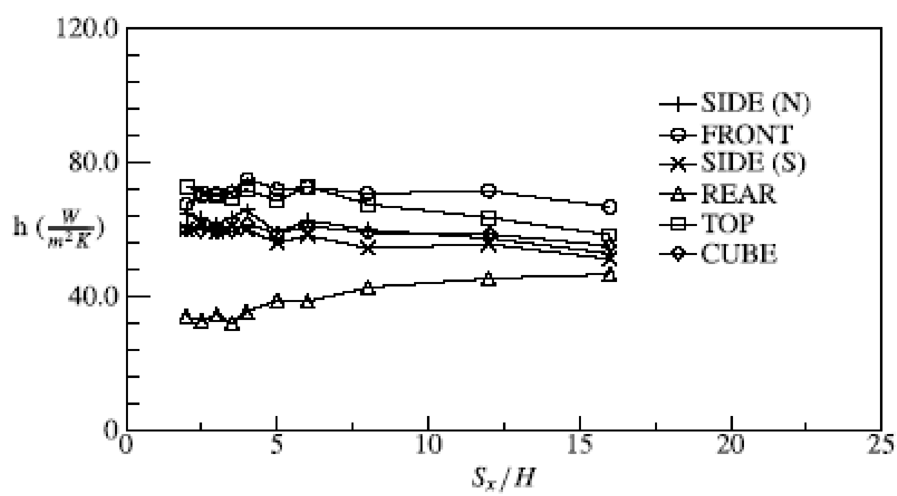

Figure 2 - 8 Averaged heat transfer coefficient for the sides of the second cube for in-line tandem as function of the normalized axial distance (Meinders and Hanjalic, 2002).

Terekhov et al (2002) conducted an experimental study on flow structure behind a step and a rib located in a square cross section wind tunnel. The flow free stream velocity was 20 m/s, thus the Re number based on the channel height was $3{\cdot}10^5$. Two obstacle heights were studied: 10 and 20 mm, respectively. Oil film flow visualization[3] was employed to observe the separated flow behind the obstacles. The authors reported that the flow structures in the secondary separation region behind a step and a rib are similar; however, due to flow "overshoot" over the rib, the flow is more strongly disturbed, hence the recirculation region is longer (see Figure 2-9).

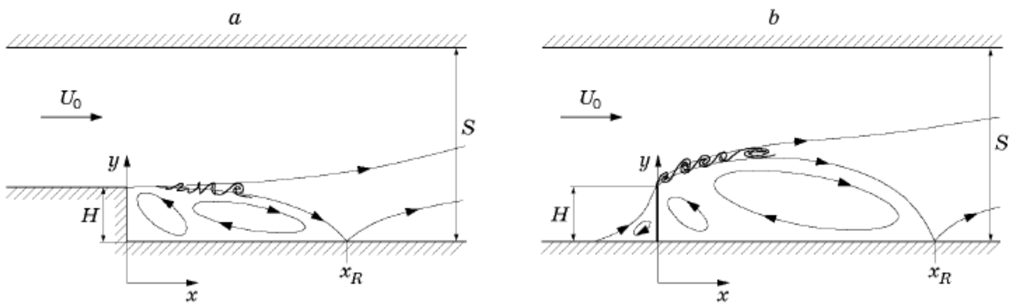

Figure 2 - 9 Separated flow over a backward facing step and a rib (Terekhov et al., 2002)

This difference could be explained by the flow history upstream from the flow obstruction. The recirculation vortex formed in the front of the rib changes the structure of the flow downstream significantly, thus the reattachment of flow to the channel floor downstream of the rib is longer: for a step with height H = 20 mm, the reattachment length was ~4.8H along the centerline and about 16.5H for the rib with the same height. The review and the experimental work performed concluded that behind a step the reattachment length varies between 4.5H and 8.5H, showing small sensitivity to Re number (when variation of Re number is achieved by the velocity variation only). However, the reattachment region is influenced by the obstruction ratio and the ratio between obstacle height and boundary layer thickness. It has been found that the maximum velocity of the back flow toward the step in the recirculation vortex is less than 30% of the free stream velocity; by contrast, in the rib type

[3] Oil film visualization is a technique employing coating the surface of interest with a layer of oil in which a finely powdered pigment was dissolved. The working fluid (e.g. air) carries away the oil and the dry pigment forms streaky patterns on the surface, indicating the direction of the flow, as well as the steady coherent structures (e.g. flow separation or reattachment)

obstacle, the back flow velocity exceeds 40% of the free stream velocity, which increases with the obstacle height.

Khan et al. (2002) conducted an experimental investigation in a rectangular channel with inclined solid and perforated baffles combined with ribs, in turbulent air flow. The development of flow was allowed over a length of 31*H*, where *H*=4.92 cm. The heated part was 19.2*H* and the exit, downstream of the heated part was 22.2*H*. The temperature of the heated section was measured by thermocouples mounted on the top of the heated surface. The experiments were performed with three perforated baffles (with holes of 1.07 cm diameter) and one solid baffle. The ribs were made of wood; they had a cross section of 0.635x0.635 cm and they were mounted on the heated surface. The pitch was approx. 6.3 cm (i.e. 10 rib heights). The flow Re number was calculated based on the free stream velocity and channel height and was 37,300 for all experiments. For the reference case (smooth channel) the measurements indicated that as the hydrodynamic and thermal boundary layers develop, the heat transfer coefficient and Nusselt number decrease. When the ribs were placed periodically in the channel, the normalized Nu number increased and reached a value of 2 at the beginning of the heated length and about 1.5 in subsequent peaks, leading to higher average Nu number for the ribbed channel. The results shown in Figure 2-10 suggest that the test section entrance and the blunt obstacles disturb the boundary layers in a similar way, hence the peak normalized Nu are practically equal.

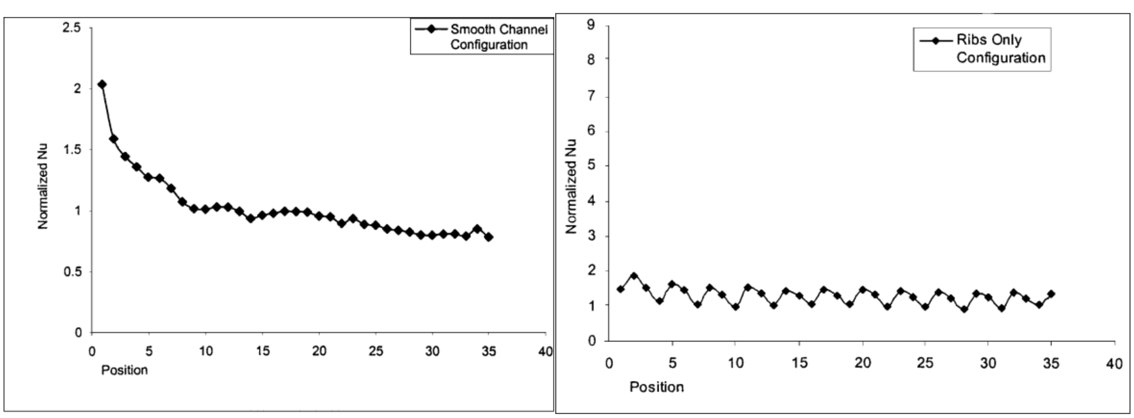

Figure 2 - 10 Local normalized Nusselt number for smooth (left) and ribbed channels (right) (Khan et al. (2000).

The separation of flow occurs upstream and downstream of the ribs and the points of separation created local hot spots where the normalized Nu decreased below the smooth channel value. The experiments also examined the effect of a baffle on the enhancement of heat transfer. The combined action of baffle and ribs yielded an average increase in Nu number and pressure drop of respectively 326% and 250%. According to the authors, the baffle enhancement effect on heat transfer was caused by jet impingement on the heated surface and the supplementary turbulence and flow mixing. It has been found that an increase in the angle of inclination of the baffle enhanced the local heat transfer coefficient. Also, the baffle with very high perforation count performed poorly, while the baffle with low perforation count had the highest heat transfer enhancement.

Holloway et al. (2004) measured the heat transfer coefficient downstream of support grids with and without flow-enhancing features (e.g. split vanes) at Re numbers between 28,000 and 42,000. The geometrical configurations consisted of support grids with disk blockages and split vanes, respectively. The measurements confirmed that the greatest heat transfer augmentation occurs just downstream of the flow obstructions. Data analysis indicated that both power-law or exponential functions can reasonably describe the decay of heat transfer augmentation with an increase of distance downstream from the obstacle. The authors propose several semi-empirical correlations of heat transfer enhancement downstream of spacers with or without flow enhancing features.

For the enhancement downstream of a standard support grid (i.e. without flow enhancing features) the proposed correlation is:

$$\frac{Nu}{Nu_0} = 1 + C_1 \varepsilon^2 \exp(-\alpha x / D) \quad , \qquad (2.4)$$

where C_1=6.5 and α = 0.8.

The same experimental data were also correlated in power-law form and the following equation resulted

$$\frac{Nu}{Nu_0} = 1 + 3.0\varepsilon^2 \left(\frac{x}{D_h}\right)^{-1.3} \qquad (2.5)$$

The newly proposed correlations were valid for a *x/D* range of 1.4 to 33.6.

A comparison between the above mentioned correlations and Yao et al. (1982) shows that the Yao correlation tends to over-predict Holloway correlations and the experimental data, as showed by Figure 2-11. Plots in Figure 2-11 are based on the results of two grid designs: grid A (standard egg-crate type grid without vanes) with an obstruction ratio 0.2 and grid G (Standard egg-crate type grid without vanes. Grid G has a longer length compared to grid A)

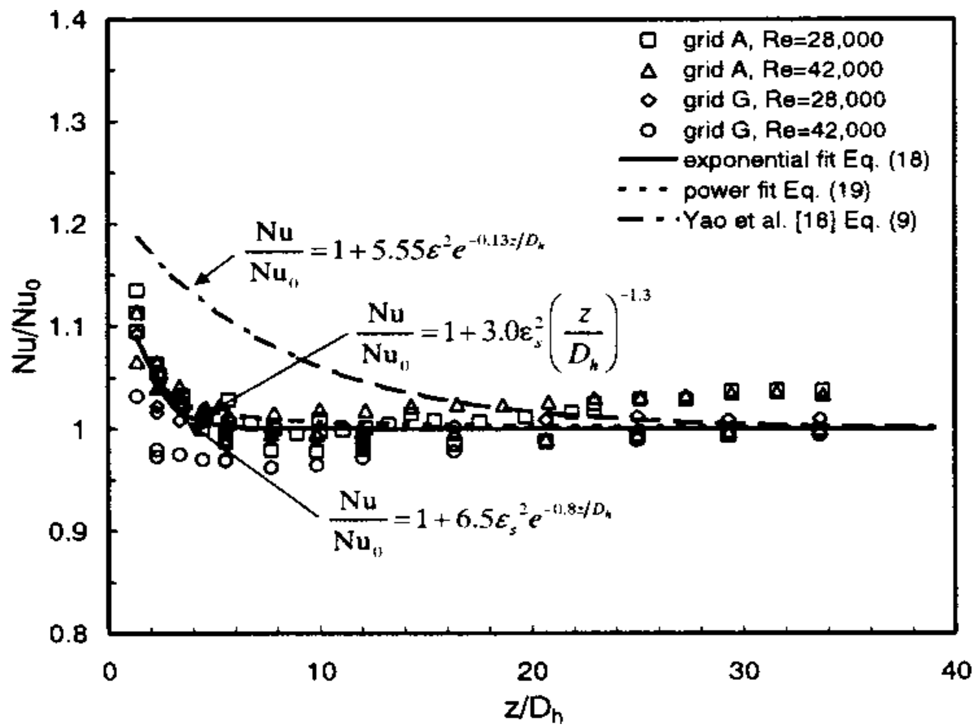

Figure 2 - 11 Nusselt number normalized by hydrodynamically fully developed Nusselt number for standard grids A and G and comparison with Yao predictions (Holloway et al., 2004).

Figure 2-11 also indicates that the axial length for which the enhancement is noticeable is approximately 10 x/D_h, which is much shorter than predicted by the Yao et al (1982) equation that showed an enhancement effect up to 35 *D*.

In addition to the previous work (Holloway et al.,, 2004) which studied mainly the axial effect of the flow obstacles, Holloway et al (2005) also studied the azimuthal variation of heat transfer coefficient in rod bundles. The azimuthal variations were measured for three specific support grid designs (standard grid, split-vane pair grid and disc grid) at axial locations between 2.2 to 36.7 D_h, at Re number 28,000 and 42,000, respectively. The split-vane pair grid creates swirling flow and enhance mixing among parallel channels. The standard grid had no flow enhancing features and was used as the reference case and a comparison basis for the grids with flow enhancing features. Disc grids were considered as blunt type obstacles, while the split-vane grids were associated with the streamlined class. As in the previous work, a 5x5 square array rod bundle was used. Azimuthal variations of Nusselt number were obtained for the central rod of the bundle. The outside diameter of the rods was 9.5 mm and D_h = 11.78 mm. Three grids were positioned at a pitch of 508 mm, first grid being located at 90 mm downstream of the test section inlet. The estimated uncertainty of the azimuthal variation in Nusselt number was 4%. The measurements indicated that the highest azimuthal variation of local Nu number occurred just downstream (at 2.2 D_h) of the grid and decreased with the development of the flow downstream. It can also be observed that the lowest values correspond to small gaps between the grid and the rod, with obvious minimums at 180º and 270 º. (see Figure 2-12) The trends were similar at high and low Re numbers. The azimuthal variations for disc type obstacle were very small and are within the experimental measurement accuracy. By contrast, much larger azimuthal variations (+30% to -15%) were observed for the split-vane pair (see Figure 2-13).

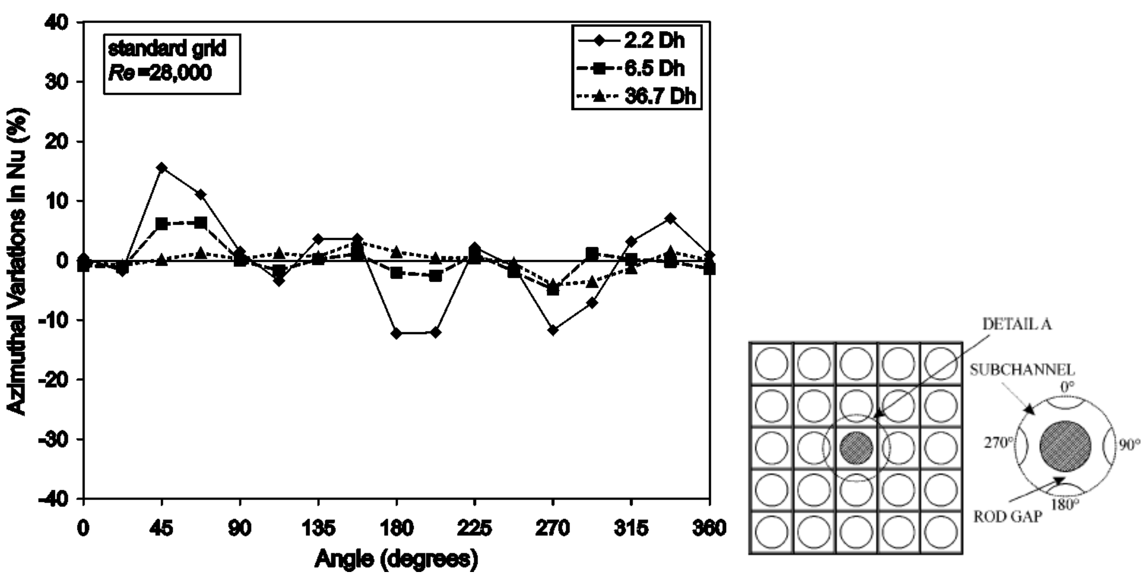

Figure 2 - 12 Azimuthal variation in Nusselt number for standard grid at Re=28,000 (Holloway et al., 2005).

In all cases the variations were the largest at the location just downstream of the obstacle. Figure 2-13 shows the colour maps of measured temperature difference between the rod surface and the bulk temperatures (T-T_b), for standard grid, disc grid and split vane pair grid. The colour maps suggest that heat transfer coefficients show azimuthal profiles that are persistent for a significant distance downstream, up to $25D_h$. The strongest azimuthal variations were observed for the split vane pair grid and the weakest for the disc grid.

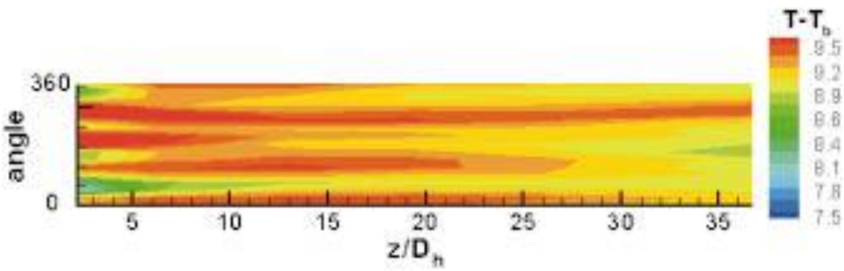

(a)

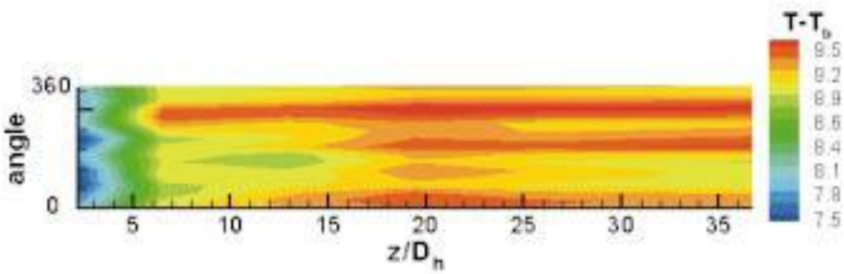

(b)

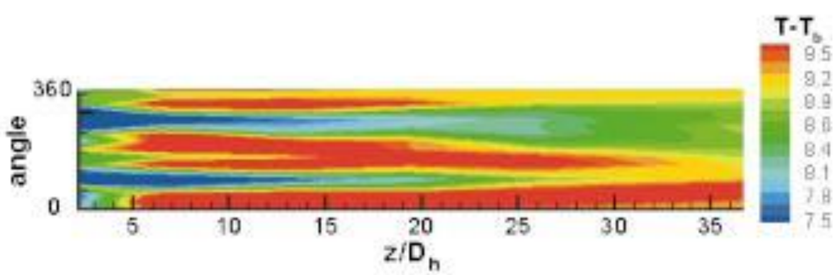

(c)

Figure 2 - 13 Contour plots of temperature difference T-T_b at Re=28,000 for (a) standard grid, (b) disc grid and (c) split-vane pair grid (Holloway et al., 2005).

2.2 Numerical simulations

A large number of numerical simulations have been performed, especially for geometries of interest in the nuclear, electronics or chemical industry. Continuous development of specialized software and computational power has allowed detailed studies of relative complicated geometries for a range of Re numbers.

Karoutas et al. (1995) performed a 3-D CFD simulation of single phase liquid flow around a nuclear fuel spacer. A single subchannel of one grid span was modelled. The software (CFDS-FLOW3D) solved Reynolds Averaged Navier-Stokes (RANS) equations to calculate the flow field; a k–ε model was employed to model the turbulence. The simulation was intended to enhance the understanding of the fluid dynamics of grid spacers and mass transfer between different adjacent subchannels in nuclear fuel bundles. The simulation results were compared to Laser Doppler Velocimetry (LDV) measurements, performed in a full scale cold water loop. The experimental fuel array consisted of 5X5 rod array test section. The velocity measurements were performed at seven axial elevations in regions with and without mixing vanes. Pressure drop measurements were performed, as well. The reported accuracy of velocity measurement (i.e. errors in data processing, seeding, laser beam geometry) was better than 0.5%. Two vane mixing devices were studied: split-vane and squeezed tube vane. Both types generate swirl flow around the heated rods, thus enhancing the heat transfer coefficient and critical heat flux (CHF). In general, a good agreement was obtained between the measurements and the simulations. The largest differences were observed at spacer locations and they were explained by the modelling simplifications of the mixing devices, which were modelled with a thin surface option (i.e. the mixing vane had no thickness and was placed between two computational cells). The lack of thickness of the mixing vanes model neglects the reduction in cross sectional flow area, therefore, the flow acceleration was not captured by the numerical simulation. Also, the choice of RANS with k-ε for computation of flow field was less than optimum due to the averaged nature of the solution. Another simplification was introduced by the application of the symmetric boundary conditions between adjacent channels. However, in spite of the simplifications mentioned above, the simulation results agreed satisfactorily with the measurements of swirling flow downstream of split vanes. The investigation was limited to flow velocities only and no heat transfer phenomena were modelled.

A numerical investigation by Youn and Vafai (1998) on a channel equipped with a heated rectangular obstacle showed that the local Nu number strongly depends on the velocity distribution and the flow pattern, results which were in agreement with the findings of Meinders and Hanjalic (2002). Special attention was given to the Nu number distributions as well as the mean Nu numbers for different faces of the obstacle. A 2-D numerical solution of mass, x-momentum, y-momentum and fluid phase energy conservation was performed. Also, 2D Laplace conduction equation inside the obstacle was solved numerically. The lower and the upper channel walls were insulated; therefore the heat transfer occurred only at the obstacle surface. The geometry and the structured mesh around the obstacle are shown in Figure 2-14.

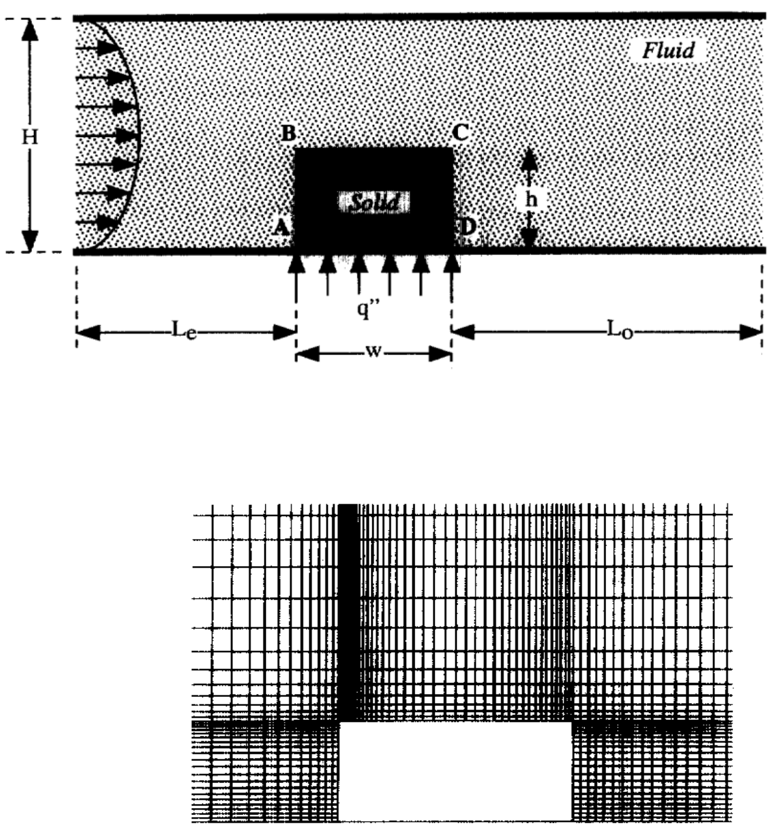

Figure 2 - 14 Channel geometry and a close-up of the mesh around the obstacle (Youn and Vafai, 1998).

Sensitivity and convergence analyses indicated that, in order to eliminate the influence of entrance conditions on the solutions near the obstacle, a flow development length of at least two channel heights was required. Similarly, to ensure that the recirculation downstream of the obstacle was captured within the computational domain -, a minimum length of eight obstacle heights was required (see Figure 2-15). The meshes ranged from 214 x 60 to 274 x 76 elements. The characteristic length of the flow was taken as the hydraulic diameter of the channel, $D_h = 2H$. The Re number range covered the laminar and transition regions - from 800 to 3200. The investigation concluded that the vortex downstream of the obstacle extends from four to fourteen obstacle heights, depending of the flow Re number. The maximum heat transfer coefficient was predicted at the top of the leading edge whilst the minimum close to the top of the trailing edge. The relatively low Re numbers investigated limited its applicability to very low flows.

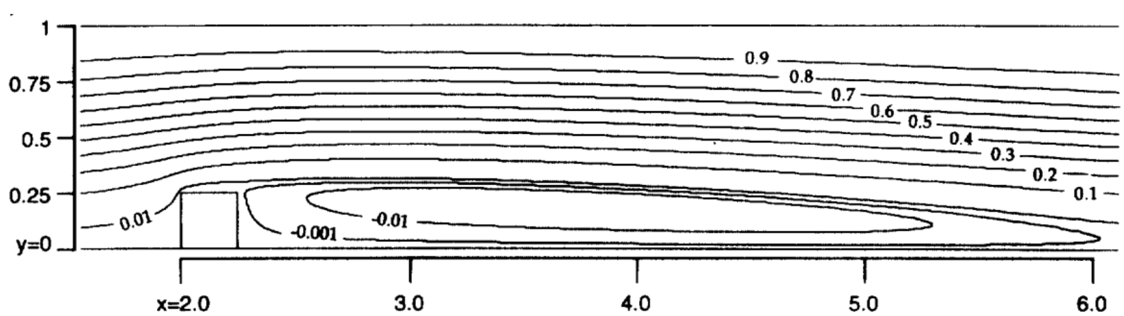

Figure 2 - 15 Streamlines of flow around the obstacle at Re=2,000 (Youn and Vafai, 1998).

Shuja et al (2000) performed numerical simulations of laminar flow past a rectangular obstacle. The steady and unsteady, 2-D Navier-Stokes and energy equations were solved at Re=500. A comparison between the steady and the unsteady solutions was performed. The length of the simulated channel was 1.1 m and the height 0.88 m. The 2-D computational grid had 80 x130 elements. The simulations showed that the vortex shedding (i.e. unsteady flow) significantly enhanced the heat transfer from the heated obstacle. It was concluded that the orientation of vortices and circulation influence the heat transfer characteristics thus the unsteady simulations, although computationally expensive, may give more realistic and better results.

Seo and Parameswaran (2001) analysis for dilute gas particle suspension heat transfer reported that the standard k-ε turbulence model underpredicts the reattachment length for recirculating flow behind a backward facing step. The authors recommend the employment of a low Re k-ε turbulence model for turbulent buoyant recirculating flows, as well as an adaptive grid and a finer mesh near the separation region to accommodate highly variable flow field gradients. In order to avoid the singularity that appears at the separating and the reattaching points, Kolmogorov velocity $u_\varepsilon = (\nu\varepsilon)^{1/4}$ was used instead of shear velocity ($u_\tau = \sqrt{\tau_w / \rho}$).

Labbe et al (2002) performed large-eddy simulations of flow over a backward-facing step to study the heat transfer in the reattachment zone. The Navier-Stokes and energy equations were solved in a second-order accurate semi-implicit scheme in space and time. The computational grid was 186 x 41 x 93, with the size in vertical direction in the near wall region varied from Δz_{min}=0.012h to Δz_{max}=0.11h, where h is the height of the obstacle. The Re number of the flow, based on the free stream velocity and step height was 7,432.

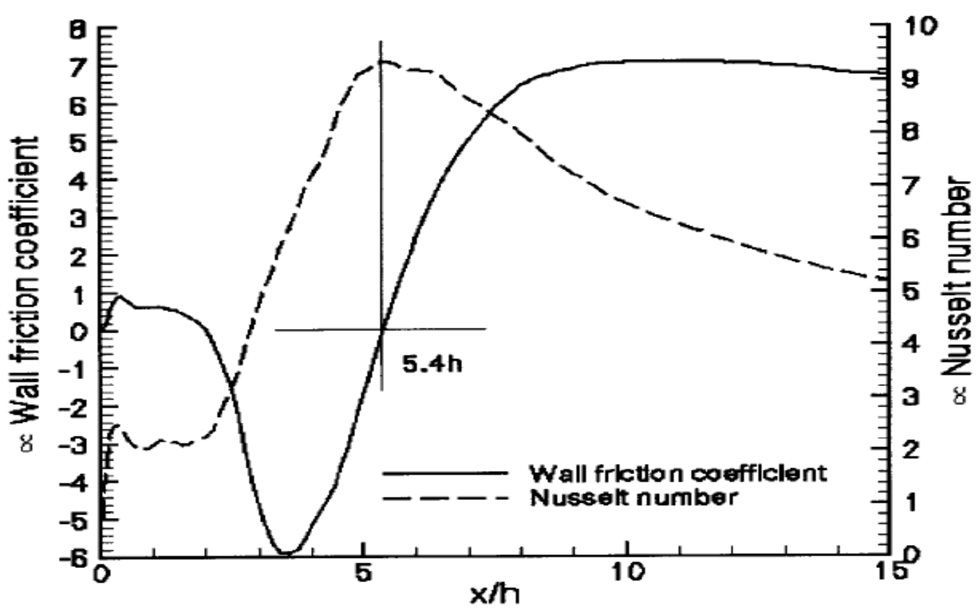

Figure 2 - 16 Bottom wall skin friction coefficient and Nusselt number (Labbe et al., 2002).

The simulations showed (see Figure 2-16) that the reattachment length was 5.4*h* and mixing in the recirculation region behind the step was weak. Plots of Nu number at the bottom wall indicated that the maximum Nu number is obtained at the reattachment point, at 5.4*h*, and is correlated with the location of zero wall skin friction. The maximum Nu number reaches 9.2 at the reattachment and decays downstream, as the boundary layer develops. At the end of the computational domain (~15*h* downstream), the enhancement effect was still significant, Nu number being around 5.2.

CFD simulations of flow around obstacles at relatively low Re numbers (100-1000) were conducted by other researchers, such as Bhattacharyya and Mahapatra (2003) that studied numerically the heat transfer around a heated obstacle of semicircular cross section cooled by an incompressible fluid. The Navier-Stokes and energy system of equations were resolved in an upwind difference scheme. The simulation results indicated that the downstream eddy length is quasi-proportional with Re number. Also, it has been found that the flow separates upstream and downstream at Re>5.

Korichi and Oufer (2005) performed numerical simulations to investigate heat transfer and pressure drop of heated obstacles mounted on the upper and lower walls in a rectangular channel. The governing equations were solved using SIMPLE algorithm with finite volume formulation and second order accuracy. They found that the overall heat transfer coefficient increased with Re number. Heat transfer enhancements of up to 21.7% for the first obstacle and 77.6% for the second were observed. The obstacle pitch had no significant effect on heat transfer and the pressure drop increased when obstacle height was increased.

Suga (2004) performed simulations of turbulent obstacle flow field with heat transfer. In the author's opinion, the poor performance of many Reynolds Averaged Navier-Stokes (RANS) turbulence models in turbulent wake flows can be due to the modelling of the pressure-diffusion term of the Reynolds transport equation, especially in the recirculating flow regions. The computational domain consisted of a rectangular channel (height 2*H*) equipped with a rectangular rib of height *H* (2D geometry). The Reynolds number based on free stream velocity and obstacle height was 3350. Constant temperatures were imposed on the upper and lower walls. The RANS results were compared with Large Eddy Simulation (LES) results. The LES Nu number on the bottom plane showed a maximum of about 20 at 3-5 obstacle heights (*x/H*) downstream the obstacle and decreases monotonically. At about *x/H*=26, the value of Nu reaches the free stream value, 6. Immediately downstream of the trailing edge of the rib the Nu number approaches 0, but then increases rapidly, reaching a maximum after ~2*H*. The work emphasized also the importance of rapid pressure-diffusion terms near the reattachment zone behind the obstacle.

Chandra et al. (2009) analysed supercritical heat transfer of CO_2 in the presence of various flow obstacles to show the impact of flow obstacles on the deteriorated heat transfer region of supercritical CO_2, at mass flux of 400 kg/m^2s. The reference case consisted of a bare annulus with inner diameter 8 mm and outer diameter 10 mm, with uniform heat flux of 120 kWm^{-2}. The enhanced tube consisted on square ring of 0.5 mm height, respectively semi-circular ring with radius 0.5 mm, as showed by the Figure 2-17. Both flow obstacles were located 200 mm from the inlet.

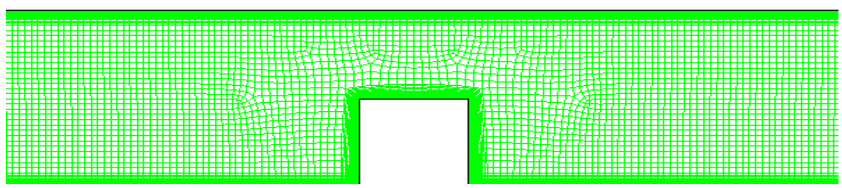

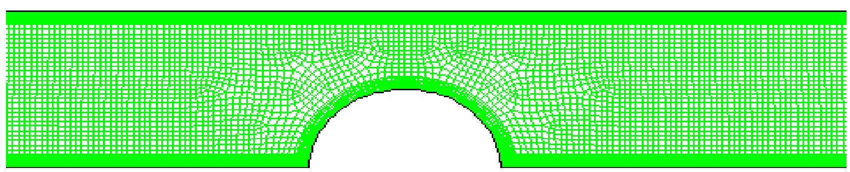

Figure 2 - 17 Channel with square cross section ring (top) and semicircular cross section ring (bottom) (Chandra et al., 2009).

A SST k-ω turbulence model with Enhanced Wall Treatment was employed for the CFD simulation. The results indicated that, both obstacle types reduced the downstream temperature for a distance of more than 0.1 m. The wall temperature reduction was significant just downstream of the flow obstacle. Qualitatively, in the downstream region the differences between the square and semi-circular rings were small. However, in front of the obstacles (upstream) the simulations indicate a temperature peak, attributed to flow stagnation that significantly reduces the local heat transfer coefficient. The magnitude of the temperature peak is about 750K for the square shaped ring and 550K for the semicircular cross-section obstacle. Although one can expect that stagnation is more severe for blunter obstacles (in this case the square shaped ring), the magnitude and shape of the predicted temperature peaks (they are very narrow) do not seem realistic. The authors acknowledge that the thermal conduction in the tube wall was not modelled and this might significantly reduce the local temperature in the front of square and semicircular obstacles.

A numerical study of heat transfer to supercritical water in vertical tubes equipped with flow obstacle was performed by Zhang et al. (2009) using FLUENT 6.1 and the RNG k-ε model with an enhanced wall treatment. Due to the annular geometry, a two-dimensional simulation with structured mesh was appropriate. Convergence was achieved when residuals summed over all computational nodes were below 10^{-6}. The predicted heat transfer coefficient was compared with experimental results of Yamagata (1972) and showed a satisfactory match. A sensitivity study of heat transfer enhancement as a function of blockage ratio, in the range of 0.1 to 0.7 revealed that heat transfer enhancement increases monotonically with the increase of blockage ratio, as the plots from Figure 2-18 suggest. It also can be observed that the effect of heat transfer enhancement decays after approximately 30 D_h downstream. A comparison of the simulated results with prediction methods suggested by Yao et al. (1982) and Holloway et al. (2004) concluded that the closest match is with the Yao correlation.

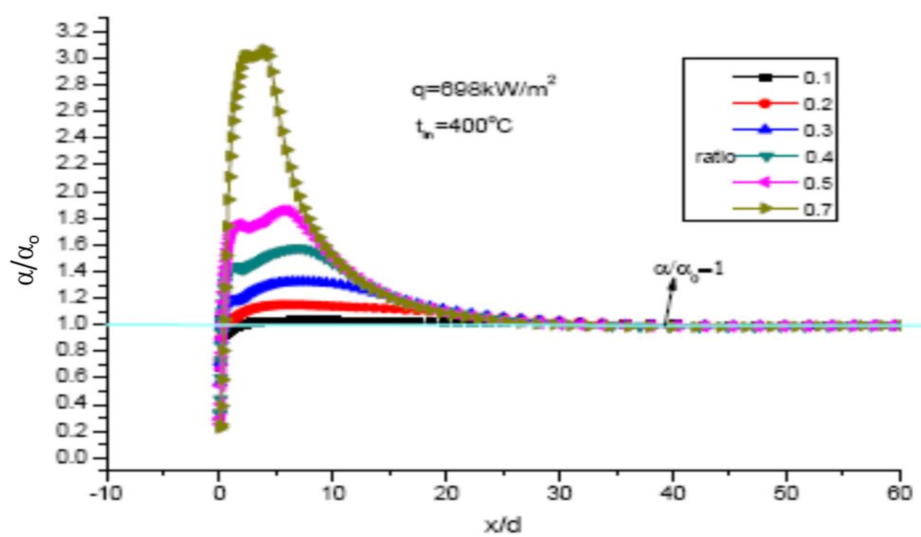

Figure 2 - 18 Heat transfer enhancement decay with downstream distance for different blockage ratios, q=698 kW/m^2 (Zhang et al., 2009).

CHAPTER 3

Experimental Facilities and Procedures

Heat transfer experiments were designed to measure the heat transfer coefficient at various axial and circumferential locations downstream from the flow obstacles. In order to determine the local heat transfer coefficient, the test section wall was Joule heated by a direct current (DC) power supply and the wall temperature was measured using thermocouples mounted on the outside wall of the test section. The inside wall temperature was determined by solving the heat conduction equation and taking into consideration measurements of the outside wall temperature, the heat generated in the wall, the test section geometry and the material properties. The local heat transfer coefficient and the local Nusselt number were calculated from the inside wall temperature, the bulk coolant temperature and the surface heat flux. In order to systematically investigate the variables of interest for the heat transfer experiment, a text matrix which defines the ranges of flow and geometric parameters, was developed. Further details regarding the heat transfer experiment are included in Section 3.1.

Pressure loss experiments were designed to measure the differential pressure between the ends of the test section which contained the flow obstacle, in order to determine the obstacle pressure loss coefficient and the pressure distribution around the flow obstacle. The distance between the pressure taps located near the ends of the test section was selected such that it contained the recirculation zone and allowed the flow to recover, so that the measured differential pressure included the friction and non-recoverable local pressure losses. The test section wall was transparent, thus permitting PIV measurements of the flow around flow obstacles. Further details regarding the pressure loss and the PIV experiments are included in Section 3.3.

Although the heat transfer and pressure loss/ PIV experiments were performed in different test sections and used different fluids (R134a and water, respectively), the results of the two experiments can be compared, because the main geometric parameters of interest (in dimensionless form, such as the shapes and aspect ratios of the flow obstacles and the blockage ratios) were comparable and the results were presented in normalized forms (e.g., as pressure loss coefficient, Reynolds number and Nusselt number.

The selected range of the flow blockage ratio and flow Reynolds number are relevant for the geometry and operating conditions of CANDU and Light Water Reactors (LWR).

The two experimental facilities used in this investigation (the multi-fluid test loop and the adiabatic water loop, both located at the University of Ottawa) are described in the following Sections.

3.1 Heat transfer experimental loop

Heat transfer experiments were performed in the multi-fluid test loop at University of Ottawa using HFC-134a as working fluid. The main components of the loop are the test section, condenser, pressurizer, pumps, preheaters, power supply and loop instrumentation. (see Figure 3-1). The test section is directly heated by a 12 kW direct current (DC) power supply. The inlet and outlet fluid temperatures of the test section are measured by two resistance temperature detectors (RTDs). The flow is recirculated by two gear pumps, installed in series, and delivering a constant volumetric flow rate. A bypass around the pumps controls the flow rate. The flow is measured by a Coriolis flow meter (MicroMotion, Model DH025) with an accuracy of at least 0.5% and a flow range from 0 to 0.34 kg s^{-1}. The pressure in the loop is controlled by the pressurizer. The pressurizer contains a heating coil, located at the bottom and a cooling coil near the top of the pressurizer. The power to the pressurizer heater (maximum 500 W) is regulated by an adjustable alternate current (AC) transformer. An electric pre-heater (maximum power 5 kW) and a coaxial heat exchanger (with hot water on the secondary side) are located between the pumps and the test section. They are used to adjust the test section inlet fluid temperature or inlet mass quality to the desired values. The vapour, if any, generated in the test section is condensed by a coaxial heat exchanger prior to the fluid being recirculated to the pump. A piezoelectric pressure sensor measures the absolute pressure at the outlet of the test section (TS), and a differential pressure sensor measures the pressure drop along the TS.

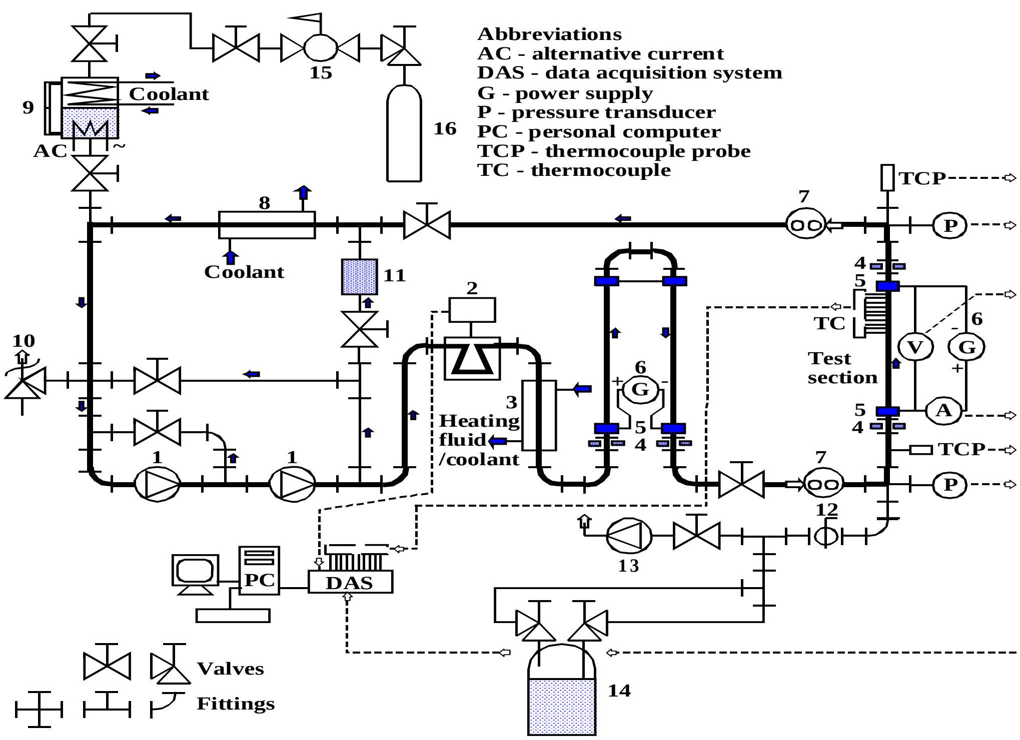

1-gear pump, 2-Coriollis type mass-flow-meter, 3-pre-heater, 4-dielectric fittings, 5-power terminals, 6-electrical pre-heater, 7-sight glass, 8-condenser, 9-pressurizer, 10-pressure relief valve, 11-refrigerant filter-dryer, 12-ball-valve, 13- vacuum pump, 14-refrigerant storage tank, 15-pressure reducer, 16-nitrogen container.

Figure 3 - 1 University of Ottawa Multi-Fluid Loop (Vertical Test Section).

Heat transfer measurements were performed in an electrically heated tube, made of Inconel 600 and having an inside diameter (*ID*) of 5.59 mm, an outside diameter (*OD*) of 8.00 mm, a total length of 2 m and a heated length of 0.9 m. The temperature of the exterior wall of the test section was measured by six K-type self-adhesive thermocouples, located in pairs 180º apart at three axial planes as shown in Figure 3-2. Three types of flow obstacles were inserted sequentially in the test section: a blunt cylinder, a rounded cylinder and an annular cylinder, coaxial with the test section. Each obstacle had a length of 10 mm and was manufactured from mild steel (see Figure 2). A ceramic magnet, located on the outside of the test section, held the obstacle at the desired location. The magnet was axially relocated during the experiment (thus relocating the obstacle) to permit the measurement of two effects on the local heat transfer coefficient: (i) the effect of distance downstream from the obstacle and (ii) the effect of azimuthal location. The heat transfer coefficient was measured at x/D = 3, 5, 7, 10, 20, 30, 50 and 70 downstream from the flow obstacles. Three obstacle shapes - hemispherical cylinder, blunt cylinder and annular cylinder, two blockage ratios (0.15 and 0.3), and four Reynolds numbers in the range of 14,000 to 97,000 were investigated.

3.2 Heat transfer uncertainties

3.2.1 Thermocouple Calibration

Ideally, the thermocouple pairs located at the same axial location (such as the three thermocouple pairs shown in Figure 3-2) should indicate the same temperature. The expected uncertainty in the thermocouple readings is 0.4 ºC (e.g. National instruments, 1999).

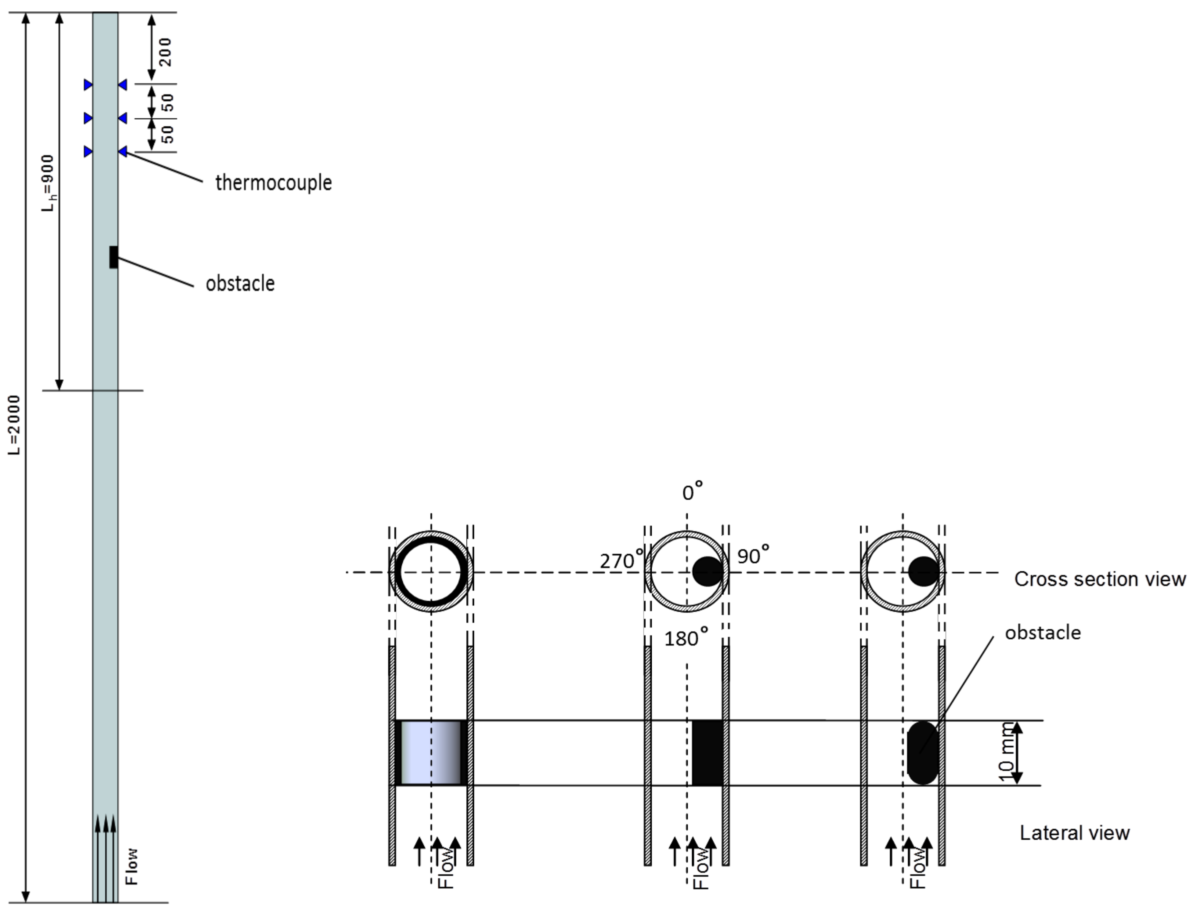

Figure 3 - 2 Schematic diagrams of the test section, thermocouple layout and obstacle types (from left to right: annular, blunt and rounded).

This uncertainty can be reduced for a given thermocouple using appropriate calibrations. In order to quantify the thermocouple inaccuracy, several adiabatic tests were performed. The thermocouple calibrations were performed by circulating single phase coolant through the test section using several bulk coolant temperatures. Because no heating was applied to the test section, wall thickness variation did not affect the readings. If the coolant temperature is close to the ambient temperature and/or the test section is thermally insulated, then heat losses and contact resistance effects are minimized or non-existent. Therefore, this test will show the inaccuracies (random and systematic) of the thermocouples and the analog-digital conversion (ADC) but for a relatively narrow range of temperatures. Note that the calibrations were performed at high mass flux (G=3500 kgm^{-2}s^{-1}) and at pressure approximately equal with 2380 kPa. The reference bulk coolant temperature is based on the averaged values from resistance temperature detectors (RTD's) located at the inlet and outlet of the test section. Thermocouple voltage outputs were converted into temperatures based on standard tables for type-K thermocouples. The maximum temperature discrepancy between the averaged RTD temperature and the two upstream test section TC temperatures for a range of coolant temperatures (10 to 80 °C in steps of 10K) is 0.35 K. These temperature discrepancies were corrected by using the correction function $\Delta T = aT + b$, where a and b were optimized for each thermocouple for the temperature range 10-80°C. This reduced the maximum discrepancy significantly (from 0.35 to 0.11K). Using the correction functions resulted in more uniform temperature distribution (smaller difference between thermocouple readings) for single phase and zero heat flux, which is closer to the ideal situation where all thermocouple measurements are equal. Note that at temperatures higher than 60ºC the RTDs indicate a systematically higher temperature than the thermocouples, suggesting that heat losses may decrease the thermocouple temperature readings by 0.1-0.15ºC.

3.2.2 Heat Balance Test

During all runs, the inlet and outlet temperatures were measured along with flow, power and pressure. This provides an additional check on the combined accuracy of these five parameters using the following heat balance equation

$$U \cdot I = \dot{m}(H_{out} - H_{in}) + q_{loss} \quad , \qquad (3\text{-}1)$$

where U is the electric voltage to test section, I – the current to the test section, $\dot{m}$ – the mass flow rate of refrigerant, H_{in} and H_{out} are the enthalpies of refrigerant at the inlet and outlet of test section and q_{loss} is the heat loss to the surroundings. For temperatures recorded during the experiments, heat loss represents a small fraction of the power to the test section, usually less than 2%. Figure 3-3 shows typical results of the heat balance error, defined as the ratio of the power error (i.e. the difference between the coolant enthalpy increase and the electric power) and the reference power (i.e. the electric power) in percentage of power as a function of flow for the conditions of interest. The average heat balance error was -1.4%, while the maximum error (corresponding to low powers and low enthalpy rise in the test section) was -3.8%. The negative sign indicates that the coolant enthalpy increase was smaller than the electric power input to test section, thus the difference can be attributed primarily to heat loss. Note also that, consistent with the previous assumption, the heat balance error decreased with an increase in flow.

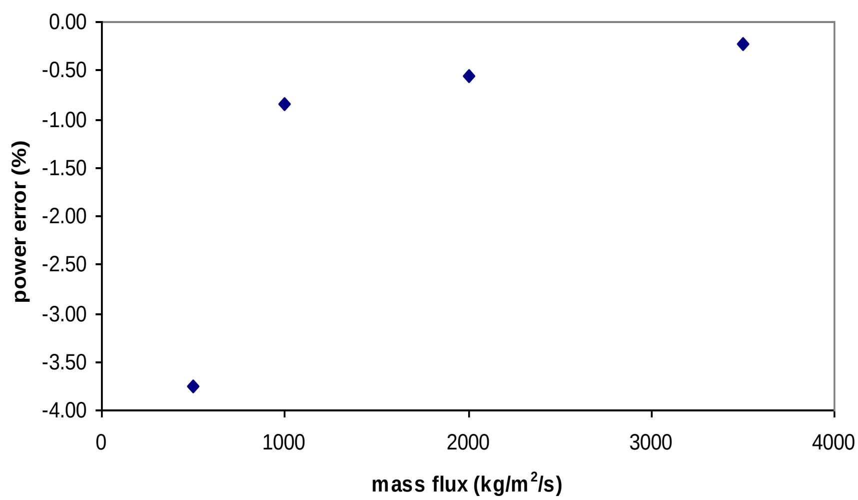

Figure 3 - 3 Heat balance error versus mass flux.

3.2.3 Repeatability

The repeatability was assessed by repeating a limited number of cases from the test matrix after a delay of several weeks. A typical example is presented in Figure 3-4, which shows the ratio Nu/Nu_o of the Nusselt numbers for the obstacle-equipped and bare test sections. The difference between the initial and repeat values ranged from 0.5 to 4%, thus being consistent with the heat balance errors and the estimated measurement uncertainty of the heat transfer coefficient.

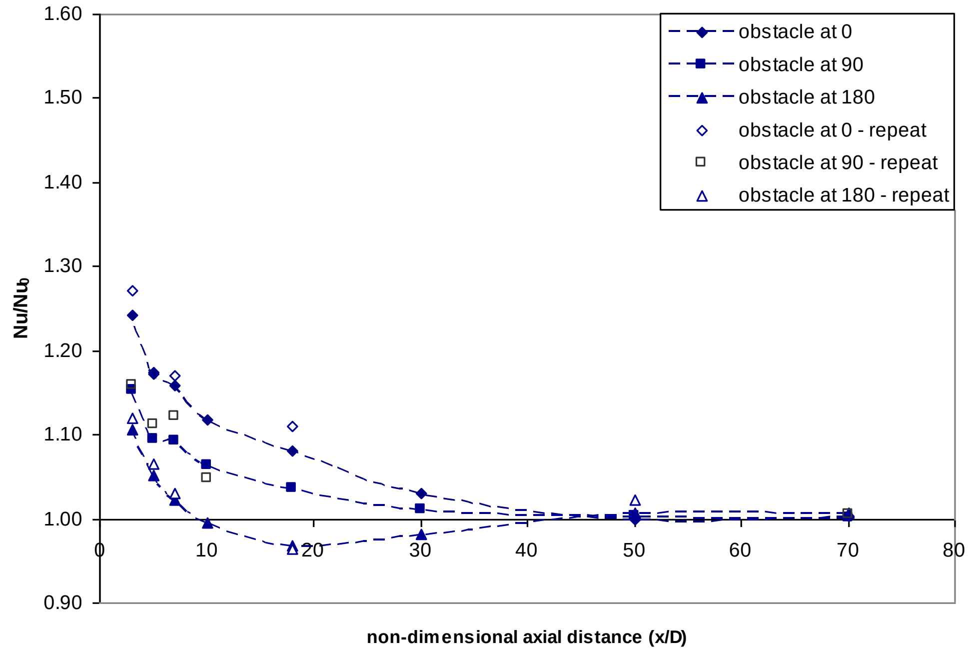

Figure 3 - 4 Repeat tests for the rounded obstacle having 0.15 obstructed ratio at Re=28,000

The uncertainty analysis was performed according to the methodology described by Tavoularis (2005). The overall uncertainty of a derived property, such as Nusselt number, is defined as:

$$u_{Nu} = \sqrt{b_{Nu}^2 + p_{Nu}^2}\ , \tag{3.1}$$

where b and p are the bias (i.e., systematic) and precision (i.e., random) uncertainties, respectively.

Bias and precision uncertainties can be computed as:

$$b_{Nu} = \sqrt{\sum_{m=1}^{M}\left(\frac{\partial Nu}{\partial x_m} b_{x_m}\right)^2} \qquad p_{Nu} = \sqrt{\sum_{m=1}^{M}\left(\frac{\partial Nu}{\partial x_m} p_{x_m}\right)^2} \quad . \tag{3.2}$$

The subsidiary properties x_m from Equation (3.2) where m=1,2,…,M are either directly measured or derived. It should be noted that for directly measured properties, the uncertainties were estimated using instrumentation manufacturer specifications and calibration data. Also, if known (e.g. calibration data) the bias errors were corrected for, thus the largest contribution to the uncertainty was given by the precision (random) components. The estimation of total uncertainty of power to test section was 31W or 1.03% P_{max}. The estimated uncertainty in heat flux due to the variation in wall thickness, based on the measurements and analysis of Appendix B, is 5%. The uncertainties in heat transfer coefficient, Nu and Re were estimated to be 4.3%, 6.1%, and 3.2%, respectively.

3.3 Isothermal flow loop

A schematic diagram of the experimental loop is presented in Figure 3 - 5. Water flow was produced by the elevation difference between the free surfaces of the head tank and the collection tank. From the head tank, water flowed to the inlet tank, which was completely full, through the feed pipe. From the inlet tank, water entered the test section from which it was returned to the collection tank and pumped back to the head tank. The head tank was separated into two compartments by a vertical wall, which acted as overflow, thus maintaining a constant head, whereas overflow water was returned directly to the collection tank. By using gravity-driven flow, we avoided flow oscillations and disturbances caused by the pump. The test section consisted of a horizontal acrylic tube with an inside diameter D = 31.75 mm and the wall thickness of 3 mm and was preceded by a flow development section having a length of approximately 80D. The flow rate to the test section was controlled by a flow control valve and/or a bypass valve that diverted a part of the flow directly to the collection tank. The test section was immersed in a rectangular sealed viewing tank filled with water, which kept light refraction at a low level.

Three flow obstacles, all with cylindrical bodies and a length-to-diameter ratio equal to 3.3, were used in this study (see Figure 3 - 6): i) a blunt (square-ended) cylinder (30B) with a 30% blockage ratio (that is, the ratio between the projected area of the obstacle and the area of the unobstructed tube), ii) a rounded cylinder (30R), having hemispherical ends and a 30% blockage ratio, and iii) a blunt cylinder (15B) with a 15% blockage ratio. All obstacles were manufactured from Teflon, and had encased cores of mild steel, so that they could be held in place by magnets located outside the pipe. By moving the magnet axially, the flow obstacle was relocated, thus permitting the measurement of local pressure and velocity distributions at various positions relative to the obstruction.

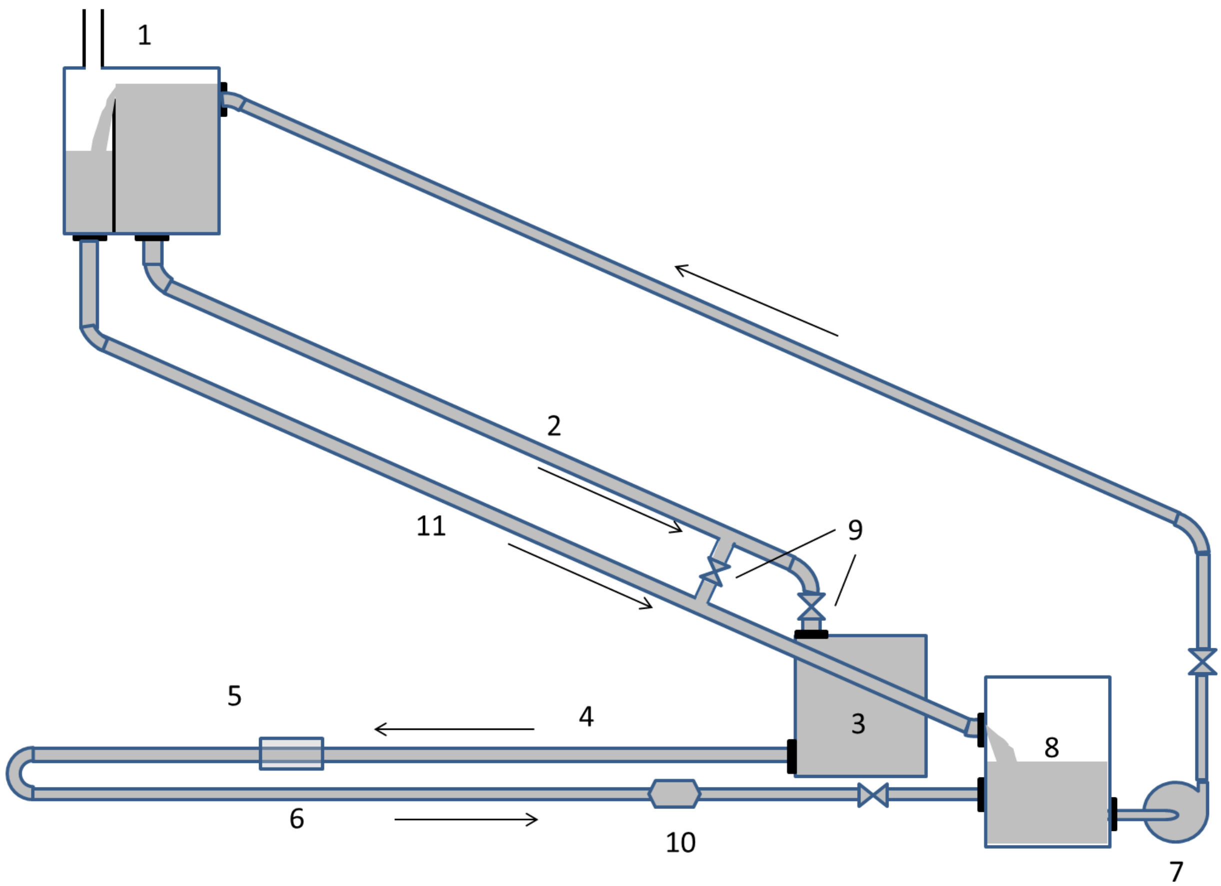

Figure 3 - 5 Experimental water loop, consisting of the head tank (1), feed pipe (2), inlet tank (3), flow development section (4), test section (5), return pipe (6), pump (7), collection tank (8), flow control valves (9), flow meter (10), and overflow return pipe (11).

3.4 Flow rate and pressure loss measurements

A digital thermometer (MASTERCRAFT, Model 52-000052) with an uncertainty of 1°C was used to monitor the water temperature, from which the density and viscosity of water were calculated. The flow rate was measured by an ultrasonic flow meter (OMEGA, Model FDT-33-T). The flow meter was calibrated by timing the filling of a tank with a known volume and the total uncertainty of the measured flow rate was estimated to be 2.8%. A differential pressure transducer (VALYDINE, Model DP103), connected to a digital carrier demodulator (VALIDYNE, Model CD23), was used to measure the difference between the pressures at two pressure taps located at the top side of the test section. The transducer was calibrated against an adjustable column of water and the total uncertainty of the differential pressure measurement was estimated to be 0.85%. A schematic diagram of the pressure loss measurement section is presented in Figure 3 - 7.

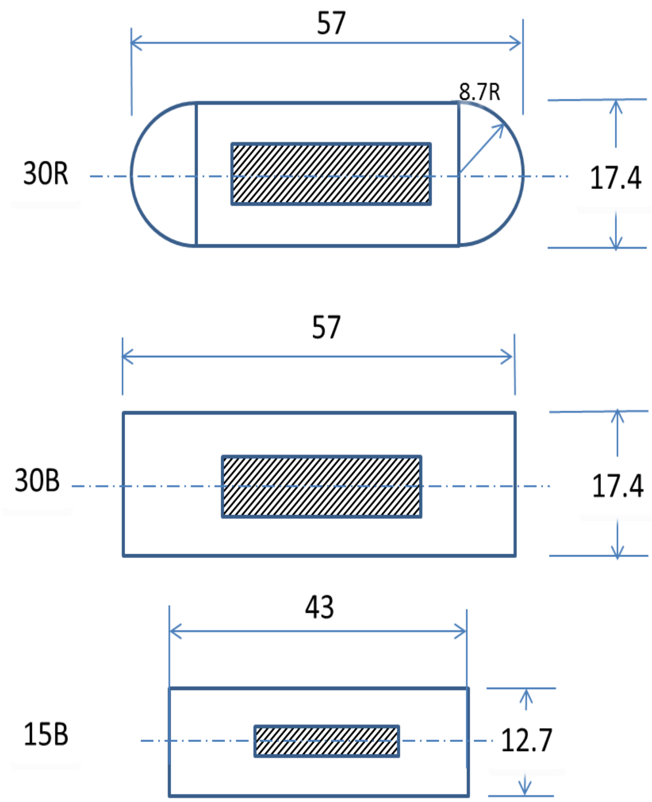

Figure 3 - 6 Sketches of the three flow obstacles; dimensions in mm; crosshatched areas indicate ferromagnetic cores.

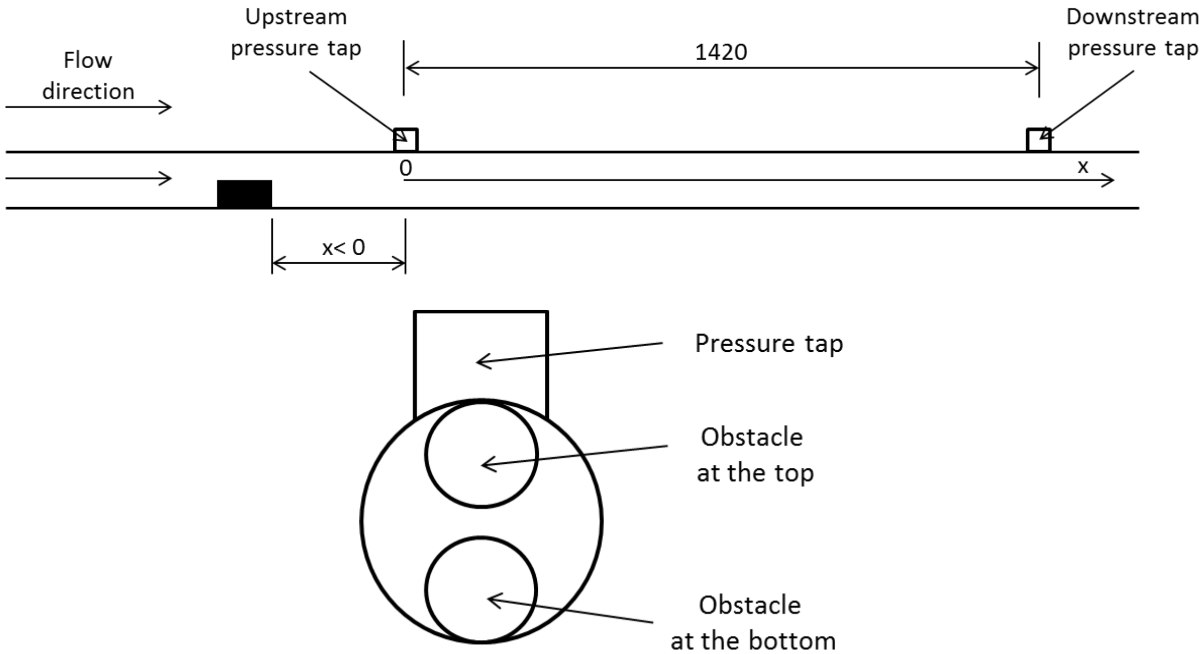

Figure 3 - 7 Sketches of the experimental setup for pressure loss measurement.

3.5 Particle Image Velocimetry

The PIV system used in these experiments consisted of a Nd:YAG pulsed laser (Solo PIV 120XT; New Wave Research, Fremont, CA), one digital camera (LaVision Imager Pro X 4M) with a resolution of 2048×2048 pixels, a programmable timing unit (LaVision PTU-9 External#1108058), and a dedicated computer. The camera was equipped with a Nikon Nikkor 50 mm f/1.8D lens and a 532 nm bandpass filter (LaVision #1108560), which allowed mainly the light emitted by the particles. The laser sheet was created with divergent sheet optics (LaVision #1108405) using a divergent lens with f = −10 mm.

Loop water was seeded with hollow glass microspheres with an average diameter of 12 μm and a specific gravity of 1.1 g cm^{-3}, mixed in the return tank. The particle concentration was adjusted to obtain 5-15 particles per interrogation area. The terminal velocity of particles falling in water was roughly 10^{-5} ms^{-1}, which is at least three orders of magnitude smaller than typical fluid velocities measured during the experiments, and is thus negligible. The time constant of the particle-fluid interaction was 14.4 μs. These particles were sufficiently large to provide an acceptable signal-to-noise ratio and followed the flow sufficiently well. Moreover, peak lock effects, which might have been a source of error if smaller particles were used, were found to be negligible for the glass microspheres.

The measurements were taken in the vertical centre plane of the test section, as shown in Figure 3 - 8. The intersection of the laser sheet with the test section formed an approximate rectangle with a length of 155 mm and a height equal to the diameter of the test section. Part of this viewing area was masked to exclude regions contaminated by parasitic reflections on the wall of the test section and image distortions caused by the tube curvature; the usable viewing area was approximately 145×28 mm. The time separation between laser pulses varied between 1500 μs at lower flow rates to 500 μs at higher flow rates. The images were corrected based on calibration, which was performed by inserting a calibration plate in the measurement plane of the test section filled with water; the bias uncertainty of location on the images was 0.11%. Measurements were taken at a rate of 4 images/s. For each test matrix case, 300 to 500 instantaneous flow images were acquired. Time averages obtained from these images were found to converge. The images were processed with DaVis7 software using a multi-pass routine starting with an interrogation window of 64×64 pixels, and then decreasing to 32×32 pixels with 50% overlap. The resolution of the velocity maps was approximately one vector per 1.18 mm × 1.18 mm. Vectors with too few particles within the interrogation volume were deleted. The vector fields were then post-processed, smoothing the results using low-pass filter with a 3×3 window, and filling up the empty spaces.

The total uncertainty of the instantaneous PIV velocity measurements was estimated to be 5% of the measured values, being dominated by the uncertainty of the mathematical convolution filtering to determine the most probable displacement of the particles in the interrogation area. The precision uncertainty of the ensemble averaged velocity measurements was 0.2-0.3%.

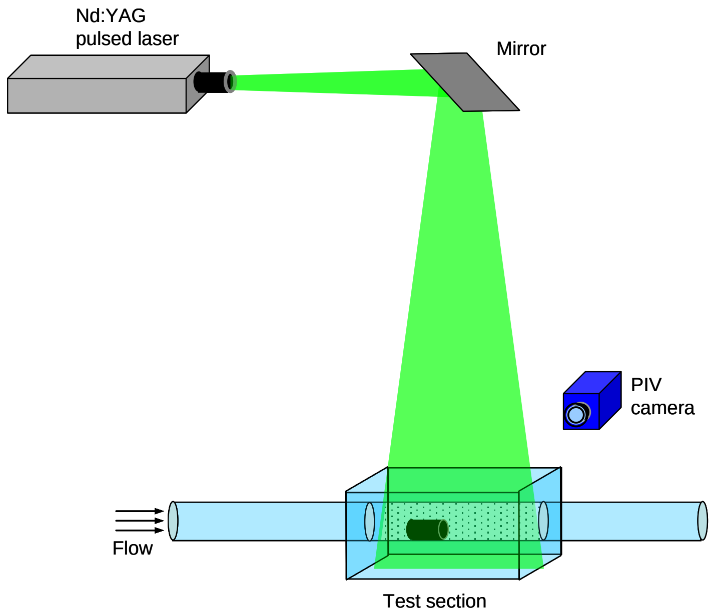

Figure 3 - 8 Sketch of the PIV setup.

3.6 PIV and pressure loss uncertainties

3.6.1 Voltage calibration of data acquisition system

The analog input 2 (CH2) of the DAQ was used to acquire the voltage signal from the flow meter and the analog input 3 (CH3) the voltage signal from the differential pressure meter. The measurement range of both channels was 0 to 10V, with resolutions of 12 bits. In order to estimate the uncertainty of the DAQ, a calibration test was conducted. The analog inputs were connected to the output of a stabilized power supply. In parallel to the DAQ a digital voltmeter MASTERCRAFT 52-000052 was connected. The voltmeter's accuracy stated by the manufacturer was better than 0.8% of reading. A second voltmeter was used to confirm several readings from the first voltmeter. The readings of both instruments were within 0.4%, thus within the manufacturer's specifications. Based on the voltmeter's readings, calibration curves for DAQ were produced. Raw DAQ values were corrected using the calibration curves. It was estimated that the corrected DAQ values had a maximum error of 3mV.

3.6.2 Differential pressure calibration

The pressure loss was measured by a differential pressure transducer VALIDYNE model DP103 with an accuracy of 0.5%. The calibration of the transducer was performed by two flexible, transparent PVC tubes partially filled with water and connected to high and low pressure ports of the cell. The low pressure branch was fixed with clamps on a vertical board equipped with a ruler with resolution of 1 mm. The differential pressure was varied by the movement of high pressure branch in the vertical direction. The branch was held in place on the board with clamps. The pressure transducer was connected to a VALIDYNE carrier demodulator model CD23. The carrier demodulator generated an excitation voltage to the transducer. The transducer provided an output signal to the demodulator input, where the signal was amplified, demodulated and filtered. The signal then emerged as a direct current (DC) (±10V) signal which was proportional to the pressure difference applied to the transducer's diaphragm. The stability of the analog output was 0.5% of full scale. The analog output of the carrier demodulator was connected to the FUTEK DAQ. In the previous Section it was estimated that uncertainty of DAQ after calibration was 3mV. The uncertainties of the main components of the measurement chain are summarized below:

$$\varepsilon_T = 0.5\%$$
$$\varepsilon_D = 0.5\%$$
$$\varepsilon_{DAQ} = 3 \cdot 10^{-3} V$$

The uncertainty of differential pressure was estimated by the ISO methodology, as described by Tavoularis (2005):

$$u_{\Delta P} = \sqrt{\left(\frac{\partial \Delta P}{\partial U_T}\varepsilon_T\right)^2 + \left(\frac{\partial \Delta P}{\partial U_D}\varepsilon_D\right)^2 + \left(\frac{\partial \Delta P}{\partial U_{DAQ}}\varepsilon_{DAQ}\right)^2} \quad , \qquad (3.3)$$

where ε_T, ε_D and ε_{DAQ} are the uncertainties of the pressure transducer, the demodulator and the DAQ, respectively. The random uncertainty of differential pressure measurement was 0.8%. It was assumed that the systematic uncertainties were corrected for by the calibration. However, as described above, the calibration was subject to an uncertainty of 1 mm, thus the uncertainty of calibration was estimated as 1 mm / 350 mm = 0.28%. The combined uncertainty (random and bias) was calculated as:

$$u_{\Delta P} = \sqrt{u_r^2 + u_b^2} = \sqrt{0.008^2 + 0.0028^2} = 0.0085 = 0.85\% \qquad (3.4)$$

3.6.3 Flow rate calibration

Flow rate was measured by an OMEGA ultrasonic flow meter, model FDT-33-T, with an accuracy better than 1%. A supplementary calibration was performed. In this a flexible hose was inserted in the loop section between the flow meter outlet and the return tank (see Figure 3 - 5). The following procedure was applied:

a) A steady flow was established.
b) With the flexible hose, the flow was manually diverted to an external tank with a known volume and a timer was started.
c) When the external tank was full, the timer was stopped and the hose was returned to the return water tank (i.e. original system configuration).

The flow rate was determined as

$$Q = V / \Delta t \quad . \qquad (3.5)$$

The volume of the external tank (*V*) was measured by a graduated cylinder of 2000 mL, with subdivisions of 20 mL. In addition to the tank volume measurement uncertainty, an additional uncertainty was caused by the turbulent flow from the hose and the surface waves generated on the free tank water surface. The above mentioned uncertainty was estimated to 1.5%. The uncertainty in time measurement (Δt) was 1s. Three tanks have been used, having volumes of respectively 18.9 L, 57.0 L and 96.6 L for higher flows.

The combined uncertainty of volumetric flow rate was therefore expressed as:

$$u_Q = \sqrt{\left(\frac{\partial Q}{\partial V}\varepsilon_V\right)^2 + \left(\frac{\partial Q}{\partial \Delta t}\varepsilon_{\Delta t}\right)^2} \quad (3.6)$$

Using the uncertainties mentioned above, the random uncertainty of the flow rates measured by the direct method was estimated to be 2.5%.

The comparison between directly measured and flow meter flow rates revealed systematic errors. Figure 3 - 9 shows that the flow meter overestimated direct measured (i.e. reference) flow rates. In order to correct for the systematic (i.e. bias) errors, a linear function has been derived. The equation that describes the correction to the flow meter reading is given by the following equation:

$$Q_{corr} = \frac{Q_{flowmeter} - 0.4677}{1.079} \quad . \quad (3.7)$$

The units in Equation 3.7 are US gallons per minute (gpm).

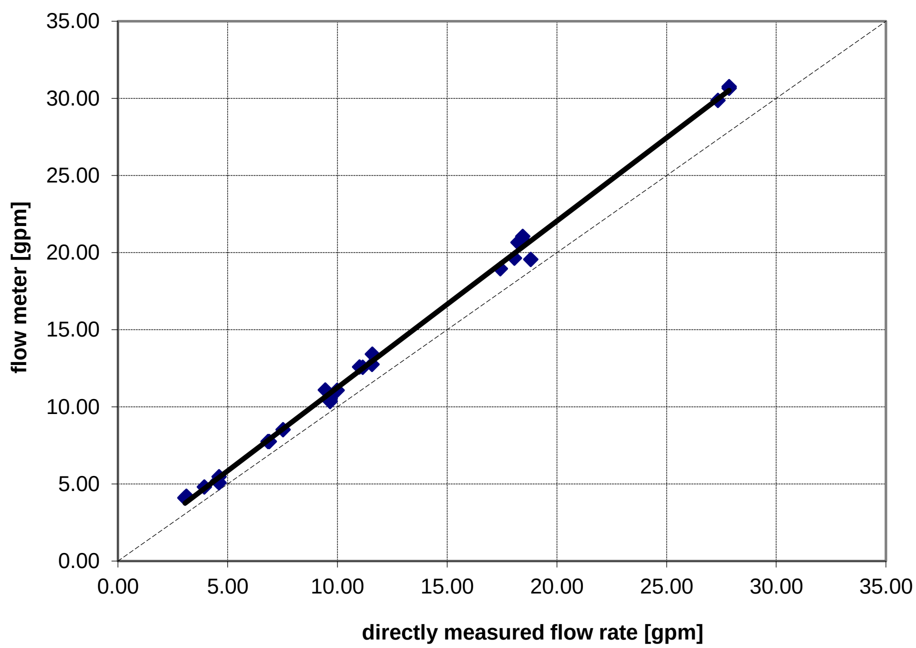

Figure 3 - 9 Calibration curve of the ultrasonic flow meter.

Flow rate measurement values were obtained by processing the analog output through the data acquisition system. The output signal of the flow meter was 4-20 mA. The current was converted to voltage by a resistor of 199.2Ω. According to the flow meter manufacturer's calibration, the maximum current output of 20 mA corresponded to 108 gallons per minute. The resistor voltage was converted to a digital signal by the DAQ. The uncertainties of each of the components of the signal path (flow meter, resistor and DAQ) were:

$\varepsilon_I = 1\%$

$\varepsilon_R = 0.5\%$

$\varepsilon_{DAQ} = 3\cdot 10^{-3}$ V

Flow measurement uncertainty is thus equal to

$$u_Q = \sqrt{\left(\frac{\partial Q}{\partial I}\varepsilon_I\right)^2 + \left(\frac{\partial Q}{\partial R}\varepsilon_R\right)^2 + \left(\frac{\partial Q}{\partial E_{DAQ}}\varepsilon_{DAQ}\right)^2} \tag{3.8}$$

The total flow measurement uncertainty was estimated to 1.4%. The uncertainty from the Equation 3.8 addresses the random uncertainty only. It was assumed that the systematic (e.g. bias) uncertainty was significantly reduced by calibration, using as reference the direct measurement of flow rate, whose uncertainty was estimated to 2.5%. Assuming that both uncertainties are independent, the total (e.g. systematic and random) mass flow rate uncertainty is given by:

$$u_Q = \sqrt{u_d^2 + u_f^2} = \sqrt{0.025^2 + 0.014^2} = 0.028 = 2.8\% \tag{3.9}$$

3.6.4 PIV measurement uncertainty

A component (U) of velocity is computed by:

$$U = \alpha \frac{\Delta X}{\Delta t} \quad , \tag{3.10}$$

where α represents the magnification factor between the object plane and the image plane, ΔX – displacement of the recorded particles and Δt - time separation between the images. The uncertainty of the magnification factor can be minimized by careful calibration of the PIV camera. For the current experiment, the calibration was performed by a calibration plate inserted in the test section filled with water, in the measurement plane. The automatic calibration procedures of DaVis7 software were applied. The reported average deviation was 2.3 pixels. The corresponding bias error is therefore 2.3/2048=0.11%. The uncertainty of the timing unit, according to the manufacturer's specifications, was 5ns. The uncertainty of time separation between two successive pulses was calculated by doubling the uncertainty for one pulse to be 10ns. The smallest time separation between pulses used for the current experiment was 500 μs, thus the relative uncertainty was 10ns/500μs=0.002%.

The uncertainty of displacement of particles ΔX is impacted by several factors, most notably:

a) The cross-correlation procedure to determine the most probable displacement of the particle pattern in the interrogation area. Typically, it seems that the fractional precision is 5%.
b) Pixel locking, which was deemed negligible (see discussion about seeding).
c) The ability of the trackers to follow the flow. It should be noted that the PIV measures the instantaneous vector fields of the *tracking particles*, and not the flow. Any "slippage" between the fluid flow and the tracking particles would cause measurement errors. For the current experiment, the time constant of the tracking particles (14.4 μs) was much smaller than the duration between pulses (500 to 1500 μs), thus this effect was considered negligible.

In summary, the total uncertainty of the instantaneous PIV velocity maps is 5% of the measured values, being dominated by the uncertainty of the mathematical convolution filtering to determine the most probable displacement of the particles in the interrogation area. It should be noted, however, that the averaged velocity fields are calculated from hundreds of instantaneous velocity fields. According to the methodology described by Tavoularis (2005) the random uncertainty component for the averaged velocity field is reduced by $1/\sqrt{N}$, thus the uncertainty of averaged flow maps is significantly reduced, being of the order of 0.2-0.3%.

3.6.5 Seeding

Seeding was made with hollow glass spheres, premixed in water in the return tank. The particle density was adjusted to obtain 5-15 particles per interrogation area, as can be seen in the close-up image of the seeding shown in Figure 3-10. If the density of the particles (ρ_P) is different than the density of the fluid (ρ), the buoyancy and gravity forces are not balanced, thus the particle would have a relative motion, with the terminal velocity U_g given by Raffel et al. (1998) as

$$U_g = d_P^2 \frac{(\rho_P - \rho)}{18\mu} g \quad . \tag{3.11}$$

In equation (3.11) d_P is the diameter of the particle, μ is the fluid viscosity and g the gravity constant. For the glass beads in water, the terminal velocity is on the order of 10^{-5} ms^{-1}, (see Table 3 -1), which is at least three order of magnitude smaller than fluid velocities measured during experiments, and is thus negligible.

Another source of errors is the delay (i.e. time constant) required by a particle dragged by the flow to follow the fluid motion. The time constant of the particle-fluid interaction is given by the equation (Tavoularis, 2005):

$$\tau_S = \frac{\rho_P d_P^2}{18\mu}\left(1 + \frac{1}{2\rho_P / \rho}\right) \quad . \tag{3.12}$$

Table 3 - 1 is reproduced from Vanderwel (2014) and provides the comparison of the properties of hollow glass spheres in comparison with other flow tracer particles and flow contaminants (such as rust) that may alter the PIV measurement uncertainty.

Table 3 - 1 Comparison between various types of seeding particles and contaminants

Particle type	**ρ_P (gcm^{-3})**	**d_P (μm)**	**U_g(ms^{-1})**	**τ_S (μs)**
Silicon carbide	3.2	2	$5.4 \cdot 10^{-6}$	0.9
Hollow glass beads	1.1	12	$8.8 \cdot 10^{-6}$	14.4
Background contaminants	5.2	5	$64 \cdot 10^{-6}$	8.9

Data from Table 3 - 1 indicate that glass beads do not follow the flow as well as silicon carbide particles; however, they are much larger, thus reflect light much better, producing clearer and less noisy images. An additional assessment with regard to the suitability of glass particles for the flow conditions and geometry relevant for the PIV experiment was performed. The main parameter of interest was the time scales of the flow field investigated.

The additional assessment estimated the ratios of turbulence time scales and the time constant of the glass beads. We believe that the time scales ratios confirm that the glass beads follow the flow accurately and especially that the turbulent velocity fluctuations are satisfactorily tracked by the glass particles. The size of the largest eddies (i.e. integral turbulent length scale) in the flow is limited by the physical boundaries of the flow domain. For the current geometry, the pipe diameter (*ID*=31.75mm) was considered as the characteristic length of the flow. The timescale corresponding to the integral length scale can be calculated as the ratio of the integral length scale and the bulk fluid velocity. The shortest time scale, ~9.4 ms was obtained for the highest Reynolds number, with a corresponding bulk fluid velocity of 3.4 m/s. Unlike the large-scale eddies, which are geometry-dependent, the small-scale motions are statistically independent of geometry, as well as of mean motions and large-scale turbulent fluctuations. According to Kolmogorov's Universal Equilibrium Theory, the small-scale turbulence is in equilibrium (independent of large-scale) and is controlled solely by the turbulent kinetic energy dissipation rate ε and the viscosity ν. The smallest length η and time τ scales, according to the Kolmogorov theory are given by the following expressions (Tavoularis, 2007):

$$\eta = \left(\frac{\nu^3}{\varepsilon}\right)^{1/4},\ \tau = \left(\frac{\nu}{\varepsilon}\right)^{1/2} \qquad (3\text{-}13)$$

A typical value of the dissipation rate in the present tests was 1W/kg, whereas the viscosity for water is approximately 10^{-6} m^2/s. Then, one can estimate the Kolmogorov microscale as η=30μm and the Kolmogorov time scale as τ=1ms.

An alternative approach in determining a length and a time scale for the flow can be based on FLUENT User's Guide (ANSYS, 2006), which recommends that the turbulent length scale L is approximately 0.07 of the characteristic length of the flow; In this case, $L = 0.07ID = 2.2$ mm. In the core of turbulent pipe flow, a typical value of the magnitude of velocity fluctuations is 5% of bulk pipe velocity (ANSYS, 2006). The correlation for the turbulence intensity recommended by FLUENT User's Guide is given by

$$I = \frac{u'}{U_b} = 0.16Re^{-1/8}\ . \qquad (3\text{-}14)$$

In the current experiments, the turbulent intensity ranged between 4 and 5%. For the highest value of bulk fluid velocity (U_b=3.4 m/s), the r.m.s. velocity fluctuations were roughly 0.17 m/s. A time scale of the velocity fluctuations can be estimated as the ratio of the estimated turbulence length scale (2.2 mm) and the estimated magnitude of velocity fluctuations (0.17 m/s), which gives the value 12.9 ms.

It is noted that the time constant of tracer particles is at least an order of magnitude smaller that all time scales derived in the previous paragraphs, which confirms with confidence the ability of these particles to track the velocity fluctuations of the flow.

Another benefit of hollow glass spheres is that, due to large particle size, the measurements are less prone to "peak lock". Peak lock occurs when the computed velocity field has a bias towards integer values, thus altering the accuracy of the measurement. Peak locking can occur, for example, when the tracker particles are too small and produce particle images on the Charged Coupled Device (CCD) of less than one pixel in diameter. For the current experiment, the procedure recommended by DaVis 7 PIV software manuals was applied. The software can generate a Probability Density Function (PDF) which computes a histogram of a vector field where the Vx, Vy and/or Vz components are separated in certain velocity intervals. The user can visually check the velocity distribution from the histograms and assess the severity of peak locking. Moreover, a parameter "peaklock" is calculated, and, depending on its value, the user is advised whether the peaklock effect is significant. If peaklock equals 0, there is no peak locking effect. If peaklock is less than 0.1, the peak locking is acceptable. For the current experiment, a sample of about one hundred vector maps were tested and the peaklock varied between 0.02 and 0.08, thus we concluded that it was not significant.

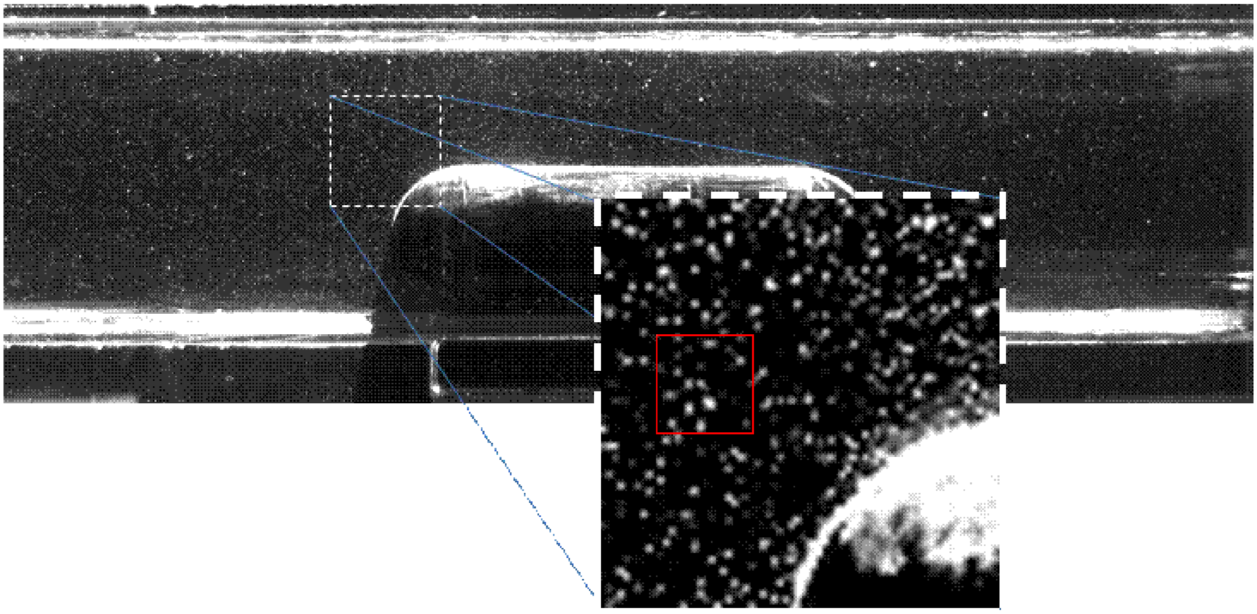

Figure 3 - 10 Example of typical PIV image with zoomed-in area showing detailed seeding. An interrogation window of 32X32 pixels is exemplified by the red square.

3.7 Flow visualization around obstacles using a hydrogen bubble technique

Prior to the PIV investigation, a series of preliminary tests employing hydrogen bubble visualization in an isothermal water loop was performed. The simplified diagram of the experimental loop is showed in Figure 1. The loop consisted of stainless steel SS304 piping with ID=10mm, a flow meter (rotameter) with an accuracy of 2.5%, a flow control valve and a transparent test section made of glass, with ID=10mm and the wall thickness of approximately 1mm. The glass test section was preceded by a straight flow development section made of stainless steel of approximately 70D. Between the stainless steel and glass sections a segment made of Teflon machined to ensure leak tightness as well as a smooth flow transition between the loop segments mentioned above. The Teflon segment contained a tungsten wire with a thickness of 40μm, installed on the middle vertical symmetry plane (i.e. the vertical diameter) and connected to a variable voltage power supply via an electronic switch. The electronic switch was controlled by an electronic pulse generator. The intensity of the hydrogen bubble generation was controlled by the voltage of the power supply. The system was able to generate continuous “bubble sheet” if the electric current was continuously applied to the tungsten wire, as well as timelines if a pulsating voltage was applied.

Some representative pictures of flow past blunt and round ended obstacles for Reynolds numbers between 350 and 3500 are shown in Figures 2 to 7. The following observations can be made:

a) At Re numbers below 700, a large steady vortex occurs upstream the blunt flow obstacle. The flow detached as it went past the front end; in the wake the flow was laminar.
b) At flow Re numbers approaching 1400, a system of multiple steady vortices formed upstream the blunt obstacle. The size of the vortices decreased as the distance upstream the obstacle increased. Three upstream vortices were clearly visible in several pictures at Re=1,400 for 30B. No vortices were identified for the 30R.
c) At Re=2,200 two to three upstream vortices were visible upstream the blunt obstacle, whilst one vortex was identified upstream the rounded obstacle. Also, in the wake of blunt obstacle the flow seemed more turbulent than the bulk whilst in the wake of rounded obstacle flow seemed laminar.
d) At Re numbers approaching 3,000 the front vortices were still visible albeit less clear than at lower Re numbers. The flow in the wake seemed turbulent.
e) At Re =3500, no upstream vortices were identifiable. The wake was turbulent.
f) Hydrogen bubble visualization seems usable in laminar flow regimes only. The experiments at Re numbers larger than 5,000 indicated that turbulence was sufficiently strong to randomly mix the bubbles pathways, rendering the images blurry.
g) During the experiments it was observed that the oxygen bubbles formed on the inside surface of the stainless steel pipe preceding the test section, were entrained by the flow and some of them were deposited on the walls of the glass tube and the obstacle. This was detrimental since, due to their large size, the oxygen bubbles scattered the light more than the hydrogen bubbles, causing parasitic reflections. Another unwanted effect was that the stagnant bubbles located on the surface of the obstacle acted as a “wall”, effectively changing the original geometry of the obstacle. In order to circumvent this issue, the obstacle was moved and rolled around the tube circumference to help detaching the bubbles.
h) The obstacles were manufactured from mild steel, covered with black paint to prevent corrosion and parasitic light reflections. However, during the experiments it was noted

that some rust spots developed on the obstacle surface and transferred by direct contact to the inside surface of the glass test section, decreasing locally its transparency, thus the quality of the captured images. In the design of the PIV experiment this feedback was considered by manufacturing the flow obstacles from Teflon which contained a core of mild steel, effectively eliminating the formation of rust.

i) The optical distortions did not alter significantly the quality of the pictures. Given the qualitative nature of this investigation, no systematic analysis of optical distortion was performed.

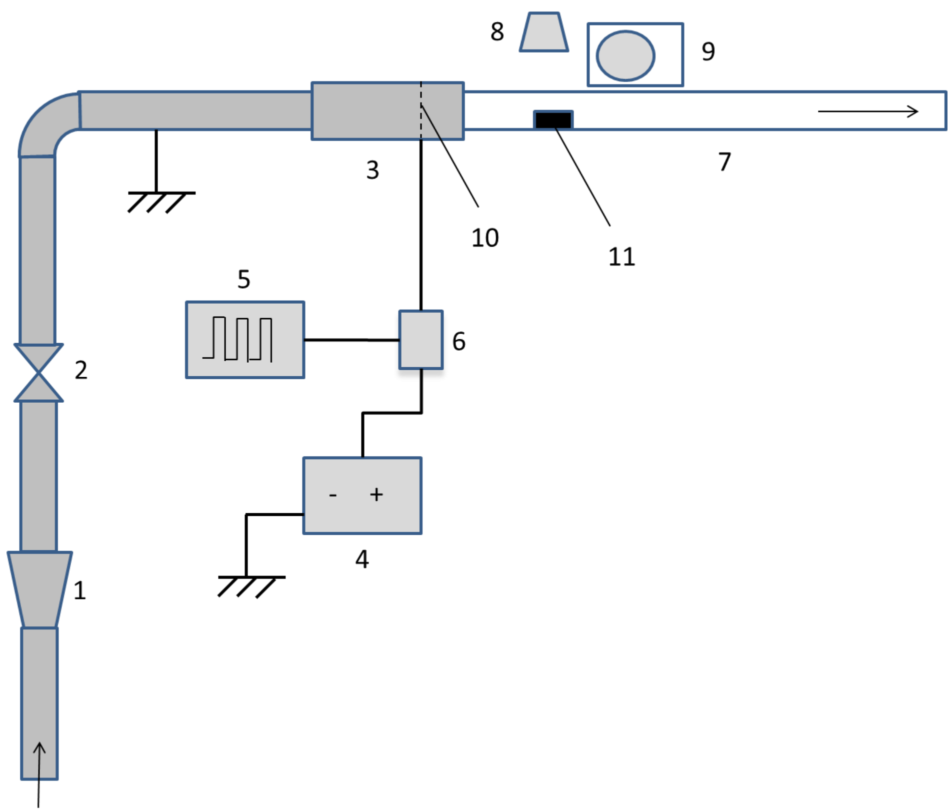

Figure 3 - 11 Experimental water loop for hydrogen bubble visualization.
1- flow meter; 2- flow control valve; 3- Teflon section; 4- Variable voltage power supply; 5 – pulse generator; 6 – electronic switch; 7- glass test section; 8- light source; 9 – camera; 10 – tungsten wire; 11- flow obstacle;

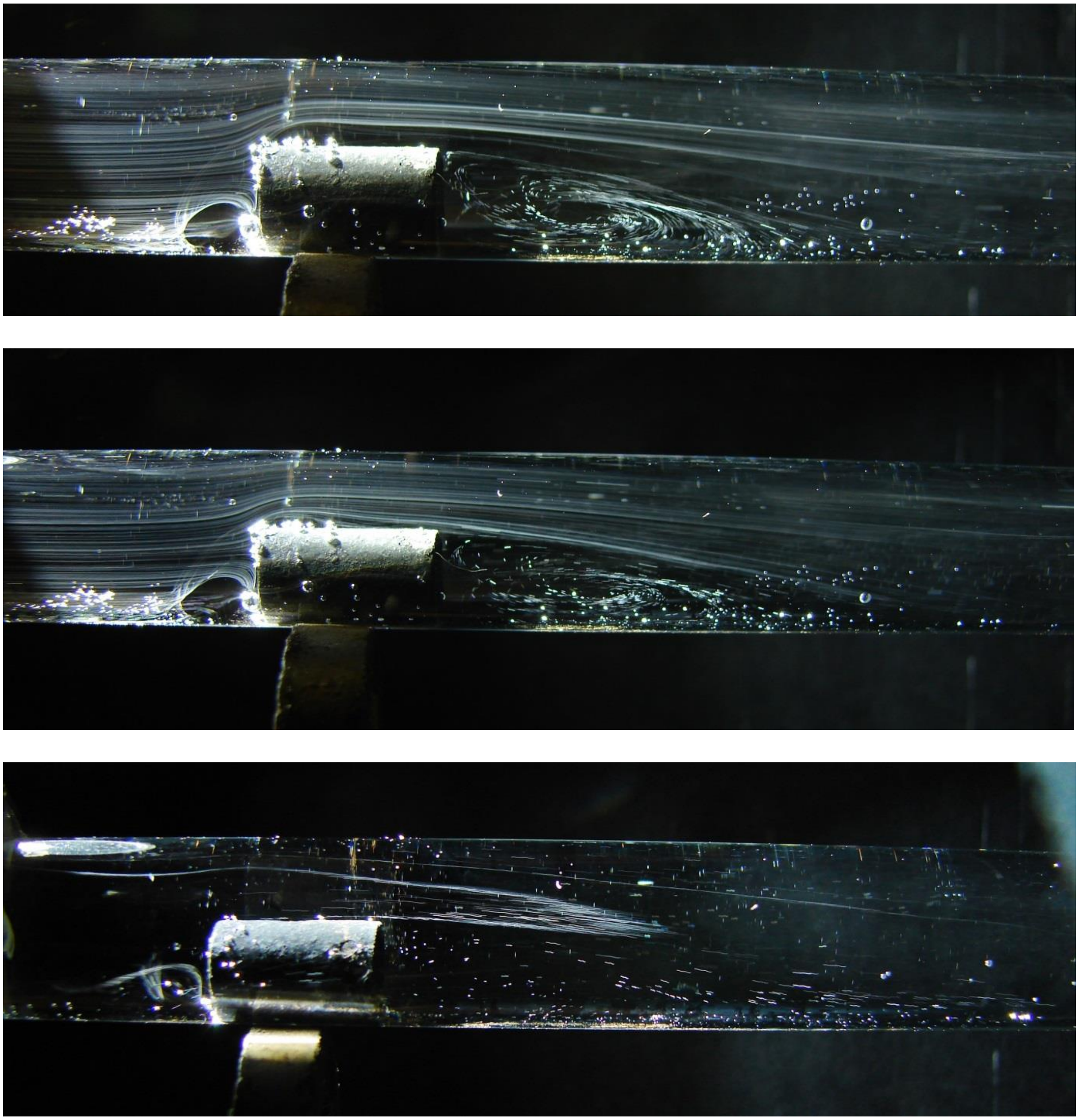

Figure 3 - 12 Flow visualization by hydrogen bubbles around 30B obstacle, Re=350.

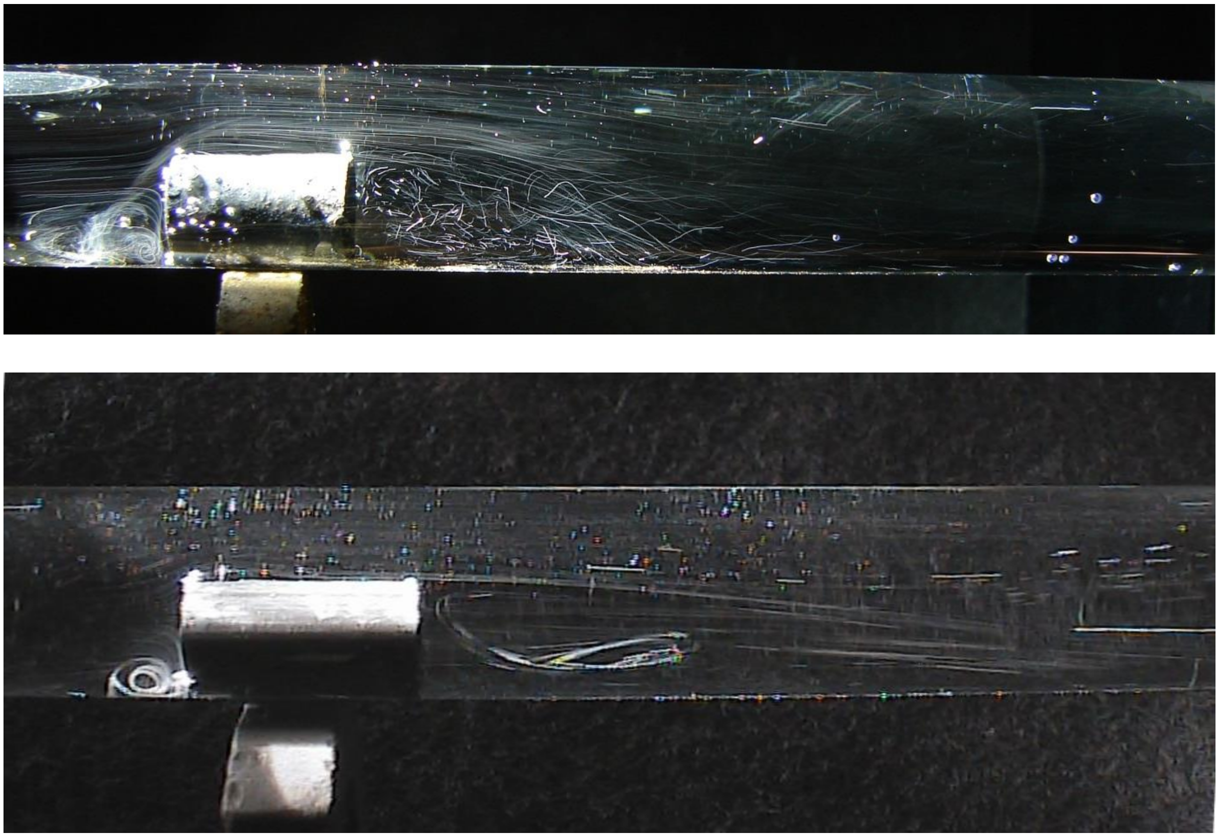

Figure 3 - 13 Flow visualization by hydrogen bubbles around 30B obstacle, Re=700.

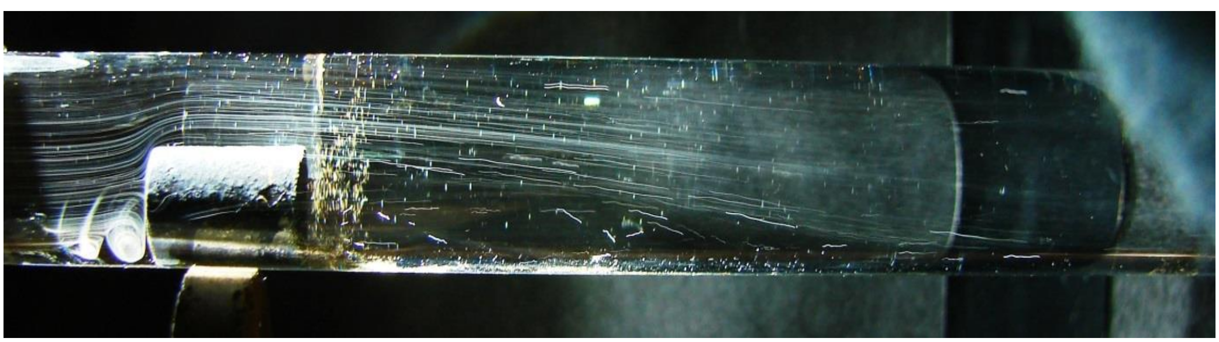

Figure 3 - 14 Flow visualization by hydrogen bubbles around 30B obstacle, Re=1400.

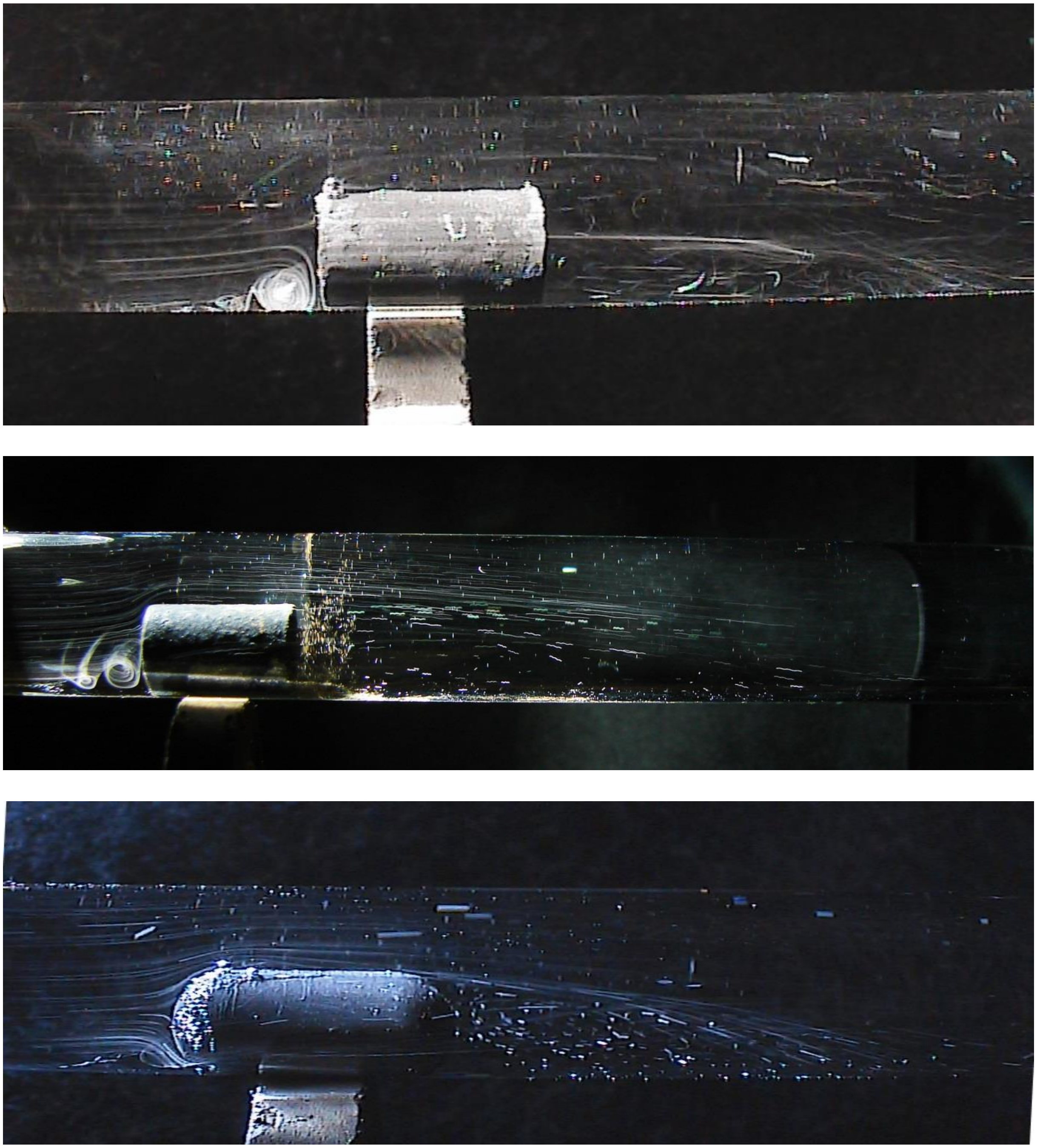

Figure 3 - 15 Flow visualization by hydrogen bubbles around 30B and 30R obstacles, Re=1400.

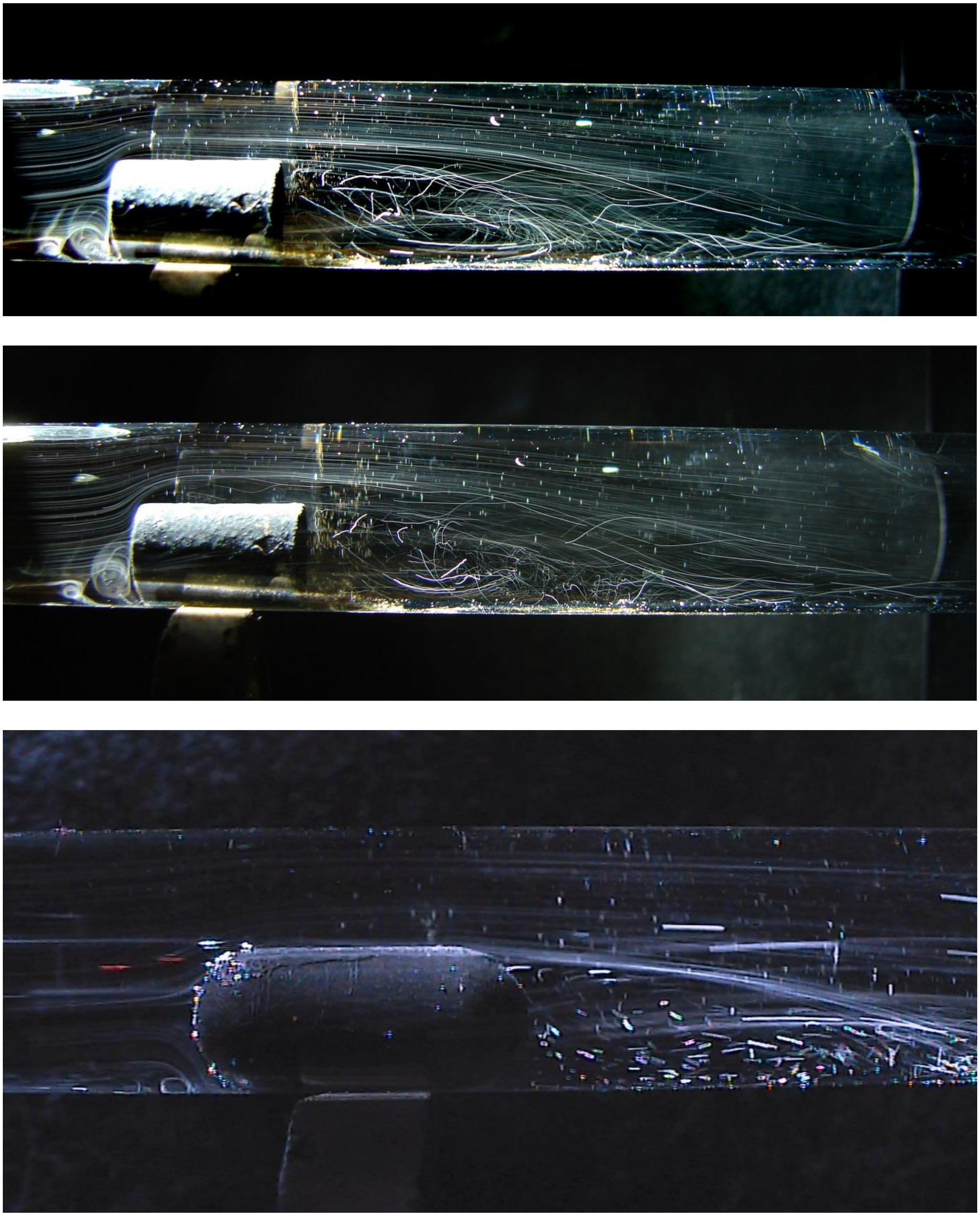

Figure 3 - 16 Flow visualization by hydrogen bubbles around 30B and 30R obstacles, Re=2200.

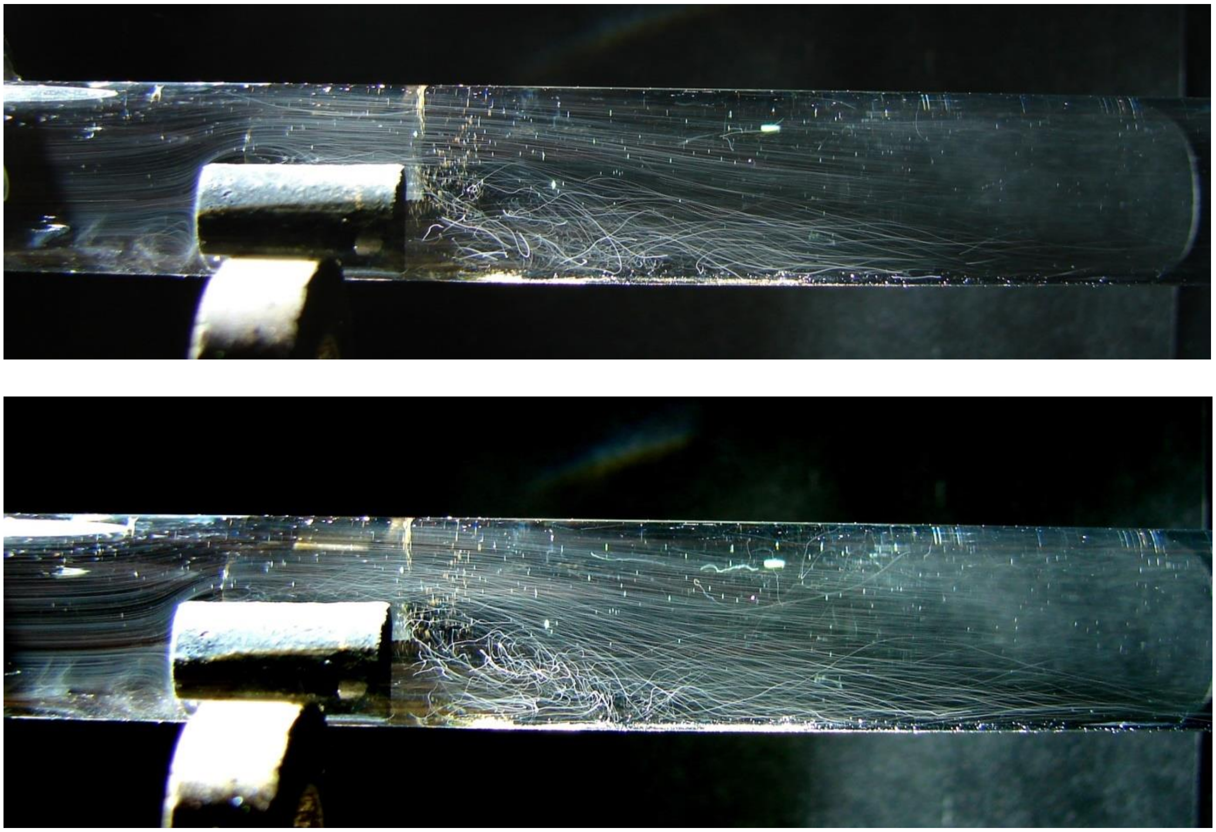

Figure 3 - 17 Flow visualization by hydrogen bubbles around 30B obstacle, Re=3000.

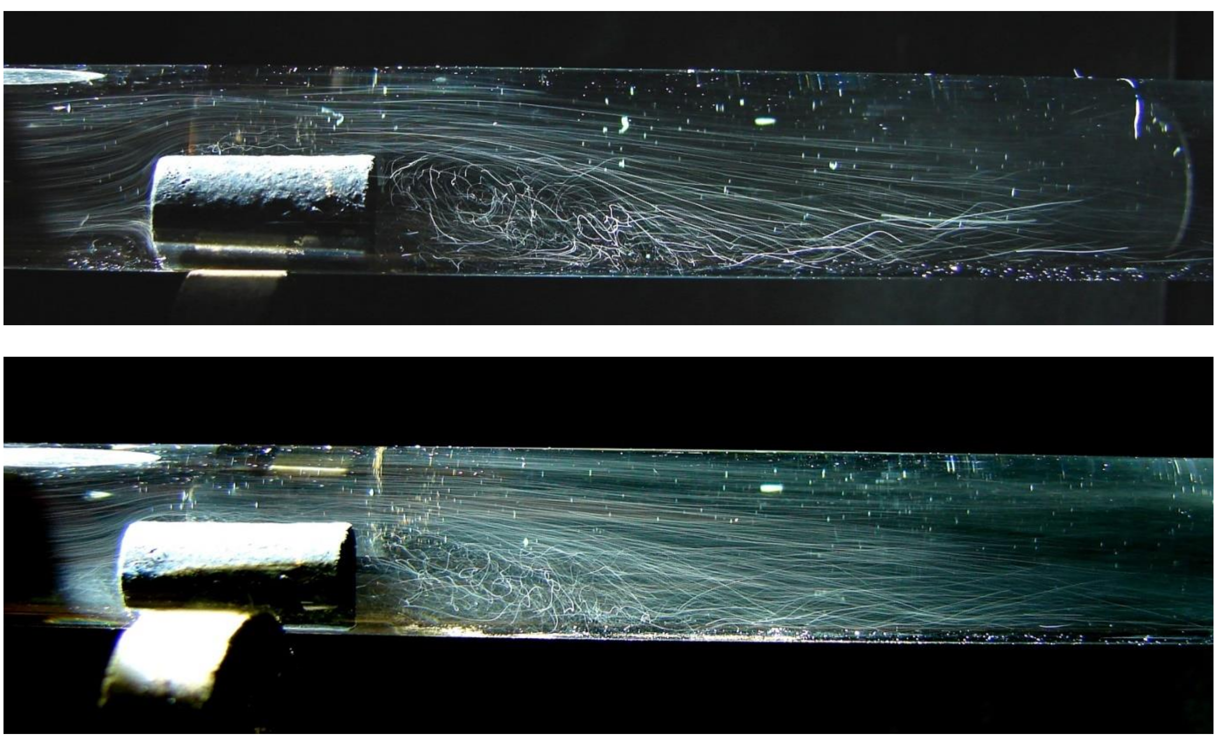

Figure 3 - 18 Flow visualization by hydrogen bubbles around 30B obstacle, Re=3500

CHAPTER 4

Computational Procedures

4.1 Theoretical foundations

4.1.1 Conservation equations

The analysis of fluid flow is based on the following three fundamental physical principles (White, 2011):

a) Mass conservation
b) Newton's second law (momentum principle)
c) First law of thermodynamics (energy principle).

The mathematical expressions of these fundamental principles are obtained by analysis of mass, forces and energy balances for a *finite control volume* or an i*nfinitesimal fluid element*, which results in the *integral* or the *differential* form of the conservation equations. The differential form of the mass conservation equation for a compressible fluid in engineering notation is

$$\frac{\partial \rho}{\partial t} + \frac{\partial}{\partial x}(\rho u) + \frac{\partial}{\partial y}(\rho v) + \frac{\partial}{\partial z}(\rho w) = 0 \quad , \tag{4.1}$$

where ρ is the fluid density, $\boldsymbol{\nabla} = \boldsymbol{i}\frac{\partial}{\partial x} + \boldsymbol{j}\frac{\partial}{\partial y} + \boldsymbol{k}\frac{\partial}{\partial z}$ is the nabla operator and $\boldsymbol{V}$ is the vector velocity field $\boldsymbol{V}=u\boldsymbol{i}+v\boldsymbol{j}+w\boldsymbol{k}$, where $\boldsymbol{i}$, $\boldsymbol{j}$, $\boldsymbol{k}$ are the Cartesian unit vectors.

Using the identity: $\frac{\partial}{\partial x}(\rho u) + \frac{\partial}{\partial y}(\rho v) + \frac{\partial}{\partial z}(\rho w) = \boldsymbol{\nabla} \cdot (\rho \boldsymbol{V})$, the mass conservation equation can be expressed in compact form as:

$$\frac{\partial \rho}{\partial t} + \boldsymbol{\nabla} \cdot (\rho \boldsymbol{V}) = 0 \tag{4.2}$$

The momentum equation in differential form is expressed as:

$$\rho \frac{d\boldsymbol{V}}{dt} = \rho g - \boldsymbol{\nabla} \mathrm{p} + \boldsymbol{\nabla} \cdot \tau_{ij} \tag{4.3}$$

where p is the static pressure, τ_{ij} is the stress tensor and g is the gravitational acceleration. The expanded form of stress tensor is given by:

$$\tau_{ij} = \begin{bmatrix} \tau_{xx} & \tau_{yx} & \tau_{zx} \\ \tau_{xy} & \tau_{yy} & \tau_{zy} \\ \tau_{xz} & \tau_{yz} & \tau_{zz} \end{bmatrix} \tag{4.4}$$

The substantial derivative $\frac{d\boldsymbol{V}}{dt}$ can be expanded as:

$$\frac{d\boldsymbol{V}}{dt} = \frac{\partial \boldsymbol{V}}{\partial t} + u\frac{\partial \boldsymbol{V}}{\partial x} + v\frac{\partial \boldsymbol{V}}{\partial y} + w\frac{\partial \boldsymbol{V}}{\partial z} \quad . \tag{4.5}$$

For Newtonian fluids and incompressible flow, the viscous stresses are proportional to the element strain rates and the viscosity μ, namely:

$$\tau_{xx} = 2\mu\frac{\partial u}{\partial x} \quad \tau_{yy} = 2\mu\frac{\partial v}{\partial y} \quad \tau_{zz} = 2\mu\frac{\partial w}{\partial z}$$

$$\tau_{xy} = \tau_{yx} = \mu\left(\frac{\partial u}{\partial y} + \frac{\partial v}{\partial x}\right) \quad \tau_{xz} = \tau_{zx} = \mu\left(\frac{\partial w}{\partial x} + \frac{\partial u}{\partial z}\right) \quad \tau_{yz} = \tau_{zy} = \mu\left(\frac{\partial v}{\partial z} + \frac{\partial w}{\partial y}\right) \ . \tag{4.6}$$

Combining equations (4.3) to (4.6), the expanded form of momentum equations, which are a coupled system of three non-linear partial differential equations and are known in the literature as Navier-Stokes equations, are obtained:

$$\begin{aligned} \rho\left(\frac{\partial u}{\partial t} + u\frac{\partial u}{\partial x} + v\frac{\partial u}{\partial y} + w\frac{\partial u}{\partial z}\right) &= \rho g_x - \frac{\partial p}{\partial x} + \mu\left(\frac{\partial^2 u}{\partial x^2} + \frac{\partial^2 u}{\partial y^2} + \frac{\partial^2 u}{\partial z^2}\right) \\ \rho\left(\frac{\partial v}{\partial t} + u\frac{\partial v}{\partial x} + v\frac{\partial v}{\partial y} + w\frac{\partial w}{\partial z}\right) &= \rho g_y - \frac{\partial p}{\partial y} + \mu\left(\frac{\partial^2 v}{\partial x^2} + \frac{\partial^2 v}{\partial y^2} + \frac{\partial^2 v}{\partial z^2}\right) \\ \rho\left(\frac{\partial w}{\partial t} + u\frac{\partial w}{\partial x} + v\frac{\partial w}{\partial y} + w\frac{\partial w}{\partial z}\right) &= \rho g_z - \frac{\partial p}{\partial y} + \mu\left(\frac{\partial^2 w}{\partial x^2} + \frac{\partial^2 w}{\partial y^2} + \frac{\partial^2 w}{\partial z^2}\right). \end{aligned} \tag{4.7}$$

The energy equation can be written in the following form:

$$\rho \frac{d\hat{u}}{dt} + p(\nabla \cdot \boldsymbol{V}) = \nabla \cdot \left(k_{eff} \nabla T\right) + \mu \left[2\left(\frac{\partial u}{\partial x}\right)^2 + 2\left(\frac{\partial v}{\partial y}\right)^2 + 2\left(\frac{\partial w}{\partial z}\right)^2 + \left(\frac{\partial v}{\partial x} + \frac{\partial u}{\partial y}\right)^2 + \left(\frac{\partial w}{\partial y} + \frac{\partial v}{\partial z}\right)^2 + \left(\frac{\partial u}{\partial z} + \frac{\partial w}{\partial x}\right)^2\right] \quad (4.8)$$

In the energy equation k_{eff} is the effective thermal conductivity $k_{eff} = k + k_t$ and $\hat{u}$ is the total energy per unit mass. Usually, the internal energy can be approximated by the following expression:

$$d\hat{u} = c_v dT \quad (4.9)$$

If $\nabla \cdot V = 0$ and c_v, μ, k, ρ are assumed constant, the energy equation is simplified to:

$$\rho c_v \frac{dT}{dt} = k \nabla^2 T + \mu \left[2\left(\frac{\partial u}{\partial x}\right)^2 + 2\left(\frac{\partial v}{\partial y}\right)^2 + 2\left(\frac{\partial w}{\partial z}\right)^2 + \left(\frac{\partial v}{\partial x} + \frac{\partial u}{\partial y}\right)^2 + \left(\frac{\partial w}{\partial y} + \frac{\partial v}{\partial z}\right)^2 + \left(\frac{\partial u}{\partial z} + \frac{\partial w}{\partial x}\right)^2\right] \quad (4.9)$$

The two terms on the right hand side of the energy equation represent the conduction heat transfer and the viscous dissipation, respectively. Similar to the substantial derivative of velocity, $\frac{dT}{dt}$ can be expanded as:

$$\frac{dT}{dt} = \frac{\partial T}{\partial t} + u \frac{\partial T}{\partial x} + v \frac{\partial T}{\partial y} + w \frac{\partial T}{\partial z} \quad . \quad (4.10)$$

4.1.2 Reynolds Averaged Navier-Stokes (RANS) Equations

A general analytical solution of conservation system of equations (mass, momentum and energy) has not been obtained to date, except for very simple flows and geometries (e.g., Couette flow, Poiseuille flow). Also, for relatively simple geometries and not very high Reynolds numbers, the system of equations was numerically solved using very fine mesh sizes and time steps, which were able to capture the finest structures of turbulence (Kolmogorov microscales). Using this method, the system of conservation equations are solved “directly”, that is, no turbulence models are employed - hence, no controversial assumptions between the flow field variables, therefore the name Direct Numerical Simulation (DNS). In spite of their accuracy and their capability to solve the whole range of turbulence scales, the DNS techniques use very fine meshes and time steps, requiring very large computational memory and CPU power. This prevented their usage in real flow systems.

To overcome the difficulties raised by DNS, methods that filter out small turbulent length scales and solve only larger scales have been developed; they fall under the generic category of Large Eddy Simulations (LES). They are based on the fact that the large scale motions (large eddies) are more flow and geometry dependent, while the fine structure of turbulence (small eddies) are more homogeneous and universal in their nature, hence easier to model. Moreover, most of the kinetic energy of a fluid is carried by large eddies. This approach is more suitable for the real flows and has been successfully applied to various laboratory and industrial flows. LES require much less computation power than DNS; however, high Re number flows or complex geometries still require significant memory and CPU resources.

A less demanding approach, in terms of computing requirements, is constituted by the Unsteady Reynolds Averaged Navier-Stokes equations (URANS) - when the flow presents distinct large-scale coherent structures (i.e. large scale vortices) - or Reynolds Averaged Navier-Stokes equations (RANS), when steady state is assumed for the equation of motions of large scale structures. The derivation of URANS/RANS is based on the application of Reynolds decomposition to fundamental conservation equations. Reynolds averaging of conservation equations involves Reynolds decomposition in mean and fluctuating components. Using this approach, a flow parameter (e.g. velocity, pressure, temperature) can be written as sum of *mean (or ensemble average)* value $\langle A \rangle$ and the fluctuations *a*:

$$A = \langle A \rangle + a \tag{4.11}$$

Furthermore, for convenience in writing the equations that contain tensors (especially momentum equations) the conservation equations can be expressed in index notation, by which the velocity vector is written as U_i, $i = 1, 2, 3$. In this notation, the Einstein summation notation is used, by which an index repeated in the same term of an equation is summed over its range. Due to its convenient features, this notation is adopted throughout this work.

It should be noted that ensemble averaging is conceptually different from time averaging. They coincide only for stationary processes (i.e. the statistical processes whose statistical properties are not affected by a shift in the time origin). Otherwise, ensemble averaging denotes averaging across a sufficient number of the members of the ensemble, at a certain time instant, thus the ensemble average may have time dependence. Obviously, time averaging produces time-independent results. In order to distinguish between the two ways of averaging, different mathematical symbols are used: angle brackets < > for ensemble averages and overbar for time averages. For example, the velocity can be decomposed as a mean component (also called ensemble-averaged) and a fluctuating component:

$$U_i = \langle U_i \rangle + u_i \tag{4.12}$$

This approach can also be applied to any scalar quantity, such as pressure, temperature, or kinetic energy.

A similar decomposition is employed by the Unsteady Reynolds Average Navier Stokes (URANS) equations. It involves the decomposition of the velocity vector in resolved and modeled components, respectively:

$$U_i = U_{i,r} + u_{i,nc} \tag{4.13}$$

The resolved component can be further decomposed in the time-averaged component and the "coherent" component:

$$U_{i,r} = \overline{U}_{i,r} + u_{i,c} \tag{4.14}$$

Combining equations (4.7) and (4.8) one can write the velocity vector as the sum of three terms, the time average, coherent and non-coherent components, hence the "triple decomposition":

$$U_{i,r} = \overline{U}_{i,r} + u_{i,c} + u_{i,nc} \tag{4.15}$$

The "coherent" component represents the motion of large scale, organized motions. The "unresolved" or "non-coherent" components are modeled by various turbulence models employed as "closure" for the system of fundamental conservation equations. The use of a specific turbulence model would provide estimates of time-dependent local statistical moments of unresolved properties. A representative quantity of turbulent motions is the instantaneous turbulent kinetic energy per unit mass, *k*, defined as:

$$k = \frac{1}{2}\langle u_i'' u_i'' \rangle = \frac{1}{2}\left(\langle u_1''^2 \rangle + \langle u_2''^2 \rangle + \langle u_3''^2 \rangle \right) \tag{4.16}$$

If triple decomposition is applied, then the time-averaged turbulent kinetic energy for the coherent (resolved) part is:

$$\bar{k}_c = \frac{1}{2}\left(\overline{u_{1,c}^2} + \overline{u_{2,c}^2} + \overline{u_{3,c}^2}\right) = \frac{1}{2}\left[\overline{\left(U_{1,r} + \bar{U}_{1,r}\right)^2} + \overline{\left(U_{2,r} - \bar{U}_{2,r}\right)^2} + \overline{\left(U_{3,r} - \bar{U}_{3,r}\right)^2}\right] \quad (4.17)$$

Similarly, for the non-coherent (unresolved) part:

$$\bar{k}_c = \frac{1}{2}\left(\overline{u_{1,nc}^2} + \overline{u_{2,nc}^2} + \overline{u_{3,nc}^2}\right) \quad (4.18)$$

Thus, the total time averaged kinetic energy is:

$$\bar{k} = \bar{k}_c + \bar{k}_{nc} \quad (4.19)$$

Applying Reynolds decomposition the mass conservation equation in index notation becomes:

$$\frac{\partial \rho}{\partial t} + \frac{\partial}{\partial x_i}(\rho U_i) = 0 \quad (4.20\quad)$$

If density is assumed constant (ρ = const.), thus, the mass conservation equation is simplified to:

$$\frac{\partial U_i}{\partial x_i} = 0 \quad (4.15)$$

Applying the decomposition properties to the instantaneous form of continuity equations we obtain:

1) continuity equations for the mean

$$\frac{\partial \langle U_i \rangle}{\partial x_i} = 0 \quad (4.16)$$

2) continuity equation for the fluctuations

$$\frac{\partial u_i}{\partial x_i} = 0 \quad (4.17)$$

Using index notation the conservation of momentum equation is

$$\frac{\partial}{\partial t}(\rho U_i) + \frac{\partial}{\partial x_j}(\rho U_i U_j) = \\ -\frac{\partial P}{\partial x_i} + \frac{\partial}{\partial x_j}\left[\mu_{eff}\left(\frac{\partial U_i}{\partial x_j} + \frac{\partial U_j}{\partial x_i} - \frac{2}{3}\delta_{ij}\frac{\partial U_k}{\partial x_k}\right)\right] + \frac{\partial}{\partial x_j}\left(-\rho\langle u_i u_j\rangle\right) \tag{4.18}$$

If the simulated flow field is subject to surface heat flux the energy equation must be solved. The conservation of energy equation in index notation is given by the expression:

$$\frac{\partial}{\partial t}(\rho E) + \frac{\partial}{\partial x_j}(u_j(\rho_e + P)) = \\ \frac{\partial}{\partial x_j}\left(k_{eff}\frac{\partial T}{\partial x_j}\right) + \frac{\partial}{\partial x_j}\left[u_i \mu_{eff}\left(\frac{\partial u_i}{\partial x_j} + \frac{\partial u_j}{\partial x_i} - \frac{2}{3}\delta_{ij}\frac{\partial u_k}{\partial x_k}\right)\right] \quad , \tag{4.19}$$

where E is the specific internal energy and is defined as:

$$E = h - \frac{P}{\rho} + \frac{U^2}{2} \tag{4.20}$$

The effective thermal conductivity k_{eff} and the effective dynamic viscosity μ_{eff} are obtained by the superposition (summation) of molecular and turbulent components, respectively:

$$k_{eff} = k + k_t \\ \mu_{eff} = \mu + \mu_t \tag{4.21}$$

Similarly with the momentum equation, the significance of the terms that constitute the energy equation is as follows:

- The left hand side is the total change of the energy in time and it is composed of the contribution of the local change over time and the convection of energy by the flow.
- The right hand side represents the sum of the effective diffusion of heat (molecular and turbulent) and viscous heating, respectively.

4.1.3 Reynolds stress equations

Using the methodology presented by Tavoularis (2007), the momentum equation for the mean velocity is

$$\frac{\partial \langle U_i \rangle}{\partial t} + \langle U_j \rangle \frac{\partial \langle U_i \rangle}{\partial x_j} = -\frac{1}{\rho} \frac{\partial}{\partial x_i} \left(\langle P \rangle \delta_{ij} + \mu \frac{\partial \langle U_i \rangle}{\partial x_j} - \rho \langle u_i u_j \rangle \right) \qquad (4.22)$$

The term $\mu \frac{\partial \langle U_i \rangle}{\partial x_j}$ represents the viscous stress and is dependent only on the velocity gradient and the dynamic viscosity of the fluid. The term $-\rho \langle u_i u_j \rangle$ is the Reynolds stress and is a property of turbulence. The physical meaning of this term can be regarded as the "friction" between neighboring turbulent eddies, which act as increased viscosity. At high Re number, such as flows in industrial processes or cooling systems of nuclear reactors the Reynolds stress is much higher than the viscous stress. However, near the walls the viscous stresses dominate.

The momentum equation for the velocity fluctuations is

$$\frac{\partial u_i}{\partial t} + \langle U_j \rangle \frac{\partial u_i}{\partial x_j} + u_j \frac{\partial \langle Ui \rangle}{\partial x_j} + u_j \frac{\partial u_i}{\partial x_j} = -\frac{1}{\rho} \frac{\partial p}{\partial x_i} + \upsilon \frac{\partial^2 u_i}{\partial x_j \partial x_j} + \frac{\partial \langle u_i u_j \rangle}{\partial x_j} \qquad (4.23)$$

By mathematical manipulation of the momentum equation for velocity fluctuations one can obtain a balance equation for the Reynolds stress tensor (known also as the Reynolds stress equation):

$$\begin{aligned} &\frac{\partial \langle u_i u_m \rangle}{\partial t} + \langle U_j \rangle \frac{\partial \langle u_i u_m \rangle}{\partial x_j} = \\ &-\langle u_j u_m \rangle \frac{\partial \langle Ui \rangle}{\partial x_j} - \langle u_i u_j \rangle \frac{\partial \langle U_m \rangle}{\partial x_j} - \frac{\partial \langle u_i u_j u_m \rangle}{\partial x_j} - \frac{1}{\rho} \left(\left\langle u_m \frac{\partial p}{\partial x_i} \right\rangle + \left\langle u_i \frac{\partial p}{\partial x_m} \right\rangle \right) + \qquad (4.24) \\ &+ \upsilon \left(\left\langle u_m \frac{\partial^2 u_i}{\partial x_j \partial x_j} \right\rangle + \left\langle \frac{\partial^2 u_m}{\partial x_j \partial x_j} \right\rangle \right) \end{aligned}$$

The left hand side represent the sum of the local and the convective derivatives of the Reynolds stress, that is the total rate of change of the Reynolds stress tensor $\frac{D\langle u_i u_m \rangle}{Dt}$.

In the right hand side, several rather complicated influences are found: terms coupling the Reynolds stress tensor with the mean velocity vector, terms coupling the velocity and the pressure fluctuations, viscous interactions of velocity fluctuations and their derivatives.

4.1.4 Turbulent kinetic energy equation

By further manipulation, the Reynolds stress transport equation becomes:

$$\begin{aligned}\frac{\partial k}{\partial t}+\langle U_j\rangle\frac{\partial k}{\partial x_j} &= -\langle u_i u_j\rangle\frac{\partial\langle U_i\rangle}{\partial x_j}-\frac{1}{\rho}\frac{\partial\langle u_j p\rangle}{\partial x_j}-\frac{1}{2}\frac{\langle u_j u_i u_i\rangle}{\partial x_j}+\\ &\upsilon\frac{\partial^2 k}{\partial x_j\partial x_j}+\upsilon\frac{\partial^2\langle u_i u_j\rangle}{\partial x_i\partial x_j}-\frac{1}{2}\upsilon\left\langle\left(\frac{\partial u_i}{\partial x_j}+\frac{\partial u_j}{\partial x_i}\right)\left(\frac{\partial u_i}{\partial x_j}+\frac{\partial u_j}{\partial x_i}\right)\right\rangle\end{aligned} \tag{4.25}$$

Equation 4.25 is known as the turbulent kinetic energy equation and the parameter k is the turbulent kinetic energy per unit mass and is defined in the Eq. 4.10.

4.2 Turbulence modelling

The previous sections presented the fundamental conservation equations of fluid flow, as well as various techniques and limitations in obtaining their solutions. The use of Reynolds averaging of the conservation equations introduces additional unknowns, the Reynolds stresses. In order to solve the new system of equations, supplementary relationships, usually named “closure equations” should be introduced. They are in most cases algebraic or differential equations of a semi-empirical nature. A common approach involves modelling of the Reynolds stresses by relating them to the mean velocity gradients (Boussinesq hypothesis):

$$-\rho\langle u_i''u_j''\rangle = \mu_t\left(\frac{\partial u_i}{\partial x_j}+\frac{\partial u_j}{\partial x_i}\right)-\frac{2}{3}\left(\rho k+\mu_t\frac{\partial u_k}{\partial x_k}\right)\delta_{ij} \tag{4.26}$$

The Boussinesq hypothesis is used in one or two-equation models, such as the Spalart-Allmaras, the k-ε and the k-ω turbulence models.

A more elaborate approach is employed by the Reynolds stress model (RSM), which determines the turbulent shear stresses by solving transport equations for each stress component. An additional scale-determining equation, typically for ε, is required, as well. It should be noted that the RSM solves five additional equations for 2-D flows and seven for 3-D flows.

4.2.1 Spalart-Allmaras (S-A) model

The Spalart-Allmaras model is one-equation model that solves the transport equation for the kinematic eddy viscosity. The model was designed specifically for the aerospace industry and systems involving wall-bounded flows with mild separation and can be implemented in unstructured CFD solvers. However, its simplicity and relative novelty may recommend it for rather crude simulations on coarse meshes where accuracy is not critical. One well known issue of the S-A approach and other one equation models is that they have difficulties to rapidly accommodate changes in length scale, such as flows that change abruptly from wall-bounded to free shear. It is also less suited for recirculating and buoyancy-driven flows.

4.2.2 Standard k-ε model

The standard k-ε model was developed by Launder and Spalding (1974). It falls within the category of the two-equation models, which solves separately the transport equations for turbulent velocity and turbulent length scales. It became very popular and is widely used in practical applications, mainly due to its robustness, economy and reasonable accuracy for a wide range of turbulent flows. The standard $k - \varepsilon$ model requires two partial differential equations, one for the turbulence kinetic energy k and another for the turbulence dissipation rate ε, in order to determine the turbulence viscosity, which then leads to the Reynolds stresses through Boussinesq's relation. One well-known limitation of the standard k-ε turbulence model is the assumption that the flow is fully turbulent and the effects of molecular viscosity are negligible, thus the difficulty of flow prediction within the viscous sublayer and boundary layer. Also, it seems that it performs rather poorly in separated flows.

4.2.3 RNG k-ε model

The RNG-based k-ε turbulence model is derived from the instantaneous Navier-Stokes equations, using a specific mathematical technique – "renormalization group" (RNG). The analytical derivation results in a model with constants different from those in the standard k-ε model, and additional terms and functions in the transport equations for k and ε. This leads to the following improvements versus the standard k-ε model:

- The RNG model has an additional term in ε equation that improves the accuracy for rapidly strained flows.
- RNG includes the effect of swirling.
- The RNG includes an analytical expression for turbulent Pr numbers; on the contrary, the standard k-ε uses user-specified, constant values.
- The RNG performs much better at low Re number flow, due to an analytically derived differential formula for effective viscosity that accounts for low-Reynolds number effects

The above mentioned features make the RNG k-ε model more accurate and reliable for a wider class of flows than the standard k-ε model.

4.2.4 Realizable k-ε model

The realizable k-ε model contains the following improvements versus the standard k-ε model:

- new formulation for the turbulent viscosity.
- new transport equation for the dissipation rate: ε has been derived from an exact equation for the transport of the mean square vorticity fluctuation.

This results in a turbulence model which more accurately determines the flow field in flows with rotation, boundary layers in adverse pressure gradients, and separation and recirculation zones (Shih et al. (1994)). Both standard and realizable models were implemented in STAR-CCM+ using a two-layer approach; that is, they are activated if the mesh is sufficiently fine to resolve the viscous sublayer.

4.2.5 Heat transfer in k-ε turbulence models

Heat transfer is accounted by solving the energy equation given by (4.14). The terms in the right side represent the contribution of heat transferred by conduction through the boundaries of the infinitesimal fluid element $\frac{\partial}{\partial x_j}\left(k_{eff}\frac{\partial T}{\partial x_j}\right)$ and the contribution of viscous heating $\frac{\partial}{\partial x_j}\left[u_i\mu_{eff}\left(\frac{\partial u_i}{\partial x_j}+\frac{\partial u_j}{\partial x_i}-\frac{2}{3}\delta_{ij}\frac{\partial u_k}{\partial x_k}\right)\right]$, respectively. For incompressible flows at low speeds (much lower than the speed of sound) the viscous heating can be several orders of magnitude lower than the conduction heating. The effective heat transfer coefficient is calculated differently, depending on the turbulence model employed.

For the standard and realizable k-ε models the effective thermal conductivity is given by

$$k_{eff} = k + \frac{c_p\mu_t}{\Pr_t} \quad , \qquad (4.27)$$

where k is the thermal conductivity of the fluid (fluid property), c_p is the specific heat and μ_t is the turbulent viscosity. The turbulent Pr number is by default 0.85, but it can be changed by the user.

For the RNG k-ε model the effective thermal conductivity is computed as:

$$k_{eff} = \alpha\frac{c_p}{\mu_{eff}} \quad , \qquad (4.28)$$

where α is given by

$$\left|\frac{\alpha-1.3929}{\alpha_0-1.3929}\right|^{0.6321}\left|\frac{\alpha+2.3929}{\alpha_0+2.3929}\right|^{0.3679}=\frac{\mu_{mol}}{\mu_{eff}} \quad , \qquad (4.29)$$

where $\alpha_0=1/Pr=k/\mu c_p$. In the high Re number range $\mu_{mol}<<\mu_{eff}$ and $\alpha_k=\alpha_\varepsilon=1.393$.

It is noted that k is characteristic of molecular heat diffusion and is a property of substance (i.e. the working fluid), while k_{eff} represents the combined contributions of molecular heat diffusion and turbulent heat diffusion.

4.2.6 Standard *k-ω* model

The standard *k-ω* model is an empirical model based on model transport equations for the turbulence kinetic energy (*k*) and the specific dissipation rate (*ω*), being an alternative to the *k-ε* model. This model incorporates modifications for low-Reynolds number effects, compressibility and shear flow spreading. It can be successfully applied for wakes, mixing layers, plane, round and radial jets, in general to wall-bounded and free-shear flows. The transport equations in the original *k-ω* model (Wilcox 1998) are given by:

$$\frac{\partial k}{\partial t} + U_j \frac{\partial k}{\partial x_j} = \vartheta_t S^2 - \beta k \omega + \frac{\partial}{\partial x_j}\left[(\vartheta + \sigma \vartheta_t)\frac{\partial k}{\partial x_j}\right]$$

$$\frac{\partial \omega}{\partial t} + U_j \frac{\partial \omega}{\partial x_j} = \alpha S^2 - \beta \omega + \frac{\partial}{\partial x_j}\left[(\vartheta + \sigma^* \vartheta_t)\frac{\partial \omega}{\partial x_j}\right]$$

$$\vartheta_t = \frac{k}{\omega}$$

$$S = \sqrt{2 S_{ij} S_{ij}}$$

$$S_{ij} = \frac{1}{2}\left(\frac{\partial U_i}{\partial x_j} + \frac{\partial U_j}{\partial x_i}\right)$$

$$\alpha = 0.52, \qquad \beta = 0.072, \qquad \beta^* = 0.09, \qquad \sigma = 0.5, \qquad \sigma^* = 0.5\,.$$

A significant advantage of this model is that it may be applied throughout the boundary layer, including the viscous subregion. Nevertheless, it seems that boundary layer computations are sensitive to the value of *ω* in the free stream.

4.2.7 Shear-Stress Transport (SST) *k-ω* model

Many two-equation turbulence models suffer from an inability to correctly model flows with an adverse pressure gradient or a recirculation zone. The goal of the SST model, developed by Menter (1994), is to eliminate this problem. This is accomplished by gradually blending the $k-\omega$ model in the near-wall region and the high Reynolds number $k-\varepsilon$ model in the core flow region, and then modeling the transport of turbulent shear stress similarly to the Johnson-King (JK) turbulence model (Menter, 1994). Previous two-equation models do not account for turbulent shear stress transport, and determine the turbulent shear stress τ_t by the method of

Menter (1994). The continuity, momentum and transport equations for k and ω in the $k\text{–}\omega$ SST turbulence model are described by:

$$\frac{\partial \rho}{\partial t} + \frac{\partial}{\partial x_i}(\rho u_i) = 0$$

$$\frac{\partial}{\partial t}(\rho u_i) + \frac{\partial}{\partial x_j}\left(\rho u_j u_i\right) = \frac{\partial}{\partial x_j}\left(-p\delta_{ij} + \hat{\tau}_{ij}\right)$$

$$\frac{\partial}{\partial t}(\rho k) + \frac{\partial}{\partial x_j}\left(\rho u_j k\right) = \tau_{ij}\frac{\partial u_i}{\partial x_j} - \beta^* \rho \omega k + \frac{\partial}{\partial x_j}\left[(\mu + \sigma \mu_T)\frac{\partial k}{\partial x_j}\right]$$

$$\frac{\partial}{\partial t}(\rho \omega) + \frac{\partial}{\partial x_j}\left(\rho u_j \omega\right)\omega = \alpha \frac{\omega}{k}\tau_{ij}\frac{\partial u_i}{\partial x_j} - \beta^* \rho \omega^2 + \frac{\partial}{\partial x_j}\left[(\mu + \sigma \mu_T)\frac{\partial \omega}{\partial x_j}\right]$$

$$\hat{\tau}_{ij} = 2\mu\left(S_{ij} - \frac{1}{3}\frac{\partial u_k}{\partial x_k}\delta_{ij}\right) + \tau_{ij}$$

$$\tau_{ij} = 2\mu_T\left(S_{ij} - \frac{1}{3}\frac{\partial u_k}{\partial x_k}\delta_{ij}\right) - \frac{2}{3}\rho k \delta_{ij}$$

$$S_{ij} = \frac{1}{2}\left(\frac{\partial u_i}{\partial x_j} + \frac{\partial u_j}{\partial x_i}\right)$$

$$\mu_T = \frac{\alpha^* \rho k}{\omega}$$

$$\alpha^* = \frac{\alpha_0^* + {Re_T}/{R_k}}{1 + {Re_T}/{R_k}} \qquad \alpha = \frac{5}{9}\frac{\alpha_0^* + {Re_T}/{R_\omega}}{1 + {Re_T}/{R_\omega}}(\alpha^*)^{-1}$$

$$\beta^* = \frac{9}{100}\frac{5/18 + \left({Re_T}/{R_\beta}\right)^4}{1 + \left({Re_T}/{R_\beta}\right)^4}$$

$$\beta = \frac{3}{40}, \qquad \sigma = \sigma^* = 0.5, \qquad \alpha_0^* = \frac{\beta}{3}, \qquad \alpha_0 = \frac{1}{10}, \qquad R_\beta = 8, \qquad R_k = 6, \qquad R_\omega = 2.7$$

$$Re_T = \frac{\rho k}{\omega \mu}\ .$$

The principal turbulent shear stress is defined as $\tau = -\rho\overline{u'v'}$ and is assumed proportional to the turbulent kinetic energy k:

$$\tau = \rho a_1 k$$

The production has been shown to be much greater than dissipation of turbulent kinetic energy in some flows with adverse pressure gradients (Menter, 1992; Blazek, 2005). The standard k-ω equations would then lead to an overprediction of turbulent shear stress, which results in overestimation of the turbulent (eddy) viscosity. As a result, predictions show that a flow tends to adhere to walls in situations at which it would actually separate. The SST model eliminates this problem with the application of a supplementary equation for the eddy viscosity (Menter, 1994). Also, the SST model incorporates a damped cross-diffusion derivative term in the ω equation. The above mentioned features make the SST k-ω model more accurate and reliable for a wider class of flows than the standard k-ω models.

4.2.8 Reynolds Stress Model

Reynolds Stress Model (RSM) is one of the most elaborate types of the turbulence models that close the RANS equations by solving the transport equation for the Reynolds stresses together with an equation for the dissipation rate, thus abandoning the isotropic eddy viscosity hypothesis. Five additional equations are required for 2-D flows and 7 for 3-D flows, respectively. Unlike two-equation and one equation models, the RSM accounts for flow history effects through terms representing the convection and diffusion of shear stress tensors. The effects of streamline curvature, system rotation and stratification can be taken into account through convection and production terms (Wilcox, 2000). The RSM model also uses modeled terms, derived from a combination of theoretical assumptions and empirical results. An important term modelled in the RSM is that of pressure-strain, which plays an important role in determining the structure of turbulent flows, distributing turbulent energy among the Reynolds stress components, and accounting for flow anisotropy. This term was initially modelled by considering homogeneous flows, but different approaches to modelling the pressure-strain term have recently been attempted. The coefficients of the RSM may need careful fine tuning in order to avoid solution divergence. The complex Reynolds stress models are known to give results superior to those of one- and two-equation turbulence models for flows with streamline curvature, sudden change in strain rate, and secondary motions of the second kind, although at the cost of increased computing time (Bradshaw, 1997).

CHAPTER 5

AN EXPERIMENTAL INVESTIGATION OF THE EFFECT OF FLOW OBSTACLES ON SINGLE PHASE HEAT TRANSFER[4]

Abstract

Heat transfer experiments on a heated tube equipped with flow obstructions have been performed. The working fluid was refrigerant R-134a and flow Reynolds (Re) number ranged from 14,000 to 97,000. Three types of flow obstruction were investigated: eccentric cylinders with blunt and rounded edges, and annular obstacles, each having a flow blockage of either 0.15 or 0.30. The axial distribution of heat transfer coefficient was measured between 3 tube diameters downstream the trailing edge of the obstruction up to 70 diameters. The experimental data indicate that heat transfer augmentation downstream from the flow obstructions depends on the obstructed area, flow Reynolds number, distance from the flow blockage and to a lesser extent on the shape and the circumferential location of the obstruction. The current experiment confirms the previous findings that heat transfer augmentation (compared to bare tube heat transfer) decreases with an increase of flow Reynolds number. Heat transfer augmentation typically extends up to 30 tube diameters downstream of a flow obstacle. An improved prediction method that correlates the obstructed flow area, *Re* number and the distance from the trailing edge of the obstacle has been derived.

[4] The results of the heat transfer experiments have been documented in a paper published in Nuclear Engineering and Design, Vol 288, pp 195-207, 2015. The manuscript of this paper is presented in this Chapter.

1. Introduction

Convective heat transfer is the dominant heat transfer mechanism within the vast majority of heat transfer systems in fossil-fuelled and nuclear power plants. Efficient, safe and reliable operation of heat transfer equipment (such as boilers, heat exchangers, and fuel bundles) significantly contributes to the overall improvement of plant safety and performance.

The complexity of flow around obstacles or relatively complicated geometries gives rise to insurmountable difficulties for a purely analytical approach; however, experimental and numerical methods are available that have given promising results. The study of flows of practical interest requires extensive investigation and understanding of turbulence, vortices formation and dynamics, boundary layers, as well as the impact of turbulent flow structures on heat transfer and pressure drop. Previous experimental studies and numerical simulations have indicated that, in general, flow obstacles act as turbulence promoters and improve the downstream heat transfer coefficient, although at the expense of increased pressure drop.

Proper design and optimization of heat transfer systems (including fuel bundles) equipped with turbulence promoters requires an understanding of the complex mechanisms that govern the flow patterns, pressure drop and heat transfer around flow obstructions.

The purpose of the present investigation is (i) to examine systematically the essential features of heat transfer in the redevelopment region of turbulent flow downstream of various shaped obstacles in a circular tube;(ii) to determine the extent of blockage-induced heat transfer augmentation; and (iii) to develop an improved prediction method, applicable primarily to obstacle-equipped heated tubes in turbulent flow.

It is expected that an enhanced prediction of the heat transfer improvement provided by the flow obstacles will result in a more precise determination of the Onset of Nucleate Boiling (ONB) boundaries, a more accurate prediction of the maximum sheath temperature during reactor accident conditions and a more reliable method for validating numerical simulation tools and models.

2. Literature review

Flow obstructions in Tubes

Krall and Sparrow (1966) performed experiments to determine the effect of flow separation on heat transfer in water. The flow obstructions consisted of flow orifices located at the inlet of a heated circular tube. Test section was preceded by a flow developing segment. Different orifice diameters were tested, specifically with d_0/D = ⅔, ½, ⅓ and ¼, where d_0 denotes the diameter of the orifice and D the diameter of the pipe. These values correspond to blockage ratios, defined as the ratio between the obstructed cross section area and the area of the unobstructed tube, of 0.55, 0.75, 0.89 and 0.937, respectively. Measurements of axial distribution of local heat transfer coefficient indicated that the maximum heat transfer augmentation occurs at 1.25 to 2.2 tube diameters downstream from the flow obstacle, which, according to the authors, corresponds to the flow re-attachment area. The Reynolds number appeared to have a strong impact on the maximum heat transfer augmentation: for a given flow obstruction and Pr number, the maximum heat transfer augmentation $\left(\frac{Nu_{\max}}{Nu_0}\right)$ occurred at the lowest Reynolds number. Table 1 presents a summary of maximum heat transfer augmentation $\left(\frac{Nu_{\max}}{Nu_0}\right)$ and non-dimensional axial location of this maximum as function of obstacle height (H). It should be noted that the numerical values reported in Table 1 were inferred from the plots, therefore they are approximate.

Table 1 Maximum convective heat transfer augmentation and non-dimensional axial location

Orifice size (d_0/D)	Blockage ratio	*Re*							
		10,000		15,200		25,000		51,500	
		$\frac{Nu_{\max}}{Nu_0}$	$\frac{x_{\max}}{H}$	$\frac{Nu_{\max}}{Nu_0}$	$\frac{x_{\max}}{H}$	$\frac{Nu_{\max}}{Nu_0}$	$\frac{x_{\max}}{H}$	$\frac{Nu_{\max}}{Nu_0}$	$\frac{x_{\max}}{H}$
2/3	**0.55**	4.6	7.5	4.2	7.5	3.7	7.5	3.15	7.5
1/2	**0.75**	5	6.0	4.6	6.0	4.2	6.0	3.7	6.0
1/3	**0.89**	6.8	6.6	6.4	6.6	5.6	5.4	5.1	6.0
1/4	**0.94**	9.0	5.9	7.6	5.9	6.7	5.3	5.7	5.3

The authors observed that within the separated region (or the recirculation region, that is the region between the trailing edge of an obstacle and the reattachment area), the heat transfer coefficient increases monotonically as the reattachment area is approached, reaches its maximum at the reattachment and decreases downstream from the reattachment area. The effect of *Pr* number on the reattachment length or peak heat transfer augmentation was inconclusive for the range of *Pr* number investigated (3 to 6).

A related study was conducted by Koram and Sparrow (1978) who investigated heat transfer in the separation, reattachment and re-development regions of water flowing in circular channels equipped with a segmental orifice plate (i.e. obstructs a segment of the cross sectional area of the bare tube) attached to the wall. Three blockage plates were investigated with nominal blockage ratios of ¼, ½ and ¾, respectively. Reynolds number ranged from 10,000 to 60,000 and *Pr* number between 4 and 8. The peak circumferentially-averaged heat transfer augmentation, at various *Re* numbers are presented in Table 2. The exponential decay of heat transfer augmentation has similar trends for all obstacles investigated and extended axially for 18 to 21 tube diameters. The maximum heat transfer augmentation typically occurred at an axial location of 1.8 tube diameters downstream from the smallest obstacle and 3.7 tube diameters for the largest. When the location of flow reattachment is expressed as a function of obstacle height (*H*), its range is significantly reduced, being between 4.8 and 5.9 obstacle heights. The authors indicated that for nonsymmetrical obstacles, two types of local heat transfer maxima occur: one associated with the reattachment of the separated flow downstream from the obstacle and another due to impingement of flow deflected by the obstacle into the heated wall located in the unobstructed cross section of the channel. Note that the numerical values reported in Table 2 were inferred from the plots, therefore they are approximate. The experimental results suggest that the maximum heat transfer augmentation has a strong dependence on the obstructed area and the flow *Re* number.

Table 2. Maximum convective heat transfer augmentation and non-dimensional axial location

Nominal blockage ratio	Effective blockage ratio	***Re***									
		11,000		**15,000**		**25,000**		**40,000**		**60,000**	
		$\frac{Nu_{max}}{Nu_0}$	$\frac{x_{max}}{H}$	$\frac{Nu_{max}}{Nu_0}$	$\frac{x_{max}}{H}$	$\frac{Nu_{max}}{Nu_0}$	$\frac{x_{max}}{H}$	$\frac{Nu_{max}}{Nu_0}$	$\frac{x_{max}}{H}$	$\frac{Nu_{max}}{Nu_0}$	$\frac{x_{max}}{H}$
¼	**0.264**	2.4	4.8	2.2	5.7	2.1	5.7	2.0	5.7	2.0	4.8
½	**0.486**	3.0	5.9	2.9	6.3	2.7	5.5	2.6	5.5	2.55	4.9
¾	**0.730**	4.8	5.1	4.4	5.0	4.0	5.4	3.65	5.0	3.6	5.0

Consistent with earlier research findings, the data from Table 2 indicate that the peak heat transfer augmentation (i.e. versus the bare tube at the same flow conditions) diminishes with increase of flow *Re* number. Moreover, flow conditions being similar, the heat transfer augmentation increases as the obstructed area increases. With regard to the axial distance required for the flow to reattach to the heated wall, it appears that the most suitable characteristic length is the obstacle height, which provides significantly more consistent values than the tube diameter. Data from the Tables 1 and 2 show that typical values for the reattachment length in circular tubes equipped with blunt orifices are in the range 5 to 6 obstacle heights. Downstream from the reattachment area, heat transfer coefficient decreases monotonically to bare tube values. The axial effect persists for 18-21 tube diameters downstream the obstacle.

An experimental investigation conducted by Yao et al. (1995) used two methods of flow visualization - hydrogen bubble and dye injection - to study the vortex dynamics and heat transfer augmentation mechanisms in the presence of flow obstacles. The obstacle, located in a rectangular channel, had a square cross section, with a blockage ratio of about 0.2; the flow *Re* number was 10,500. The experiment showed that the Karman vortices were shed from the wake of the obstacle, with a velocity close to the mainstream velocity and they tend to move in a criss-cross motion along the channel. The paper concluded that the "washing" action exerted by discrete vortices islands was the main mechanism of heat transfer augmentation.

The experimental results of Doerffer et al (1996) showed that for a ring-shaped flow obstacle with a blockage ratio of 0.178, the maximum heat transfer augmentation (versus the bare tube) occurred just downstream from the obstacle and was 38% for $Re = 3.9 \cdot 10^4$ and decreased to 14% for $Re = 2.3 \cdot 10^5$. For the annular obstacle having a blockage ratio of 0.3, the heat transfer augmentation was 61% at $Re = 3.9 \cdot 10^4$ and 34% at $Re = 2.3 \cdot 10^5$. The heat transfer augmentation decreased exponentially with an increase in axial distance downstream from the obstacle. It was observed that, for the obstacle having the lowest blockage ratio, the heat transfer augmentation was significant up to 5 tube diameters (x/D=5) downstream and for the highest blockage ratio the enhancement region extended to about 15 tube diameters. The authors explained the augmentation effect of a flow obstacle by two mechanisms: flow acceleration at the location of obstacle and increased turbulent mixing downstream from the obstacle. Their work confirmed the previous findings that the highest heat transfer augmentation occurs at lower Re numbers and decreases monotonically as flow Re number increases.

Flow Obstructions in Bundle Geometries

Most experiments examining the effect of flow obstacles on heat transfer have been performed on bundle geometries, e.g. Yao et al., (1982), Rehme (1977), Kidd and Hoffman (1968), Hassan and Rehme, (1981).

Yao, S.C. et al. (1982) performed a study of heat transfer augmentation in rod bundles near grid spacers, for single phase and post critical-heat-flux flow regimes. They observed that the Nusselt number reaches a maximum at, or slightly behind the flow obstacle. After the fluid leaves the spacer, the hydrodynamic and thermal boundary layers begin to re-establish their fully developed profiles. The authors claimed that the boundary layer phenomenon was similar to the entry length effect of turbulent tube flow. According to the authors, the main mechanism of heat transfer augmentation at spacer location was flow acceleration due to flow area contraction. For relatively large obstacles, the fin effect cooling (i.e. conduction effect) constituted another effective cooling mechanism, especially for metals with high thermal conductivity. In the wake region, the heat transfer was enhanced by the turbulent wakes created downstream from an obstacle as flow decelerates. Downstream from an obstacle heat transfer augmentation was observed to be an exponentially decaying function of *x/D* where *x* is the distance downstream from the blockage:

$$\frac{Nu}{Nu_0} = 1 + 5.55\varepsilon^2 \exp\left(-0.13\frac{x}{D_h}\right) \tag{1}$$

where Nu_o is the Nusselt number of the bare tube and Nu refers to the tube equipped with flow obstacles, ε is the blockage ratio, x represents the axial distance downstream from the trailing edge of the obstacle and D_h is the hydraulic diameter of the heated channel. The authors recommended Equation (1) for flows having Reynolds number higher than 10^4. The exponentially decaying trend has been matched reasonably well by the predictions.

Similar results were obtained by Hassan and Rehme (1981), who performed tests with air in a three-rod subassembly, equipped with honeycomb-type spacer grids. Three sizes of the spacers were used, obstructing the flow respectively by 0.253, 0.3 and 0.35. The flow

Reynolds number was varied between 600 and $2 \cdot 10^5$, to simulate gas-cooled reactor conditions. The authors found a significant improvement in heat transfer downstream from the spacer grid. In particular: (i) the highest increase (from 50% to 100%) was observed at the downstream end of the grid (this improvement decayed exponentially with distance downstream from the obstacle), (ii) grids with the largest flow obstruction area resulted in the highest heat transfer augmentation, and (iii) with increasing Reynolds number the improvement decreased and was felt over a shorter downstream distance. Hassan and Rehme (1981) also developed and recommended a correlation accounting for the spacer grid effect on heat transfer.

Holloway et al. (2004) measured the circumferentially-averaged heat transfer coefficient in a 5-rod bundle geometry downstream from support grids at *Re* numbers between 28,000 and 42,000. The support grids were either standard support grids (with no flow enhancing features), or grids equipped with disk blockages or split vanes to enhance the heat transfer. The experimental results suggested that both power-law or exponential functions can reasonably describe the decay of the augmentation effect with distance downstream from the grid. The authors proposed several semi-empirical correlations to predict the heat transfer augmentation downstream from spacers with or without heat transfer enhancing features, such as discs or mixing vanes: for a standard support grid (without flow enhancing features) the downstream heat transfer was described by :

$$\frac{Nu}{Nu_0} = 1 + 6.5\varepsilon^2 \exp\left(-0.8\frac{x}{D_h}\right) \tag{2}$$

The same experimental data were also correlated in the power-law form:

$$\frac{Nu}{Nu_0} = 1 + 3.0\varepsilon^2 \left(\frac{x}{D_h}\right)^{-1.3} \tag{3}$$

The correlations are recommended for $1.4 < x/D < 33.6$. The definition of the parameters of Equations (2) and (3) are the same as for Equation (1).

While Holloway's (2004) experiment investigated mainly the axial effects of flow obstacles, their subsequent study (Holloway et al., 2005) also examined the circumferential variation of heat transfer coefficient in rod bundles. The circumferential variations were measured for three specific support grid designs (standard grid, split-vane pair grid and disc grid) at axial locations between 2.2 to 36.7 hydraulic diameters downstream from the grid position, at *Re* numbers of 28,000 and 42,000, respectively. The geometrical setup consisted of a 5 x 5 square array rod bundle. The experimental results indicated that the largest circumferential variation of *Nu* number occurred just downstream (at $x = 2.2\ D_h$) from the grid and decreased with the development of the flow downstream. The circumferential variations for disc type obstacle were very small and within the experimental measurement accuracy. By contrast, much larger variations (+30% to -15%) were observed for split-vane pair grids. The axial distance required for the circumferential effect to disappear was between 25 to 35 D_h.

A more recent correlation was developed by Miller et al. (2013), based on 7 x 7 pressurized water reactor (PWR) bundle heat transfer data obtained from the Penn State/NRC Rod Bundle Heat Transfer (RBHT) facility. The improved heat transfer correlation accounted for the effect of obstructed area, axial distance downstream from the grid and flow Reynolds number:

$$\frac{Nu}{Nu_0} = 1 + 465.4\,\mathrm{Re}^{-0.5}\,\varepsilon^2 e^{-7.31 \cdot 10^{-6}\,\mathrm{Re}^{1.15}(x/D)}. \quad (4)$$

The correlation was recommended for $0.156<\varepsilon<0.362$ and *Re* numbers between 8,000 and 30,000. The geometry was typical of a PWR fuel bundle cooled by superheated steam.

3. Heat transfer experiment

Heat transfer experiments were conducted in the multi-fluid test loop at University of Ottawa using HFC-134a as working fluid. The main reason for selecting the refrigerant HFC-134a as working fluid was that its specific heat and latent heat are much smaller than those of water, thus allowing us to use a compact experimental loop and a relatively smaller power supply, Moreover, it allowed more accurate temperature measurements. The main components of the loop were the test section, condenser, pressurizer, pumps, preheaters, power supply and loop instrumentation (see Figure 1). The test section was directly heated by a 12 kW direct current (DC) power supply. The inlet and outlet fluid temperatures of the test section were measured by two resistance temperature detectors (RTDs). The flow was recirculated by two gear pumps, installed in series, and delivering a constant volumetric flow rate. A bypass around the pumps controlled the flow rate. The flow rate was measured by a Coriolis flow meter with an accuracy of better than 0.5% and a flow range 0 to 0.34 kg s^{-1}. The pressure in the loop was controlled by the pressurizer. The pressurizer contained a heating coil, located at the bottom and a cooling coil near the top of the pressurizer. The power to the pressurizer heater (maximum 500 W) was regulated by an adjustable alternate current (AC) transformer. An electric pre-heater (maximum power 5 kW) and a coaxial heat exchanger (with hot water on the secondary side) were located between the pumps and the test section. They were used to adjust the test section inlet fluid temperature or inlet mass quality to the desired values. The vapour generated in the test section (if any) was condensed by a coaxial heat exchanger prior to the fluid being recirculated to the pump. A piezoelectric pressure sensor measured the absolute pressure at the outlet of the test section (TS), and a differential pressure sensor measured the pressure drop along the TS.

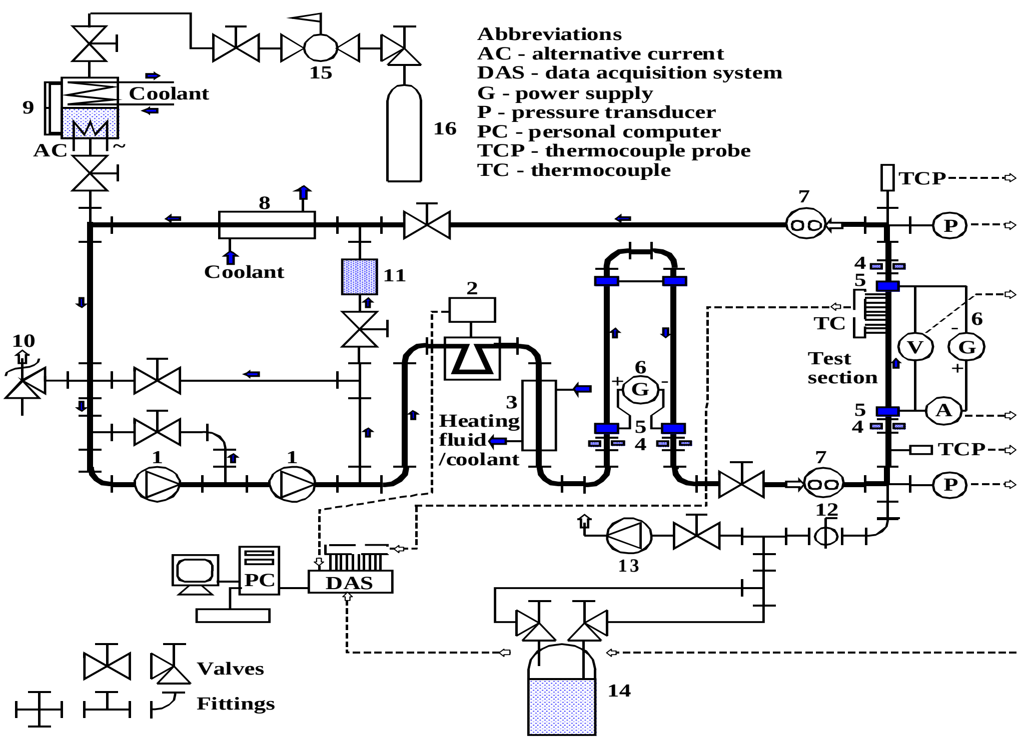

1-gear pump, 2-Coriollis type mass-flow-meter, 3-pre-heater, 4-dielectric fittings, 5-power terminals, 6-electrical pre-heater, 7-sight glass, 8-condenser, 9-pressurizer, 10-pressure relief valve, 11-refrigerant filter-dryer, 12-ball-valve, 13- vacuum pump, 14-refrigerant storage tank, 15-pressure reducer, 16-nitrogen container.

Figure 1 Multi-Fluid Loop (Vertical Test Section).

Heat transfer measurements were performed in an electrically heated tube, made of Inconel 600 and having an inside diameter (D_i) of 5.59 mm, an outside diameter (D_o) of 8.02 mm, a total length of 2 m and a heated length of 0.9 m. The temperature of the exterior wall of the test section was measured by six K-type self-adhesive thermocouples, located in pairs 180º apart at three axial planes as shown in Figure 2. Only the upstream two thermocouples were used in the analysis. Three types of flow obstacles were inserted sequentially in the test section: a blunt cylinder (B), a rounded cylinder (R) and an annular cylinder (A), coaxial with the test section. Each obstacle had a length of 10 mm and was manufactured from mild steel (see Figure 2). A ceramic magnet, located on the outside of the test section, held the obstacle at the desired location. The magnet was relocated during the experiment to permit the measurement of two effects on the local heat transfer coefficient: (i) the effect of distance downstream from the obstacle and (ii) the effect of azimuthal location. The axial location effect was measured at x = 3, 5, 7, 10, 20, 30, 50 and 70 test section diameters (D_i) downstream from the trailing edge of flow obstacles, thus the distance between the obstacle and the beginning of the heated length varied between 580 mm and 200 mm. The heated length (L_h=900mm) was selected such that the minimum distance between the obstacle and the beginning of the heated length was 200mm (>35 x/D) thus ensuring hydrodynamically and thermally developed flow upstream of the flow obstacle. Three obstacle shapes - hemispherical cylinder, blunt cylinder and annular cylinder, two blockage ratios (0.15 and 0.3), and four Reynolds numbers in the range of 14,000 to 97,000 were investigated.

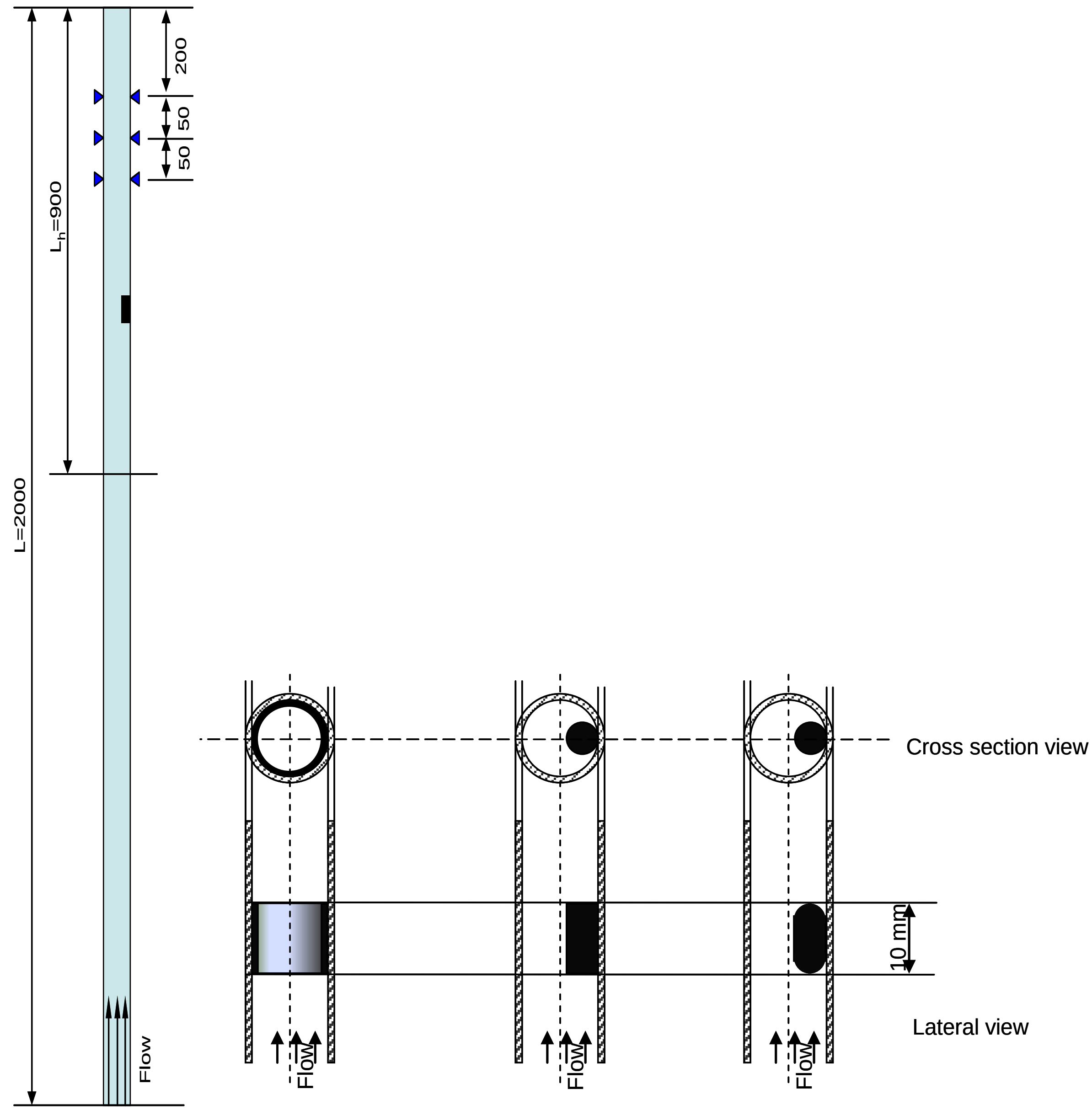

Figure 2 The schematic of test section, thermocouples layout and the obstacle types (from left to right: annular (A), blunt (B) and rounded (R))

3.1 Thermocouple Calibration

Ideally, the thermocouple pairs located at the same axial location (such as the three thermocouple pairs shown in Figure 2) should indicate the same temperature. The expected uncertainty in the thermocouple readings was 0.4 ºC (e.g. National instruments, 1999) . This uncertainty could be reduced for a given thermocouple using appropriate calibrations. In order to quantify the thermocouple uncertainty, several tests were performed. The thermocouple calibrations were performed by circulating single phase coolant through the test section using several bulk coolant temperatures. Because no heating was applied to the test section, wall thickness variation did not affect the readings. If the coolant temperature was close to the ambient temperature and/or the test section was thermally insulated, then heat losses and contact resistance effects were minimized or non-existent. Therefore, this test would show the inaccuracies (random and systematic) of the thermocouples and the analog-digital conversion (ADC) but for a relatively narrow range of temperatures.

Note that the calibrations were performed at high mass flux (G=3500 kgm^{-2}s^{-1}) and at pressure approximately equal to 2380 kPa. The reference bulk coolant temperature was based on the averaged values from resistance temperature detectors (RTD's) located at the inlet and outlet of the test section. Thermocouple voltage outputs were converted into temperatures, based on standard tables for type-K thermocouples. The maximum temperature discrepancy between the averaged RTD temperature and the two upstream test section TC temperatures for a range of coolant temperatures (10 to 80 °C in steps of 10K) was 0.35 K. These temperature discrepancies were corrected by using the correction function $\Delta T = aT + b$, where a and b were optimized for each thermocouple for the temperature range 10-80 °C. This reduced the maximum discrepancy significantly (from 0.35 K to 0.11K). Using the correction functions resulted in more uniform temperature distribution (smaller difference between thermocouple readings) for single phase and zero heat flux, which is closer to the ideal situation where all thermocouple measurements are equal.

Note that at temperatures higher than 60 ºC the RTDs indicate a systematically higher temperature than the thermocouples, suggesting that heat losses may decrease the thermocouple temperature readings by 0.1-0.15 ºC.

3.2 Heat Balance

During all runs, the inlet and outlet temperatures were measured along with flow, power and pressure. This thus provides and additional check on the combined accuracy of these five parameters using the heat balance equation:

$$U \cdot I = \dot{m}(h_{out} - h_{in}) + q_{loss} , \tag{5}$$

where U is the electric voltage to test section, I – the current to test section, $\dot{m}$ – the mass flow rate of refrigerant, h_{in} and h_{out} are the enthalpies of refrigerant at the inlet and outlet of test section and q_{loss} is the heat loss to the surroundings. For temperatures recorded during the experiments, heat loss represents a small fraction from total power to test section, usually less than 2%.

Figure 3 shows a typical results of the heat balance error, defined as the difference between the thermal power (i.e. coolant enthalpy increases) and electric power in % of power as a function of flow for conditions of interest. Note that the average heat-balance error is -1.4% while the maximum error (corresponding to low powers and low enthalpy rise in the test section) is -3.8%. The negative sign indicates that the coolant enthalpy increase is smaller than the electric power input to test section, thus it can be assumed that the difference can be attributed primarily to heat loss. Note also that, consistent with the previous assumption, the heat balance error decreases with an increase of flow.

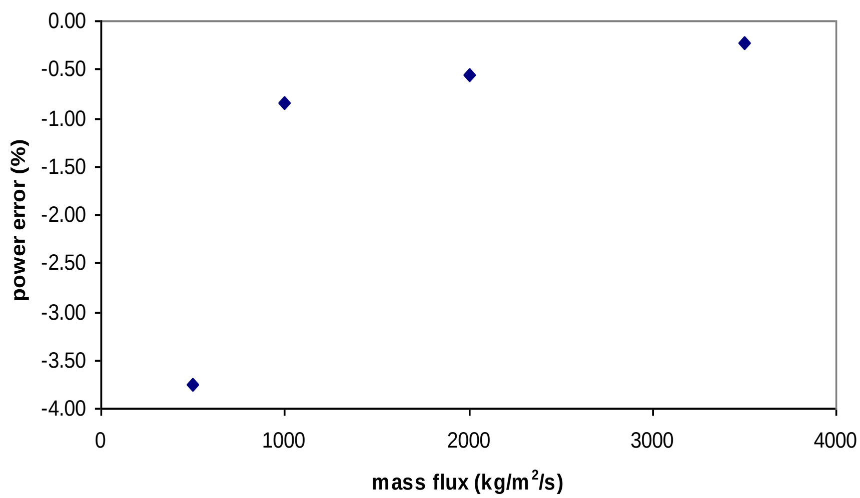

Figure 3. Heat balance error versus mass flux.

3.3 Temperature drop across the wall and wall thickness variations

Although the outside diameter and inside diameter of the supplied Inconel tubing can be measured fairly accurately at each end, the wall thickness may vary along the length due to eccentricities that can be introduced during the tube extrusion process. Tanase et al. (2008)

developed a methodology to examine the wall thickness variation for internally cooled tubes, based on outside wall temperature measurements during single-phase heat transfer, ONB and fully developed nucleate boiling. These three methodologies are all based on the following equations:

- The wall temperature drop across the wall can be expressed as a function of outside tube radius *R* and tube wall thickness :

$$\Delta T_w(\delta) = \frac{q_v(2R-\delta)\delta}{4k} - \frac{q_v R^2}{2k}\ln\frac{R}{R-\delta} \qquad , \qquad (6$$

where q_v is the Joule volumetric heat generation in the wall, *R* – the outside radius of the test section, *k*- thermal conductivity of test section and δ – the local thickness of the heated wall.

- The temperature difference between two thermocouples located at different circumferential positions (but the same axial location) ΔT_{WO}, having slightly different local wall thickness $\delta_1$and δ_2 respectively is given by:

$$\Delta T_{WO} = \frac{q_v R^2}{2k}\ln\frac{R-\delta_2}{R-\delta_1} + \frac{q_v}{4k}\left[2R(\delta_2-\delta_1)+(\delta_1-\delta_2)(\delta_1+\delta_2)\right] \qquad , \qquad (7)$$

where the average wall thickness, $R\text{-}r = \delta_{avg} = (\delta_1\text{-}\delta_2)/2$. This equation is based on the observation that the wall thickness variation is primarily due to bore eccentricity (Cubizolles et al., 2009)

- The local heat flux can be predicted from

$$q_s = q_v\left(\frac{R+r}{2r}\right)\delta = \frac{U^2}{\rho L_h}\left(\frac{R+r}{2r}\right)\delta \qquad . \tag{8}$$

Equation (8) shows that that the local surface heat flux (q_s) is proportional to the local wall thickness δ but the volumetric heat generation rate q_v is independent of wall thickness. Because of proportional relationship between q_s and δ, a variation of few percent in wall thickness (3-4% are typical values) will results in practically the same variation in the surface heat flux. In order to find the unknown variation in wall thickness, several nucleate boiling tests were performed on this test section at different heat flux levels. As expected, the wall superheat (T_{wi}-T_{sat}), is small (around 1K for the measurement conditions) and is a weak function of heat flux ($d(T_{wi}-T_{sat})/dq_s$= 0.018 K/(kW/m^2)) .

Based on the equations above mentioned, and the nucleate boiling measurements, Tanase et al. (2008) showed that wall thickness variation for the circumferential locations of the thermocouples of Figure 2 can be estimated: 1.26 mm on the side of TCs 1, 3 and 5, and 1.14 mm on the opposite side (corresponding to TCs 2, 4 and 6). These wall thicknesses were verified by subsequent measurements and a separate analysis using the ONB data, and single phase data, also shown by Tanase et al. (2008)[5]. Note that in most of the analysis below, we employ the azimuthal-averaged HTC based on the corrected temperatures from the two most upstream thermocouples in which case the impact of wall thickness variation on heat flux and HTC disappears.

3.4 Repeatability

The repeatability was assessed by re-running a limited number of cases from the test matrix after several weeks from the initial experiment. A typical example is presented in Figure 4. The difference between the initial and repeated values ranged from 0.5 to 4%, thus being consistent with the heat balance errors and the estimated measurement uncertainty of heat transfer coefficient.

[5] More details on the determination of wall thickness are included in Appendix B: Analysis of Wall Thickness Eccentricity

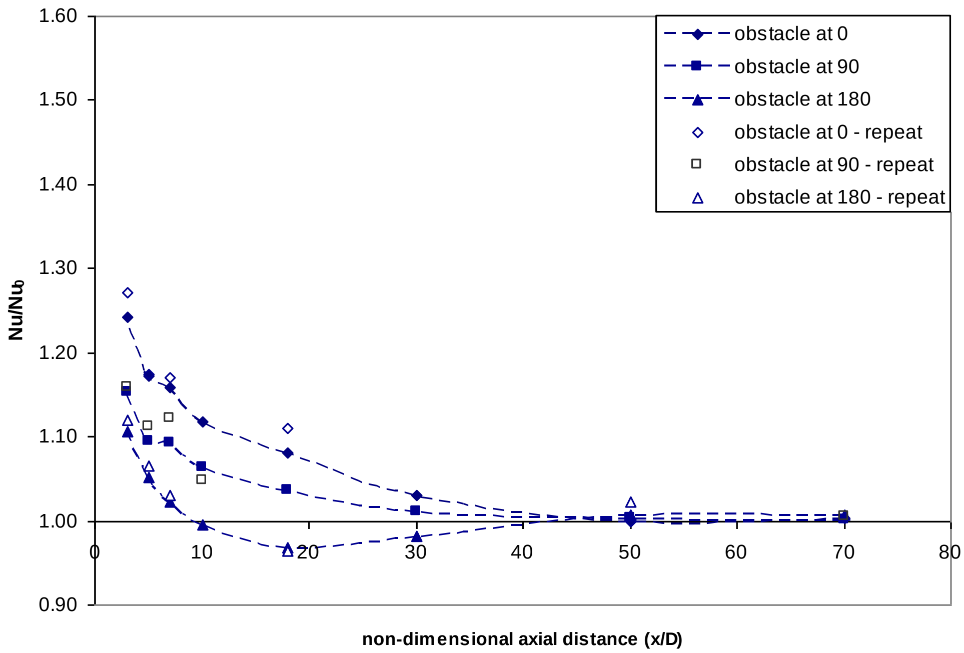

Figure 4 Repeated tests for the rounded obstacle having 0.15 obstructed ratio at *Re*=28,000.

3.5 Uncertainty analysis

The uncertainty analysis was performed according to the methodology described by Tavoularis (2005). The overall uncertainty of a derived property, such as Nusselt number, is defined as:

$$u_{Nu} = \sqrt{b_{Nu}^2 + p_{Nu}^2}\ , \tag{9}$$

where b and p are the bias (i.e. systematic) and precision (i.e. random) uncertainties, respectively.

Bias and precision uncertainties can be computed as:

$$b_{Nu} = \sqrt{\sum_{m=1}^{M}\left(\frac{\partial Nu}{\partial x_m} b_{x_m}\right)^2} \qquad p_{Nu} = \sqrt{\sum_{m=1}^{M}\left(\frac{\partial Nu}{\partial x_m} p_{x_m}\right)^2} \tag{10}$$

The subsidiary properties x_m from Equation (10) where m=1,2,…,M are either directly measured or derived. It should be noted that for directly measured properties, the uncertainties were estimated using instrumentation manufacturer specifications and calibration data. Also, if known (e.g. calibration data) the bias errors were corrected for, thus the largest contribution to uncertainty was given by the precision (random) components. The estimation of total uncertainty of power to test section was 31W or 1.03% P_{max}. The uncertainties in heat transfer coefficient, *Nu* number and *Re* number were estimated to 4.3%, 6.1%, and 3.2%, respectively.

4. Results and discussion

After calibrating the thermocouples and correcting for the temperature drop across the wall, the inside wall temperatures were subsequently evaluated. The local heat transfer coefficient (HTC) was calculated and azimuthally-averaged for the selected pair of thermocouples located at the same axial location. Based on the averaged HTCs, the local Nusselt numbers (Nu_x) were evaluated and were subsequently divided by the corresponding Nusselt number Nu_o based on measurements by the same thermocouple pair but in the absence of obstacles. This Nusselt number ratio was used in our subsequent analysis of the enhancement effect.

A detailed analysis of the heat transfer measurements with the bare tube without obstacles was performed by comparing our measurements against predictions of six leading single-phase heat transfer correlations. The Gnielinski (1976) equation was found to provide the best prediction (avg error -6.5%, RMS error 7.8%). To remove the bias in the prediction, the measured Nu_0 instead of the predicted value was used in our subsequent analysis.

Figures 5 and 6 show the current experimental data in terms of Nusselt number ratio (Nu_x/Nu_o) as a function of dimensionless distance from the obstacle. A comparison of the experimental results - for the annular (A), blunt (B) and rounded (R) obstacle shapes - with the prediction methods of Yao et al (1982), Holloway (2004) and Miller (2013), is also shown and reveals significant differences. All prediction methods underpredicted the current experimental data, especially in the low *Re* number range. However, at *Re* > 50,000, the correlation of Yao et al. (1982) showed better agreement with the current experimental data.

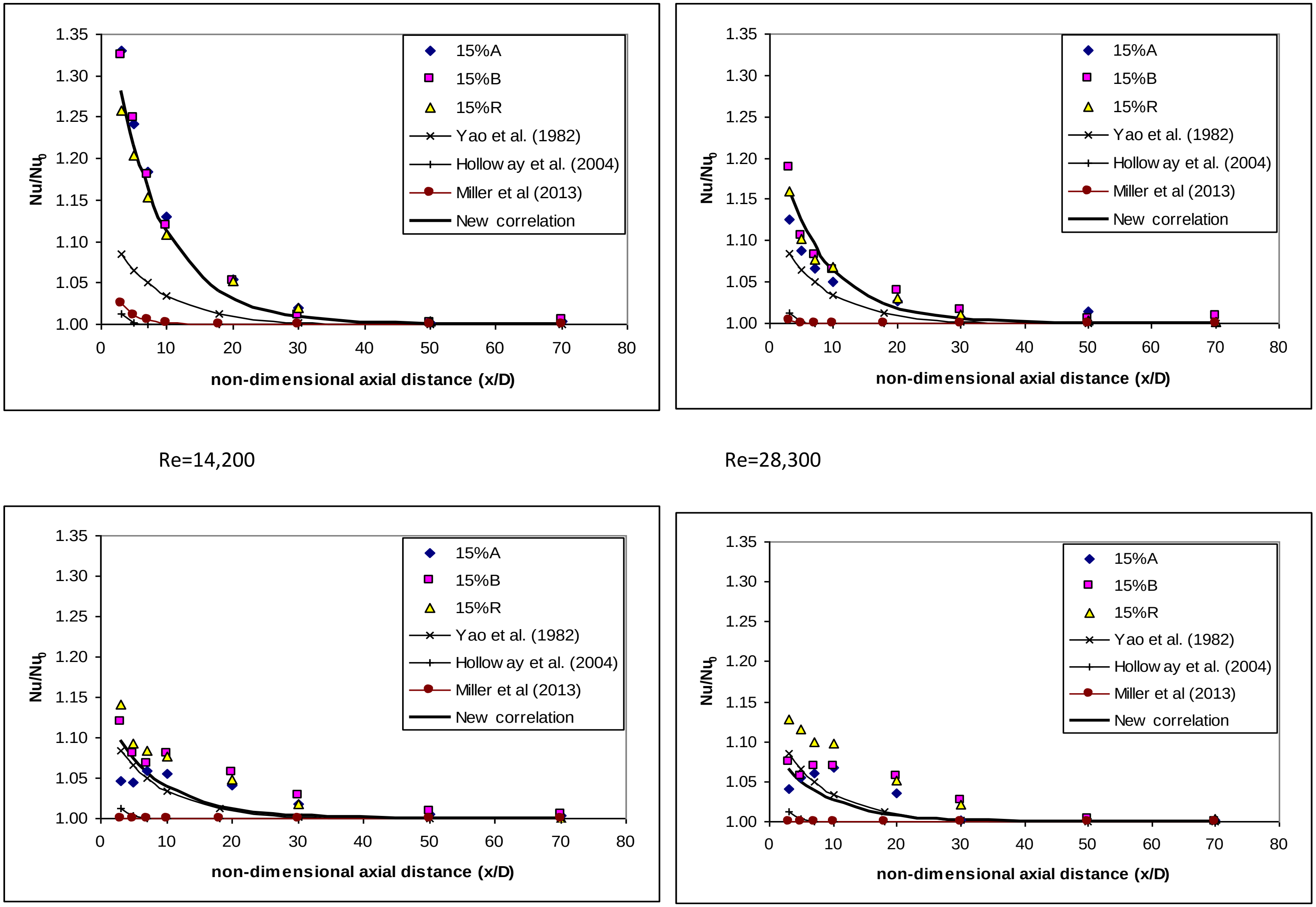

Re=14,200 Re=28,300

Re=56,000 Re=97,000

Figure 5 Comparison of current experimental data with existing prediction methods for obstacles having 0.15 blockage ratio, at various *Re* numbers.

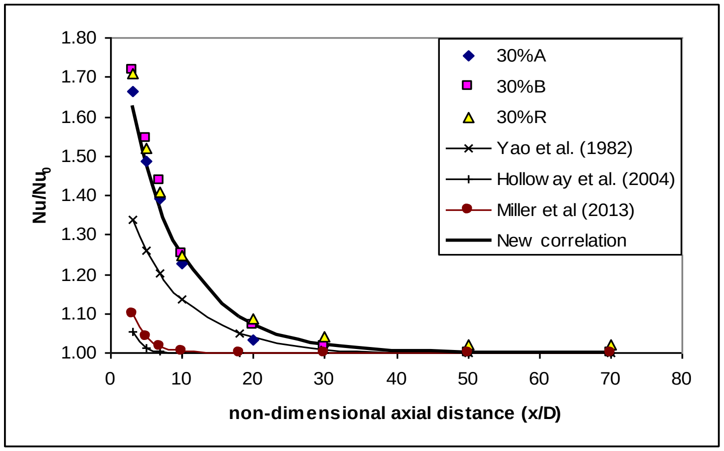

Re=14,200

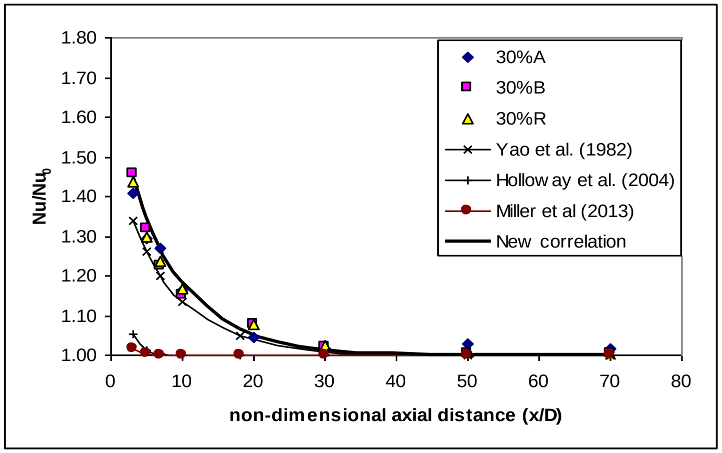

Re=28,300

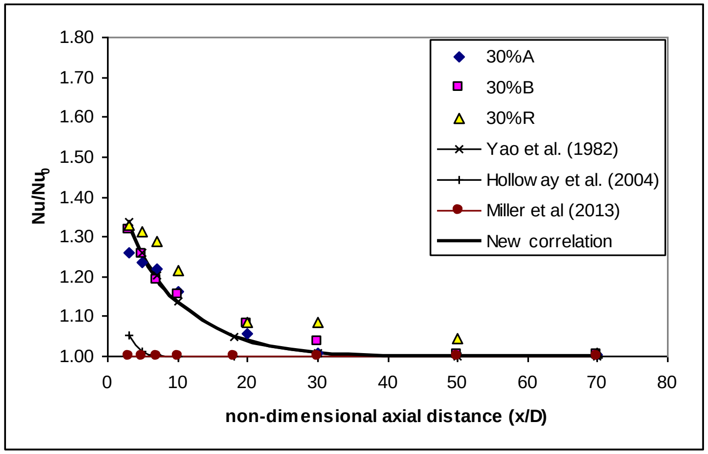

Re=56,000

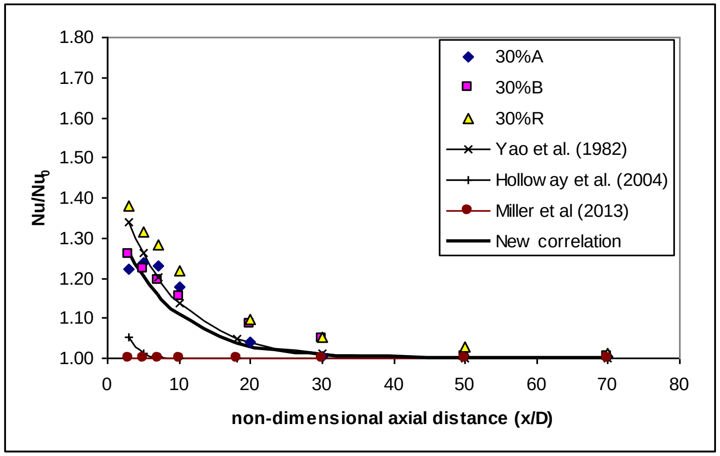

Re=97,000

Figure 6 Comparison of current experimental data with existing prediction methods for obstacles having 0.3 blockage ratio, at various *Re* numbers.

4.1 Improved prediction method

The prediction methods described in Section 2 were assessed against current experimental data. The same correlations and experimental data are plotted in Figures 5 and 6, respectively. The error, average of errors and root mean square (r.m.s) of errors are defined by Equations 11.

$$error = \frac{\left(\frac{Nu}{Nu_0}\right)_{predicted} - \left(\frac{Nu}{Nu_0}\right)_{measured}}{\left(\frac{Nu}{Nu_0}\right)_{measured}}$$

$$Avg = \frac{\sum_{i=1}^{N} error_i}{N} \qquad (11)$$

$$RMS = \sqrt{\frac{\sum_{i=1}^{N} error_i^{\,2}}{N}}$$

The error statistics are summarized in Table 3:

Table 1. Comparison between existing prediction methods vs current experimental data

Correlation	Average of errors (%)	r.m.s of errors (%)
Yao et al. (1982)	-3.14	5.8
Holloway et al. (2004)	-8.93	12.8
Miller et al. (2013)	-10.02	12.9

An examination of Table 3 indicates large differences between prediction accuracy of various correlations. It appeared that the prediction methods derived from experimental data obtained for fuel bundles generally underpredicted the experimental results obtained for tubes, especially in the lower flow range. The relatively large difference between the prediction methods for fuel bundles indicates that they are primarily suitable for the geometry and flow conditions used for their derivation. It is noted that the Yao et al.

correlation is the most suitable for the new experimental data, especially in the high Re number range.

In order to derive an improved prediction method, the following assumptions were made:

- the augmentation decays exponentially with an increase of axial distance downstream from obstacle;
- heat transfer enhancement is distributed uniformly around the tube circumference
- three obstruction ratios were considered: 0, 0.15 and 0.30; 0 was selected in order to ensure correct asymptotic trends;
- the variables that correlate heat transfer augmentation are blockage ratio (ε), axial distance (*x/D*) and the flow Re number;

The correlation of the current experimental data by the least squares method produced the following expression:

$$\frac{Nu}{Nu_0} = 1 + A\varepsilon^B e^{-0.13\frac{x}{D_h}}$$

$$A = 3.58 + 10^{-5}\,\mathrm{Re} \qquad (12)$$

$$B = 0.47\ln(\mathrm{Re}) - 3.32$$

The newly developed prediction method has improved error statistics, having an average of errors of -1.09% and RMS of errors 2.8%.The comparison of the proposed correlation against experimental data and other correlations is plotted in Figures 5 and 6, respectively.

4.2 Comparison of existing and newly developed prediction methods with experimental data of Koram and Sparrow (1978)

To further substantiate the accuracy of current and newly developed prediction methods, a comparison with the Koram and Sparrow (1978) experimental data has been performed. It worth noting that their experiments were conducted in circular tubes with an inside diameter of 30.15 mm, direct current (DC) heated and using water as working fluid. Three blockage ratios were investigated, specifically 0.264, 0.486 and 0.720; only the first two blockage ratios were used in the current comparison, since they were within or not very far from the recommended applicability range of the prediction methods. The results of comparison are summarized in Table 4. Sample plots of comparison for the obstacle with blockage ratios of 0.264 and 0.486 are shown in Figures 7 and 8, respectively.

Table 2. Comparison between new and existing prediction methods vs. Koram and Sparrow experimental data

Correlation	Average of errors (%)	r.m.s of errors (%)
Yao et al. (1982)	-8.49	17.4
Holloway et al. (2004)	-25.2	31.6
Miller et al. (2013)	-25.91	29.4
New correlation	**-4.66**	**16.9**

The results indicate that convective heat transfer augmentation correlations derived from bundle data tend to underestimate the circular tubes experimental data by a significant amount. The prediction of the newly proposed correlation is closest to the experimental data, albeit with relatively large r.m.s errors. Note that the experimental data were read from the plots presented by Koram and Sparrow (1978), thus the comparison may have 1-2% uncertainty.

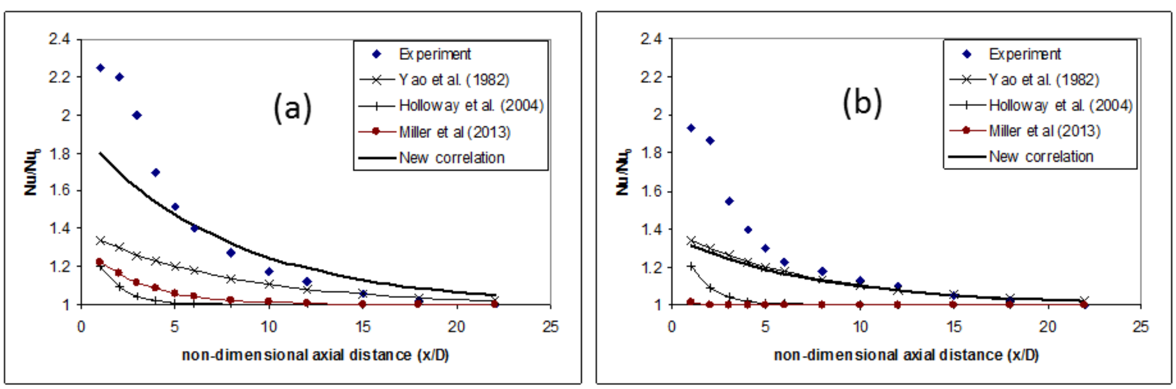

Figure 7 Comparison of new and existing prediction methods for heat augmentation with experimental data of Koram and Sparrow (1978), at *Re* = 11,000 (a) and 60,000 (b) and ε = 0.264.

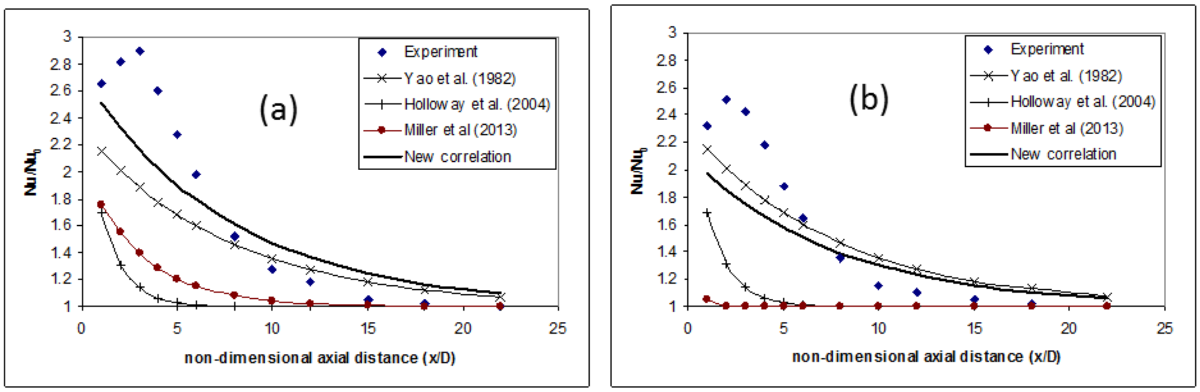

Figure 8 Comparison of new and existing prediction methods for heat augmentation with experimental data of Koram and Sparrow (1978), at *Re* = 11,000(a) and 60,000(b) and ε = 0.486.

4.3 Parameters influencing heat transfer augmentation

This subsection discusses the parameters affecting the heat transfer downstream of a flow obstacle.

Blockage ratio

The blockage ratio significantly influences the convective heat transfer augmentation downstream from a flow obstacle. Figures 5 and 6 show that for the entire range of flow Reynolds numbers investigated, an increase of the blockage ratio caused a significant increase of heat transfer augmentation. For example, for the rounded obstacle at *x/D* = 3, an increase in the blockage ratio from 0.15 to 0.30 resulted in an increase in heat transfer augmentation (i.e. ratio between the obstacle equipped Nu number and bare tube Nusselt number) from 1.35 to 1.7 at *Re* = 14,000 and from 1.13 to 1.34 at *Re* = 97,000, respectively.).

Axial distance downstream from an obstacle

The present experimental data indicate that heat transfer augmentation is still measurable up to *x/D*=50 for the blunt and rounded obstacles; however the axial impact of the annular obstacle disappeared at *x/D*=30.

Yao et al. (1982) and Holloway et al., (2004) reported that the heat transfer augmentation effect decreases exponentially with an increase of axial distance downstream from an obstacle. However, different authors disagree on the axial extent of blockage-induced heat transfer augmentation. Yao et al. (1982) suggested that the obstacle effect is similar to the entrance effect in turbulent channel flow. Koram and Sparrow (1978) stated that in case of obstacle equipped tubes the heat transfer augmentation has a more complex pattern since "Nusselt number increases at first, attains a maximum, and then decreases monotonically toward its fully developed value. This pattern is fundamentally different from the monotonic decrease that is characteristic of the conventional thermal entrance region. Furthermore, the blockage-related Nusselt numbers are very much greater than those for the conventional entrance region." Experimental data of Krall and Sparrow (1966) and Koram and Sparrow (1978) indicate that the axial extent of heat transfer augmentation is 18 to 27 tube diameters downstream from the flow obstacle.

Doerfer et al (1996) reported that the heat transfer augmentation lasted up to 15 tube diameters downstream from an obstacle.

Obstacle shape

Examination of Figures 5 and 6 indicates that in the lower Re number range, blunt obstacles induced higher heat transfer augmentation than rounded obstacles. However, at higher Re numbers, in the order of 90,000, rounded obstacles consistently induce higher heat transfer augmentation. The rounded obstacle with blockage ratio of 0.3 outperforms the blunt obstacle starting at Re = 50,000. Furthermore, a notably longer axial effect is exhibited by the rounded obstacle. The annular obstacle typically gives the lowest convective heat transfer augmentation and exhibits shorter decay lengths over which the heat transfer augmentation is noticeable.

Flow Reynolds number

The impact of flow Re number is generally significant: the experimental data show that the blockage-induced augmentation decreases as Re number increases. This observation holds for all obstacle shapes and blockage ratios investigated. For example, for a rounded obstacle having a blockage ratio of 0.3, the maximum augmentation ratio decreased from 1.7 at Re = 14,500 to 1.35 at Re = 97,000. For a blunt obstacle with a 0.15 blockage ratio, it decreased from 1.33 at Re = 14,500 to 1.13 at Re = 97,000. Similar trends were reported by other investigators (e.g. Koram and Sparrow (1978), Doerfer et al (1996)).

Circumferential location

The measurement of circumferential distribution of heat transfer coefficient downstream from an asymmetrically located obstacle indicated that, in general, the heat transfer coefficient was the highest on the obstructed side of the wall. The azimuthal distribution of heat transfer coefficient was measured at three circumferential locations by shifting the obstacle location from 0º to 90º and 180º respectively. The values at 270º were assumed identical to 90º. Typical examples of the circumferential distribution of local Nu are presented in Figures 9 and 10. The measurements suggest that the local heat transfer is the highest at the azimuthal location of the obstacle and decreases monotonically, reaching a minimum at the opposite side of the heated wall (i.e. 180 º). The azimuthal distribution of heat transfer is similar for all obstacle shapes and sizes investigated. It is noted, however, that the blunted cylinder with the blockage ratio of 0.3 has stronger local effects which can be attributed to stronger modification of velocity field around the obstacle. The axial extent of azimuthal heat transfer distribution was measurable over 30 test section diameters downstream from the trailing edge, which is consistent with the findings of Koram and Sparrow (1978) and Holloway (2005). The HTC distribution at 50 diameters downstream from the trailing edge is almost flat and practically equal to unity for all cases, suggesting that the axial and circumferential effects have fully decayed. It worth noting that the asymmetrical obstacles with the smallest obstructed area (0.15) show a peculiar behaviour at distances between 10 to 30 tube diameters, where the local heat transfer on the heated wall located on the opposite side of the obstacle may be slightly lower (on the order of 2 to 5%) than fully developed bare tube values. However, at higher *Re* numbers, this trend tends to reverse, such that the local heat transfer opposite to the obstacle has a slightly higher heat transfer coefficient than the bare tube. At flows in the higher *Re* number range, the distribution of circumferential heat transfer is more complex: up to 10 test section diameters the distribution is similar to that of the lower *Re* numbers (i.e. highest heat transfer at the obstacle side, lowest on the opposite), while further downstream this trend reverses. The small size of the test section (D_i=5.6mm) and conduction through the relatively thick heated wall could have affected the accuracy of circumferential heat transfer measurements.

Data by Krall and Sparrow (1968) indicate that the circumferential effect of asymmetrically positioned flow obstructions has an axial extent up to 27 tube diameters downstream from the flow obstruction. Experimental data reported by Krall and Sparrow (1968) suggest that downstream from the reattachment, the augmentation of heat transfer on the obstructed side of the wall is 12-15% higher than on the unobstructed side. Upstream of the reattachment area, the local structure of heat transfer is significantly more complex, being a strong function of obstructed area and *Re* number. Generally, for smaller obstructed ratios, below 0.5, the local heat transfer is higher on the obstructed side. However, larger obstacles tend to have strong flow diversion toward the opposite wall, causing higher heat transfer augmentation on that side of the heated wall (Krall and Sparrow, 1968).

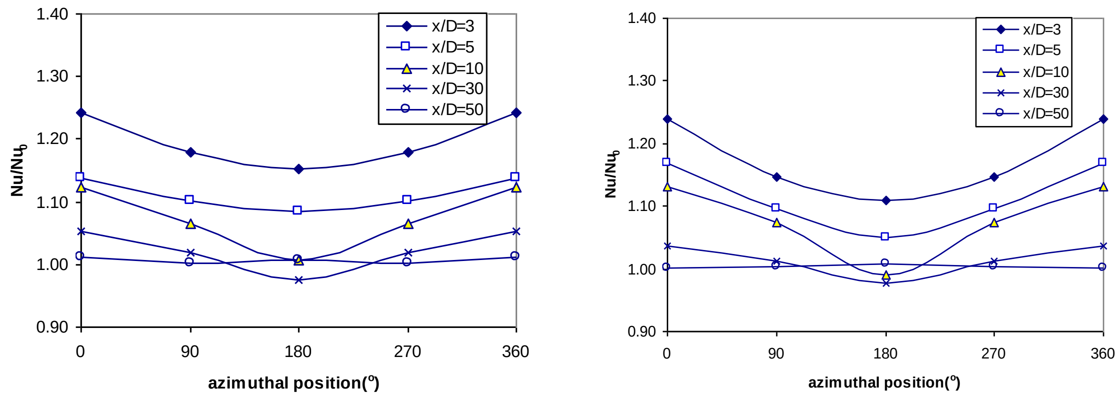

Figure 9. Azimuthal distribution of local *Nu* number for asymmetrical obstacles having 0.15 blockage ratio at *Re*=28,000, blunt (LHS) and round (RHS). The obstruction is at 0º (360 º).

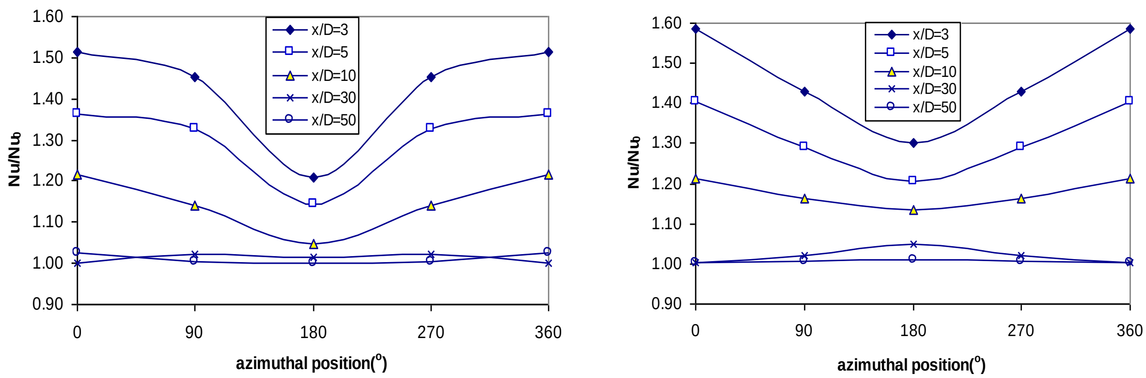

Figure 10. Azimuthal distribution of local *Nu* number for asymmetrical obstacles having 0.3 blockage ratio at *Re*=28,000, blunt (LHS) and round (RHS). The obstruction is at 0º (360 º).

4.4 The mechanisms of heat transfer augmentation

i) Disruption of boundary layer: It can be assumed that when a fully developed turbulent flow intersects an obstacle with a height larger than the viscous sublayer thickness, the viscous sublayer at the location of the obstacle is disrupted. Heat is transferred through the viscous sublayer by thermal conduction only, thus resulting in relatively weak heat transfer rates; removal or disruption of this layer significantly enhances the heat transfer rate. This mechanism can be effective for the obstacles larger than the thickness of viscous sublayer (5-7y^+). Asymmetrical obstacles will not have full circumferential contact with the heated wall; thus, the viscous sublayer thickness in the un-obstructed area, although not completely disrupted, is expected to decrease. The decrease can be due to (i) flow contraction because of the local increase in flow velocity and (ii) flow impingement towards the wall opposite from the flow blockage. Some researchers (e.g. Yao et al., 1982) suggested that the redevelopment of the boundary layer is similar to the entrance effect in a heated channel. This similarity is based on the hypothesis that in both cases the viscous boundary layer develops and needs a certain distance to reach its fully developed profile. This observation is supported by current experimental data (see Figures 5 and 6).

ii) Increase of turbulent mixing: Previous research work (Yao et al., 1985, Doerfer et al., 1996) indicate that around and downstream from a flow obstruction, a system of steady and unsteady coherent structures (eddies) are formed. Depending on the flow Reynolds number, large unsteady eddies travel downstream, break down and transfer their mass and energy to smaller eddies, and this process continues until the smallest eddies are dissipated by molecular viscosity. All these processes are known as the energy cascade and are very effective in transferring momentum and energy within the fluid. Furthermore, the interaction between larger eddies and the boundary layer may disrupt the boundary layer, thus enhancing the heat transfer (Yao et al., 1995). Of particular interest is the reattachment area downstream from the flow obstacle (i.e. the region behind the recirculating wake vortex, where the main flow impinges on the heated wall). Several authors (Terekhov et al, 2002, Koram and Sparrow, 1978) indicate that that this area represents a local maximum in heat transfer augmentation.

iii) Flow acceleration: Some investigators (e.g. Yao et al, 1982) stated that flow acceleration due to reduction of flow cross-section area constitutes a significant means of heat transfer augmentation at the obstacle location. This mechanism seems to be important in close proximity of the flow obstruction.

iv) Fin effect: This mechanism is effective for relatively large obstacles and high thermal conductivity, that is, the obstacle acts as a fin. Due to its pure conductive nature, the area of influence is limited around the obstacle and varies with material and geometrical properties of the heated tube and flow obstruction.

4.5 Discussion

The review of available relevant literature suggests that overall heat transfer augmentation, as well as its local distribution, depends mainly on the specific geometry of the flow (e.g. obstructed area, shape, position of the obstacle in the heated channel) and the flow conditions, especially the *Re* number. Intuitive reasoning suggests that obstructions that are not in direct contact with the heated wall may affect primarily the turbulent mixing (i.e. outer layer) and to lesser extent the boundary layer. On the contrary, small obstructions (i.e. with height smaller than ~$30y^+$) that do not protrude significantly in the turbulent region of the flow may enhance heat transfer primarily by disruption of boundary layer. Experimental observations suggested that for similar obstruction ratio and flow *Re* number, flow obstructions that do not have direct contact with the heated wall (such as spacer grids in PWR fuel assemblies) have significantly smaller heat transfer augmentation than flow obstructions attached to the wall. This may explain the poor agreement between various empirical correlations, derived from different geometries. If the flow obstacle is located further from the wall, such that there is no flow reattachment of the flow to the heated wall, the maximum heat transfer augmentation is typically located just downstream of the obstacle and decays monotonically as downstream distance increases. A qualitative schematic of this situation is shown in Figure 11, LHS. A different distribution is found when the recirculation vortex intersects the heated wall, such as wall-mounted flow obstacles. The typical (qualitative) variation of the average heat-transfer augmentation is shown in Figure 11, RHS. The maximum heat transfer augmentation occurs in the reattachment area. Experimental data indicates that in the recirculation area (i.e. between trailing edge and reattachment) the heat transfer coefficient increases monotonically from a value higher than the fully developed bare tube up to the point of reattachment. The average heat-transfer enhancement in the recirculation area is typically 2-4 times higher than fully developed bare tube heat transfer. Experimental data suggest that for wall-mounted obstacles in turbulent flow, reattachment is dependent mainly on the obstacle height and geometry and is located within 4.5-6 obstacle heights downstream from the trailing edge of the obstacle. Lower values are more suitable for prismatic obstacles, whereas higher values for orifice plates and disks. Note that Equations 12 should be applied with careful consideration of the specific geometry. From Tables 3 and 4 it is apparent that the newly proposed correlation is suitable mostly for heated tubes equipped with flow obstacles. The correlation predicts the average heat-transfer augmentation just *downstream* from the trailing edge of the flow obstacle. A reasonable approximation of augmentation *upstream* from the peak heat-transfer augmentation is to assume linear variation from the fully developed bare tube 1.5-2 tube diameters upstream the obstruction up to the maximum heat transfer enhancement.

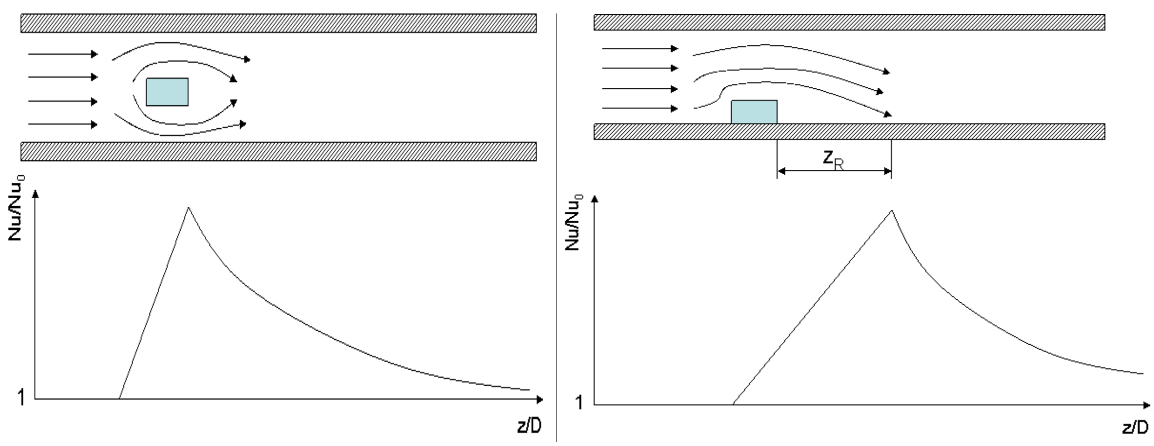

Figure 11. Comparison between heat transfer profile for flow obstacles that do not induce flow reattachment (LHS) and obstacles that induce flow reattachment (RHS).

All correlations predicting heat-transfer enhancement assume a monotonic decrease with an increase of axial distance downstream from an obstacle. The experiments indicate that for very thin obstructions or obstructions located sufficiently far from the heated wall this assumption holds. However, for obstructions that induce recirculation and flow reattachment, the monotonically decreasing predictions do not adequately represent the real axial variation of heat transfer coefficient, especially in the region very close to the trailing edge of the obstruction. In order to improve the prediction accuracy one could apply the correlations downstream from the *reattachment area* instead of downstream from the *trailing edge* of an obstruction. The above mentioned approach was applied to experimental data by Krall and Sparrow (1978) and the results are presented in Table 5. The axial distance correction was performed by subtraction of the reattachment length (calculated as 5.5 times the obstruction height) from the reported non-dimensional axial distance.

Table 3. Comparison between new and existing prediction methods with correction for flow reattachment vs. Koram and Sparrow experimental data

Correlation	Average error (%)	RMS error (%)
Yao et al. (1982)	**-0.04**	15.1
Holloway et al. (2004)	-18.1	22.6
Miller et al. (2013)	-20.3	25.9
New correlation	4.4	**13.7**

The most significant improvement of prediction accuracy is noted for correlations derived for bundle data, most notably Holloway (2004) and Miller (2013). This can be regarded as a confirmation that, when applying empirical correlations derived from flow configurations without flow reattachment to re-attached flows, a correction of axial distance that accounts for the reattachment length improves the accuracy of prediction. Nevertheless, even with the axial correction, the correlations significantly under predict the experimental data, thus correlations derived for re-attached flow are recommended. It is noted that only the correlation of Miller et al. (2013) and the newly derived correlation include the effect of flow *Re* number. The variation of heat transfer augmentation with flow *Re* number is presented in Figure 12. In agreement with experimental observation, at a fixed axial distance, the heat transfer augmentation decreases as flow *Re* number increases; both prediction methods show this trend; it is observed, however, that the Miller correlation predicts a stronger decay in heat transfer augmentation with an increase of Re number.

Figures 5 and 6 suggest that at low flows, blunt obstacles have significantly higher augmentation of heat transfer than rounded obstacles, while at higher flows the trend reverses. Hydraulic textbooks (e.g. Idelchick, 1996) indicate that in turbulent pipe flow, rounded obstacles have a consistently lower pressure loss coefficient (K-factor) than blunt obstacles at all Reynolds numbers. Based on the previous observation, it appears that the current experimental data do not correlate heat transfer augmentation with pressure loss; that is, the Reynolds analogy approach does not appear to apply to flow obstacles.

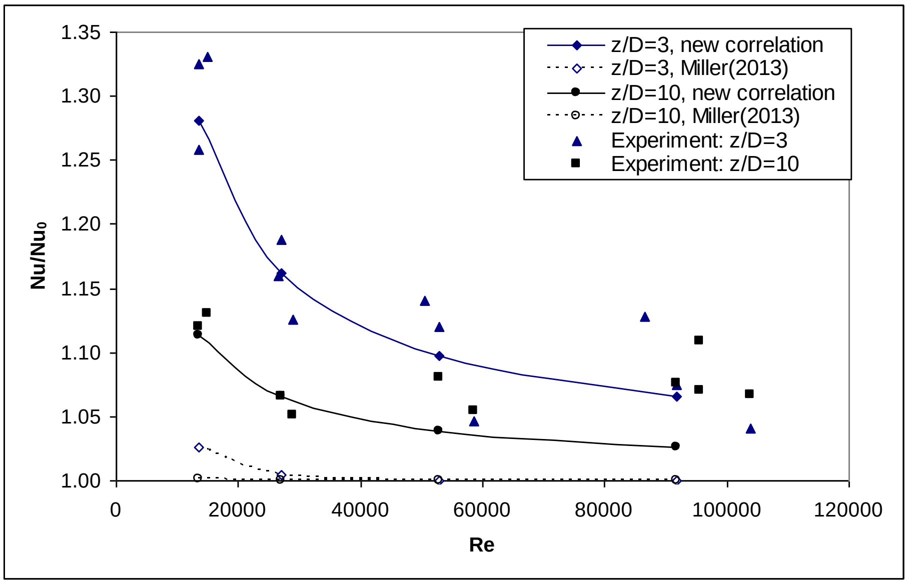

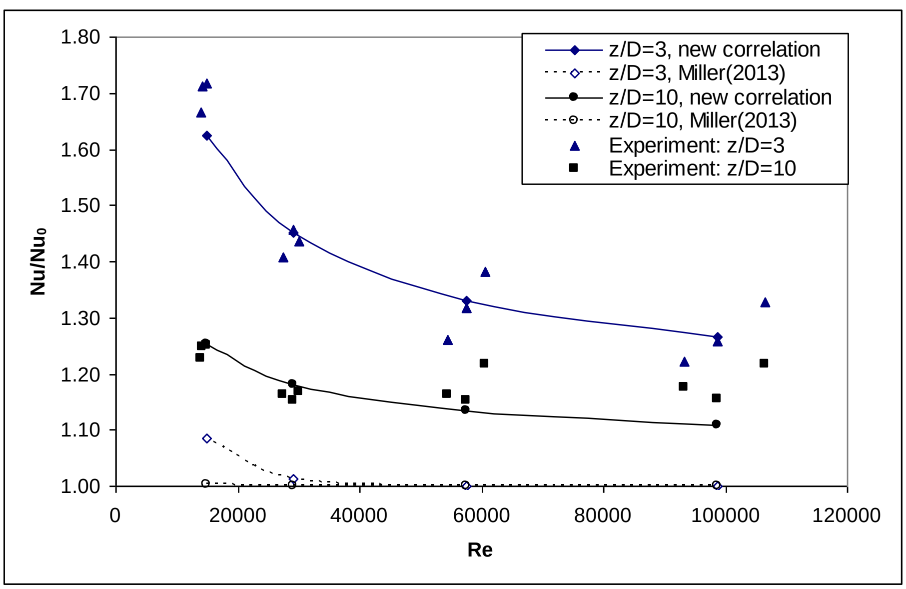

Figure 12. Effect of flow *Re* number at fixed axial distance for obstruction ratio 0.15 (top) and 0.3 (bottom).

5. Conclusions and final remarks

- The current experimental investigation suggested that the following parameters influence the augmentation of forced convective heat transfer downstream from flow obstacles:
    1) Blockage ratio
    2) Non-dimensional axial distance downstream from obstacle
    3) Flow Reynolds number
    4) Circumferential location of the obstacle (for eccentric geometries)
    5) Obstacle shape

  The results have shown that the first three parameters are the most significant for predicting the heat transfer augmentation downstream of a flow obstruction in turbulent flow in heated pipes.

- Caution should be exercised when applying prediction methods for heat transfer augmentation derived from experimental data on bundles, to other flow geometries. The current investigation indicates that bundle-based correlations significantly underpredict the experimental results obtained for heated tubes with wall mounted flow obstacles. The relatively large differences between the prediction methods for bundles suggest that the prediction methods should only be used for the geometry and flow conditions of their data base.
- The proposed prediction method, which correlates the blockage ratio, non-dimensional axial distance and flow Reynolds number, provides satisfactory prediction accuracy when compared against the current experimental data and a relevant experimental dataset from literature. It is expected that a correlation that is developed from a larger experimental database that includes reliable circumferential measurements and accounts for the shape of the obstacle would further improve the prediction accuracy and applicability.
- The present measurements indicate that for the lower Re number range ($13{,}000<Re<50{,}000$), for a given blockage ratio, the heat transfer augmentation of flow obstacles of various shapes was comparable; however, for higher flows ($50{,}000<Re<100{,}000$) the rounded shaped obstacle produced a noticeably higher

augmentation. This effect was observed for both (0.15 and 0.3) blockage ratios investigated.

- Interpretation of current experimental data and the review of former investigations suggested that the main heat-transfer augmentation mechanisms are: i) disruption of boundary layer; ii) increase of mixing by obstacle induced turbulence; and iii) flow acceleration. Their relative importance may vary depending of flow geometry, axial and circumferential location and Re number.

Nomenclature

A	annular obstacle
B	blunt obstacle
D_h	hydraulic diameter
D, *Di*	inside tube diameter (mm)
Do	outside tube diameter (mm)
G	mass flux (kgm^{-2}s^{-1})
H	obstacle height (mm)
h	enthalpy (J kg^{-1})
I	electric current (A)
k	thermal conductivity (W·m^{-1}·K^{-1})
L_h	heated length (m)
$\dot{m}$	mass flow rate (kg·s^{-1})
Nu	Nusselt number
P	pressure (kPa)
Pr	Prandtl number
R	tube outside radius (mm)
R	rounded obstacle
Re	Reynolds number

r	tube inside radius (mm)
q_s	surface heat flux (kW·m^{-2})
q_v	Joule volumetric heat source (kW m^{-3})
T	temperature (°C)
T_f	bulk fluid temperature (°C)
T_{WI}	inside wall temperature (°C)
T_{WO}	outside wall temperature (°C)
ΔT	temperature difference = T_{WO}-T_{WI} (°C)
U	electric voltage (V)
x	distance downstream the obstacle trailing edge (m)

Acronyms

AC	Alternate Current
ADC	Analog to Digital Convertor
DAS	Data Acquisition System
DC	Direct Current
HTC	Heat Transfer Coefficient
LHS	Left Hand Side
NB	Nucleate Boiling
ONB	Onset of Nucleate Boiling
PDO	Post Dryout
PWR	Pressurized Water Reactor
RBHT	Rod Bundle Heat Transfer
RHS	Right Hand Side
RMS	Root Mean Square

RTD	Resistance Temperature Detector
TC	Thermocouple
TS	Test Section

Greek letters

δ	wall thickness (mm)
ε	blockage ratio - the ratio between the obstructed cross section area and the area of the unobstructed tube
ρ	electric resistivity (Ω m)

Subscripts

avg	average
i	inside
in	inlet
max	maximum
o	outside
ref	reference
out	outlet
sat	saturation
0	reference

References

[1] G. Cubizolles, J. Garnier, D. Groeneveld and A. Tanase, (2009), *Methods for determining the wall thickness variation of tubular heaters used in thermalhydraulic studies*, Proceedings, 13th International Topical Meeting on Nuclear Reactor Thermal Hydraulics (NURETH-13), Kanazawa City, Ishikawa Prefecture, Japan, September 27-October 2,

[2] Doerffer, S., D.C. Groeneveld and J.R. Schenk, (1996), Experimental Study of the Effects of Flow Inserts on Heat Transfer and Critical Heat Flux, *Proceedings of the 4th Int. Conference on Nuclear Engineering, vol. 1 - Part A, pp.41-49, March 10-14, New Orleans, Louisiana, USA*

[3] Gnielinski, V. (1976), New equations for heat and mass transfer in turbulent pipe and channel flow. *International Journal of Chemical Engineering, 16, 359-368*

[4] Hassan, M.A., Rehme, K. (1981), Heat transfer near spacer grids in gas-cooled rod bundles, *Nucl. Technol. Vol. 52, 410–414*

[5] Holloway, M.V., McClusky, H.L., Beasley, D.E. and Conner, M.E., (2004), The effect of support grid features on local, single-phase heat transfer measurements in rod bundles, *Journal of Heat Transfer, Vol. 124*

[6] Holloway, M., Conover, T., McClusky, H., Beasley, D. and Conner, M.E. (2005), The effect of support grid design on azimuthal variation in heat transfer coefficient for rod bundles, *Journal of Heat Transfer, Vol. 127*

[7] Idelchik, I.E., (1996), *Handbook of hydraulic resistance, third edition*, Begell House

[8] Krall, K.M and Sparrow, E.M. (1966), Turbulent heat transfer in the separated, reattached, and redevelopment regions of a circular tube, Journal of Heat Transfer, January, pp. 131-136

[9] Koram, K.K and Sparrow, E.M. (1978), Turbulent heart transfer downstream from an unsymmetric blockage in a tube, Journal of Heat Transfer, Vol. 100, pp. 588-594

[10] Miller, D.J., Cheung, F.B. and Bajorek, S.M. (2013) *On the development of grid-enhanced single-phase convective heat transfer correlation*, Nuclear Engineering and Design,Vol. 264, pp. 50-56

[11] National Instruments – Measurement and Automation Catalogue, 1999

[12] Rehme, K. (1977), Pressure drop of spacer grids in smooth and roughened rod bundles, *Nuclear Technology, Vol. 33*

[13] Tanase, A., Groeneveld, D.C., (2008), *An accurate method of assessing tube wall thickness based on flow boiling and single phase heat transfer measurements*, Proceedings, Canadian Nuclear Society 2008 Simulation Conference, Ottawa, November.

[14] Tavoularis, S. (2005), Measurement in Fluid Mechanics, Cambridge University Press

[15] Yao, M, Nakatani, M and Suzuki, K. (1995), Flow visualization and heat transfer experiments in a turbulent channel flow obstructed with an inserted square rod, *Int. J Heat and Fluid Flow 16, 389-397*

[16] Yao, S.C., Hochreiter, W.J. and Leech, W.J. (1982), Heat transfer augmentation in rod bundles near grid spacers, *Transactions of the ASME, Vol. 104, 76-81*

CHAPTER 6

Experimental Investigation of Turbulent Pipe Flows with Obstructions[6]

Abstract

Pressure loss and Particle Image Velocimetry experiments in tubes equipped with flow obstacles have been performed at flow Reynolds number in the range 11,000 to 65,000. Obstacles used included blunt and rounded cylinders with a blockage ratio of 30% and a blunt cylinder with a blockage ratio of 15%. The experiments described in this paper complement our previous heat transfer enhancement investigation. Pressure loss measurements suggested that blockage ratio and shape of flow obstacles impact obstacle pressure loss coefficient significantly; it confirmed previous research findings that this coefficient decreases with an increase in bulk Reynolds number. Measurements of reattachment length downstream from flow obstacles indicated that the reattachment length for turbulent flow around square-shaped cylinders is significantly shorter than that in two-dimensional flow over a backward-facing step. An important finding of the present investigation is that, for the flow range investigated, heat transfer augmentation could not be correlated with the local pressure loss coefficient of the obstruction, which is contrary to the generally accepted Reynolds analogy for smooth heated channels, where the heat transfer coefficient and friction factor behave in similar ways.

1.0 Introduction

Demonstration of safe operation is of paramount importance in licensing of nuclear reactors. An essential component of the safety case of nuclear reactors is safety analyses, performed to demonstrate compliance with regulatory requirements. Safety analyses use specific means, such as computer codes, to predict the response of the reactor during postulated transients and accident scenarios. One of the most significant parameters of interest

[6] The pressure loss and velocity measurements/analysis as documented in Chapter 6, will be submitted to Nuclear Engineering and Design.

in demonstrating reactor safety is fuel cladding temperature during normal operation and accident conditions. Understanding the effects of components and features of fuel elements, such as spacers, appendages and grids on heat transfer and pressure drop contributes to optimization of their design, as well as improves the accuracy of prediction of cladding temperature, thus enhancing the confidence in the results of safety analyses.

Experimental investigations of flow around surface-mounted, prismatic obstacles placed in fully developed turbulent channel flows have been conducted extensively (Castro and Robins, 1977; Martinuzzi and Tropea, 1993; Hussein and Martinuzzi, 1996; Meinders and Hanjalic, 2002; Pattenden et al., 2005). A comprehensive review of experimental work investigating flow around surface-mounted finite-height circular cylinders was performed by Sumner (2013). It is noted that the vast majority of experimental work investigating turbulent flows around surface-mounted flow obstacles by means of flow visualization focused on prismatic obstacles (e.g. rectangular cylinders, cubes, ribs) placed typically in rectangular channels rather than circular pipes.

In general, the experiments indicated that steady and unsteady vortex systems form around a wall mounted flow obstacle in turbulent flow. Although the extent and the location of the vortices may vary depending on the experimental setup and flow conditions, several representative flow features have been identified. In the region upstream of the obstacle-wall junction, a vortex which extends over the upstream end and the sides of the obstacle, having a typical “U” shape (horseshoe vortex) is formed. On the top of the obstacle a separation bubble occurs, caused by the flow that “overshoots” the upstream end and reattaches behind the separation bubble. A larger separation region (wake) occur just downstream from the downstream end. Martinuzzi and Tropea (1993) conducted experiments at Reynolds numbers ranging from 11,000 to 80,000 using prismatic obstacles with square cross-sections of various widths. The authors concluded that, for obstacles with aspect ratio (W/H) higher than 10, the main flow features were consistent with those for the two-dimensional ribs, whereas, for smaller aspect ratios, the three-dimensional flow features became more significant. Therefore, it appears that, for flow obstacles with low aspect ratios, (e.g. cube-shaped) the reattachment length X_R/H is typically 1.6-1.8 and increases monotonically with an increase of the aspect ratio. At aspect ratios larger than 10, the reattachment length approaches asymptotically 7, which is comparable to the reattachment length of a backward facing step.

The experiments conducted by Pattenden et al. (2005) investigated the flow over a finite-height cylinder of aspect ratio 1 by means of flow visualization, Particle Image Velocimetry (PIV) and surface pressure measurements at Reynolds numbers (based on the obstacle diameter) of 200,000. Consistent with the previous research findings, the main vortex system consisted of a horseshoe vortex, a tip vortex, an arch vortex and two trailing vortices. The authors reported that the wake region was highly unsteady, and that instantaneous velocity fields were very different from the mean fields.

The experiments described in this paper complement our previous heat transfer enhancement investigation (see Section 5). We investigated experimentally the adiabatic turbulent flow field in the proximity of flow obstacles with the use of PIV. Obstacles used included blunt and rounded cylinders with a blockage ratio of 30% and a blunt cylinder with a blockage ratio of 15%; the tests covered the Reynolds number range from 11,000 to 65,000. We report maps of the mean flow and turbulence properties and document the formation of coherent structures, in an effort to identify and understand the mechanisms of heat transfer augmentation. The PIV data were supplemented by the measurement of local (i.e., minor) pressure loss caused by the flow obstructions.

2.0 Experimental facility and procedures

2.1 The flow loop

A schematic diagram of the experimental loop is presented in Figure 1. Water flow was produced by the difference in elevation between the free surfaces of the head tank and the collection tank. From the head tank, water flowed to the inlet tank, which was completely full, through the feed pipe. From the inlet tank, water entered the test section from which it was returned to the collection tank and pumped back to the head tank. The head tank was separated into two compartments by a vertical wall, which acted as overflow, thus maintaining a constant head, whereas overflow water was returned directly to the collection tank. By using gravity-driven flow, we avoided flow oscillations and disturbances caused by the pump. The test section consisted of a horizontal acrylic tube with an inside diameter D = 31.75 mm and was preceded by a flow development section having a length of approximately 80D. The flow rate to the test section was controlled by a flow control valve and/or a bypass valve that diverted a part of the flow directly to the collection tank. The test section was immersed in a rectangular sealed viewing tank filled with water, which kept light refraction at a low level.

Three flow obstacles, all with cylindrical bodies and a length-to-diameter ratio equal to 3.3, were used in this study (see Figure 2): i) a blunt (square-ended) cylinder (30B) with a 30% blockage ratio (that is, the ratio between the projected area of the obstacle and the area of the unobstructed tube), ii) a rounded cylinder (30R), having hemispherical ends and a 30% blockage ratio, and iii) a blunt cylinder (15B) with a 15% blockage ratio. All obstacles were manufactured from Teflon, and had encased cores of mild steel, so that they could be held in place by magnets located outside the pipe. By moving the magnet axially, the flow obstacle was relocated, thus permitting the measurement of local pressure and velocity distributions at various positions relative to the obstruction.

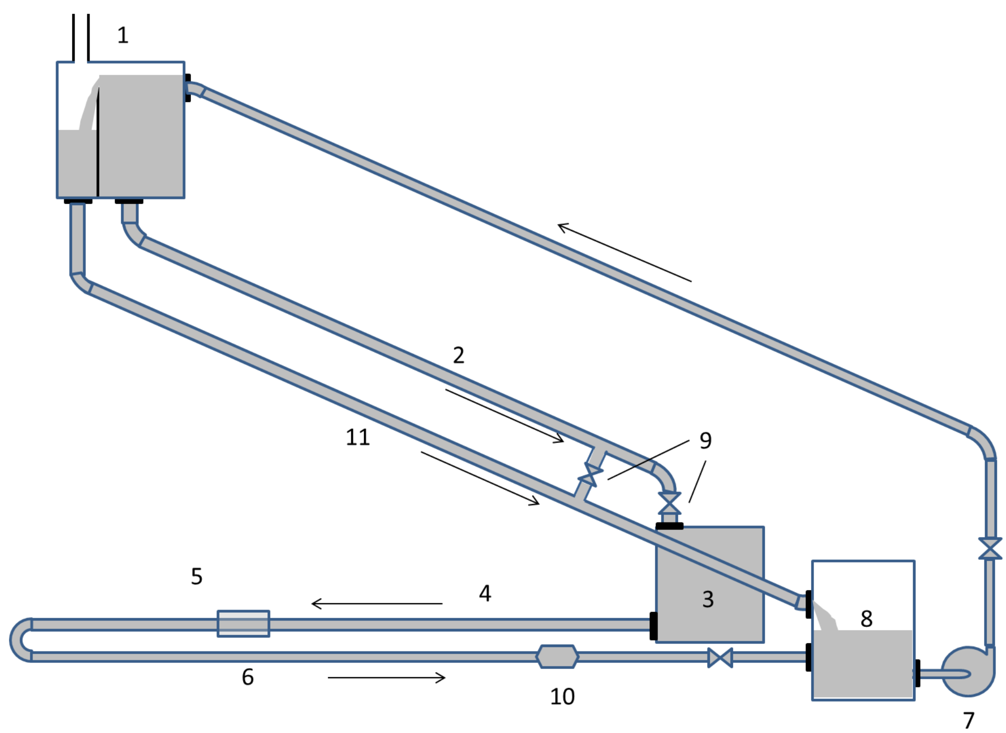

Figure 1 Experimental loop, consisting of the head tank (1), feed pipe (2), inlet tank (3), flow development section (4), test section (5), return pipe (6), pump (7), collection tank (8), flow control valves (9), flow meter (10), and overflow return pipe (11).

2.2 Flow rate and pressure loss measurements

A digital thermometer (MASTERCRAFT, Model 52-000052) with an uncertainty of 1°C was used to monitor the water temperature, from which the density and viscosity of water were calculated. The flow rate was measured by an ultrasonic flow meter (OMEGA, Model FDT-33-T). The flow meter was calibrated by timing the filling of a tank with a known volume and the total uncertainty of the measured flow rate was estimated to be 2.8%. A differential pressure transducer (VALYDINE, Model DP103), connected to a digital carrier demodulator (VALIDYNE, Model CD23), was used to measure the difference between the pressures at two pressure taps located at the top side of the test section. The transducer was calibrated against an adjustable column of water and the total uncertainty of differential pressure measurement was estimated to be 0.85%. A schematic diagram of the pressure loss measurement section is presented in Figure 3.

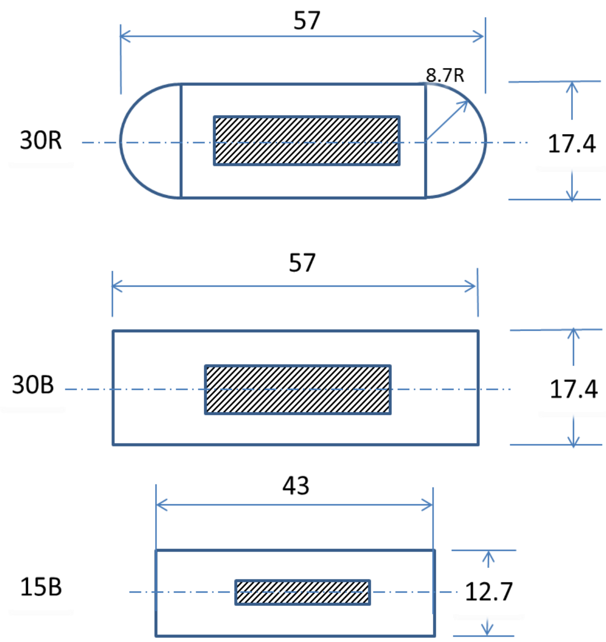

Figure 2 Sketches of the three flow obstacles; dimensions in mm; crosshatched areas indicate ferromagnetic cores.

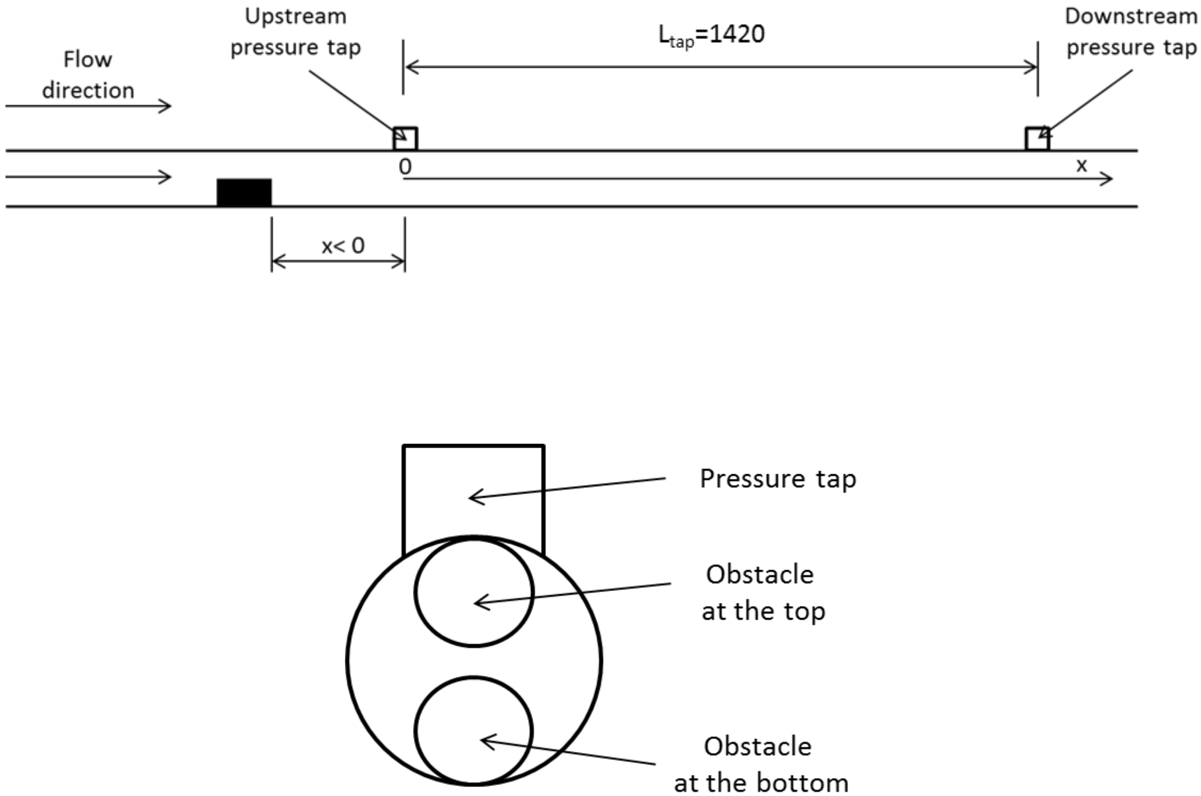

Figure 3 Sketch of the experimental setup for pressure loss measurement.

2.3 Particle Image Velocimetry

The PIV system used in these experiments consisted of a Nd:YAG pulsed laser (Solo PIV 120XT; New Wave Research, Fremont, CA), one digital camera (LaVision Imager Pro X 4M) with a resolution of 2048×2048 pixels, a programmable timing unit (LaVision PTU-9 External#1108058), and a dedicated computer. The camera was equipped with a Nikon Nikkor 50 mm f/1.8D lens and a 532 nm bandpass filter (LaVision #1108560), which allowed mainly the fluorescent light emitted by the particles. The laser sheet was created with divergent sheet optics (LaVision #1108405) using a divergent lens with f = −10 mm.

The water was seeded with hollow glass microspheres with an average diameter of 12 μm and a specific gravity of 1.1 g/cm^3 mixed in the return tank. The particle concentration was adjusted to obtain 5-15 particles per interrogation area. The terminal velocity of particles falling in water was roughly 10^{-5} ms^{-1}, which is at least three orders of magnitude smaller than typical fluid velocities measured during the experiments, and is thus negligible. The time constant of the particle-fluid interaction was 14.4 μs. These particles were sufficiently large to provide an acceptable signal-to-noise ratio and followed the flow sufficiently well. Moreover, peak lock effects, which might have been a source of error if smaller particles were used, were found to be negligible for the glass microspheres.

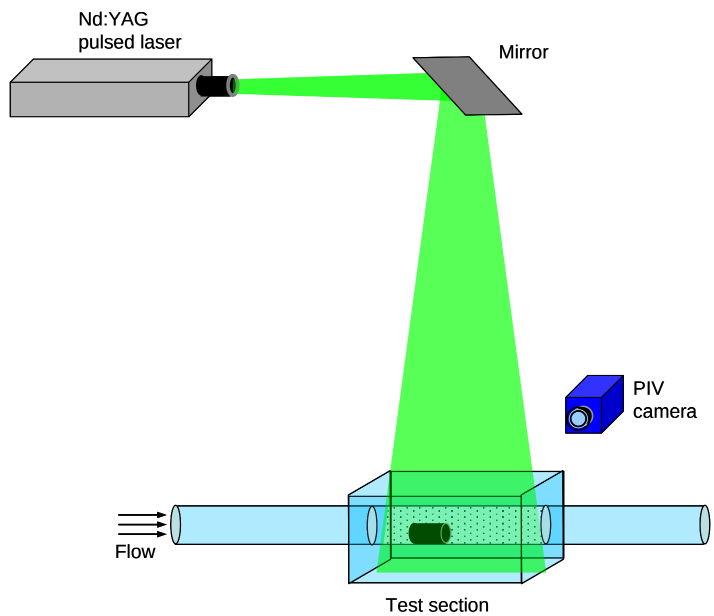

Figure 4 Sketch of the PIV setup.

The measurements were taken in the vertical centre plane of the test section and the obstacle, as shown in Figure 4. The intersection of the laser sheet with the test section formed an approximate rectangle with a length of 155 mm and a height equal to the diameter of the test section. Part of this viewing area was masked to exclude regions contaminated by parasitic reflections on the wall of the test section and image distortions caused by the tube curvature; the usable viewing area was approximately 145×28 mm. The time separation between laser pulses varied between 1500 μs at lower flow rates to 500 μs at higher flow rates. The images were corrected based on calibration, which was performed by inserting a calibration plate in the measurement plane of the test section filled with water; the bias uncertainty of location on the images was 0.11%. Measurements were taken at a rate of 4 images/s. For each test matrix case, 300 to 500 instantaneous flow images were acquired. Time averages obtained from these images were found to converge. The images were processed with DaVis7 software using a multi-pass routine starting with an interrogation window of 64×64 pixels, and then decreasing to 32×32 pixels with 50% overlap. The resolution of the velocity maps was approximately one vector per 1.18 mm × 1.18 mm. Vectors with too few particles within the interrogation volume were deleted. The vector fields were then post-processed, smoothing the results using low-pass filter with a 3×3 window, and filling up the empty spaces.

The total uncertainty of the instantaneous PIV velocity measurements was estimated to be 5% of the measured values, being dominated by the uncertainty of the mathematical convolution filtering to determine the most probable displacement of the particles in the interrogation area. The precision uncertainty of the ensemble averaged velocity measurements was 0.2-0.3%.

2.4 Measurements in the bare tube

As an overall test of the accuracy of velocity measurements, mean velocity profiles were measured in the bare test section (i.e., without flow obstacles) for several flow rates. As shown in Figure 5, the PIV results were in good agreement with power laws fitted to fully developed pipe flows at the corresponding Reynolds number and available in the literature (e.g., Cengel and Cimbala, 2010).

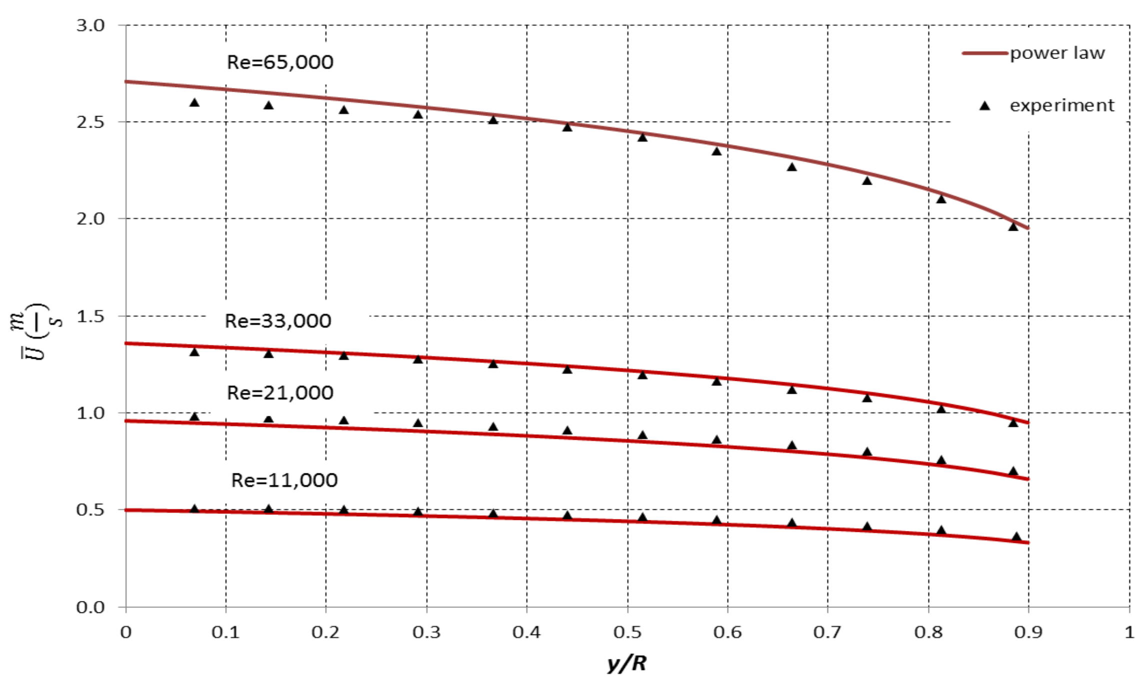

Figure 5 Comparison of mean velocity measurements in the bare test section and power laws available in the literature.

The bare tube pressure loss was measured after moving the obstacle axially upstream so that it was located more than $50D$ from the upstream pressure tap. The main reasons for this experimental approach were: a) dismantling the test section to remove the obstacle was avoided, and b) maintaining the obstacle in the loop, the overall hydraulic resistance was preserved, thus contributing to flow rate consistency and stability. The bare tube pressure loss was used as the reference when compared with the pressure drop measurements of the obstacle-equipped tube with the obstacle located at various axial and circumferential locations. The measured friction factor f for the bare tube was within 0.5% of values determined from the widely used Colebrook equation for smooth pipe flows (White, 2011).

3.0 Analysis of Pressure Measurements

3.1 Pressure Distribution

The pressure difference ΔP between the two taps was measured by gradually moving the obstacle in the axial direction toward the upstream pressure tap. These measurements are presented in Figure 6, normalized by the reference pressure difference $\Delta P_{ref} = f \frac{L_{tap}}{D} \rho \frac{U_b{}^2}{2}$ in the bare tube, which was measured with the obstacle positioned far upstream from the upstream pressure tap. Measurements were taken with the obstacle positioned either at the bottom of the pipe (away from the pressure taps) or at the top of it, in which case the obstacle would block the upstream pressure tap when it was in the appropriate range. In general, the presence of an obstacle was detectable when it was located in the range $-3 < x/D < 3$. In a central part of this range, $\frac{\Delta P}{\Delta P_{ref}}$ was less than 1, as expected, considering that the flow around the obstacle was faster than the unobstructed flow. A small pressure overshoot is noted for the rounded obstacle for $\frac{x}{D} \approx -1.5$, which may be attributed to flow reattachment. When an obstacle was positioned at the top of the pipe, relatively high pressure was measured in the proximity of its upstream tip, presumably caused by local stagnation. The normalised pressure difference reached a constant value at approximately $1D$ upstream of the leading edge of all obstacles.

Next, we calculated the obstacle pressure loss coefficient K. The permanent pressure drop ΔP_{perm} was determined as the pressure difference between the two taps with an obstacle located between them and sufficiently far from either of them. The permanent pressure loss is related to K as

$$\Delta P_{perm} = f\frac{L_{tap}}{D}\rho\frac{U_b^{\,2}}{2} + K\rho\frac{U_b^{\,2}}{2}, \qquad (1)$$

where f is the friction factor for the bare pipe, $L_{tap} = 1420$ mm is the distance between the taps, ρ is the water density, and U_b is the bulk (i.e. average) velocity. Values of K are shown in Figure 7. As expected, K decreased with increasing Reynolds number for all obstacles investigated. It is noted that both obstruction (i.e. K) and friction (i.e. f) pressure losses decrease monotonically with increasing Reynolds number, which is also confirmed by earlier experiments (Shiia et al., 1991). Both the obstacle shape and the obstructed ratio affect K. The flow obstacle with hemispherical ends (30R) has a K value that was approximately 40% lower than that of the blunt cylinder (30B), with the same blockage ratio. For blunt cylinders, a decrease of the blockage ratio from 30% to 15% resulted in a reduction of K by approximately 60%.

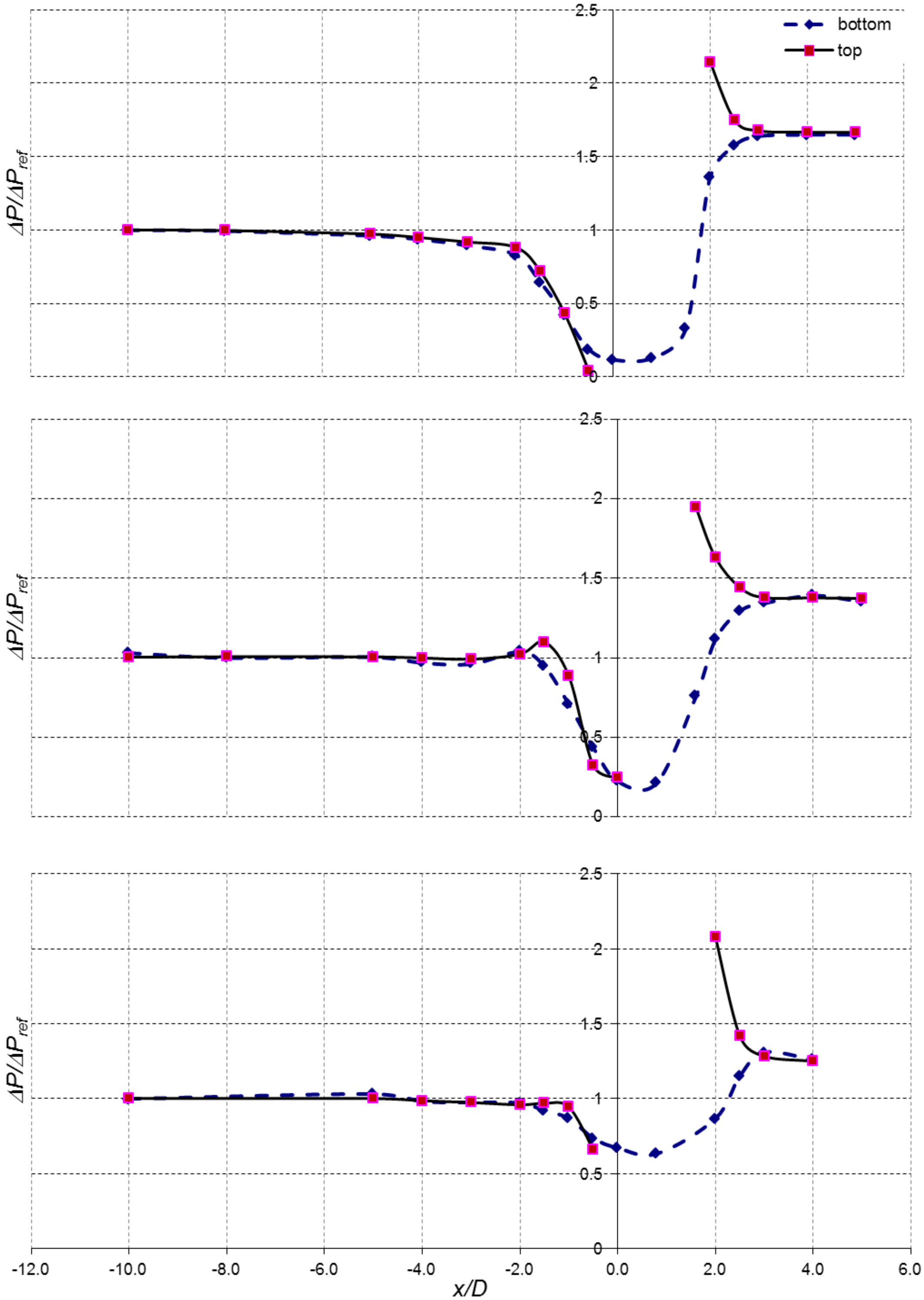

Figure 6 Normalized static pressure difference between the two pressure taps for different positions of the obstacle; top: obstacle 30B, Re = 37,000; middle: obstacle 30R, Re=35,000; bottom: obstacle 15B, Re=34,000.

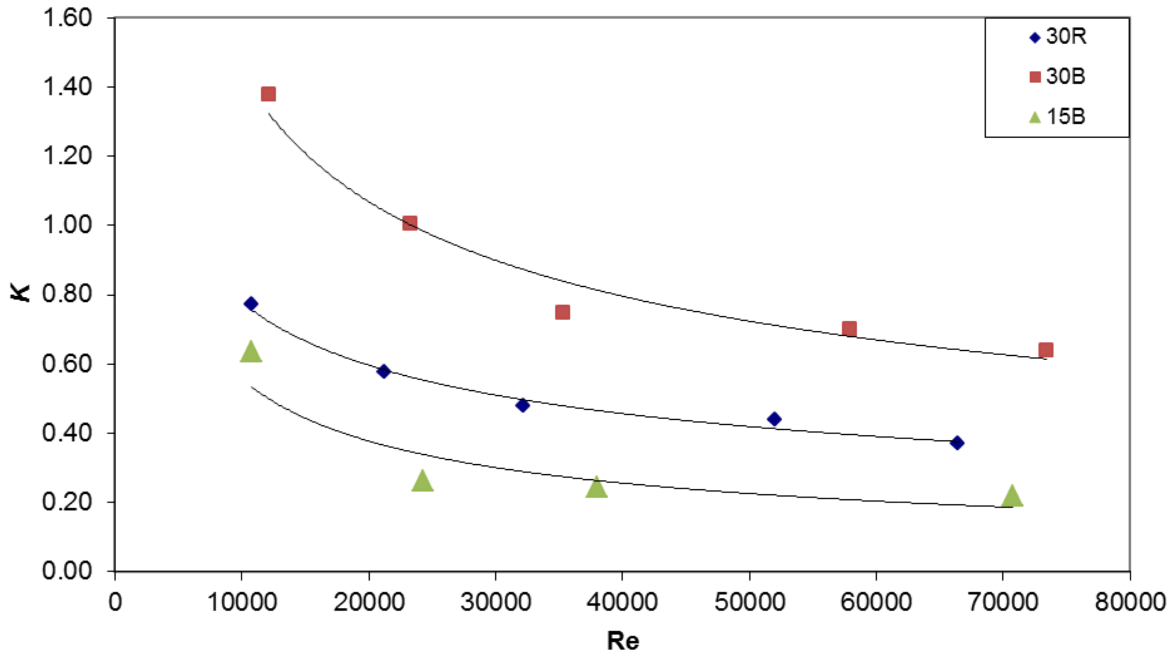

Figure 7 Variations of obstacle pressure loss coefficients with Reynolds number.

4.0 Analysis of Velocity Measurements

4.1 Instantaneous and time averaged planar velocities

Planar velocity maps at the centre plane of the test section around and in the vicinity of the obstacle were obtained using planar PIV for three bulk Reynolds numbers (11,000, 33,000 and 65,000) and for the three obstacles (30B, 30R and 15B), as described in Section 2. Representative instantaneous maps and maps averaged over all acquired PIV images are shown in Figures 8 and 9. For the blunt obstacles, first flow separation occurs just downstream from the upstream end. It is expected that the separation occurs around the obstacle circumference, thus having an annular shape. The length of the obstacles was sufficient to allow flow reattachment. However, no flow separation in the proximity of the upstream end of the rounded obstacle was observed. The most significant coherent structure is the recirculation vortex, downstream from the downstream end of the obstacle.

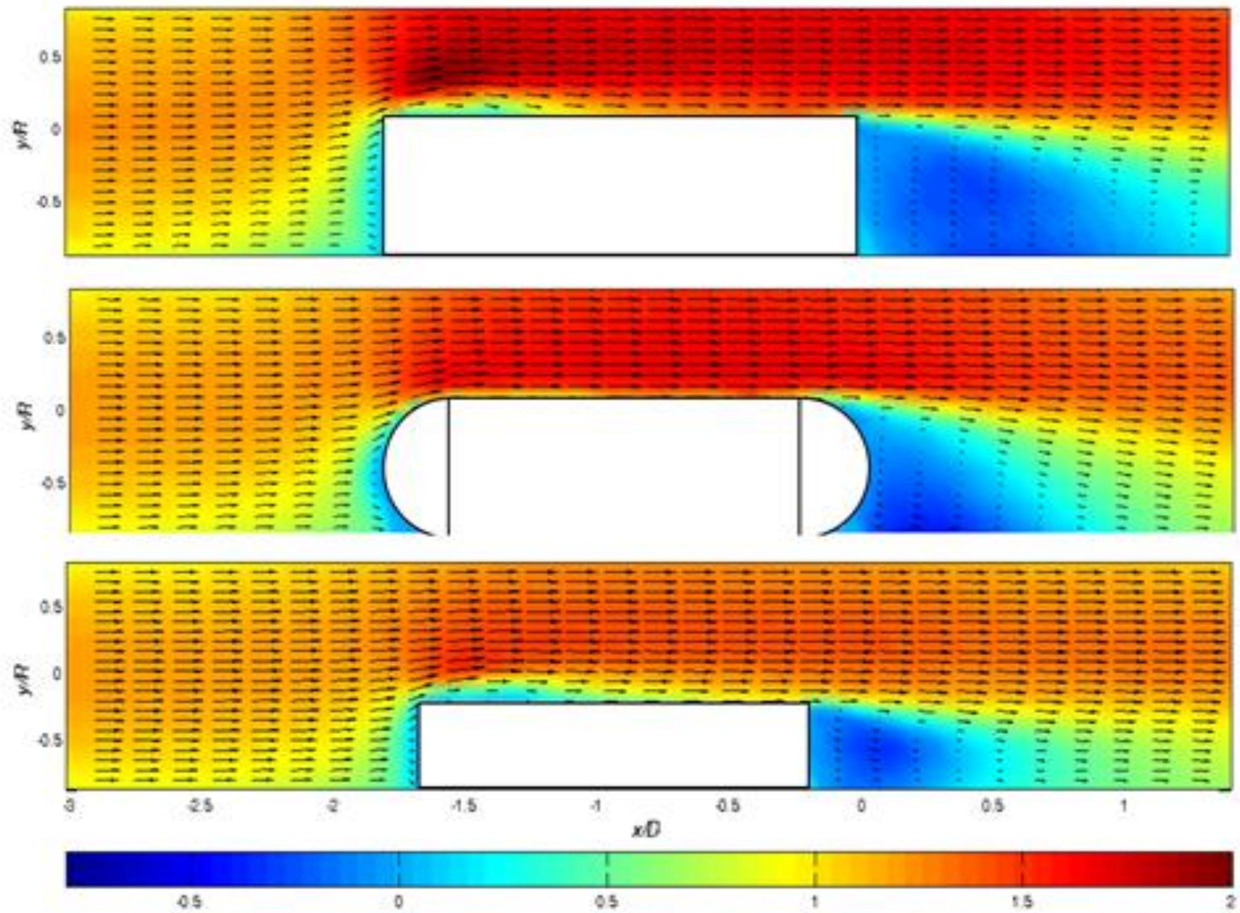

Figure 8 Representative average planar velocity maps around obstacles (Re=35,000), normalized by U_b.

The recirculation vortex may be caused by the flow that detaches from the downstream end of an obstacle and is "trapped" in the low pressure region (see Figure 8) created downstream from the trailing edge and diverted toward the wall. The flow in the wake region was highly turbulent, as shown by the instantaneous flow maps. Although the reattachment area is not obvious in the instantaneous flow maps, the averaged flow maps show distinct reattachment areas, that is, clearly delineate the recirculation zone. The mean axial velocity profiles at various axial locations are plotted in Figure 11. The following observations can be made:

i) The average velocity measured at $\frac{x_{ob}}{D} \approx -2.7$ (which is $1D$ upstream from the upstream end of flow obstacles) showed that the average flow velocity is not significantly disturbed by the obstacle, being approximately identical to the bare tube velocity profile (see Figure 11). This is consistent with the normalized pressure difference, which reached a constant value at approximately 1*D* upstream from the leading edge of all obstacles.

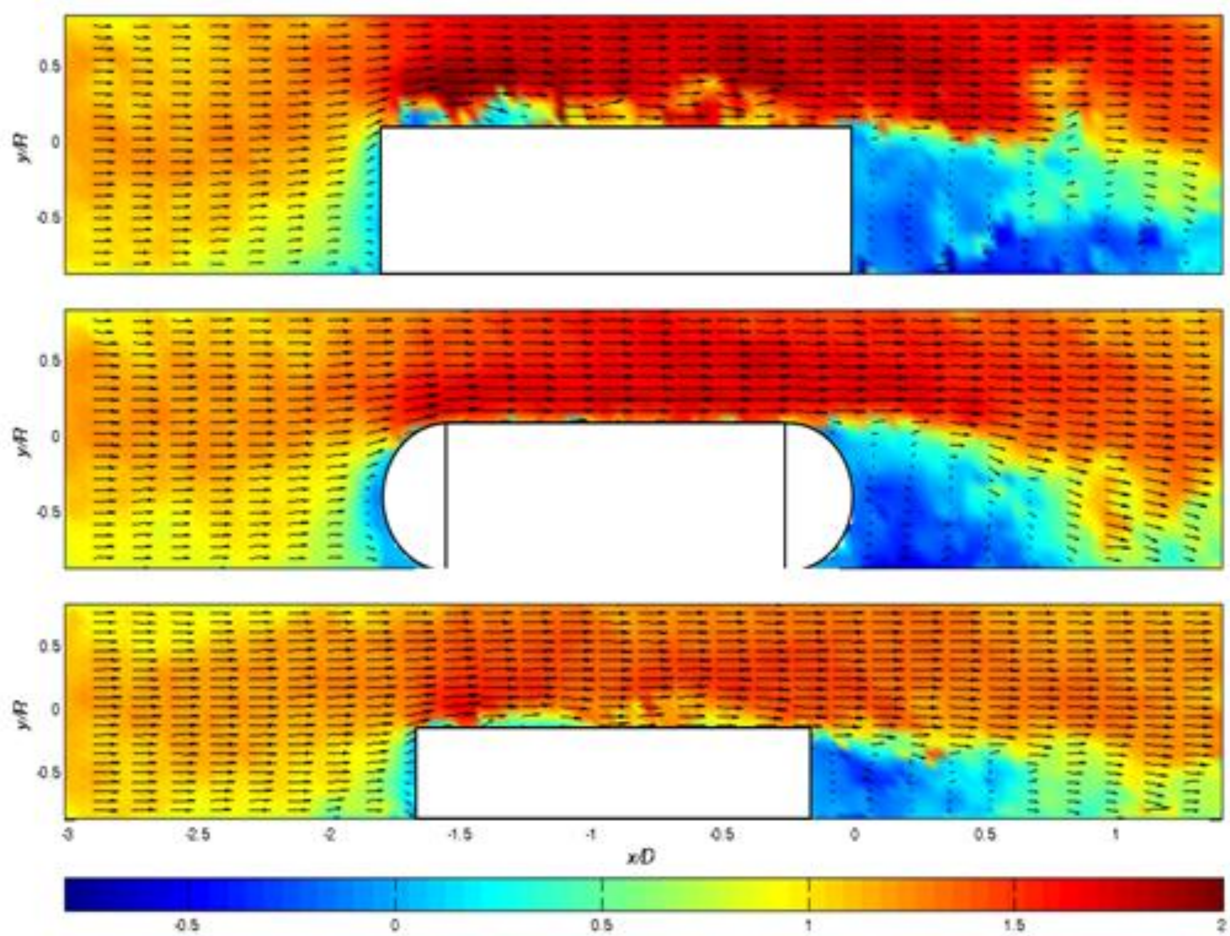

Figure 9 Representative instantaneous planar velocity maps around obstacles (Re=35,000), normalized by U_b.

ii) The maximum average flow velocity was measured at the cross section that contains the obstacle. This is consistent with measurements of the minimum local pressure, see also Figure 6.

iii) Inside the recirculation vortex, the axial velocity was negative due to the negative pressure gradient, whilst outside of this vortex, the axial velocity was relatively high, with the maximum shifting towards the bottom side of the test section with an increase of the axial distance from the trailing edge.

iv) The large obstructions (30B or 30R) do not show a full flow recovery at $\frac{x_{ob}}{D} \approx 9.5D$, especially at higher flows (i.e. Re>35,000). The maximum of the average axial velocity was "skewed" towards the bottom of the test section, as presented by Figure 11. Although the flow distortion is measurable, it is not very strong. Flow recovery for the smaller obstacle (15B) was almost complete at *x/D ~ 9*.

The reattachment length

After the flow separates from the obstacle's downstream end, the low pressure wake area constricts towards the test section wall, thus the flow reattaches somewhere downstream from the trailing edge of the obstacle. The reattachment area can be regarded as the boundary of the recirculation vortex, and is an important parameter for experiments and simulations involving detached flows.

The reattachment length was determined from the observation that at the reattachment point local flow stagnation occurs, thus the time-averaged velocity components must be zero ($\bar{U} = \bar{V} = 0$). However, an issue with the above mentioned approach was that the lowest boundary of the measurement window was situated approximately 1.8 mm away from the pipe wall, hence the velocity components at the wall were not available. In such circumstances, we plotted the time averaged axial velocity closest to the wall as a function of axial position. In the plots all values were positive, with the notable exception of the recirculation area. The point where the axial velocity crossed form negative (i.e. recirculation) to positive values indicated the downstream boundary of the recirculation vortex and, in conjunction with the time-averaged planar velocity flow maps, was identified as the reattachment of the flow to the test section wall.

Table 1 summarises the reattachment length at three Reynolds numbers (11,000, 33,000 and 65,000) and for the three obstacles (30B, 30R and 15B), normalised by the diameter (i.e. height) of the obstacles. Data from Table 1 suggest that the reattachment length decreases with an increase of Re numbers, for all obstacles investigated. It is also noted that the reattachment length is consistent with the values reported by previous research papers, such as Martinuzzi and Tropea (1993), as described in the introduction. The current measurements indicate that the reattachment length for three-dimensional turbulent flow around flow obstacles is significantly shorter than two-dimensional flow over a backward-facing step.

Examination of time averaged and instantaneous flow velocity maps indicate that the reattachment area is defined far more precisely in the averaged velocity maps.

Table 4 Reattachment length, normalized by obstacle diameter

Obstacle	**Re**		
	11,000	33,000	65,000
30B	2.20	2.06	1.83
30R	1.60	1.30	1.14
15B	1.70	1.13	1.13

4.2 Reynolds stress

Radial profiles of Reynolds stress $\overline{u'v'}$ normalized by U_b^2 at various axial locations are presented in Figure 12. Examination of Reynolds stress plots suggest that significant negative Reynolds stresses were present in the wake of the obstacles, for all obstacles investigated. The relative magnitude of Reynolds stress is comparable for the 30B and 30R and noticeably smaller for the 15B.

Reynolds stress measurements in the proximity of the most downstream boundary of the measurement window indicate that sufficiently far downstream from the flow obstacle, the Reynolds stress approaches the fully developed bare pipe values. It appears that the axial distance required for the bulk of the flow to fully redevelop downstream of an obstacle has a weak dependence on the obstacle size and the flow Reynolds number. Therefore, it seems that for the smallest obstacle (15B), the flow fully recovered at 9D downstream from the downstream end, for the whole range of Re numbers investigated. For the larger obstacles (30B and 30R), the radial profile of Reynolds stress still showed a noticeable, albeit minor (of the order of 5 to 10%), departure from the fully developed values. At approximately 9D downstream from the downstream end of an obstacle, the departure from the fully developed profile seemed to increase with an increase of the bulk Re number.

A distinctive feature at the flow cross section containing the blunt obstacles (that is, 30B and 15B) was that the Reynolds stress was significantly distorted, whilst for the rounded obstacle (30R) the Reynolds stress was very close to its fully developed bare tube values. This can be attributed to flow separation downstream from the upstream end of the blunt obstacles, as observed in the average planar velocity maps.

From Figure 12 it can be concluded that the most significant disturbances of Reynolds stress are just downstream of the trailing edge of an obstacle and decays with increasing distance from the obstacle. As previously noted, it seems that the Reynolds stress approaches the fully developed values at approximately 9.5*D* downstream from the downstream end of an obstacle.

5.0 Discussion

Some authors (Oosthuizen and Naylor, 1998) argue that Reynolds stresses have the physical meaning of a turbulent advection term (or turbulent flux) of momentum and that the same rationale can be applied to turbulent transport of scalar quantities, such as concentration or temperature. Reynolds analogy for pipe flows assumes that the total shear stress and heat transfer rate are governed by similar equations. Using the analogy between the momentum transport and heat transport in turbulent pipe flow, expressions that correlate the Nusselt number with Reynolds and Prandtl numbers have been derived, as exemplified by the following equation (Oosthuizen and Naylor, 1998)

$$\mathrm{Nu} = \frac{\mathrm{Re}_D \mathrm{Pr}\sqrt{f/8}}{\frac{5}{6}\left[2.5\ln\left(\frac{\mathrm{Re}}{30}\sqrt{\frac{f}{32}}\right)+5\ln(5\mathrm{Pr}+1)+5\mathrm{Pr}\right]} \tag{2}$$

This equation was derived assuming that the flow domain was divided into three regions, that is, the viscous, the buffer and the outer layers.

Figure 10 presents the normalized thermal resistances of the viscous, buffer and outer layers for water and Freon R134a, derived by manipulation of Equation (2), as a function of bulk Reynolds number. In order to derive the thermal resistances, the Nusselt number was expressed as a function of heat transfer coefficient, as per its definition:

$$\mathrm{Nu} = \frac{hD}{k} \tag{3}$$

where h is the heat transfer coefficient, D is a characteristic length (e.g. internal pipe diameter) and k is the fluid thermal conductivity. The total thermal resistance of all layers can be calculated as the sum of thermal resistance of the viscous, buffer, and outer layers, namely as:

$$R_{tot}=R_{visc}+R_{buffer}+R_{outer} \quad (4)$$

Noting that $h=1/R$, the equations describing the thermal resistances of each layer can be derived from Equations 2, 3 and 4 and the results are summarized in Table 2:

Table 2 Thermal resistances of viscous, buffer and outer layers in turbulent pipe flow

R_{visc}	$\frac{5}{6}\frac{5Pr}{U_b c_p \sqrt{\frac{f}{8}}}$
R_{buffer}	$\frac{5}{6}\frac{5\ln(5Pr+1)}{U_b c_p \sqrt{\frac{f}{8}}}$
R_{outer}	$\frac{5}{6}\frac{2.5\ln\left(\frac{\mathrm{Re}}{30}\sqrt{\frac{f}{32}}\right)}{U_b c_p \sqrt{\frac{f}{8}}}$

An important note is that, in general, at Reynolds numbers of the order of 10,000 to 100,000 in fully developed turbulent pipe flow, the viscous layer appears to have the highest thermal resistance, thus being the limiting factor to the convective heat transfer. This can be attributed to molecular effects which are dominant in the viscous layer, heat being transferred practically by thermal conduction. Molecular diffusion is significantly smaller than turbulent diffusion, thus this layer practically acts as a thermal “insulator” and causes very large temperature and velocity gradients. A substantial increase in heat transfer can be expected if this layer is disrupted. This is especially important at lower Re numbers, where the weight of viscous layer thermal resistance is the highest.

Figure 10 suggests that the convective turbulent heat transfer is also impacted by the outer layer, especially at high Re numbers. Within this layer, molecular diffusion is negligible in comparison with turbulent diffusion, thus the velocity and temperature gradients are much smaller than within the viscous layer. The augmentation of convective heat transfer within the outer layer appears to be correlated with the supplementary Reynolds stress caused by the flow obstacles. The plots from Figure 12 indicate that flow obstacles distort and increase significantly Reynolds stress in the flow downstream from the obstacle. The current experimental results suggest that augmentation of heat transfer in the outer layer throughout the Reynolds stress persists up to 9-10*D* downstream the flow obstacle.

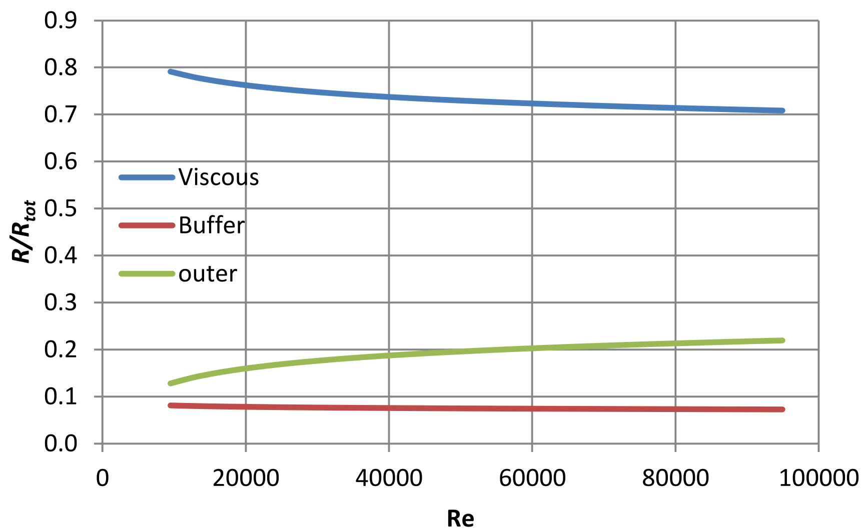

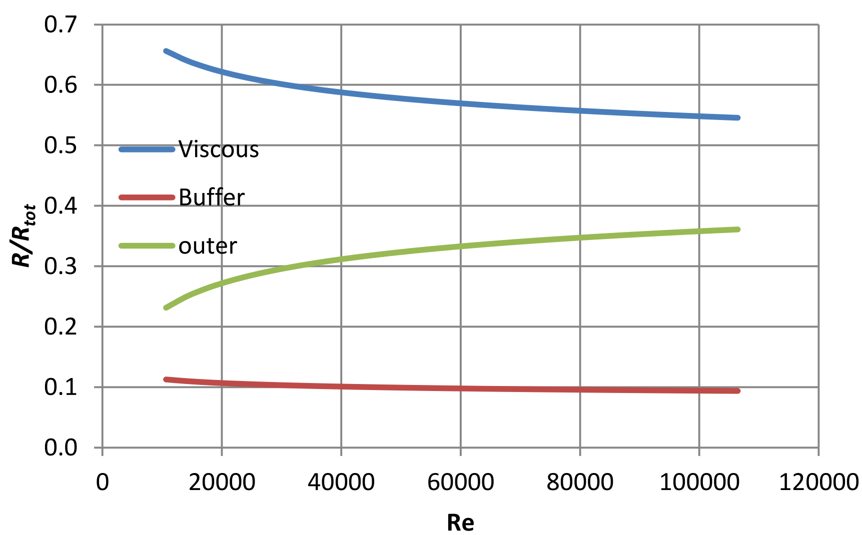

Figure 10 Normalized thermal resistances of the viscous, buffer and the outer layers for water (top) and R134a (bottom) for fully developed turbulent pipe flow, as a function of bulk Reynolds number.

Figure 13, which presents the axial variation of circumferentially averaged normalized heat transfer coefficient (Tanase and Groeneveld, 2015), indicates that the obstacle induced augmentation of heat transfer was still significant at 9*D* downstream from the downstream end for all obstacles and all ranges of Re number investigated; moreover, the augmentation of heat transfer typically persisted at least up to 30*D* downstream from a flow obstacle. Since Reynolds stresses recover within approximately 9-10D and heat transfer is augmented at least up to 30D downstream from a flow obstacle, it can be reasonably assumed that the main mechanism of heat transfer augmentation between 10 to 30D downstream is related to the redevelopment of the viscous layer. This is consistent with the values reported for the entry length of turbulent pipe flow.

It is also noted that the weight of the thermal resistance of the viscous layer decreases with an increase of bulk Re number. A consequence of this is that the effectiveness of the viscous layer disruption as a heat transfer augmentation mechanism decreases with an increase of flow Re number, and this was confirmed by experiments as was shown in Figure 13 (Tanase and Groeneveld, 2015).

In conclusion, it appears that the augmentation of turbulent convective heat transfer in heated channels may be affected by two main mechanisms:

1) Disruption of viscous layer – controlled by thermal conduction; this heat transfer augmentation occurs for geometries where flow obstruction is in contact or very close to the heated wall and is able to physically disrupt the viscous layer, either by direct contact with the heated wall or throughout the coherent structures (e.g. vortices) formed around an obstacle. It seems that, similar to the pipe entrance effects, this mechanism is effective up to 30-50*D* downstream the flow obstacle.
2) Augmentation of turbulent mixing (e.g. Reynolds stress) in the core of the flow – controlled by advection/fluid mixing; this mechanism seems shorter-lived, being effective up to 9-10D downstream the trailing edge of an obstacle.

Depending on the system geometry, the weight of the above mentioned mechanisms may vary.

6.0 Conclusions and Final Remarks

- Obstacle pressure loss coefficients (*K*) were obtained using a magnet-controlled obstacle positioning method. The K-factors derived from the measurements were compared with the CFD simulations and good agreement was obtained provided that a fine mesh was used (more details are presented in Appendix F). The K-factors were found to decrease with an increase of flow Re number.

- Blockage ratio and shape of flow obstacle affect the obstacle pressure loss coefficient (*K*) significantly; the highest pressure loss coefficient was determined for 30B, followed by 30R and 15B, respectively.

- The recovery length for static pressure seems significantly shorter than that of the mean velocity or Reynolds stresses. Current experimental data suggest that the axial and circumferential distortions of static pressure caused by flow obstacle were measurable up to 5*D* downstream from the trailing edge of an obstacle, while the velocity and turbulence distortions were still measurable at approximately 9.5*D* downstream from the trailing edge of the flow obstacle.

- It appears that the supplementary turbulence caused by a flow obstacle decays almost completely after -9*D* downstream from the trailing edge; however, the measured heat transfer augmentation persists up to 30-50*D* downstream.

- Augmentation of turbulent convective heat transfer in heated channels can be attributed to the following mechanisms.
    a) disruption of the viscous sublayer, within which heat transfer is controlled by thermal conduction; this heat transfer augmentation occurs for geometries or flow conditions able to physically disrupt the viscous layer, either by direct contact with the heated wall or throughout the coherent structures (e.g. vortices) formed around an obstacle; similar to the pipe entrance effect, this mechanism is effective up to 50*D* downstream the flow obstacle, and.

b) augmentation of turbulent mixing (e.g. Reynolds stress) in the core of the flow, which is controlled by advection/fluid mixing; this mechanism seems shorter-lived, being effective up to 9-10*D* downstream from the trailing edge of an obstacle.

- The heat transfer enhancement and pressure loss coefficients due to obstacles show some similarity, e.g. they both increase with the square of the flow blockage ratio and decrease with an increase in Reynolds number. However, for the range of flow obstacles investigated, the heat transfer augmentation cannot be correlated with the local pressure loss coefficient of the obstruction, which is contrary to the generally accepted Reynolds analogy for smooth heated channels, where the heat transfer coefficient and friction factor behave similarly.[7]

- Current pressure loss and heat transfer experimental data suggest that, at bulk Re number over 50,000, a streamlined flow obstacle (e.g. 30R) augment the heat transfer better than a blunt cylinder with the same obstruction ratio, while causing significantly lower pressure loss. This conclusion is consistent with other research findings (e.g. Shiina et al, 1991).

[7] Example: K for the rounded obstacles were significantly smaller than for blunt obstacles with the same blockage ratio for all Re numbers investigated, whilst the augmentation of heat transfer by the corresponding obstacles were quite close to each other. Actually, at Re>50,000 the rounded obstacle consistently outperformed the blunt one. My explanation for these observations is that heat transfer is limited by the viscous layer, which is adjacent to the wall. If the wall roughness changes, the viscous sublayer thickness as well as the friction loss change, as indicated by the Moody diagram. Both momentum diffusivity and heat diffusivity take place at the wall and are closely related, being controlled by the wall roughness. However, pressure loss induced by large obstacles (much larger than the wall roughness) takes place in the core of the flow, which has less significant impact on heat transfer. If a streamlined obstacle mechanically disrupts the boundary layer to the same extent as a bluff one, then the heat transfer in both cases would be comparable but the pressure loss, however, would be much higher for the bluff obstacle.

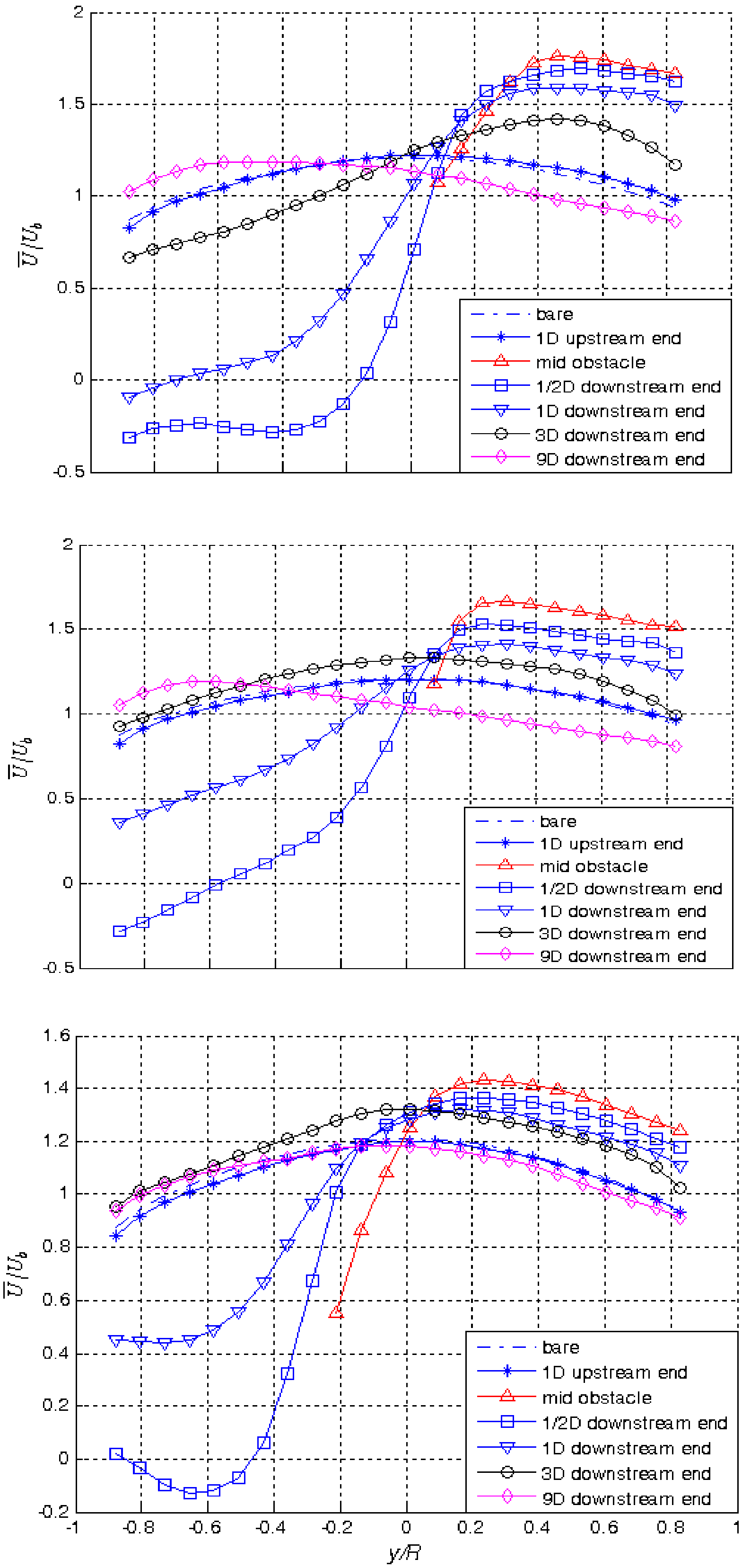

Figure 11 Normalized mean velocity at bulk Re=35,000 for 30B (top), 30R (middle) and 15B (bottom).

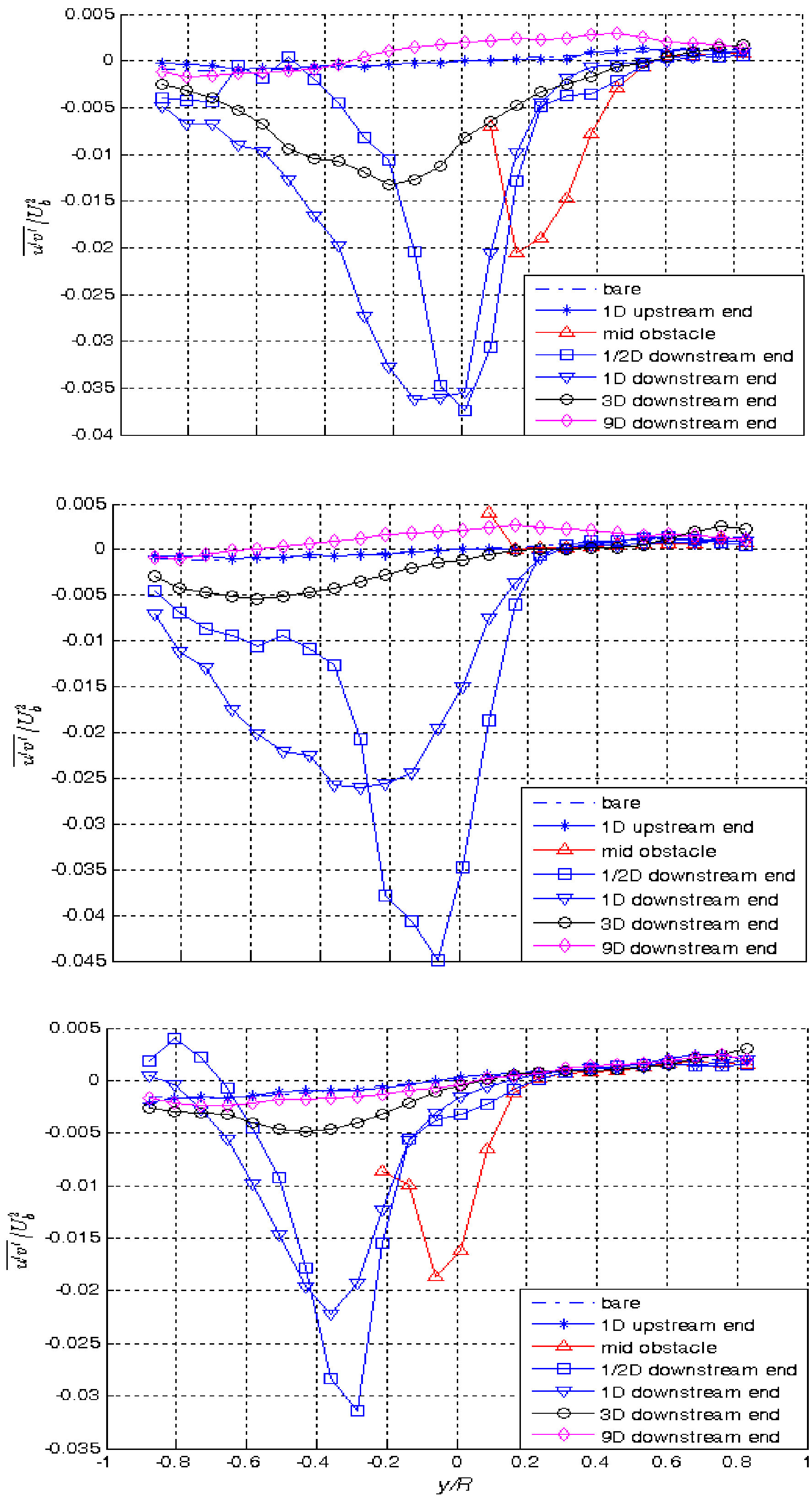

Figure 12 Normalized Reynolds stress $\overline{u'v'}$ at bulk Re=35,000 for 30B (top), 30R (middle) and 15B (bottom).

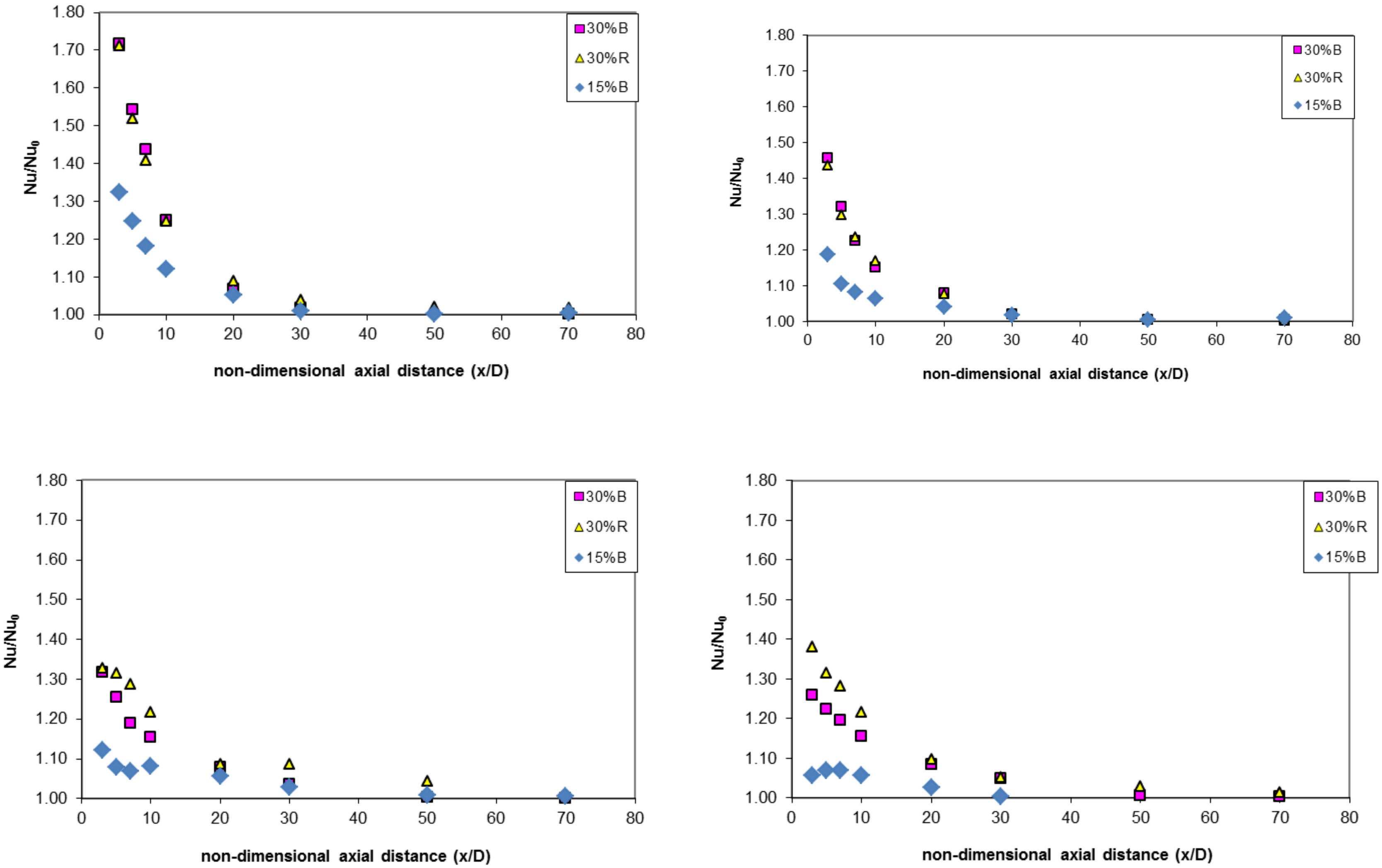

Figure 13 Normalized circumferentially averaged Nu number for 30B, 30R and 15B flow obstructions at Re=14,000 (upper left), Re=28,000 (upper right), Re=56,000 (lower left) and Re=90,000 (lower right) (Tanase and Groeneveld, 2015).

References

Becker, S., Lienhart, H. and Durst, F., 2002. Flow around three-dimensional obstacles in boundary layers. J. of Wind Eng. and Ind. Aerodynamics 90, 265–279.

Casarsa, L and Arts, T., 2005. Experimental Investigation of the Aerothermal Performance of a High Blockage Rib-Roughened Cooling Channel. J. of Turbomachinery 127, 580-588.

Castro I. P. and Robins A. G. , 1977. The flow around a surface-mounted cube in uniform and turbulent streams. J. of Fluid Mechanics 79(2), 307- 335.

Cengel, Y.A and Cimbala, J.M., 2010. Fluid Mechanics: Fundamentals and Applications, 2nd edition. McGraw-Hill.

Hussein, H. J. and Martinuzzi, R. J. 1996. Energy balance for turbulent flow around a surface mounted cube placed in a channel. Phys. Fluids 8 (3), 764-780.

Martinuzzi, R. and Tropea, C. 1993. The Flow Around Surface-Mounted, Prismatic Obstacles Placed in a Fully Developed Channel Flow (Data Bank Contribution). *J. Fluids Eng.* 115(1), 85-92.

Meinders E.R. and Hanjalic, K, 2002. Experimental study of the convective heat transfer from in-line and staggered configurations of two wall-mounted cubes. Int. J. of Heat and Mass Transfer 45, 465-482.

Oosthuizen, P.H. and Naylor, D.,1998. An introduction to Single Phase Convective Heat Transfer Analysis. William C Brown Pub.

Pattenden, R.J., Turnock, S.R., Zhang, X., 2005. Measurements of the flow over a low-aspect-ratio cylinder mounted on a ground plane. Exp Fluids 39(1),10–21.

Rafel, M., Willert, C. E. and Kompenhans, J. 1998 Particle Image Velocimetry: A practical guide.Springer.

Soussa, J.M.M., 2002. Turbulent flow around a surface-mounted obstacle using 2D-3C DPIV. Exp. in Fluids 33, 854–862.

Shiina, K., Nakamura, S. and Sagawa, W., 1991. Enhancement of forced convective heat transfer in a rectangular channel using plate-type obstacles, Part 2 – heat transfer and pressure drop characteristics using spacer configuration. ASME/JSME Thermal Engineering Proceedings, 4.

Sumner, D., 2013. Flow above the free end of a surface-mounted finite-height circular cylinder: a review. Journal of Fluids and Structures 43, 41-63.

Tanase, A. and Groeneveld, D.C., 2015. An experimental investigation on the effects of flow obstacles on single phase heat transfer. Nucl. Eng. Des. 288, 195-207.

Tavoularis, S., 2005. Measurement in Fluid Mechanics.Cambridge University Press.

White, F.M., 2011. Fluid Mechanics, Seventh edition. McGraw-Hill.

CHAPTER 7

CONCLUSIONS

7.1 Summary of results

Convective turbulent heat transfer in a heated tube equipped with flow obstacles was measured for Reynolds numbers in the range from 14,000 to 97,000. Heat transfer experiments were complemented by isothermal PIV and pressure loss experiments and numerical simulations.

Heat transfer experiments indicated that the following parameters influence the augmentation of forced convective heat transfer downstream from flow obstacles:

1) Blockage ratio
2) Distance downstream from the obstacle
3) Flow Reynolds number
4) Circumferential location of the obstacle (for eccentric geometries)
5) Obstacle shape

The results have shown that the first three parameters are the most significant for prediction of heat transfer augmentation downstream of a flow obstruction in turbulent flow in heated pipes.

The current investigation indicates that bundle-based correlations significantly under-predict the experimental results obtained for heated tubes with wall mounted flow obstacles. The relatively large differences between the prediction methods for rod bundles suggest that the prediction methods should only be used for the geometry and flow conditions of their database. Caution should be exercised when applying prediction methods for heat transfer augmentation derived from experimental data on rod bundles to other flow geometries.

The proposed prediction method correlates the blockage ratio, non-dimensional distance and flow Reynolds number and provides satisfactory prediction accuracy when compared against the current experimental data and a relevant experimental dataset from the literature. It is expected that a correlations based on a larger experimental database (e.g.

including reliable circumferential measurements) would further improve prediction accuracy and applicability.

The present measurements indicate that for the lower Re number range (13,000 < *Re* < 50,000) and a given blockage ratio, the heat transfer augmentation of flow obstacles of various shapes was comparable; however, for higher flows (50,000 < *Re* < 100,000) the rounded shaped obstacle produced noticeably higher heat transfer augmentation. This effect was observed for both the 0.15 and 0.3 blockage ratios investigated.

The interpretation of the current experimental data and a review of previous investigations suggested that the main heat-transfer augmentation mechanisms are: i) disruption of boundary layer, ii) increase of mixing by obstacle induced turbulence, and iii) flow acceleration. Their relative importance may vary depending on flow geometry, axial and circumferential location and Reynolds number.

The blockage ratio and the shape of flow obstacle both affect the obstacle pressure loss coefficient significantly; the highest pressure loss coefficient was determined for 30B, followed by 30R and 15B, respectively. It was also noted that the obstacle pressure loss coefficient decreases with an increase of bulk Reynolds number.

The recovery length for static pressure seems to be significantly shorter than that of the mean velocity or Reynolds stresses. Current experimental data suggest that the axial and circumferential distortions of static pressure caused by flow obstacle were measurable up to 5*D* downstream from the trailing edge of the obstacle, while the velocity and turbulence distortions were still measurable at approximately 9.5*D* downstream of the downstream end of the obstacle.

It appears that the supplementary turbulence caused by a flow obstacle decays almost completely after 9*D* downstream from the trailing edge; however, the measured heat transfer augmentation typically persists up to 30*D* downstream.

We offer the following possible explanations for the observed augmentation of turbulent convective heat transfer in heated channels::

a) Disruption of the viscous layer, within which heat transfer is controlled by thermal conduction; this heat transfer augmentation occurs for geometries or flow conditions able to physically disrupt the viscous layer, either by direct contact with the heated wall or through the coherent structures (e.g. vortices) formed around an obstacle. It seems that, similar to the pipe entrance effects, this mechanism is effective up to 50*D* downstream from the flow obstacle.

b) Augmentation of turbulent mixing (e.g. Reynolds stress) in the core of the flow which is controlled by advection/fluid mixing; this mechanism seems shorter-lived, being effective up to 9-10*D* downstream of the trailing edge of an obstacle.

It should be noted that the mechanisms of heat transfer augmentation mentioned above were based on our review of relevant literature and the interpretation of our own and other researchers experimental data.. In order to confirm and further enhance our understanding of these mechanisms, future investigations, as suggested in Section 7.3, are recommended. Nevertheless, in our opinion, our study is the first one to offer these possible explanations for the apparent discrepancies among the empirical prediction methods reported in the literature.

Current pressure loss and heat transfer experimental data suggest that, at bulk Re number over 50,000 more streamlined flow obstacle (e.g. 30R) augment heat transfer better than a blunt cylinder with the same obstruction ratio, while causing significantly lower pressure loss. This conclusion is consistent with other research findings (e.g. Shiina et al, 1991).

The heat transfer enhancement and pressure loss coefficients due to obstacles show some similarity, e.g. they both increase with the square of the flow blockage ratio and decrease with an increase in Reynolds number. However, for the range of flow obstacles investigated, the heat transfer augmentation cannot be correlated with the local pressure loss coefficient of the obstruction, which is contrary to the generally accepted Reynolds analogy for smooth heated channels, where the heat transfer coefficient and friction factor behave similarly.

7.2 Main contributions of this work

The overall objective of this study is to improve our understanding of heat transfer and pressure loss in tubes equipped with flow obstacles by experimentally investigating the axial and circumferential distributions of convective heat transfer in heated tubes, complemented by adiabatic Particle Image Velocimetry (PIV) and pressure loss measurements, as well as numerical simulations. To our knowledge, this investigation is the first to employ multiple and complementary measurement techniques, such as measurement of heat transfer coefficient, Particle Image Velocimetry and pressure loss measurement as well as numerical simulations. We believe that proper combination of complementary measurement techniques provides a more complete insight and understanding of the flow around flow obstacles and the heat transfer augmentation mechanisms.

An important objective of the current investigation is to recommend an optimum flow obstacle shape, designed to maximize heat transfer enhancement while minimizing the pressure drop penalty. Therefore, two distinctive flow obstacles shapes were investigated: obstacles with straight (i.e. blunt) ends and obstacles with hemispherical (rounded) ends, at flow Reynolds numbers ranging between 14,000 and 97,000. The results of the heat transfer experiments showed that the differences in heat transfer augmentation between blunt and rounded obstacles were comparable in magnitude, whilst the pressure loss coefficient of the blunt obstacle was considerably higher than the rounded obstacle. It was concluded that rounded shapes outperform the blunt shaped obstacles, when heat transfer and pressure loss are the primary factors in assessing their overall performance. Obviously, the design of flow obstacles needs to consider other factors, such as the manufacturing costs, positioning constraints and impact on critical heat flux (for nuclear fuel elements). Nevertheless, we believe that the experimental database and our conclusions are relevant to the design and optimization of flow obstacles.

A significant finding of this research is that, for the Reynolds number range investigated, heat transfer augmentation could not be correlated with the local pressure loss coefficient of the obstruction, using the Reynolds analogy which works well in smooth heated channels. Nevertheless, an empirically derived prediction method, which correlates the blockage ratio, normalized axial distance downstream the obstacle and flow Reynolds number provides satisfactory prediction accuracy when compared against the current experimental data and other relevant experimental datasets from literature. This is the first tube-based correlation that explicitly takes into account the flow Reynolds number. Due to its good accuracy, simplicity and robustness we expect that the present correlation may be incorporated in specialized best estimate computer codes for the design and safety assessment of nuclear reactors.

A geometrical analysis of distortions was performed and showed that the optical distortions in the usable area of the measurement plane were of the order of 2%. The results of the geometrical analysis were confirmed by the analysis of images of calibration grids inserted in the test section at the location of the measurement plane and outside the test section. We believe that our experimental approach introduced several innovative features (e.g. the attempt to use a Teflon test section and analysis of optical distortions by various methods), which might prove useful for the design of future experiments.

The current investigation is also relevant to the safety assessment of water-cooled nuclear reactors during accident conditions where the Critical Heat Flux is exceeded. Here the main heat transfer mechanism to a spacer-equipped bundle is film boiling heat transfer, i.e. cooling of the heated wall by a vapour blanket, while the bulk flow still contains some liquid. The flow disturbance and heat transfer enhancement effects of flow obstacles investigated in this thesis are expected to be similar to those in a spacer-equipped fuel bundle at high temperatures experiencing film boiling or superheated steam cooling only. This is because the pertinent flow behaviour and heat transfer mechanisms during film boiling around the spacers generally follow single phase flow and heat transfer principles.

7.3 Recommendations for future work

The planar PIV system used for this study measured only two components of the velocity vector in a three-dimensional flow, which resulted in underestimation of the turbulent and viscous stresses. Moreover, the measurements were made in one plane - the vertical symmetry plane. Future measurements should include additional planes, thus allowing better characterization of flow and turbulent stresses around obstacles. Future studies should also use stereoscopic PIV to obtain the third velocity component and provide better estimates of the stresses.

A significant improvement of the experimental setup can be made by the procurement or the design of a heated test section with thinner, transparent walls, which would allow simultaneous measurement of heat transfer coefficient, pressure loss and PIV. This would eliminate the need for separate test sections for heat transfer experiments and the scaling issues.

For future measurements it is recommended that heat transfer and PIV measurements have sufficient axial lengths in order to ensure that, within the measurement uncertainties, the velocity, turbulent and viscous stresses reach their fully developed bare tube values downstream the flow obstacle. Moreover, special attention should be given to the recirculation and reattachment areas.

It is recommended that future work examine in more detail and provide further confirmation of the two heat transfer enhancement mechanisms identified by this investigation. Also, although the current investigation recommended rounded obstacles when the optimization of heat transfer versus the pressure drop is required, further refinement of rounded and streamlined obstacle shapes (e.g. elliptical vs hemispherical) is expected to result in an even more optimized obstacle shape, which would be beneficial for practical applications.

REFERENCES

ANDERSON, J.D. JR 1995 *Computational Fluid Dynamics: The Basics with Applications*. McGraw-Hill

Ansys 2006 *FLUENT 6.3 User's Guide*. Ansys Inc.

Ansys 2006 *GAMBIT 2.3 Documentation*. Ansys Inc

BHATTACHARYYA, S. AND MAHAPATRA, S. 2003 Flow and heat transfer around a surface-mounted blunt obstacle. *Numerical Heat Transfer, Part A,* **43**, 465-479.

BLAZEK, J., 2005 *Computational Fluid Dynamics: Principles and Applications* (2nd ed.). Elsevier Boston.

BOUSSINESQ, J.1877 Essai sur la theorie des eaux courantes, memoires presentes par divers savants. *l'Académie des Sciences 23,* **24**, Paris, France, 1—680.

BRADSHAW, P. 1997 Understanding and prediction of turbulent flow – 1996. *International Journal of Heat and Fluid Flow* **18**, 45—54.

CHANDRA, L., NIJEHOLT, J.L., VISSER, D.C., ROELOFS, F. 2009 CFD analysis on the influence of wire wrap on the heat transport in supercritical fluid. *The 13th International Topical Meeting on Nuclear Reactor Thermal Hydraulics (NURETH-13) N13P1050 Kanazawa City, Ishikawa Prefecture, Japan, September 27-October 2, 2009.*

CORSAN, J.M., BUDD, J.N., AND HEMMINGER, W.F.1990 An intercomparison involving PTB and NPL of thermal conductivity measurements on stainless steel, Inconel and Nimonic alloy reference materials, and an iron alloy.*12th European Conference on Thermophysical Properties, Vienna, Austria,* **23**(2), 119-128.

DAVIS, E.J. AND ANDERSON, G.H.1966 The incipience of nucleate boiling in forced convection flow. *AIChE Journal* **12** (4), *774–780.*

DALOGU, A. AND UNAL, A. 2000 Heat transfer form a cylinder in the wake flow. *Int. Comm. Heat Mass Transfer*, **27**(4), *569-580.*

DOERFFER, S., GROENEVELD D.C. AND SCHENK, J.R. 1996 Experimental Study of the Effects of Flow Inserts on Heat Transfer and Critical Heat Flux. *Proceedings of the 4th Int.*

Conference on Nuclear Engineering, vol. 1 - Part A, 41-49, March 10-14, New Orleans, Louisiana, USA.

FUSEGI, T. 1995 A computational study of turbulent diffusion in a thermally-stratified channel with obstruction. *Journal of Wind Engineering and Industrial Aerodynamics* **58**, *19-32*

HASSAN, M.A., REHME, K.1981 Heat transfer near spacer grids in gas-cooled rod bundles, *Nucl. Technol.* **52**, *410–41*.

HOLLOWAY, M.V., MCCLUSKY, H.L., BEASLEY, D.E. AND CONNER, M.E. 2004 The effect of support grid features on local, single-phase heat transfer measurements in rod bundles. *Journal of Heat Transfer* **124**, 43-53.

HOLLOWAY, M., CONOVER, T., MCCLUSKY, H., BEASLEY, D. AND CONNER, M.E. 2005 The effect of support grid design on azimuthal variation in heat transfer coefficient for rod bundles, *Journal of Heat Transfer* **127**, 598-605.

IACCARINO, G., 2001 Predictions of a turbulent separated flow using commercial CFD codes, *J. of Fluids Engineering* **123**, 819-828.

INCROPERA, F.P. AND DEWITT, D.P. 2007 *Fundamentals of Heat and Mass Transfer*, (*6th ed.*). John Wiley & Sons.

KHAN, J.A., HINTON, J AND BAXTER, S.C. 2002 Enhancement of heat transfer with inclined baffles and ribs combined. *Journal of Enhanced Heat Transfer* **9**, 137-151.

KAROUTAS, Z., GU, C.Y., SCHOLIN, B. 1995 3-D flow analyses for design of nuclear fuel spacers. *Proceedings of the 7th International Meeting on Nuclear Reactor Thermal-Hydraulics NURETH-7, Sessions 17-24.*

KORICHI, A AND OUFER,L. 2005 Unsteady heat transfer and pressure drop in channels with obstacles mounted on the upper and lower walls. *Numerical Heat Transfer, Part A* **78**, *711 – 72.*

LAUNDER, B. AND D. SPALDING 1974 The numerical computation of turbulent flows.*Computer Methods in Applied Mechanics and Engineering* **3**(2), 269—289.

LABBE, O., SAGAUT, P AND MONTREUIL, E. 2002 Large-eddy simulation of heat transfer over a backward-facing step, *Numerical Heat Transfer, Part A*, **42**, 73-90.

MEINDERS E.R. AND HANJALIC, K, 2002 Experimental study of the convective heat transfer from in-line and staggered configurations of two wall-mounted cubes. *International Journal of Heat and Mass Transfer* **45**, 465-482.

MENTER, F., 1992 Performance of popular turbulence models for attached and separated adverse pressure gradient flows. *AIAA Journal* **30** (8), 2066—2072.

MENTER, F., 1994 Two-equation eddy-viscosity turbulence models for engineering applications. *AIAA Journal* **32** (8), 1598—1605.

National Instruments, 1999 Measurement and Automation Catalogue.

RAFFEL, M., WILLERT, C. E. & KOMPENHANS, J. 1998 Particle Image Velocimetry: A practical guide. Springer.

REHME, K., 1977 Pressure drop of spacer grids in smooth and roughened rod bundles. *Nuclear Technolog,* **33**, 314-317.

SHUJA, B.Z., YILBAS, B.S. AND IQBAL, M.O., 2000 Heat transfer characteristics of flow past a rectangular protruding bod., *Numerical Heat Transfer, Part A*, **37**, 307-321.

SUGA, K., 2004 Improvement of second moment closure for turbulent obstacle flow and heat transfer. *Int. Journal of heat and Fluid Flow* **25**, 776-784.

SLANCIAUKAS, A, 2001 Two friendly rules for the turbulent heat transfer enhancement. *Int. Journal of Heat and Mass Transfer* **44**, 2155-2161.

SHIINA, K., NAKAMURA, S. AND SAGAWA, W., 1989 Enhancement of forced convective heat transfer in a rectangular channel using plate-type obstacles, Part 2 – heat transfer and pressure drop characteristics using spacer configuration. *Transactions of Japan Society of Mechanical Engineers B* **55**(515), 2041-2047.

SHIH, T.-H., LIOU, W., SHABBIR, A., YANG , Z., AND ZHU, J., 1994 A new k—ε eddy viscosity model for high Reynolds number turbulent flows-model development and validation. *Technical Report NASA TM-106721, Institute for Computational Mechanics in Propulsion and Center for Modeling of Turbulence and Transition, Lewis Research Center.*

TAKASE, K., 1996 Experimental results of heat transfer coefficients and friction factors in a 2D/3D Rib-roughened annulus. *Experimental Thermal and Fluid Science* **13**, 142-151.

TAVOULARIS, S., 2005 *Measurements in Fluid Mechanics*. Cambridge University Press.

TAVOULARIS, S., 2007 *Theory of Turbulence*. *Course notes.* University of Ottawa.

TEREKHOV, V.I., YARYGINA, N.I., ZHDANOV, R.F., 2002 Some features of a turbulent separated flow and heat transfer behind a step and a rib. *Journal of Applied Mechanics and Technical Physics*, **43**(6), 888-894.

WILCOX, D., 1994 Simulation of Transition with a Two-Equation Turbulence Model, *AIAA Journal **32** (2)*, 247-255.

WILCOX, D., 2000 *Turbulence Modeling for CFD* (2nd ed.). DCW Industries.

YAO, M, NAKATANI, M AND SUZUKI, K., 1995 Flow visualization and heat transfer experiments in a turbulent channel flow obstructed with an inserted square rod. *Int. J Heat and Fluid Flow* **16**, 389-397.

YAO, S.C., HOCHREITER, W.J. AND LEECH, W.J., 1982 Heat transfer augmentation in rod bundles near grid spacers. *Transactions of the ASME* **104**, 76-81.

YOUNG, J.T AND VAFAI, K., 1998 Convective cooling of a heated obstacle in a channel. *Int. Journal of Heat and Mass Transfer* **41**, 3131-3148.

ZHANG, B., SHAN, J., JIANG, J., 2009 Numerical analysis of supercritical water heat transfer in vertical tube with different obstacles. *The 13th International Topical Meeting on Nuclear Reactor Thermal Hydraulics (NURETH-13) N13P1050 Kanazawa City, Ishikawa Prefecture, Japan.*

APPENDIX A: LIST OF PUBLICATIONS BY A. TANASE

TANASE, A., NAKLA, M., ZAHLAN EL, H., GROENEVELD, D.C. AND CHENG, S.C., 2006 Impact of circumferential location of a flow obstacle on critical heat flux in tubes. *UO-MCG-TH-2006-002, Technical Report.*

G. CUBIZOLLES, J. GARNIER, GROENEVELD, D. AND TANASE A., 2009, Methods for determining the wall thickness variation of tubular heaters used in thermalhydraulic studies, *Proceedings, 13th International Topical Meeting on Nuclear Reactor Thermal Hydraulics (NURETH-13), Kanazawa City, Ishikawa Prefecture, Japan, September 27-October 2, 2009*

SHAN, J. Q. ,VASIC, A. , GROENEVELD , D. C., PENG S.W, CHENG S.C., TANASE, A , 2005 Methods in improvement of 2005 CHF Look up table. *UO-MCG-TH-2004-003, Technical Report.*

GROENEVELD, D.C., SHAN, J.Q., VASIC , A.Z., LEUNG, L.K.H., DURMAYAZ ,A., YANG, J., CHENG, S.C. , TANASE, A., 2005 The 2005 CHF Look-up Table. *11th International Topical Meeting on Nuclear Reactor Thermal-Hydraulics (NURETH-11), Avignon, France, October 2-6.*

GROENEVELD, D.C. , VASIĆ , A.Z. , YUAN, L.Q., LEUNG, L.K.H., TANASE, A. , SHAN, J.Q. AND CHANDRAKER, D. K., 2007, Tube CHF database compilation and assessment. *12th Intern'l Topical Meeting on Nuclear Reactor Thermalhydraulics, Pittsburgh, October 2007*

TANASE, A., GROENEVELD, D.C., ZAHLAN, H., CHENG, S.C., 2008 Experimental investigation of flow obstacles effect on single phase heat transfer. *29th Canadian Nuclear Society Annual Conference, Toronto, June 1-4.*

ZAHLAN, H., GROENEVELD, D.C., LEUNG, L.K.H, TANASE, A., AND CHENG, S.C., 2008 Investigation of the combined effect of appendages and axial power profile on post-dryout heat transfer in tubes. *29th Canadian Nuclear Society Annual Conference, Toronto, June 1-4.*

TANASE, A., GROENEVELD, D.C., SHAN, J.Q., CHENG, S.C. , 2009 Diameter effect on critical heat flux. *Nuclear Engineering and Design* **239** (2).

TANASE, A., GROENEVELD, D.C., 2008, An Accurate Method of Assessing Tube Wall Thickness Based on Flow Boiling and Single Phase Heat Transfer Measurements, *Proceedings, Canadian Nuclear Society 2008 Simulation Conference*, Ottawa, 2008 November.

TANASE, A., AND GROENEVELD, D.C., 2015 An experimental investigation on the effects of flow obstacles on single phase heat transfer, *Nuclear Engineering and Design* **288**, 195-207

TANASE, A., SZYMANSKI, J., EL-HAWARY, M. AND DELJA, A., 2015 Numerical Predictions of Heat Transfer and Pressure Tube/Calandria Tube Deformation During Calandria-Tube Strain Contact Boiling (CSCB) Tests. *7th International Conference on Modeling and Simulation in Nuclear Science and Engineering, Ottawa, Ontario, Canada, October 18-21.*

VIKTOROV, A., EL-HAWARY, M AND TANASE, A. 2016 New Contact Boiling Experiments to Evaluate Calandria Tube Strain Acceptance Criteria, *13th International Conference on CANDU Fuel, Kingston, ON, Canada, August 12-14.*

APPENDIX B: ANALYSIS OF WALL THICKNESS ECCENTRICITY

AN ACCURATE METHOD OF ASSESSING TUBE WALL THICKNESS BASED ON FLOW BOILING AND SINGLE PHASE HEAT TRANSFER MEASUREMENTS

A. Tanase*, D.C. Groeneveld†*

*University of Ottawa, Ottawa, ON Canada K1N 6N5
†Atomic Energy of Canada Limited, Chalk River, ON Canada K0J 1J0

Abstract

Fuel bundle simulators used in thermalhydraulic studies typically consists of bundles of directly heated tubes. It is usually assumed that these tubes have a uniform circumferential heat flux distribution. In practice, this heat flux distribution is not uniform because of wall thickness variations. Ignoring the non-uniformity in wall thickness will lead to underestimating the critical heat flux and overestimating the film boiling temperature.

It is the objective of this paper to present an accurate method for determining this wall thickness variation. The method is based on the principle that for directly heated tubes, cooled internally, the single phase heat transfer coefficient (or the wall superheat in nucleate boiling or at ONB) is uniform around the circumference and is therefore independent of the variation in wall thickness.

Three analytical methods for evaluating the wall thickness variation have been compared:

- based on single phase heat transfer data,
- based on nucleate boiling data,
- based on ONB data

The wall thickness evaluations have subsequently been validated by two direct measurements: (i) based on direct caliper measurements, and (ii) based on photographic measurements

The agreement between these five methods is good. The results show that the proposed analytical approach is a highly accurate method for determining the circumferential wall thickness variation.

1. Introduction

The method for determining the circumferential wall thickness variation presented in this paper is based on the measurement of the non-uniformity in circumferential wall temperature distribution. The accuracy of the estimated wall thickness variation depends strongly on the accuracy of the surface temperature measurement. In this paper we will therefore first describe a method for calibrating the thermocouples used to measure the surface temperature of a direct current (DC) heated tube and for detecting the geometrical asymmetries (eccentricity, variation of tube radii) at the location of thermocouples. The method can be effectively used for estimating the local tube wall thickness (at the middle of the tube for example) from measurement of inside and outside tube radii at the end of the tube and the assumption that their variation is negligible along the tube length.

1.1 Experimental setup

The test section used for current experiment is an Inconel 600 tube having heated length L_h=2m and measured inside diameter Di=5.585±0.0013 mm and outside diameter Do=8.020±0.0013 mm. The test section is cooled internally and equipped on the outside with three pairs of K-type thermocouples. They are located at opposite sides at three axial locations of the test section, as shown in Figure 1.

Ideally, the thermocouple pairs located at the same axial location (such as thermocouple 1 and thermocouple 2) should indicate the same temperature. The expected uncertainty in the thermocouple readings is 0.4 °C [4] , i.e. we are 95% confident that replacing any thermocouple with a similar type the difference between the measurement and the true temperature is less than 0.4 °C. This uncertainty can be reduced for a given thermocouple using appropriate calibrations. In order to quantify the thermocouple inaccuracy, several tests were performed.

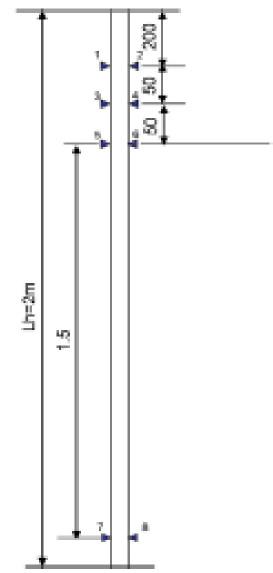

Figure 1 Test section and thermocouple axial positions

1.2 Thermocouple calibration

The thermocouple calibrations were performed by circulating single phase coolant through the test section using several bulk coolant temperatures. Because no heating is applied to the test section, wall thickness variation do not affect the readings. If the coolant temperature is close to the ambient temperature and/or the test section is thermally insulated, then heat losses and contact resistance effects are minimized or non-existent. Therefore, this test will show the inaccuracies (random and systematic) of the thermocouples and the analog-digital conversion (ADC) but for a relatively narrow range of temperatures.

Note that the calibrations were performed at high mass flux (G=3500 $kgm^{-2}s^{-1}$) and at pressure approximately equal with 2380 kPa. The reference bulk coolant temperature is based on the averaged values from resistance temperature detectors (RTD's) located at the inlet and outlet of the test section. Thermocouple voltage outputs were converted into temperatures based on standard tables for type-K thermocouples. Table 1 shows the averaged "error" values for all thermocouples

The general form of the correction function is $\Delta T = aT + b$. Table 2 gives the optimized coefficients a and b. The correction is performed as $T_{corrected}=T_{raw}-(aT_{raw}+b)$.

Table 1 Average difference (K) between measured thermocouple temperature and the reference temperature (T_{ref})

T_{ref} (°C)	T_{WO1}	T_{WO2}	T_{WO3}	T_{WO4}	T_{WO5}	T_{WO6}
10	0.16	0.19	0.04	-0.05	0.06	-0.05
20	0.21	0.14	0.07	-0.01	-0.01	-0.03
30	0.16	0.11	0.04	-0.01	0.02	0.00
40	0.28	0.21	0.15	0.07	-0.02	-0.01
50	0.23	0.11	0.06	-0.02	-0.13	-0.08
60	0.19	0.02	0.05	-0.08	-0.20	-0.03
70	0.07	-0.09	-0.08	-0.12	-0.35	-0.12
80	0.12	-0.19	0.13	-0.17	-0.28	0.18

Table 2 Coefficients of the 1st degree calibration polynomials

	TC1	**TC2**	**TC3**	**TC4**	**TC5**	**TC6**
a	0.0016	-0.0008	0.0017	0.0012	-0.0033	-0.0001
b	0.1069	0.126	-0.0347	-0.1087	0.0119	-0.0975

Using the correction functions will result in more uniform temperature distribution (smaller difference between thermocouple readings) for single phase and zero heat flux, which is closer to the ideal situation where all thermocouple measurements are equal.

The insulation of the test section minimizes heat loss. Previous tests have shown that at ~ 60 °C the insulated test section has a higher surface temperature (~0.63 °C) compared with un-insulated test section. Table 3 shows the difference between averaged RTD and averaged thermocouple at different fluid temperatures, for the insulated test section.

Table 3 Difference between averaged RTD measurement and averaged thermocouple measurements

Tref (°C)	**10**	**20**	**30**	**40**	**50**	**60**	**70**	**80**
T_{RTD}-T_{TC} (K)	-0.06	-0.06	0.00	-0.11	-0.03	0.01	0.15	0.10

Note that at temperatures higher than 60 °C the RTDs indicate a systematically higher temperature than the thermocouples, suggesting that that heat losses may decrease the thermocouple temperature readings by 0.1-0.15 °C.

2. Circumferential temperature variation in eccentric heated tubes

Tubes used in heat transfer experiments have some circumferential variation in wall thickness, which result in small temperature variations between thermocouples located at the same axial position, but different circumferential position. This wall thickness variation is usually due to a slight eccentricity of the outside diameter w.r.t. the inside test section diameter.

In order to assess the effects of this asymmetry, a simple geometrical analysis of eccentricity has been performed (see Figure 2).

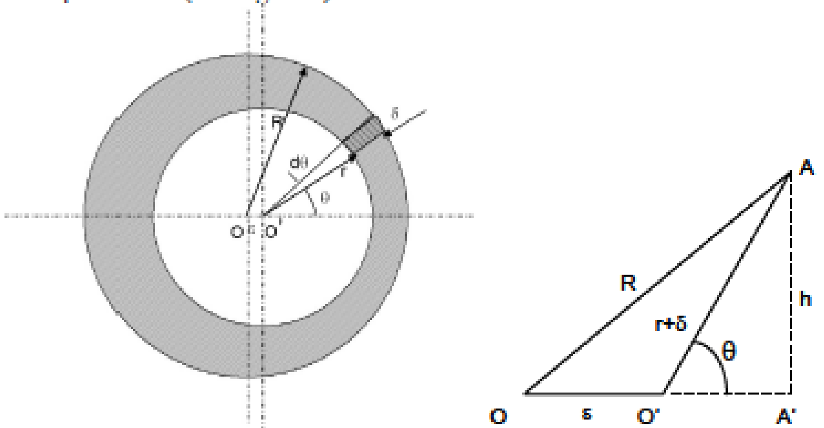

Figure 2 Test section eccentricity

If the outside radius of a test section is R and the inside radius is r, in the ideal situation the both circles are concentric so the wall thickness (δ) is the same regardless the circumferential position (angle θ). For a small eccentricity ε (defined as the distance between the centers of inside and outside circles), the wall thickness varies with θ. The wall thickness can then be expressed as a function of R, r and θ. Considering the triangle OO'A, where O is the center of circle with radius R and O' is the centre of the circle with radius r and A is an arbitrary point on the test section surface angular coordinate θ and applying Pythagora theorem, we have:

$$(\varepsilon + O'A')^2 + h^2 = R^2 \quad (1)$$

$$O'A' = (r+\delta)\cos\theta \quad (2)$$

$$h = (r+\delta)\sin\theta \quad (3)$$

Combining Eq. (1) (2) and (3) and solving for δ we obtain:

$$\delta = \sqrt{R^2 - (\varepsilon\sin\theta)^2} - \varepsilon\cos\theta - r \quad (4)$$

Indeed, checking the wall thickness at some particular points where it is known (such as θ= 0 or 180 deg) we obtain δ=R−ε−r and δ=R+ε−r which confirms the correctness of eq. 4.
For very small eccentricities (one order of magnitude less than r, ε<0.5 mm) the product $(\varepsilon \sin\theta)^2$ can be neglected, hence the expression of wall thickness is simplified as:

$$\delta = R - r - \varepsilon\cos\theta \quad (5)$$

Assuming that the geometry parameters and material properties do not change in axial direction of the test section, the voltage applied to it is U and the electric resistivity is ρ, the volumetric heat source is:

$$dq_v = \frac{dP}{dV} = \frac{U^2}{\rho L^2} \quad (6)$$

The surface heat flux is:

$$q_s = q_v\left(\frac{R+r}{2r}\right)\delta = \frac{U^2}{\rho L}\left(\frac{R+r}{2r}\right)\delta \tag{7}$$

From equations (6) and (7) it can be seen that the local surface heat flux (q_s) is proportional to the local wall thickness δ but the volumetric heat generation rate q_v is independent of wall thickness. Because of proportional relation between q_s and δ, a variation of few percent in wall thickness (3-4% are typical values) will results in practically the same variation in the surface heat flux. This is detected by slightly different readings of thermocouple located at the same axial position, but at different angles. The difference between thermocouple readings will increase with the heat flux.

Another factor that may influence the local surface heat flux is the non-uniformity in the material composition which may results in a non-uniformity in thermal conductivity and electrical resistivity. This additional uncertainty is considered negligible compared to the impact of a typical 3-4% variation in wall thickness

The heat conduction equation for a tubular geometry with internal heat sources and neglecting heat loss, is:

$$T_{wi} - T_{wo} = (R^2 - r^2)\frac{q_v}{4k} - \frac{q_v R^2}{2k}\ln\frac{R}{r} \tag{8}$$

or, as a function of wall thickness (δ),

$$T_{wi} - T_{wo} = (R + r)\cdot\delta\frac{q_v}{4k} - \frac{q_v R^2}{2k}\ln\frac{R}{r} \tag{9}$$

The wall temperature drop can be expressed as a function of outside tube radius R and tube wall thickness δ :

$$\Delta Tw = \frac{q_v(R^2 - r^2)}{4k} - \frac{q_v R^2}{2k}\ln\frac{R}{r} = \frac{q_v(R+r)(R-r)}{4k} - \frac{q_v R^2}{2k}\ln\frac{R}{R-\delta} \tag{10}$$

$$\Delta Tw(\delta) = \frac{q_v(2R-\delta)\delta}{4k} - \frac{q_v R^2}{2k}\ln\frac{R}{R-\delta} \tag{11}$$

The temperature difference between two thermocouples located at different circumferential positions (but the same axial location) ΔT_{WO}, having local wall thickness $\delta_1$and δ_2 respectively is given by:

$$\Delta T_{WO} = \frac{q_v R^2}{2k}\ln\frac{R-\delta_2}{R-\delta_1} + \frac{q_v}{4k}\left[2R(\delta_2 - \delta_1) + (\delta_1 - \delta_2)(\delta_1 + \delta_2)\right] \tag{13}$$

If we assume that δ_1 and δ_2 are located at the opposite side of the test section (180° apart) then average between δ_1 and δ_2 is the nominal wall thickness δ_0:

$$\delta_0 = \frac{\delta_1 + \delta_2}{2} \tag{14}$$

Solving equations (13) and (14) we can find the unknown δ_1 and δ_2, respectively.
Experimental measurements performed to determine outside wall temperatures at different heat fluxes are shown in Table 4 and graphically in Figure 3:

Table 4 Corrected outside wall temperatures as function of averaged surface heat flux

q_s, kWm^{-2}	q_v kWm^{-3}	T_{WO1} °C	T_{WO2} °C	T_{WO3} °C	T_{WO4} °C	T_{WO5} °C	T_{WO6} °C	Observations
151.57	102210	80.92	77.15	79.28	75.35	77.42	73.72	Single phase
154.78	104380	82.24	78.43	80.69	76.56	78.76	74.94	
156.49	105530	82.96	79.10	81.40	77.42	79.53	75.61	
158.12	106630	83.68	79.72	81.86	77.98	80.12	76.11	
159.78	107750	84.32	80.37	82.61	78.59	80.79	76.87	
161.44	108870	83.38	81.04	83.38	79.31	81.46	77.54	
165.18	111390	83.81	81.92	83.48	80.74	83.04	79.01	
166.37	112190	84.00	82.20	83.71	81.07	83.55	79.49	
167.89	113220	84.05	82.40	83.79	81.45	84.12	80.09	
171.22	115460	84.24	82.71	84.07	82.34	83.91	81.08	
174.17	117450	84.52	83.04	84.37	82.70	84.08	81.94	
176.59	119080	84.63	83.17	84.45	82.95	84.30	82.38	
178.09	120100	84.76	83.38	84.55	83.07	84.41	82.63	
181.12	122140	84.98	83.51	84.86	83.41	84.72	82.99	
185.94	125390	85.22	83.84	85.14	83.65	84.96	83.33	
190.28	128320	85.43	84.13	85.28	83.85	85.18	83.67	
195.71	131980	85.82	84.33	85.61	84.21	85.50	83.99	Fully developed nucleate boiling
205.97	138900	86.45	84.89	86.24	84.82	86.15	84.63	
225.82	152280	87.75	86.09	87.46	85.82	87.38	85.59	

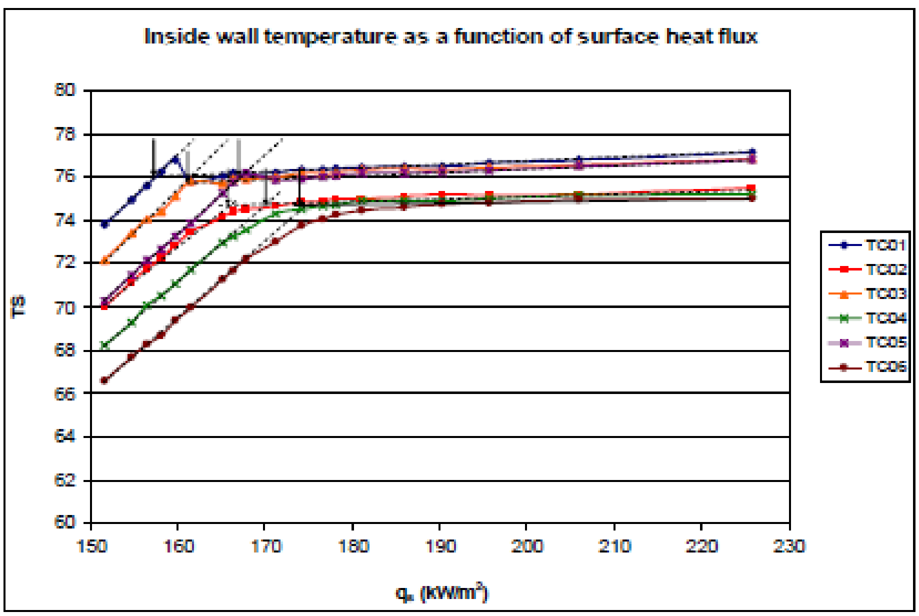

Figure *3 Corrected inside wall temperatures as function of averaged surface heat flux*

3. Estimation of wall thickness using fully developed nucleate boiling

The last three rows of Table 4 were considered representative of fully developed nucleate boiling; therefore they were used for estimating of wall thickness:

Table 5 Average qs, qv, nominal ΔT across the wall, wall conductivity and outside measured temperature for fully developed nucleate boiling

q_s, kWm^{-2}	q_v, kWm^{-3}	ΔT_0 K	K_s $Wm^{-1}K^{-1}$	T_{WO1} °C	T_{WO2} °C	T_{WO3} °C	T_{WO4} °C	T_{WO5} °C	T_{WO6} °C
195.71	**131980**	8.01	13.815	85.82	84.33	85.61	84.21	85.50	83.99
205.97	**138900**	8.43	13.819	86.45	84.89	86.24	84.82	86.15	84.63
225.82	**152280**	9.24	13.825	87.75	86.09	87.46	85.82	87.38	85.59

Starting from Table 5 and taking the nominal wall temperature drop (ΔT_0) corresponding to nominal wall thickness (δ_0) one can estimate the inside wall surface temperature T_{wi}. For the current experiment the wall inside temperature for each thermocouple location is calculated in Table 6 as $T_{WOi}-\Delta T_0$, i=1 to 6:

Table 6 Estimated inside wall temperature (°C), for nominal conditions (no eccentricity)

q_s, kWm^{-2}	q_v, kWm^{-3}	T_{WI1} °C	T_{WI2} °C	T_{WI3} °C	T_{WI4} °C	T_{WI5} °C	T_{WI6} °C
195.71	**131980**	77.81	76.32	77.60	76.20	77.49	75.98
205.97	**138900**	78.02	76.46	77.81	76.39	77.72	76.20
225.82	**152280**	78.51	76.85	78.22	76.58	78.14	76.35

Note the systematic difference between even and odd thermocouple value, explained by the wall thickness difference, since during nucleate boiling the difference between inside wall surface temperatures should be much smaller. If at one geometric location (i.e. TC1) the heat flux is increased, the variation of outside surface temperature is given by the variation of temperature drop inside the tube wall plus the increase in the inside wall temperature. Because the wall thickness is generally constant for a given angle, hence the wall temperature drop is proportional to q_s (or q_v) the radial conduction component can be deducted and the inside wall temperature can be estimated. Even if the real inside wall temperature can not be known at this stage, its variation with q_s can be found with good accuracy.

Eqn. 7 showed that the surface heat flux is proportional to wall thickness; therefore a difference of few percent in wall thickness will produce a similar difference in heat flux. The contribution of this component can be evaluated by calculating the slope dT_{WI}/dq_s using data from Table 6. The average slope is 0.018 °C/kW/m^2, therefore a variation of 10 kW/m^2 in heat flux (which is roughly 5%) will increase the inside wall temperature on average by 0.18 °C, which is much smaller than the corresponding change in temperature drop across the wall. Therefore for the first estimate of wall thickness this may be neglected (this assumption may be not true if the wall thickness is very thin) . Using equation (13) and (14) and assuming that the inside wall temperatures are equal (neglecting the influence of wall superheat on heat flux, for the first iteration only) one finds:

Table 7 First estimation of wall thickness

Position	TC1	TC2	TC3	TC4	TC5	TC6
Thickness [mm]	1.270	1.165	1.267	1.168	1.270	1.165

For the second iteration, the local surface heat flux can be estimated rewriting eq (7) in the following form:

$$q_{sloc} = q_{savg}\frac{\delta}{\delta_0} \qquad (15)$$

Using the wall thickness obtained from the first iteration, one can calculate the local surface heat flux using eq (16). The results are shown in Table 8:

Table 8 Local surface heat flux at 2nd iteration

q_{savg}, kWm^{-2}	Local surface heat flux q_s (kWm^{-2})					
	TC1	TC2	TC3	TC4	TC5	TC6
195.71	204.1	187.2	203.3	187.8	203.5	187.6
205.97	214.9	195.2	213.6	195.7	213.8	195.6
225.82	235.4	216.3	234.8	216.6	235.1	216.5

The difference in surface heat flux between opposite thermocouple and the corresponding difference for the inside wall temperatures (calculated by multiplying the difference in heat fluxes and the average slope 0.018 °C/kWm^{-2}) are shown in Table 9:

Table 9 Difference in heat flux and nucleate boiling temperatures between two opposite sides of test section

$\Delta q=q_1-q_2$ (kWm^{-2})	$\Delta q=q_3-q_4$ (kWm^{-2})	$\Delta q=q_5-q_6$ (kWm^{-2})	$\Delta T_{NB\,1\text{-}2}$(K)	$\Delta T_{NB\,3\text{-}4}$(K)	$\Delta T_{NB\,5\text{-}6}$ (K)
16.9	16.1	17.2	0.30	0.29	0.31
17.8	16.1	17.1	0.32	0.29	0.31
19.1	18.7	20.2	0.34	0.34	0.36

As it can be noticed the differences in surface temperatures due to differences in local surface heat flux are relatively small but they can be accounted for in order to achieve a better estimation of wall thickness. For the next iteration the temperature difference due to different heat fluxes at the opposite sides of the tubes is not neglected, but corrected with values estimated in Table 9. Applying the procedure explained above, the final estimation of wall thickness is shown in Table 10 (there is no difference between the 3rd and 4th iteration):

Table 10 Third and fourth iteration of wall thickness

Position	TC1	TC2	TC3	TC4	TC5	TC6
Thickness [mm]	1.261	1.174	1.259	1.176	1.262	1.173

4. Estimation of wall thickness using onset of nucleate boiling (ONB)

This method is based on the fact that at the ONB the wall superheat (T_{wi}-T_{sat}) is relatively small and can be predicted by empirical correlations (such as Davis and Anderson (1966), see eq. 16). Because the wall superheat is small, even if the correlation is not very accurate, the error in the temperature prediction is also relatively small. The ONB test was performed at system pressure P=2386.9 kPa and G=3060 kgm^{-2}s^{-1}.

$$q_{wONB} = \frac{k_l h_{fg} \ \rho_v (\Delta T_w)^2}{8\sigma T_{sat}} \tag{16}$$

To detect the ONB the power to test section was increased in very small steps and multiple scans were taken at each power level.

If ONB is used to calculate the wall thickness, one should be aware of the fact that the ONB starts towards the end of the heated length and advances upstream as the surface heat flux increases; therefore the ONB heat flux depends on the axial and circumferential location of the thermocouple on the test section. Examining Figure 6 one can notice that first ONB point is found at TC1 - the most downstream and located on the higher heat flux side of the test section. The next ONB is found at the TC2 and TC3, respectively. It can also be noticed that on the even side (2-4-6, lower local heat flux) the sudden wall temperature reduction typical for the ONB is not as obvious as for the odd side (1-3-5). The experimental data for ONB are presented in Table 11:

Table 11 Onset of nucleate boiling (ONB), corrected wall temperature, predicted wall superheat and wall thickness

Location	TC1	TC2	TC3	TC4	TC5	TC6
qs_{avg} at ONB	157.31	166.37	161.44	171.22	166.37	176.59
T_{WO}	83.55	82.35	83.53	82.49	83.70	82.53
Tsat	75.47	75.46	75.46	75.46	75.47	75.47
ΔT_{ONB}	0.99	1.01	1.00	1.03	1.01	1.04
T_{WI}	76.46	76.47	76.46	76.49	76.48	76.51
ΔT_{wall}	7.09	5.88	7.07	6.00	7.22	6.03
δ (mm)	1.271	1.137	1.255	1.133	1.250	1.12

T_{WO} was corrected by 0.15 °C to compensate heat loss, as explained in Section 1. Unlike other methods, the ONB wall thickness estimation is performed based on wall superheat correlation at each thermocouple location, which requires very accurate estimation of outside wall temperature. For the first iteration a perfectly symmetric (no eccentricity) tube was considered. Knowing the average heat flux and fluid properties, one can estimate the wall superheat at ONB for TC1-TC6. For the second iteration, starting from wall thickness calculated at the previous step and using equation (15), q_{sloc} is found; with q_{sloc} we recalculate wall superheat at ONB and find the final value of wall thickness (Table 12):

Table 12 Second iteration for wall thickness using ONB

Location	TC1	TC2	TC3	TC4	TC5	TC6
qs_{avg} at ONB	157.31	166.37	161.44	171.22	166.37	176.59
q_{sloc} at ONB	163.32	155.37	166.41	159.34	170.81	162.45
T_{WO}	83.55	82.35	83.53	82.49	83.70	82.53

Tsat	75.47	75.46	75.46	75.46	75.47	75.47
ΔT_{ONB}	1.01	0.98	1.01	0.99	1.03	1.00
T_{WI}	76.48	76.44	76.47	76.45	76.50	76.47
ΔT_{wall}	7.07	5.91	7.06	6.04	7.2	6.06
δ (mm)	1.27	1.14	1.255	1.136	1.249	1.122

5. Assessment of wall thickness using single phase data

For single phase data the following four experimental data were selected (see Table 13):

Table 13 Average q_s, q_v, nominal ΔT across the wall, wall conductivity and outside measured temperature (°C) single phase regime

q_{s} kWm^{-2}	q_{v} kWm^{-3}	ΔT_0 K	K_s W/mk	T_{WO1}	T_{WO2}	T_{WO3}	T_{WO4}	T_{WO5}	T_{WO6}
151.57	102210	6.21	13.800	80.92	77.15	79.28	75.35	77.42	73.72
154.78	104380	6.34	13.801	82.24	78.43	80.69	76.56	78.76	74.94
156.49	105530	6.41	13.802	82.96	79.10	81.40	77.42	79.53	75.61
158.12	106630	6.48	13.802	83.68	79.72	81.86	77.98	80.12	76.11

It is assumed that for the above range of heat fluxes, the heat flux has little effect of the local heat transfer coefficient. In order to assess the local heat transfer coefficient, an average inside wall temperature is calculated between opposite TC. The local bulk fluid temperatures are calculated based on the measurements of RTD located at the inlet and outlet of the test section as follows:

$$T_z = T_{in} + \frac{T_{out} - T_{in}}{L_h} z \tag{17}$$

From the correlation:

$$q_{s\,loc} = h(T_{WI\,loc} - T_f) \tag{18}$$

and using the estimated inside wall temperatures calculated based on nominal temperature drop, q_{sloc} is calculated and is tabulated below (Table 14):

Table 14 Estimated local heat flux

q_{savg}	Local surface heat flux qs (kWm^{-2})					
kWm^{-2}	TC1	TC2	TC3	TC4	TC5	TC6
151.57	159.69	143.40	159.97	143.12	159.45	143.69
154.78	162.98	146.53	163.60	145.91	162.90	146.65
156.49	164.85	148.12	165.01	147.96	164.84	148.13
158.12	166.73	149.51	166.49	149.75	166.69	149.51

Using equation (7) , and the local surface heat flux and assuming that q_v is constant regardless of the location, one may calculate the local wall thickness (Table 15):

Table 15 Estimated local wall thickness after first iteration

q_{savg}	Wall thickness (mm)

kWm^{-2}	TC1	TC2	TC3	TC4	TC5	TC6
151.57	1.283	1.152	1.285	1.150	1.281	1.154
154.78	1.282	1.153	1.287	1.148	1.281	1.154
156.49	1.283	1.152	1.284	1.151	1.282	1.152
158.12	1.284	1.151	1.282	1.153	1.283	1.151

With the new wall thickness, the iterative process described above is repeated until the wall thickness for two consecutive iterations became very close. Table 16 summarizes wall thickness obtained at subsequent iterations until convergence is reached:

Table 16 Local wall thickness (mm) at subsequent iterations

TC1	TC2	TC3	TC4	TC5	TC6
Third iteration					
1.268	1.167	1.270	1.166	1.266	1.169
1.267	1.178	1.271	1.171	1.268	1.179
1.266	1.167	1.267	1.166	1.267	1.168
1.270	1.168	1.266	1.169	1.268	1.166
Fourth iteration					
1.263	1.170	1.266	1.169	1.262	1.172
1.263	1.171	1.267	1.165	1.264	1.172
1.262	1.169	1.263	1.168	1.263	1.170
1.265	1.170	1.262	1.171	1.264	1.168
Fifth iteration					
1.265	1.170	1.268	1.169	1.263	1.172
1.265	1.171	1.268	1.165	1.266	1.172
1.264	1.169	1.265	1.168	1.265	1.170
1.267	1.170	1.263	1.171	1.265	1.168

One can notice that the fourth and fifth iterations are reasonably close; therefore the final result is taken by averaging wall thickness values from the fifth iteration.

6. Direct measurements

Direct measurement of the wall thickness was performed using an electronic caliper having 0.01 mm accuracy. In order to obtain a better estimate of the wall thickness, the measurement were repeated seven times and averaged. They are presented in Table 17:

Table 17 Results of wall thickness measurement (mm) using an electronic caliper

Location	Measurement #							Average (mm)
	1	2	3	4	5	6	7	
TC1-3-5	1.26	1.25	1.25	1.24	1.26	1.25	1.25	**1.25**
TC2-4-6	1.17	1.18	1.17	1.18	1.17	1.17	1.19	**1.18**

In addition to the caliper measurement, a photographic method was also employed. A 15 mm long slice of the test section was cut, the edges chamfered and several photos (see Figure 4) were taken

with a Sony DSC H2 digital camera. The resolution was set at 6 MP. The clearest photos were magnified, and digitally processed to enhance the contrast and printed. Wall thickness measurements were performed with an electronic caliper (0.01mm accuracy) on the printed photos. The blue marks in Figure 4 represent thermocouple locations. Although a ruler was included in the picture, the scaling was based on the outside diameter of the test section (Do=8.020 mm), which was measured with a mechanical caliper having 0.0013 mm accuracy.
The results of the photographic measurement are shown in Table 18 , along with a summary of the results obtained with all the other previously-described methods:

Table 18 Summary of wall thickness estimation

Method	Wall thickness (mm)		Observations
	Avg(1-3-5)	Avg(2-4-6)	
Direct (caliper)	1.250	1.180	Precision limited to 3 significant digits (depending on the caliper accuracy) Cannot be used in the middle of test section.
Photographic	1.240	1.140	Affected by optical distortions, smooth edges and scaling errors Cannot be used in the middle of test section
Single phase	1.265	1.170	Slow convergence, seems less accurate than boiling methods.
ONB	1.258	1.133	Fastest convergence. For the even side of test section (low heat flux) is difficult to determine with acceptable accuracy the ONB. Because of weak dependence of wall superheat on heat flux, this method may be more suitable for irregular geometries than other methods
Nucleate boiling	1.261	1.174	Moderate convergence, good accuracy.

7. Conclusions

1. The proposed method can be a valuable tool for determining the circumferential heat flux variation in directly heated tubes, cooled internally or externally as is done frequently in thermalhydraulic studies employing tubes as fuel element simulators.
2. The proposed method will also provide confirmation for mechanical, ultrasonic or photographically based wall thickness measurement methods, and may well be more accurate than these conventional method.
3. The method is based on the principle that for directly heated tubes, cooled internally, the single phase heat transfer coefficient (or the wall superheat in nucleate boiling or at ONB) is uniform around the circumference and is therefore independent of the variation in wall thickness.
4. This method is applied to a R-134a cooled tube. After careful calibration of the surface thermocouples located on the insulated side of the test section, the inside wall temperature is evaluated using the simple Fourier equation applied to a directly heated annulus. The variation in surface heat flux to the coolant is also evaluated.
5. The three analytical methods for evaluating the wall thickness variation (based on (i) single phase heat transfer data (ii) nucleate boiling data and (iii) ONB data) have been compared to two direct methods (direct caliper measurements, and photographic-based measurements). The agreement between these five methods is good.

6. The direct measurements confirm that the proposed analytical methods are an accurate method for determining the circumferential wall thickness variation.
7. The proposed methods are thought to be especially valuable for thermalhydraulic studies where a nominally uniform wall thickness can have a variation of ±5% and will results in a similar variation in surface heat flux. A more accurate knowledge of the actual circumferential wall thickness will permit for a more precise measurement of CHF and PDO heat transfer coefficient.

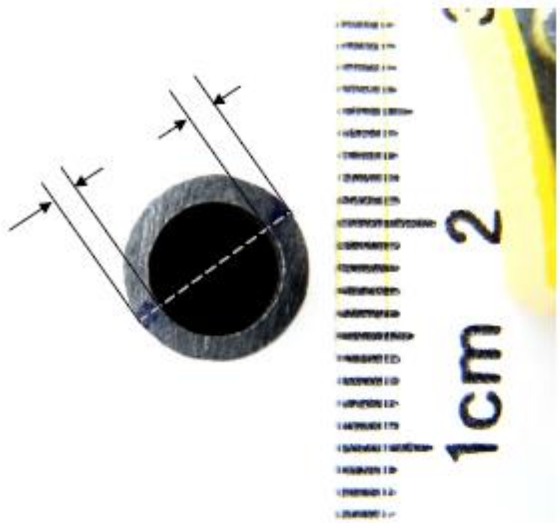

Figure 4 Magnified photo of the end of the test section

8. References

[1] Corsan, J.M., Budd, J.N., and Hemminger, W.F., An intercomparison involving PTB and NPL of thermal conductivity measurements on stainless steel, Inconel and Nimonic alloy reference materials, and an iron alloy, 12th European Conference on Thermophysical Properties, Vienna, Austria, 1990

[2] Davis, E.J., Anderson, G.H., The incipience of nucleate boiling in forced convection flow, AIChE Journal 12 (4), 774–780, 1966.

[3] Incropera, F.P. and DeWitt, D.P., Fundamentals of Heat and Mass Transfer, Fourth edition, 1996.

[4] National Instruments – Measurement and Automation Catalogue, 1999.

[5] Tavoularis, S., Measurements in Fluid Mechanics, Cambridge University press, 2005.

APPENDIX C: PRELIMINARY INVESTIGATION OF THE EFFECT OF FLOW OBSTACLES ON SINGLE PHASE HEAT TRANSFER

EXPERIMENTAL INVESTIGATION OF FLOW OBSTACLES EFFECT ON SINGLE PHASE HEAT TRANSFER

A. Tanase*, D.C. Groeneveld†*, H. Zahlan* and S.C. Cheng *

*University of Ottawa, Ottawa, ON Canada K1N 6N5
†Atomic Energy of Canada Limited, Chalk River, ON Canada K0J 1J0

Abstract

Previous experimental studies of the effect of flow obstacles on heat transfer in bundles suggest an analogy between the increased pressure drop at the flow obstacle, and the enhancement in wall heat transfer. Right behind the blockage, the flow decelerates and turbulent wakes are generated. The wakes agitate the wall boundary layer and enhance the heat transfer from the wall.

It was generally assumed that that heat flux, mass flux and shape of the flow obstruction do not play a major role on the heat transfer enhancement. To investigate these effects, an experiment was performed at the University of Ottawa's Thermalhydraulics Laboratory. The test section consisted of a directly heated Inconel 600 tube having inside diameter of 5.46 mm and the outside diameter of 8.00 mm, cooled internally by Freon 134a. The outside temperature of the test section was measured by six K type thermocouples, located in pairs, 180 deg apart at three planes. A flow obstacle, having a 24% obstruction ratio, was located inside the test section. A strong ceramic magnet, located on the outside of the test section, fixed the location of the obstacle, and allowed the relocation of the obstacle circumferentially and axially during the experiments. The heat transfer enhancement effect downstream of the obstacles was measured at 3 , 5, 7, 10, 20, 30, 50 and 70 diameters downstream the flow obstacle. Two obstacle leading and trailing edge shapes (streamlined and blunt, having the same obstruction ratio, 24%), four mass fluxes and six heat fluxes were investigated.

1. Introduction

Several experimental studies of the flow obstacle effect on heat transfer have been performed on bundle geometries. References [1-5], [9], [10], [13] discuss the analogy between the increased pressure drop at the flow obstacle such as a grid spacer, and the enhancement in wall heat transfer. Just downstream of the obstacle, the flow decelerates and turbulent wakes are generated. The wakes agitate the wall boundary layer and enhance the heat transfer from the wall. For simplicity, [13] assumed that the wake induced heat transfer augmentation is directly proportional to the obstacle pressure drop. Assuming that this assumption is valid, the equation for heat transfer augmentation due to the flow obstacles will be of a similar form as that for the pressure drop increase caused by the obstacle. This increase in heat transfer can be explained by a gradual contraction of the flow upstream of the obstacle. Using Equation 1, [9] correlated the maximum heat transfer augmentation at the obstacles on smooth rods in single-phase flow as

$$Nu/Nu_0 = 1+5.55\ \varepsilon^2 \qquad \text{Eqn. 1}$$

Where ε is the flow blockage ratio and Nu_0 is the Nusselt number for a channel without any flow obstacles. The Nusselt numbers reach a maximum at, or slightly downstream of the flow obstacle. Further downstream the hydrodynamic and thermal boundary layers are slowly approaching their fully developed profiles. This developing boundary layer phenomenon is similar to the entry length effect in turbulent tube flow. The augmentation of heat transfer has been observed to be an exponentially decaying function of z/D where z is the distance downstream of the obstacle.

$$Nu^* = Nu/Nu0 = 1+5.55\ \varepsilon^2 \exp(-0.13\ z/D) \qquad \text{Eqn. 2}$$

for Reynolds number higher than 10^4. Equation 2 shows a typical variation in heat transfer enhancement downstream of a bundle spacer for various flow blockage ratios. The results of [13] clearly show that there is an influence of the Reynolds number on the maximum and on the axial distribution of the Nusselt numbers for different blockage factors. The improvement in heat transfer due to the obstacle decreases with increasing Reynolds numbers for Re > 3000. For the same Reynolds number, the improvement in heat transfer is higher for higher flow blockage ratios. The reason is that higher flow blockage ratios produce higher flow velocities and turbulence resulting in a greater improvements in heat transfer [3]. The correlation proposed by [13] - Equation 2 - is applicable for a specific type of grids and does not take into account the obstacle-location effect on heat transfer enhancement

More recently, the authors of [8] have investigated the impact of various flow obstacles on single phase heat transfer, film boiling heat transfer and pressure drop based on internally cooled tube data. This paper describes the film boiling experiment with an obstacle-equipped tube and presents a new method for predicting the enhancement in heat transfer (expressed as Nu/Nu_0) for both the single-phase gas-cooled region and the post-dryout heat transfer region.

2. Experimental setup

The experiment was conducted in the multi-fluid test loop at University of Ottawa (Figure 1) using HFC-134a as working fluid. The main components of the loop are test section, condenser, pressurizer, pumps, preheaters, power supply and related instruments.

The test section is directly heated by a 12 kW DC power supply (40V, 300 A). The inlet and outlet fluid temperatures of the test section are measured by two RTDs. The flow is recirculated by two gear pumps, installed in series, and delivering a constant volumetric flow rate.

A bypass around the pumps controls the flow rate. The flow is measured by a Coriollis flow meter with an accuracy of better than 0.5% (flow range 0 – 0.34 kg s^{-1}). The pressure in the loop is controlled by the pressurizer. The pressurizer contains a heating coil, located at the bottom of the pressurizer, and a cooling coil near the top of the pressurizer. The power to the pressurizer heater (maximum 500 W) is regulated by an adjustable AC transformer. An electric pre-heater (maximum power 5 kW) and a coaxial heat exchanger (with hot water on the secondary side) are located between the pumps and the test section. They are used to adjust the test section inlet fluid temperature or inlet mass quality to the desired values. The vapour generated in the test section is condensed by a coaxial heat exchanger prior to the fluid being recirculated to the pump.

The experiment was performed in a DC heated Inconel 600 tube having an inside diameter of 5.46 mm, the outside diameter of 8.00 mm, and a heated length is Lh = 2 m. The experimental loop consists of two gear pumps, connected in series, two preheaters, mass flow measuring device, test section (see Figure 1), condenser (for two-phase flow experiments), pressurizer, filter and the recirculation valves. RTDs measure the bulk fluid temperature at the inlet and outlet of the test section(TS), a piezoelectric pressure sensor measures the absolute pressure at the outlet of TS, and a differential pressure sensor measures the ΔP along the TS.

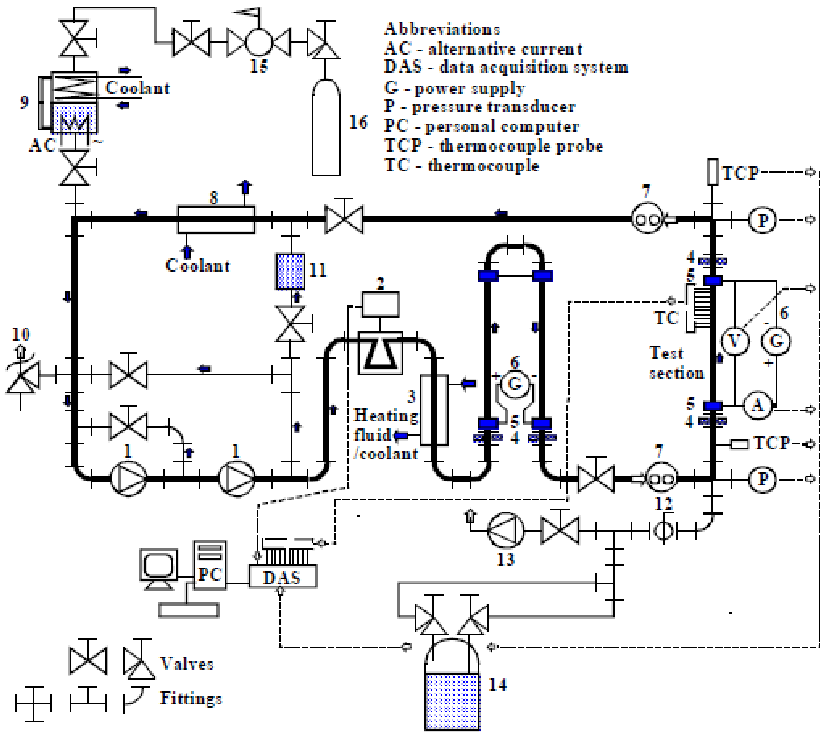

1-gear pump, 2-Coriollis type mass-flow-meter, 3-pre-heater, 4-dielectric fittings, 5-power terminals, 6-electrical pre-heater, 7-sight glass, 8-condenser, 9-pressurizer, 10-pressure relief valve, 11-refrigerant filter-dryer, 12-ball-valve, 13-vacuum pump, 14-refrigerant storage tank, 15-pressure reducer, 16-nitrogen container.

Figure 1 Experimental Multi-Fluid Loop (Vertical Test Section).

The outside temperature of the test section was measured by six K-type self-adhesive thermocouples (TC), located in pairs 180° apart at three planes (blue triangles in Figure 2). A flow obstacle, having a 24% obstruction ratio, was located inside the test section. A strong ceramic magnet, located on the outside of the test section, fixed the location of the obstacle. The obstacles have cylindrical shape, a length of 10 mm and a diameter 2.72 mm; they are manufactured from mild steel and located eccentrically in the test section (see Figure 2).

The L/D effect was measured at 3, 5, 7, 10, 20, 30, 50 and 70 diameters downstream from the flow obstacles. Two obstacle shapes (streamlined and blunt), four mass fluxes and six heat fluxes were investigated. The test matrix is shown in Table 1:

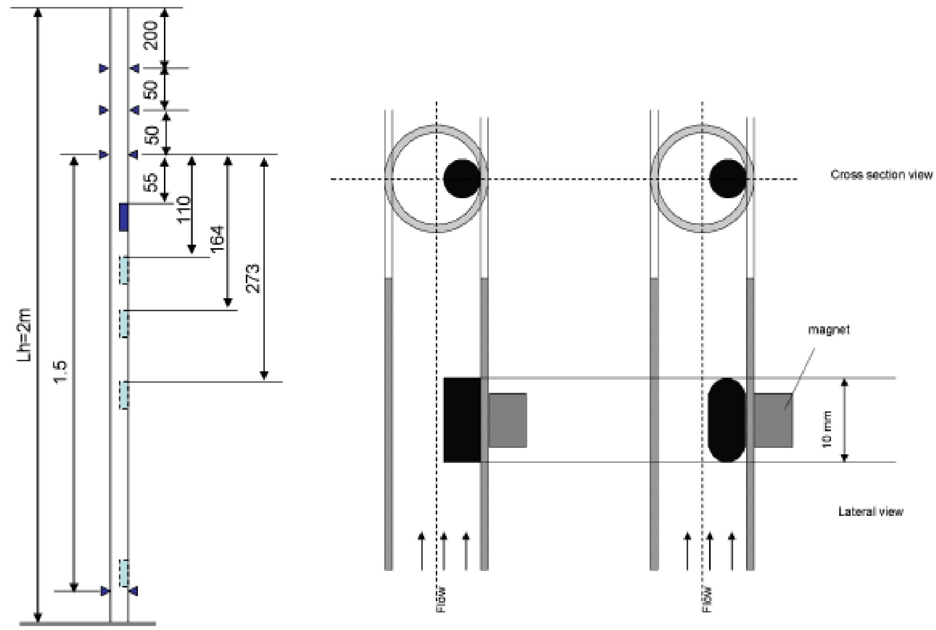

Figure 2: The schematic of test section, thermocouples and the obstacle layout

Table 1: Test matrix

G (kg m^{-2} s^{-1})	500			1000			2000			3500		
q_s (kW m^{-2})	10	15	20	15	20	35	20	35	60	35	60	120

The inlet fluid temperature for all experiments was 20 °C. The experimental procedure followed these steps:

1. Set the inlet temperature at 20 °C
2. Set the required mass flux
3. Place the obstacle far upstream from the TC locations (more than 100 L/D), in order to obtain the bare tube geometry. It is assumed that, for L/D > 100, no axial effect of obstacle on heat transfer is observed.
4. Set the required heat flux and wait for the system to reach steady conditions. If needed, the mass flux is readjusted.
5. Scan and record the reference (bare tube) data (take 10-15 scans, to be screened and averaged during the subsequent data processing)
6. While keeping the heat flux and mass flux steady, move the obstacle to 70 L/D upstream from the TC line. Scan and save.
7. Repeat (6) for all L/D considered in the test matrix.

2.1 Calibration and verification

Every three months the RTDs and thermocouples were re-calibrated using a single phase flow without heating the test section, two–phase inlet without heating the test section and at the onset of nucleate boiling method. The calibration tests confirmed an accuracy of 0.25 °C for an interval between 20 and 80 °C. In order to confirm the results, some tests were repeated randomly.

3. Results and discussion

The experimental results for two types of obstacles (round and blunt) having the same obstruction ratio, 24% are presented in Figure 3.

3.1 Effect of obstacle shape.

The obstacle shape has a significant influence at relatively short distances downstream obstacle (~ 3L/D). At low mass flux (500 kg $m^{-2}s^{-1}$) the blunt obstacle gives higher relative enhancement (42-50% for blunt shape compared to 32-38% for rounded) for the heat flux range investigated. The difference decreases as the mass flux increases and at G=1000 kg $m^{-2}s^{-1}$ although the blunt obstacle enhancement is still higher, the difference is less significant. At higher mass flux (approx 2000 kg $m^{-2}s^{-1}$) the round-shape obstacle seems to have noticeable higher relative enhancement that increases as the mass flux increases.

3.2 Effect of mass flux.

As mentioned by previous work, the relative heat transfer coefficient enhancement is dependent on Reynolds number of flow and, therefore, on the mass flux. For both types of obstacle and for all heat fluxes investigated the relative heat transfer coefficient enhancement decreases with increasing the mass flux, which confirm the previous findings. A novel finding from this research is that the variation of heat transfer enhancement with flow for blunt-type obstacles (from about 50% to 17%) is much larger than for rounded obstacles (from 35% to 27%).

3.3 Effect of heat flux.

It appears that the effect of heat flux is not significant, mixed trends have been noted but no clear effect can be found.

3.4 Effect of relative distance.

It has been reported previously ([1], [4], [10]) that the relative enhancement decays exponentially downstream from an obstacle. This is also confirmed by the observed trends of Figure 3, where it is shown that the enhancement becomes negligible at about L/D > 50 regardless of mass flux, heat flux or obstacle shape. An "unusual" trend occurs at L/D ~ 5 for the blunt shape obstacle (and to a smaller extent also for the rounded obstacle) at high mass flux, when a sudden decrease of relative enhancement is observed just downstream the obstacle. Although this effect is not specifically documented in the literature, it can be assumed that it is caused by the structure of the flow in the wake of a blunt obstacle. The investigators agreed that at the obstacle location the mechanism of convective heat flux enhancement is due to flow acceleration due to cross section reduction. At several relative distances downstream the flow deceleration occurs but the turbulence induced by the obstacle mixes the bulk fluid and the boundary layer, enhancing heat transfer. At high velocities flow separation at the trailing edge of the obstacle could have occurred and it appears that at several relative distances downstream obstacle the flow deceleration and/or flow reversal due to low pressure wake or large eddies which adversely affects the local heat transfer enhancement. For the current experiment the above mentioned effect becomes first noticeable at G = 2000 kg $m^{-2}s^{-1}$ and is much stronger for the blunt obstacle. Figure 3 shows that G=2000 kg $m^{-2}s^{-1}$ the maximum relative increase is at L/D = 3 but at L/D = 5-7 there is a local minimum followed by another local maximum at L/D = 10. This suggests that the wake region lasts for about 10 L/D, after which the diverted streamlines reattach to the heated wall and enhances the heat transfer coefficient (second relative maximum). At G = 3500 kg $m^{-2}s^{-1}$ the maximum heat transfer enhancement is at L/D = 5 for the rounded obstacle and at L/D = 10 for the blunt one. These effects will be investigated further by subsequent measurements, CFD simulations and/or flow visualization (see Figure 4).

3.5 Comparison with the available prediction methods.

A direct comparison with Rehme's (1977) equation for heat transfer enhancement (Eqn.2) has been performed and suggests that this correlation underpredicts the relative enhancement in most cases (see Figure 3). The underprediction is greatest at low mass fluxes and becomes smaller as the mass flux increases. These results were somehow expected because the experiment suggests that the mass flux and the obstacle shape play also a significant role in the relative heat transfer enhancement, while Rehme's equation ignores these effects. Moreover, Rehme's equation can not predict the "unusual" trends found in the wake of an obstacle at high mass fluxes; therefore a more accurate prediction method is desirable.

3.6 Pressure loss coefficient (K) and relative heat transfer enhancement.

A supplementary investigation has been conducted in order to estimate the pressure loss coefficient for different types of obstacles (12% and 24% obstruction ratio, blunt and rounded flow obstacles). The experiments have been performed in adiabatic (zero heat flux) single phase flow and revealed a weak dependence of K in respect to Re: as Re increases, K decreases slightly (see Figure 5 a). From the same investigation it was found that the difference between the pressure loss coefficient for blunt and rounded obstacles is very high for the whole range of mass flux considered (1400 – 3500 kg $m^{-2}s^{-1}$). Although a significant difference in pressure loss coefficient between blunt and rounded obstacles was noticed, the difference in enhancement of heat transfer coefficient is minor. Moreover, it appears that at high flows, although the difference in K is high, at L/D>10 the relative enhancement is very close for both types of obstacles and at L/D<10 the rounded obstacle gives even better heat transfer augmentation (see Figure 5 b). It can be concluded that unlike two-phase flow, where the critical heat flux enhancement is strongly influenced by the obstacle shape, for the single phase the difference is minor, especially at L/D>10. Also, the hypothesis of proportionality between the pressure drop and the heat transfer enhancement, although intuitive and convenient may be questionable, at least for some geometries/flow conditions. As previously mentioned, the enhancement mechanisms downstream of an obstacle are very complex and new experiments and analysis should be performed to improve our understanding and to confirm the current findings.

4. Conclusion.

The present study is focused on the effect of obstacle shape, mass flux, heat flux and relative distance on the enhancement of heat transfer coefficient in a round tube. As reported in previous papers, flow obstacles significantly enhance the downstream heat transfer, the strongest effect being near the obstacle location. The heat transfer enhancement decays exponentially with distance downstream of the flow obstacle. A novel finding is that the enhancement decreases with an increase in mass flux for a constant L/D. The present experiment shows that the enhancement effect can be found up to 50 L/D, for various mass fluxes, obstacle shapes and heat fluxes. Unlike the blunt obstacle, the rounded obstacle shows relatively constant heat transfer enhancement over a large range of mass fluxes. The heat flux has a weak effect on relative heat transfer enhancement. The available prediction methods tend to underpredict the current experimental data.

5. References

1. Groeneveld, D.C., Yousef, W.W., Spacing devices for nuclear fuel bundles: a survey of their effect on CHF, post-dryout heat transfer and pressure drop. In: Proceedings of the ANS/ASME/NRC International Topical Meeting on Nuclear Reactor Thermal-Hydraulics, vol. 2, Saratoga Springs, New York, NY, October 5–8, pp. 1111– 1125. 719, 1980

2. Guo, Y., Groeneveld, D.C. and Cheng, S.C., Prediction of CHF enhancement due to flow obstacles, *Int. J. Heat Mass Transfer,* Vol 44, pp. 4557-4661, 2000

3. Hassan, M.A., Rehme, K., Heat transfer near spacer grids in gas-cooled rod bundles. Nucl. Technol. 52, 410– 414. 721, 1981

4. Hudina, M., Nothigen, H., Experiment Study of Local Heat Transfer under and near Grid Spacers Developed for GCFR, Swiss Federal Institute for Reactor Research Wirenlingen. Report TM-IN-526, 1972

5. Kidd, G.J., Hoffman, H.W., The Temperature Structure and Heat Transfer Characteristics of an Electrically Heated Model of a Seven-Rod Cluster Fuel Element, ASME 68-WA/HT-33, 1968.

6. Krett, V., Majer, J.,Temperature Field Measurement in the Region of Spacing Elements. Skoda Works
Nuclear Power Construction Department, Information Centre Plzen, Czechoslovakia. Report ZJE-114. 1971

7. Oka, Y., S. Koshizuka, T. Jevremovic and Y. Okano, Supercritical-pressure, light-water-cooled reactors for mproving economy, safety, plutonium utilization and environment", Prog. Nucl. Energy, Vol. 29 (supplement), pp. 31-438, 1995.

8. Pioro, I.L., Groeneveld, D.C., Cheng, S.C., Doerffer, S., Vasic, A.Z., Effect of flow obstruction shape on the critical heat flux. In: Proceedings of ICONE-8, Baltimore, MD, April 2–6, (paper #8350),2000

9. Rehme, K., Pressure drop of spacer grids in smooth and roughened rod bundles. Nucl. Tech. 31, 314–317, 1977

10. Stosic, Z., On the role of spacer grids on conditions of dryout/rewetting and local thermal hydraulics in boiling water channels, NURETH-9, San Francisco, California, Oct. 3 – 8, 1999

11. Tsiklauri, G., R. Talbert, B. Schmitt, G. Filippov, R. Bogoyavlensky and E. Grishanin, "Supercritical steam cycle for nuclear power plant", Nucl. Eng. Des., Vol. 235, pp. 1651-1664, 2005.

12. Vleck, J., Weber, P.,. The Experimental Investigation of A Local (Spot) Heat Transfer Coefficient in The Fuel Spacer Area. Australian Atomic Energy Commission Research Establishment Report LIB/TRANS 250, 1970

13. Yao, S.C., Hochreiter, L.E., Leech, W.J., Heat transfer augmentation in rod bundles near grid spacers. Heat Transfer 104 (1), 76–81. 778, 1982

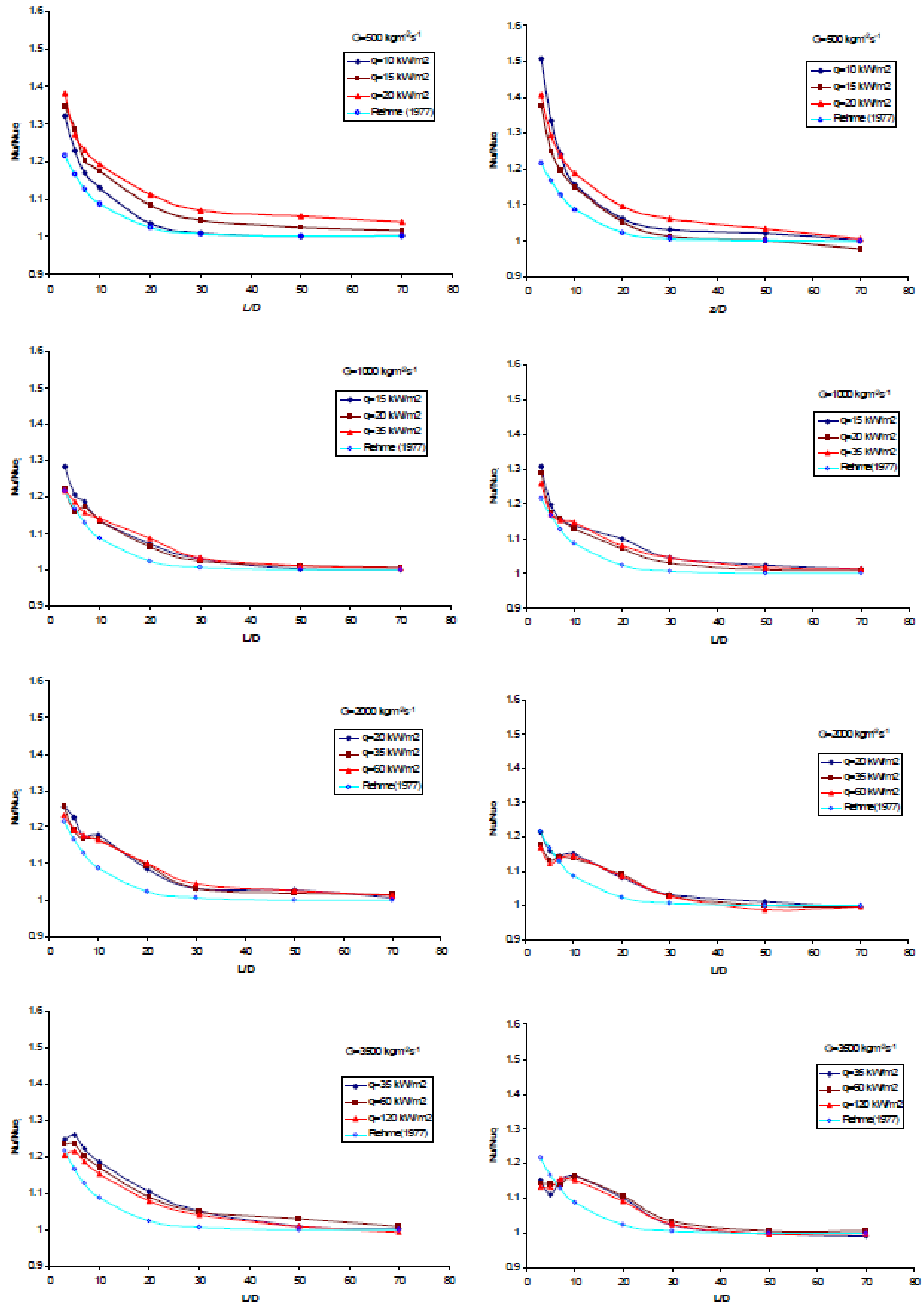

Figure 3 Nu/Nu_0 (enhanced/bare) versus relative distance (L/D) for various mass flux and heat flux, round shape obstacle (left) and blunt shape obstacle (right), 24% obstruction ratio.

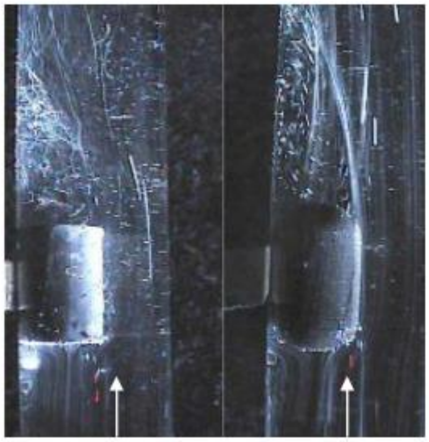

Figure 4 Flow visualization around blunt and rounded obstacle, Re~ 3000, upward flow direction

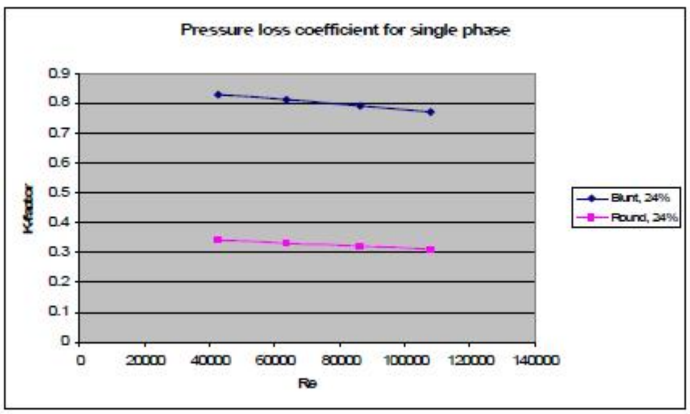

a)

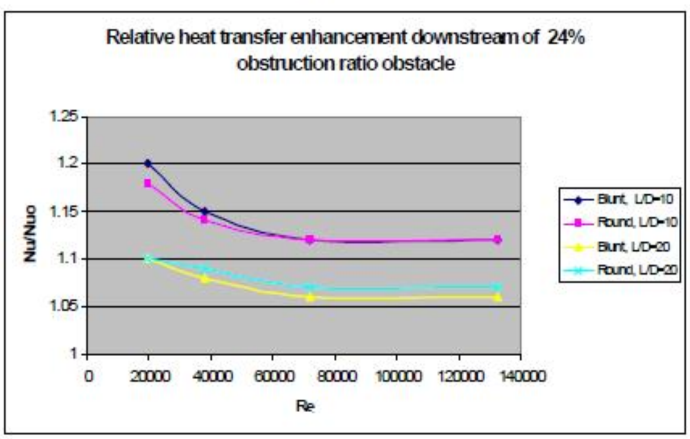

b)

Figure 5 Variation of pressure loss coefficient and the relative heat transfer enhancement in respect to Reynolds number

APPENDIX D: CFD SIMULATIONS USING the SST k-ω TURBULENCE MODEL

As described in Section 1, the main objective of the numerical simulations is to provide an assessment of the overall performance of some widely-used turbulence models, particularly the k-ω model. It was aimed to complement the experiments and to help improve the understanding of the experimental results. The selection of the turbulence model was impacted by the following considerations:

a) *Practicability* – DNS or more elaborated turbulence models, such as LES or RSM typically provide fairly accurate results; however, they are computationally expensive and more difficult to implement for practical applications than simple turbulence models. Therefore, for the current simulations only robust and inexpensive turbulence models, such as k-ε or k-ω were considered.
b) *Suitability and applicability* to the given geometry and flow conditions. The author of k-ω SST turbulence model (Menter, 1994) claimed that, due to modification of the eddy viscosity which accounts of the effect of the transport of the principal turbulent shear stress, the model leads to a major improvement in the predictions of adverse pressure gradients flows. These claims were confirmed by independent studies, such as those authored by Iaccarino (2001) and Zhang (2007).
c) *Availability* of the model in the CFD software package STAR-CCM+, 9.04 009, that was accessible at the University of Ottawa.

Numerical simulations were performed for the blunt (square-ended) cylinder (30B) and the rounded cylinder (30R), having hemispherical ends, 30% blockage ratios, at the bulk flow velocity of 1.1 ms^{-1} and Re=35,000. The computational domain had a length of 2000 mm and was divided axially in three sections: i) a section upstream the obstacle (section 1), ii) a section which contains the obstacle (section 2) iii) a section downstream the obstacle (section

3). The lengths of each axial section were 900 mm, 500 mm and 600 mm, respectively. The diameter was consistent with the inside diameter of the acrylic test section D = 31.75 mm. Figure D - 1 exemplifies a region of the computational mesh developed for the blunt square-ended cylinder (30B); the section which contains the obstacle is located between the upstream and downstream sections. A structured grid has been employed for the sections upstream and downstream of the obstacle. An unstructured grid was used for the section containing the obstacle; however, prism layers were imposed in the proximity of solid walls.

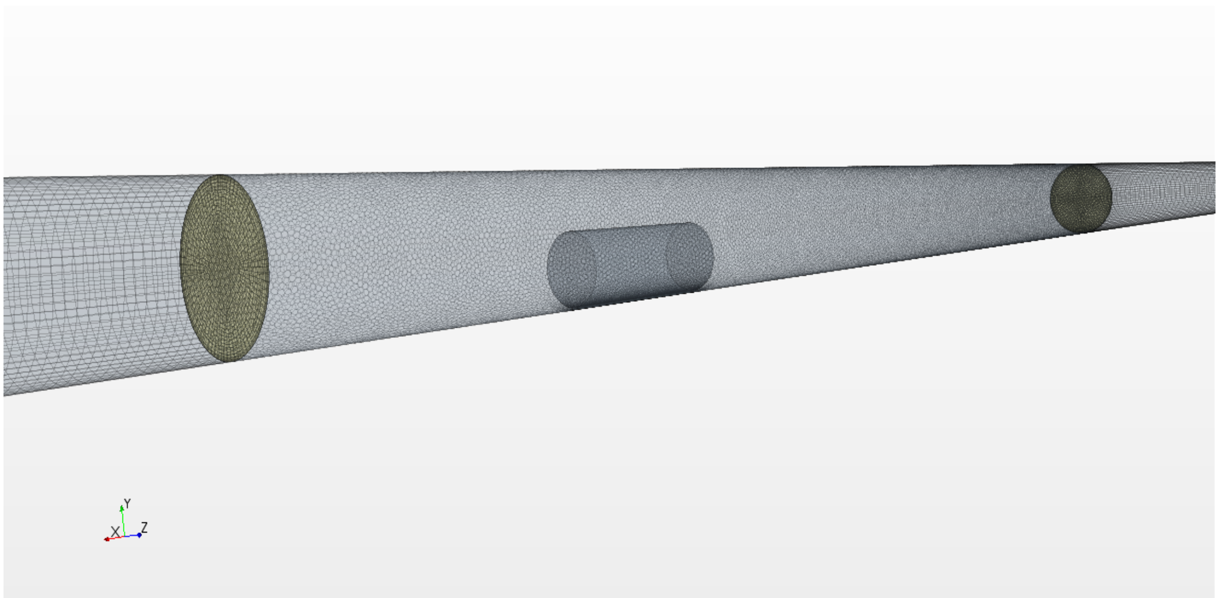

Figure D - 1 Example of a region of the computational mesh developed for the square-ended cylinder (30B).

Mesh convergence has been investigated by the development of three meshes - coarse, medium and fine - for each geometry, 30B and30R. Representative mesh sections and details .for 30B and 30R geometries are shown in Figures D-2 to D -6.

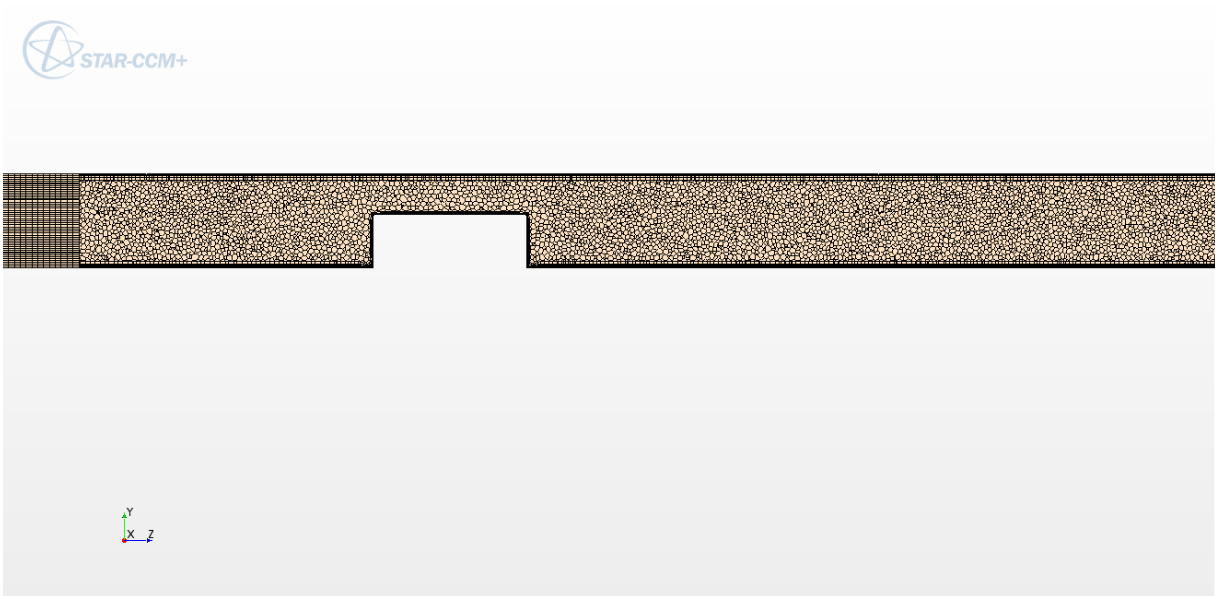

Figure D - 2 Example of a mid-plane section of average mesh for 30B, with upstream structured section visible on the left.

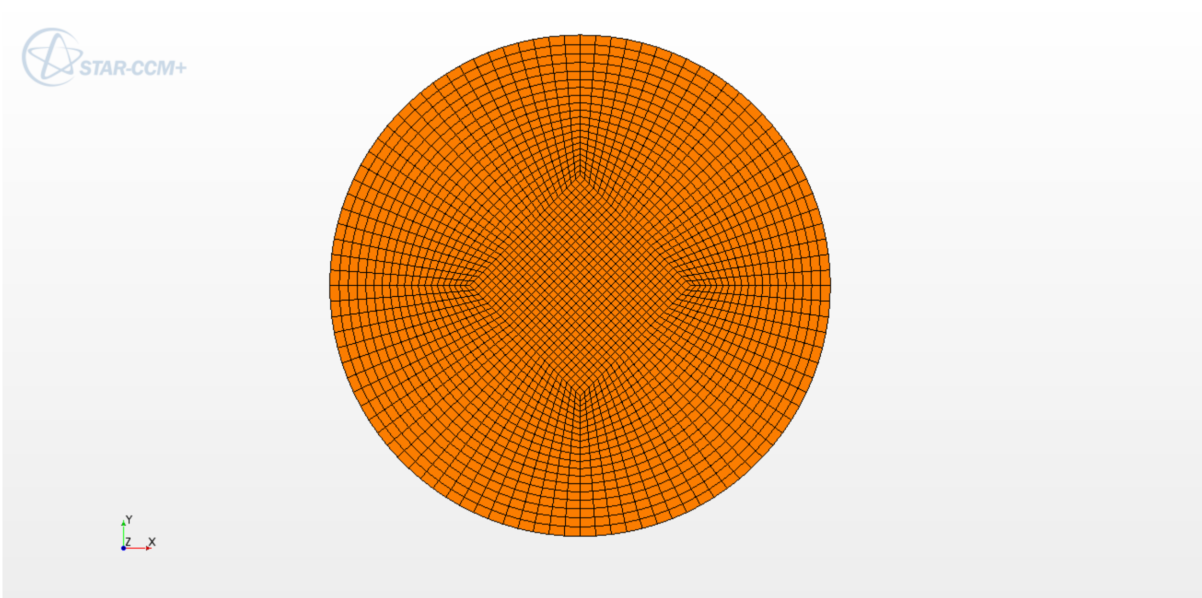

Figure D - 3 Example of structured mesh cross section at the inlet of the computational domain.

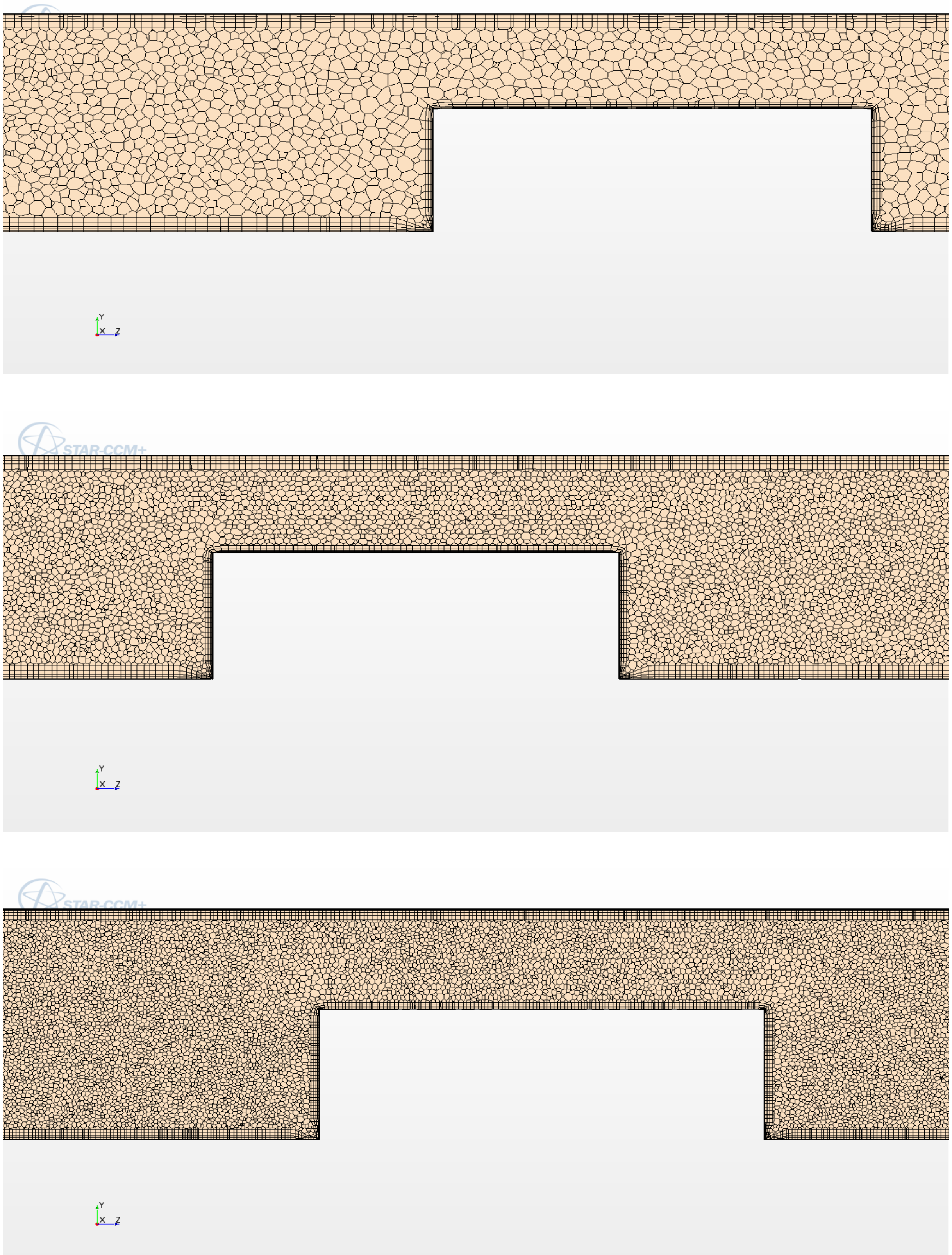

Figure D - 4 Details of the mid-plane section of unstructured mesh in the proximity of the 30B obstacle, coarse (top), average (middle) and fine (bottom).

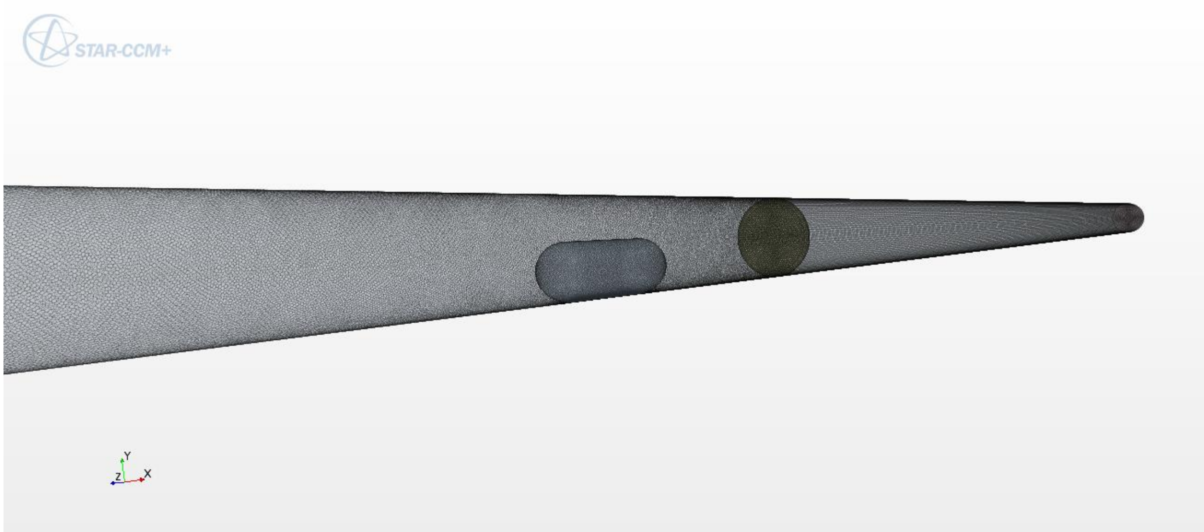

Figure D - 5 Example of a region of the computational mesh developed for the rounded-ended cylinder (30R).

The CFD software employed for numerical simulations was STAR-CCM+, 9.04 009, installed on a PC with AMD 64 CPU, OS Windows Vista version 6.0. Based on the rationale presented at the beginning of this section, the SST k-ω turbulence model was used. The numerical procedure employed by STAR-CCM+ software is the finite volume method, in which the partial differential equations are integrated over individual control volumes using the mathematical properties of surface integrals (i.e. Gauss divergence theorem). The fluxes at the surface of each finite volume are conserved throughout the domain. A second-order upwind numerical scheme for the continuity and momentum equations and first order upwind scheme for the turbulent kinetic energy and the turbulent energy frequency have been employed. Other options used for the computation were: segregated, isothermal, three dimensional flow. The segregated solver resolves the governing equations sequentially and obtains a converged solution by performing several iterations of the solution loop as the governing equations are coupled and non-linear. In the first iteration, the properties of the working fluid are based on the initialization solution (user defined initialization) and for every following iteration the fluid properties are updated based on the current solution. The temperature dependent fluid properties - IAPWS-IF97 (International Association for the Properties of Water and Steam[8]-Industrial Formulation 1997) were available as the default option in STAR-CCM+ and were used in the simulations. Current values for pressure and face mass fluxes are used to solve the three momentum equations in order to update the velocity field. These velocities may not satisfy the continuity equation locally and therefore an equation for the pressure correlation

[8] IAPWS is an international non-profit association of national organizations concerned with the properties of water and steam, particularly thermophysical properties, cycle chemistry guidelines, and other aspects of high-temperature steam, water and aqueous mixtures relevant to thermal power cycles and other industrial and scientific applications. Current Members are Britain and Ireland, Canada, the Czech Republic, Germany, Japan, New Zealand, Russia, Scandinavia (Denmark, Finland, Norway, Sweden), and the United States, plus Associate Members Argentina & Brazil, Australia, China, Egypt, France, Greece, Italy, and Switzerland.

derived from the continuity and linearized momentum equations is solved to obtain corrections to the pressure and velocity fields and the face mass fluxes. Equations for scalars such as turbulence kinetic energy are solved using the updated values of the other variables. If the solution is converged, the iteration process is stopped and if convergence criteria are not met, then the iteration process is continued. The convergence threshold for all residuals was 10^{-4}.The above mentioned options were applied for all cases simulated. The inlet boundary of the computational domain was defined as *velocity inlet* (used to define the velocity and scalar properties of the flow at inlet boundaries), whilst the outlet boundary was defined as a *pressure outlet*. The use of a pressure outlet boundary condition instead of an outflow condition often results in a better rate of convergence when backflow occurs during iteration (Ansys, 2006). The type and values of initial conditions are summarized in Table D - 1.

Table D - 1 Types and values of initial conditions

Turbulence specification	**intensity and length scale**
Turbulence intensity	0.05%
Length scale	0.03175 m
Inlet velocity	1.1 m/s
Outlet pressure	0 Pa

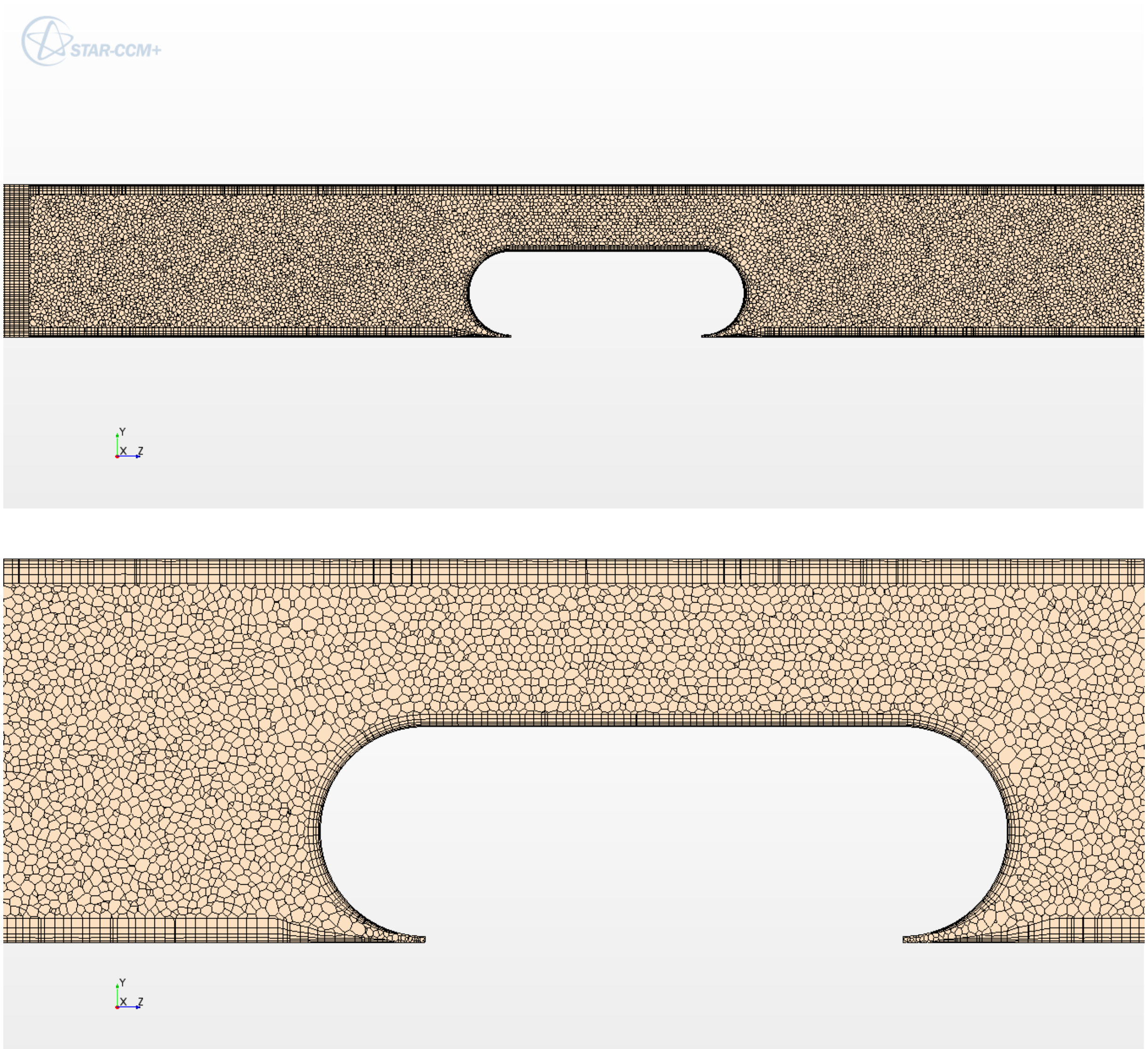

Figure D - 6 Example of a mid-plane section of the average mesh for 30R, with upstream structured section visible on the left (top) and detail in the proximity of the obstacle (bottom).

MESH PROPERTIES

In order to investigate mesh convergence, three meshes –coarse, medium and fine - were developed. The total cell numbers are presented in Table D-2 and their main features in Table D-3.

Table D - 2 Number of cells for 30B and 30R, coarse, medium and fine meshes

Mesh	30B	30R
Coarse	$1.09\cdot10^{6}$	$1.08\cdot10^{6}$
Medium	$2.53\cdot10^{6}$	$2.54\cdot10^{6}$
Fine	$4.74\cdot10^{6}$	$4.75\cdot10^{6}$

Table D - 3 Mesh main features

Section	Mesh type		Coarse	Medium	Fine
1,3	Structured	radial divisions	60	80	80
		distribution	One sided hyperbolic		
		spacing at start	$6\cdot10^{-4}$m		
		axial spacing source	$5\cdot10^{-3}$m		
		axial spacing target	$2\cdot10^{-3}$m	10^{-3}m	10^{-3}m
		stretching function	Two sided hyperbolic		
2	Unstructured	base size	$15\cdot10^{-4}$m	$8\cdot10^{-4}$m	$5\cdot10^{-4}$m
		number of prism layers	5		
		prism layer stretching	1.5		
		prism layer thickness	$2\cdot10^{-3}$m	$2\cdot10^{-3}$m	$1.5\cdot10^{-3}$m

RESULTS OF NUMERICAL SIMULATIONS

Pressure loss

Comparisons between the results of numerical simulations and experiments for the pressure differences between the pressure taps are presented in Figures D-7 (for the 30B obstacle) and D-8 (for the 30R obstacle). It is noted that the figures include simulation results from the three meshes described above. Figure D-7 shows that for the 30B the medium and fine meshes match the experimental data closer than the coarse mesh simulations, especially in the flow regions further from the obstacle. Numerical simulations for 30R show better convergence between the meshes, although they have a tendency to overestimate the pressure drop.

Pressure loss coefficient

Table D-4 presents obstacle pressure loss coefficients (K) for 30B and 30R, determined from the numerical simulations and comparisons with the results from the experimental measurements. The pressure loss coefficient was calculated according to the methodology described in Chapter 6. The results of numerical simulations for the 30B geometry indicate that the coarse mesh tends to overestimate the pressure loss coefficient by a significant amount, whilst the medium and fine meshes predicted values closer to the experimental data. These observations are consistent with Figure D-7. The results of numerical simulations for the 30R geometry show better agreement between the three meshes investigated; however, all simulation results tend to overestimate the measured K.

It is also noted that the measured axial and circumferential pressure profiles are satisfactorily matched by the simulations for all meshes investigated, which confirms that they were sufficient to capture the major flow features, such as flow stagnation upstream the obstacle, flow separation and reattachment, albeit with some differences. Although computationally more expensive, it appears that a finer mesh would be the best option when good accuracy of simulations is needed.

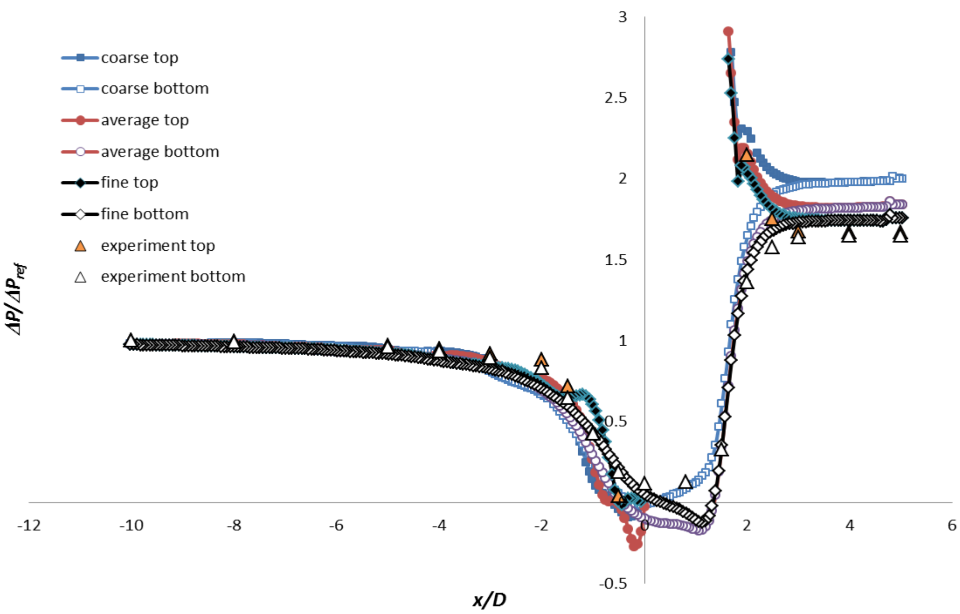

Figure D - 7 Comparison between the results of numerical simulations (coarse, average, fine meshes) and experiments for normalized *ΔP* between pressure taps (30B).

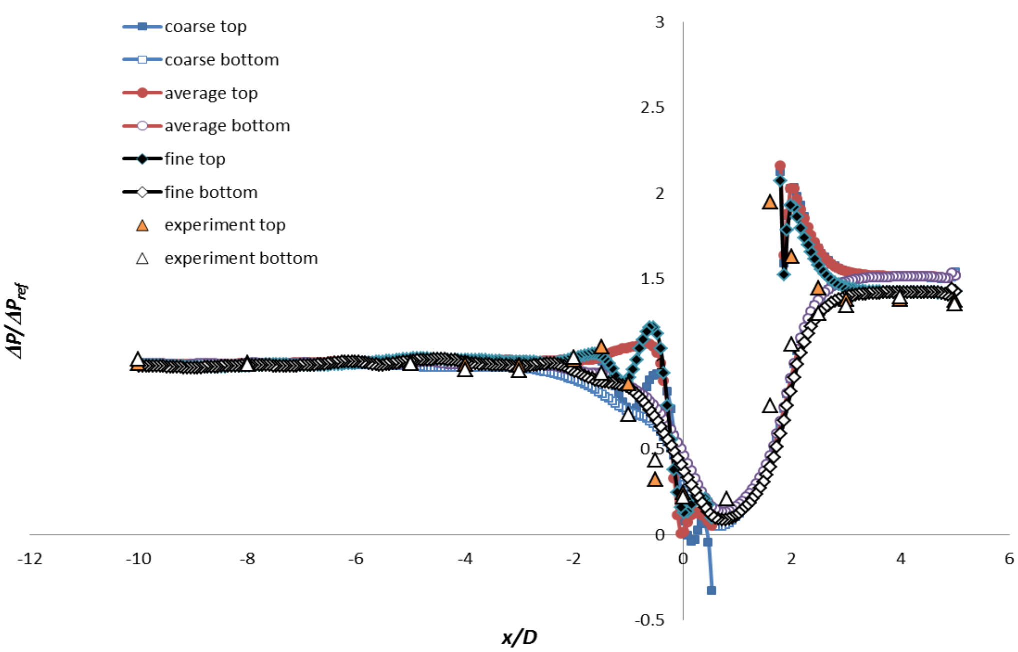

Figure D - 8 Comparison between the results of numerical simulations (coarse, average, fine meshes) and experiments for normalized *ΔP* between pressure taps (30R).

Table D - 4 Obstacle pressure loss coefficient (*K*) for 30B and 30R, Re=35,000.

Obstacle	**30B**		**30R**	
Mesh	Simulations	Experiment	Simulations	Experiment
Coarse	0.96	0.75	0.56	0.47
Medium	0.76		0.59	
Fine	0.79		0.53	

<u>Computed center plane streamwise velocity profiles</u>

The normalized center-plane streamwise-velocity profiles at various axial positions are plotted Figures D-10 to D-23 for the 30B and 30R obstacles. The PIV experimental values are plotted for comparison. The plots reveal excellent mesh convergence (i.e. coarse, medium and fine meshes) in the bare section of the simulation domain. In this region the results of numerical simulations were very close to the experimental values. At the flow section corresponding to the mid-length of the obstacle (see Figure D-12), good mesh convergence and very good agreement with the measurements was achieved far from the obstacle wall, whilst near the wall only the medium and fine meshes showed convergence. Furthermore, the simulations underestimated the experimental values.

Downstream from the 30B obstacle, in the flow recirculation region, the simulations showed acceptable agreement between the meshes and very good agreement with the experimental data. A particular situation is noted in Figure D-16, which shows the axial profile of the time-averaged streamwise velocity at 9D downstream from the trailing edge of the blunt obstacle. The measurements indicate that the flow is skewed towards the side of the obstacle due to the reattachment downstream from the obstacle, whilst the simulations predict flow skewness on the side of the test section away from the obstacle.

Similar to the blunt cylinder, upstream from the rounded obstacle, the agreement between the numerical simulations and the experiment is excellent as shown in Figures D-17 and D-18. Nevertheless, downstream from the 30R obstacle and in the recirculation region, the convergence between the coarse, medium and fine meshes was poor; also, the agreement between all numerical simulations and the experiment was poor, as illustrated in Figures D-20 and D-21. Figures D-22 and E-23 show that the agreement between the numerical simulations and the experiment improved with an increase of the distance from the obstacle. Unlike 30B, the flow skewness at 9D downstream the 30R was adequately predicted by the simulations.

Excellent mesh convergence and very good agreement between the simulations and experiments was observed in regions away from flow separation, flow recirculation and reattachment for both 30B and 30R obstacles.

Computed center plane turbulent kinetic energy

The normalized center-plane turbulent kinetic energy (TKE) profiles at various axial positions are plotted in Figures D-24 to D-37 for 30B and 30R, respectively. The agreement between the experiments and numerical simulations was very good in regions where separation, recirculation and reattachment did not occur, such as the bare test section. Just downstream from the trailing edge of 30B (see Figures D-26 and D-27), the convergence between the coarse, medium and fine meshes was poorer than in other regions of the flow. Also, in the wake of the 30B, in general, the numerical simulations underestimated the measured TKE. The difference between the simulations and measurements decreased as the distance downstream of the obstacle increased and flow recovered. Significantly larger discrepancies between the numerical simulations and the measurements were observed in the wake of the 30R, as illustrated by Figures D-25 to D-34. Similar to the 30B cases, the difference between the simulations and measurements decreased as the distance downstream from the obstacle increased.

A noteworthy observation is that the PIV measurements indicate that for Re=35,000 the normalized TKE in the wake of 30B and 30R were not identical but comparable; their peak values at 1/2D downstream of the trailing edge were approximately two orders of magnitude higher than the bare tube values, for both obstacle types. This observation is consistent with the results of heat transfer experiments, which indicated relatively small differences between heat transfer augmentation of 30B and 30R (Tanase and Groeneveld, 2015). However, the current numerical simulations predicted significantly lower TKE downstream of 30R than 30B.

The above mentioned observations outline some merits and limitations of the SST k-ω turbulence model for adiabatic turbulent flow in a round tube equipped with a flow obstacle.

Flow reattachment length

A parameter of paramount importance for studies of separated flows is the flow reattachment length. Most authors report the reattachment length as the distance from the trailing edge of a flow obstacle to the flow reattachment point, normalized by the obstacle height (H). A significant number of heat transfer studies report that the flow reattachment point corresponds to the location of maximum augmentation of heat transfer.

For the numerical simulations presented in this work, identification of flow reattachment was performed by plotting the wall shear stress and detecting the axial location where the stress equaled zero. This procedure is based on the observation that, at the reattachment point, the axial velocity crossed from negative (i.e. recirculation) to positive values. This indicated the downstream boundary of the recirculation vortex and, in conjunction with the time-averaged planar velocity flow maps, was identified as the reattachment of the flow to the test section wall.

To perform a meaningful comparison with the experimental data, the streamwise velocity at 1.8 mm from the test section wall was plotted as well. Because the reattached flow impinges the wall at an angle, the reattachment length derived from the streamwise velocity at 1.8 mm from the wall underestimates the reattachment length derived from the wall shear stress, and this is illustrated in Figure 7-3, which plots the normalized streamwise velocity and normalized wall shear stress predicted by numerical simulations, for obstacle 30R, and a fine mesh.

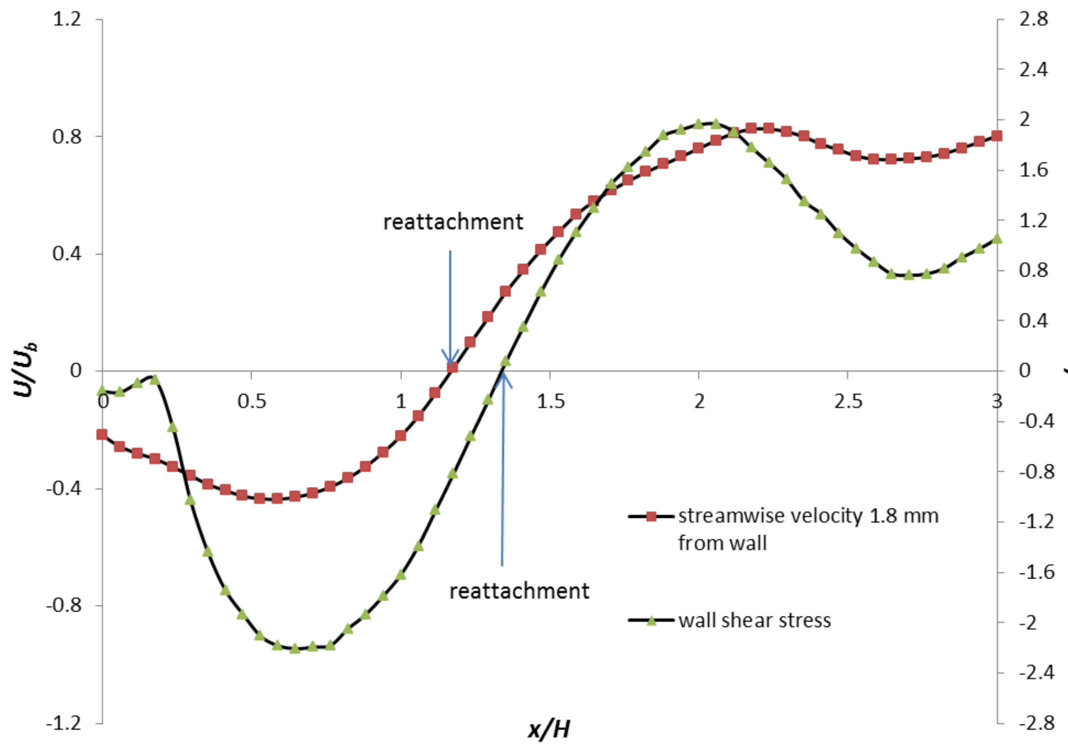

Figure D - 9 Identification of flow reattachment location from streamwise velocity and wall shear stress; 30R, fine mesh, Re=35,000.

Table D-5 summarizes the reattachment lengths determined from numerical simulations along with the experimental values for 30B and 30R, at Re=35,000. The values marked with * denote the values derived from the streamwise velocity at 1.8 mm from the wall. Data from Table D-2 indicates that for both obstacle types the fine mesh provides the closest predictions to the experimental measurements. It is also noted that for obstacle 30B the simulation results obtained from the coarse and medium meshes overestimate the experimental values, whilst the results from the fine mesh underestimate them. For 30R, all simulation results underestimate the experimental values, the closest match being noted for simulations using the fine mesh.

Flow reattachment length normalized by obstacle height (H) for 30B and 30R, Re=35,000.

Obstacle	**30B**			**30R**		
Mesh	Simulations		Experiment	Simulations		Experiment
Coarse	2.82	2.53*	2.06	1.12	0.94*	1.3
Medium	2.94	2.76*		1.35	1.06*	
Fine	2.01	1.76*		1.35	1.18*	

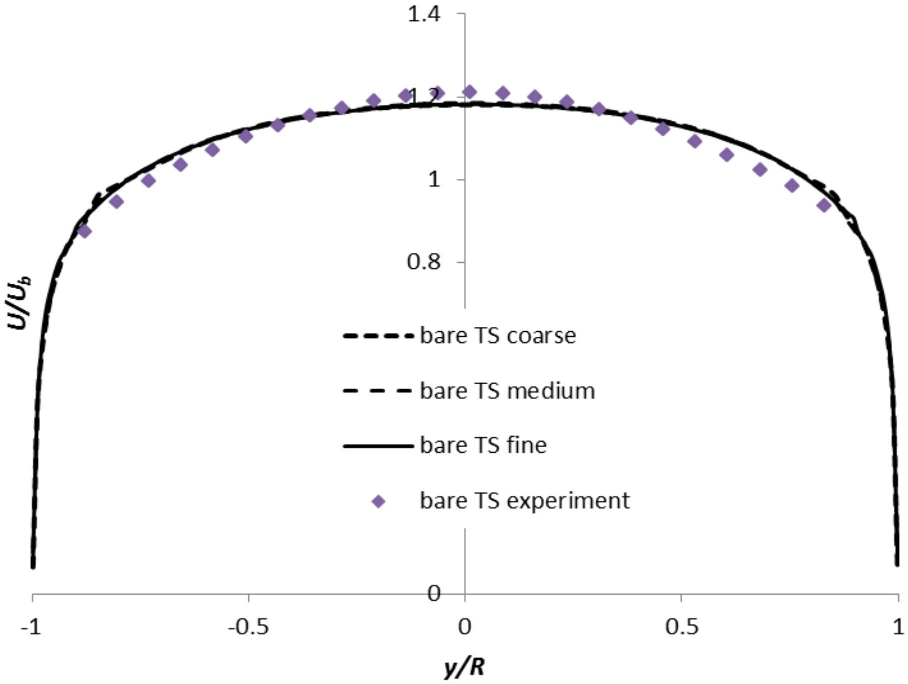

Figure D - 10 Computed normalized streamwise centerplane velocity, fully developed flow bare test section, Re=35,000.

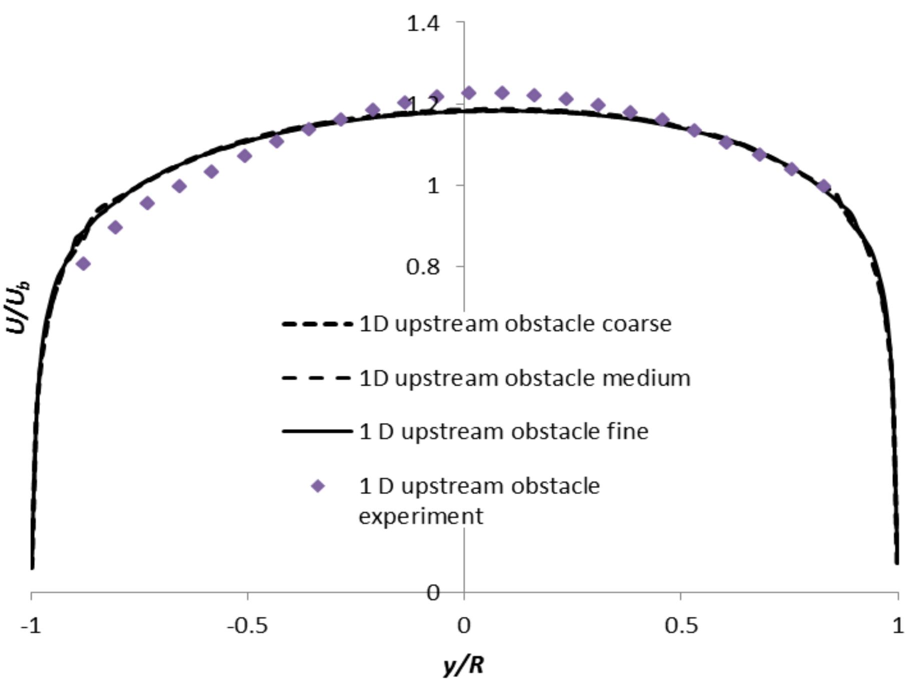

Figure D - 11 Computed normalized streamwise centerplane velocity, at 1D upstream the 30B obstacle, Re=35,000.

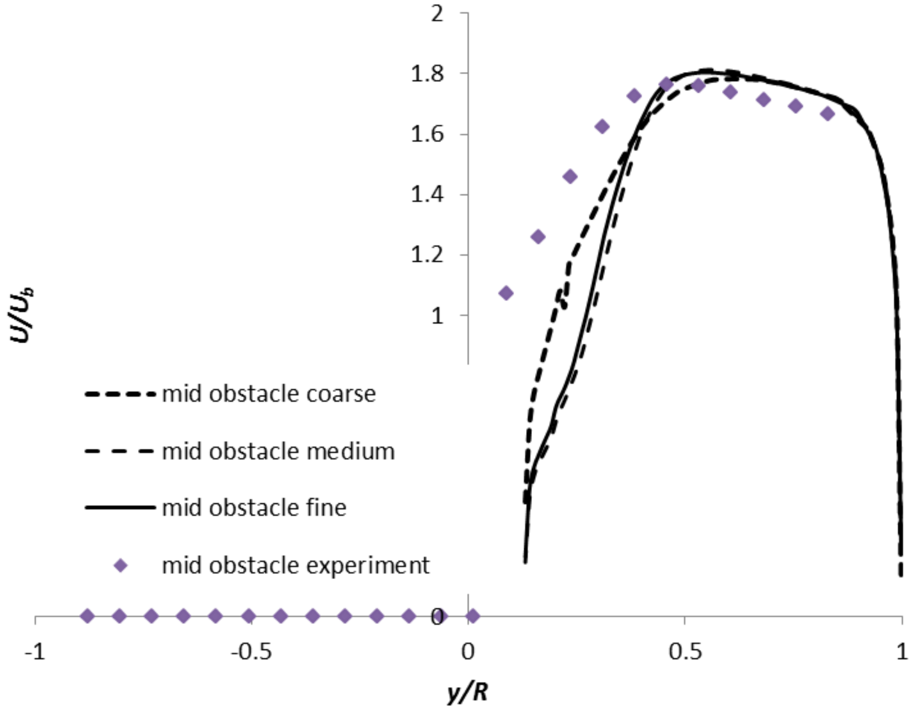

Figure D - 12 Computed normalized streamwise centerplane velocity, at mid of 30B obstacle, Re=35,000.

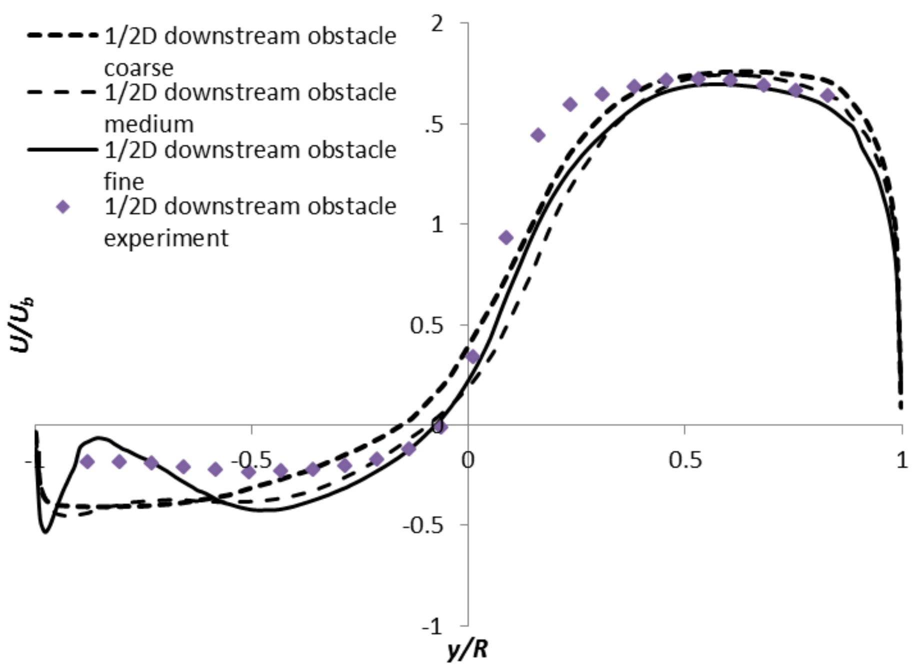

Figure D - 13 Computed normalized streamwise centerplane velocity, at 1/2D downstream 30B obstacle, Re=35,000.

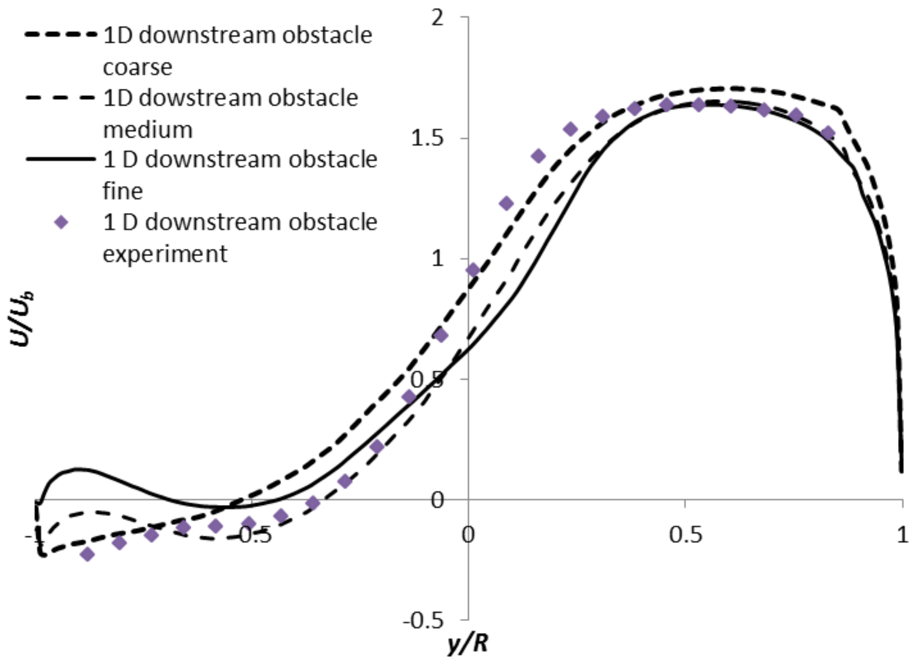

Figure D - 14 Computed normalized streamwise centerplane velocity, at 1D downstream 30B obstacle, Re=35,000.

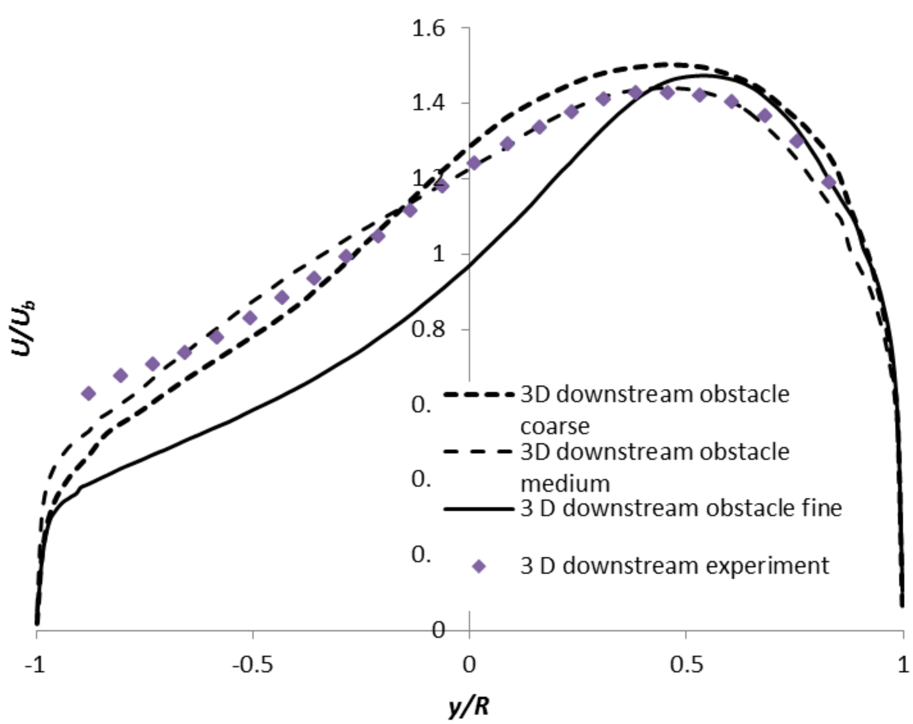

Figure D - 15 Computed normalized streamwise centerplane velocity, at 3D downstream 30B obstacle, Re=35,000.

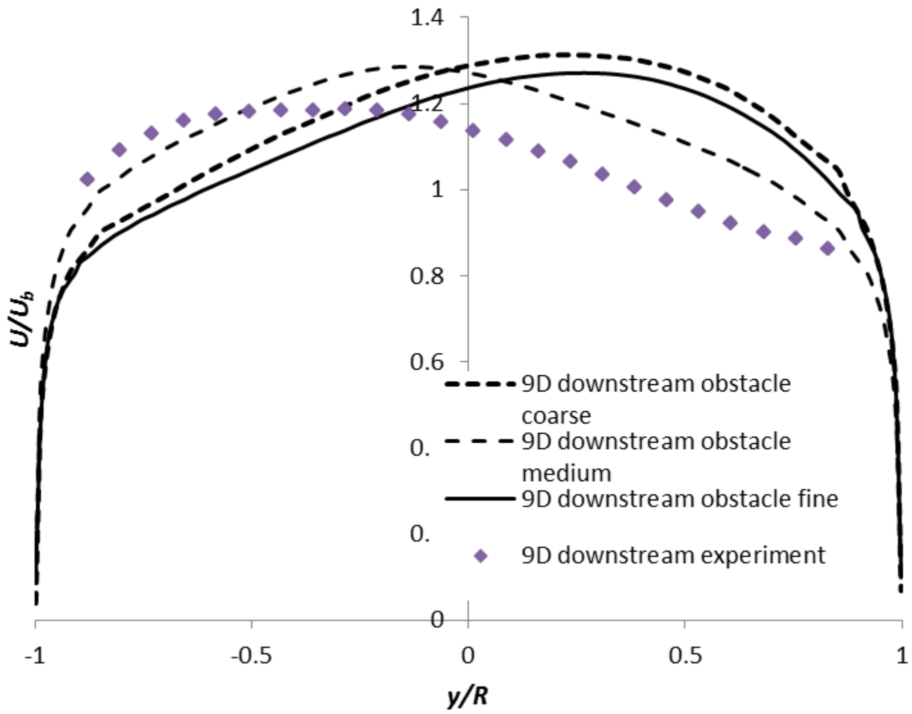

Figure D - 16 Computed normalized streamwise centerplane velocity, at 9D downstream 30B obstacle, Re=35,000.

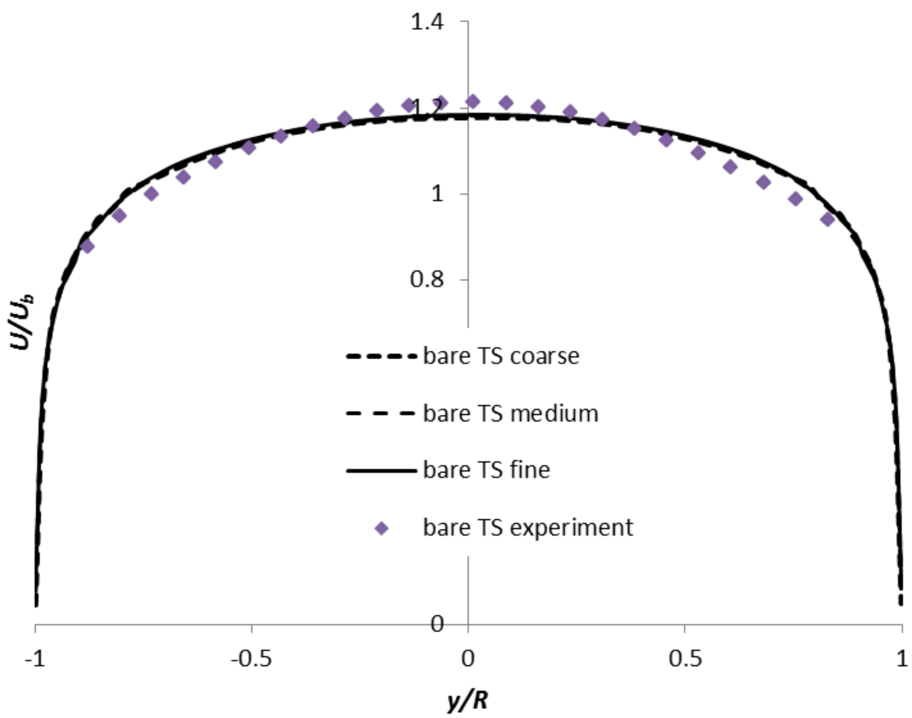

Figure D - 17 Computed normalized streamwise centerplane velocity, fully developed flow bare test section, Re=35,000.

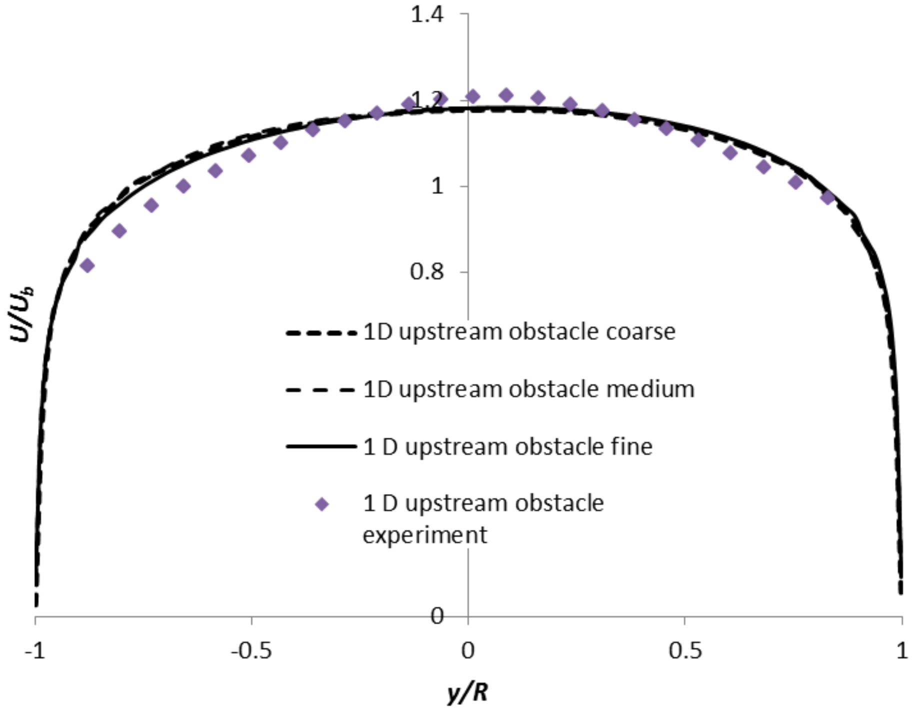

Figure D - 18 Computed normalized streamwise centerplane velocity, at 1D upstream 30R obstacle, Re=35,000.

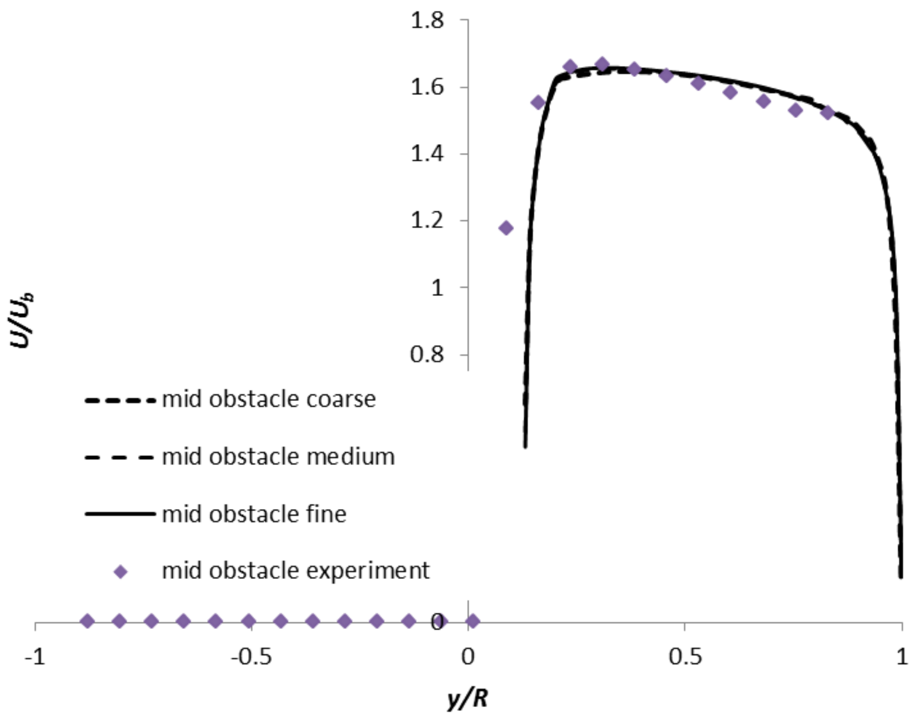

Figure D - 19 Computed normalized streamwise centerplane velocity, at mid 30R obstacle, Re=35,000.

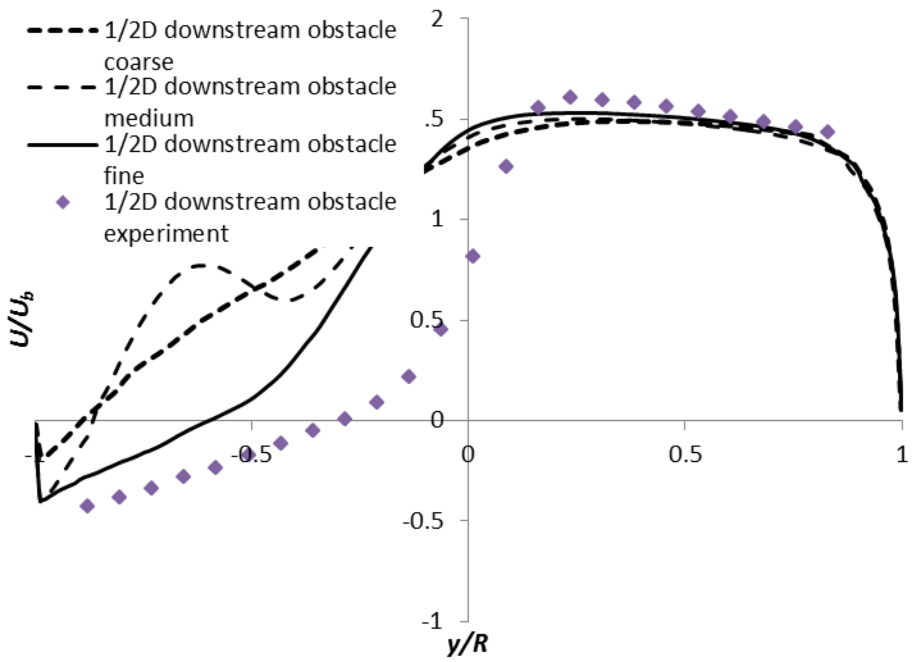

Figure D - 20 Computed normalized streamwise centerplane velocity, at 1/2D downstream 30R obstacle, Re=35,000.

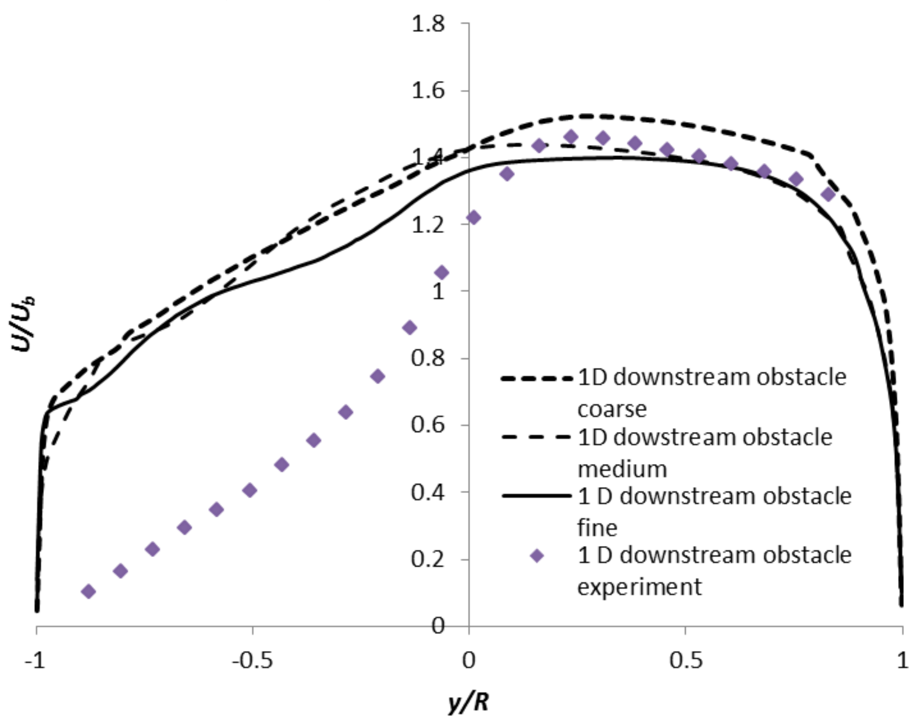

Figure D - 21 Computed normalized streamwise centerplane velocity, at 1D downstream 30R obstacle, Re=35,000.

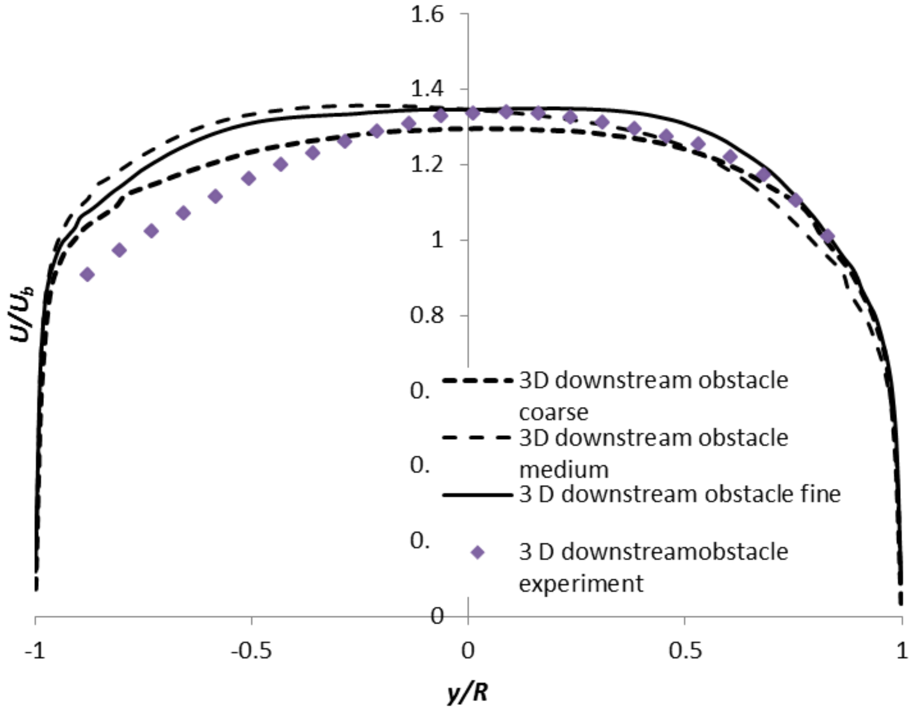

Figure D - 22 Computed normalized streamwise centerplane velocity, at 3D downstream 30R obstacle, Re=35,000.

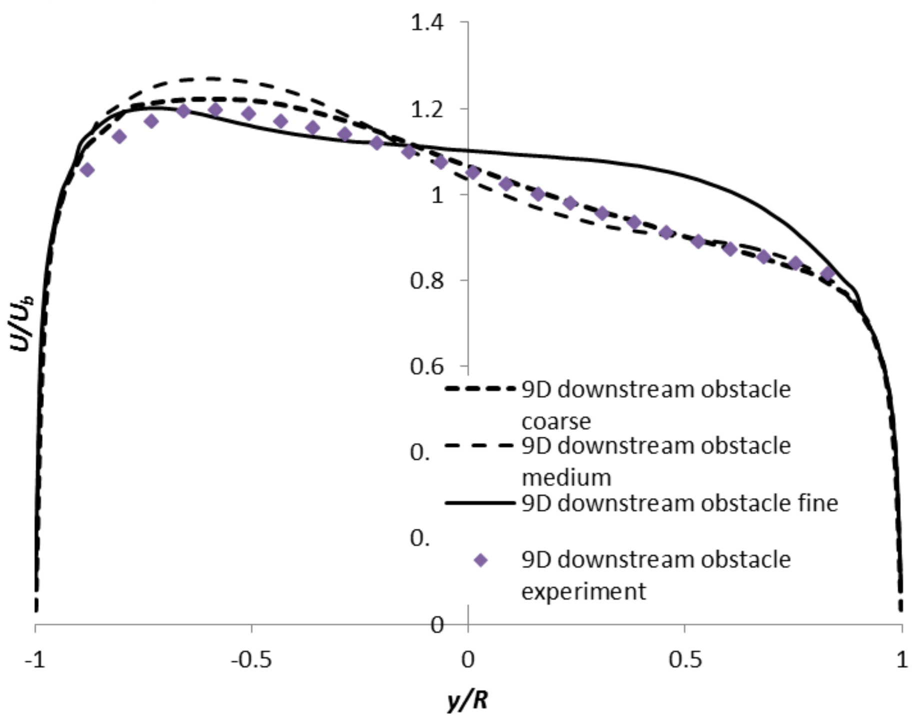

Figure D - 23 Computed normalized streamwise centerplane velocity, at 9D downstream 30R obstacle, Re=35,000.

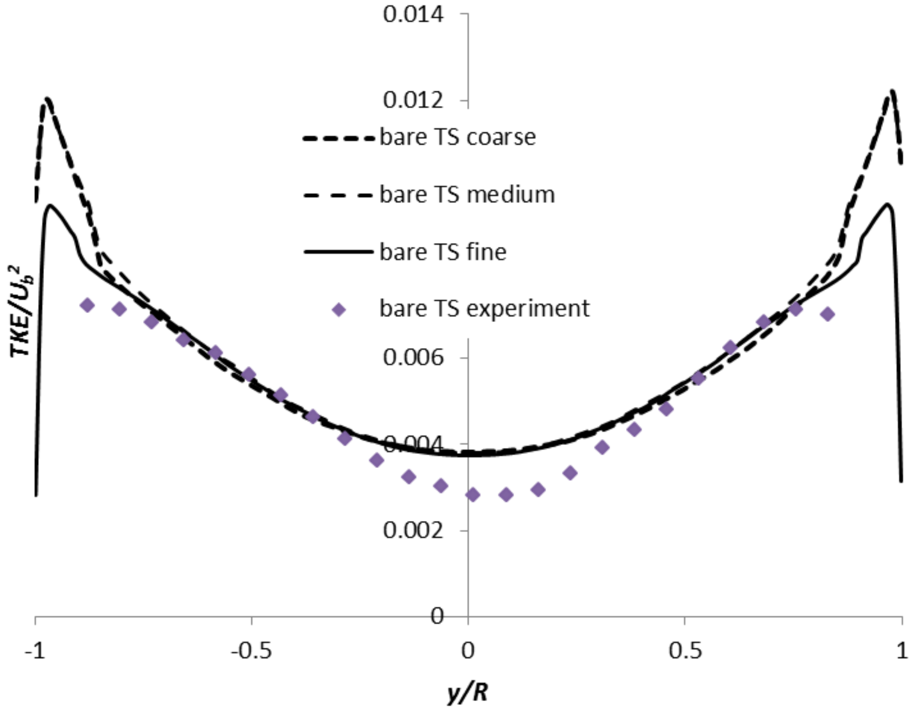

Figure D - 24 Computed normalized TKE at centerplane, fully developed flow bare test section, Re=35,000.

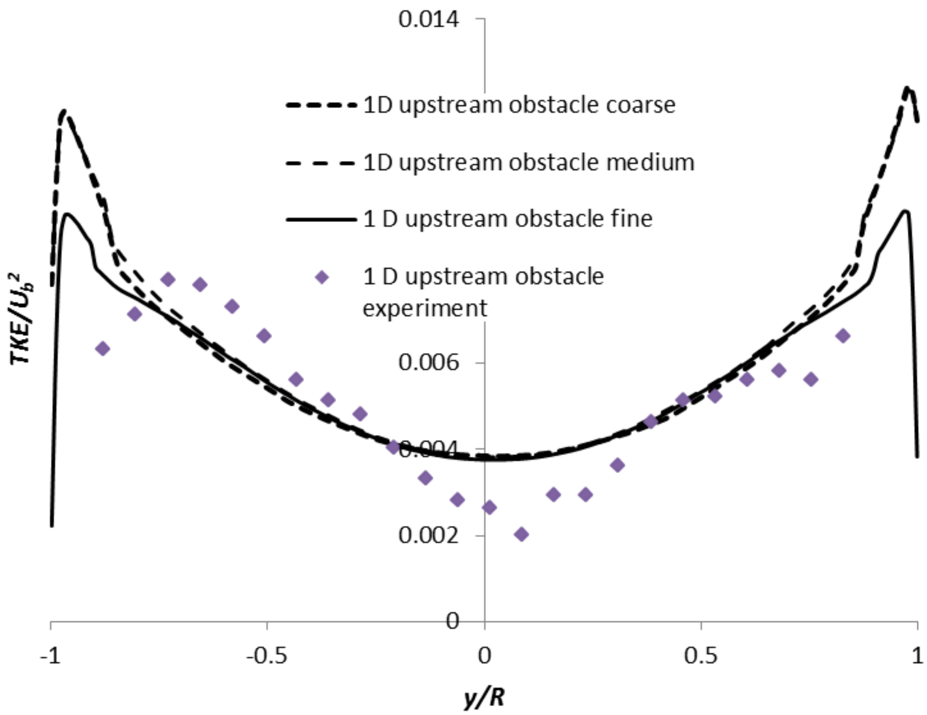

Figure D - 25 Computed normalized TKE at centerplane, at 1D upstream 30R obstacle, Re=35,000.

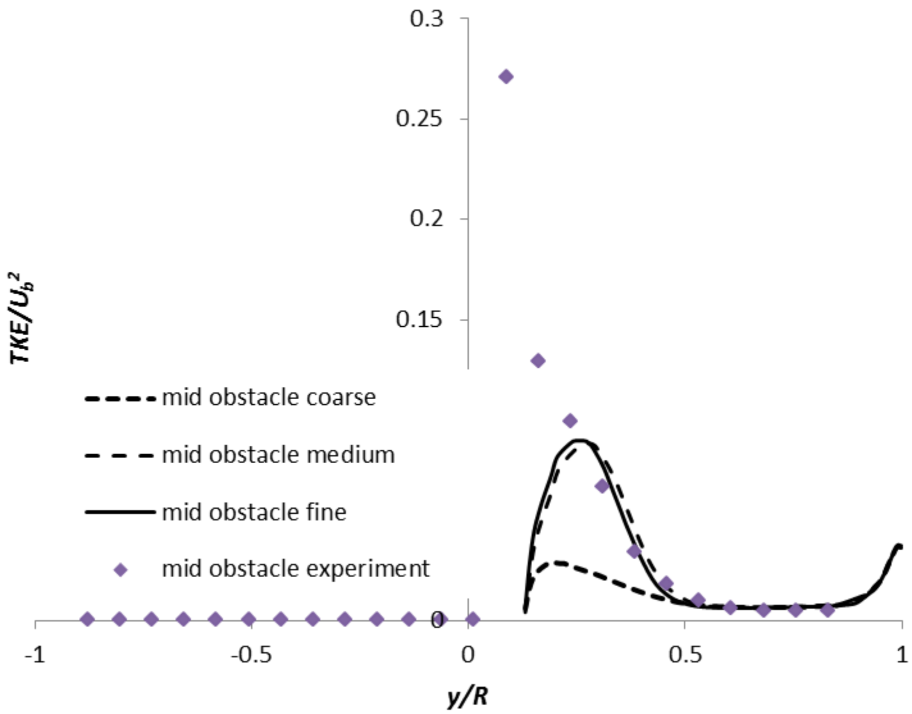

Figure D - 26 Computed normalized TKE at centerplane, mid 30B obstacle, Re=35,000.

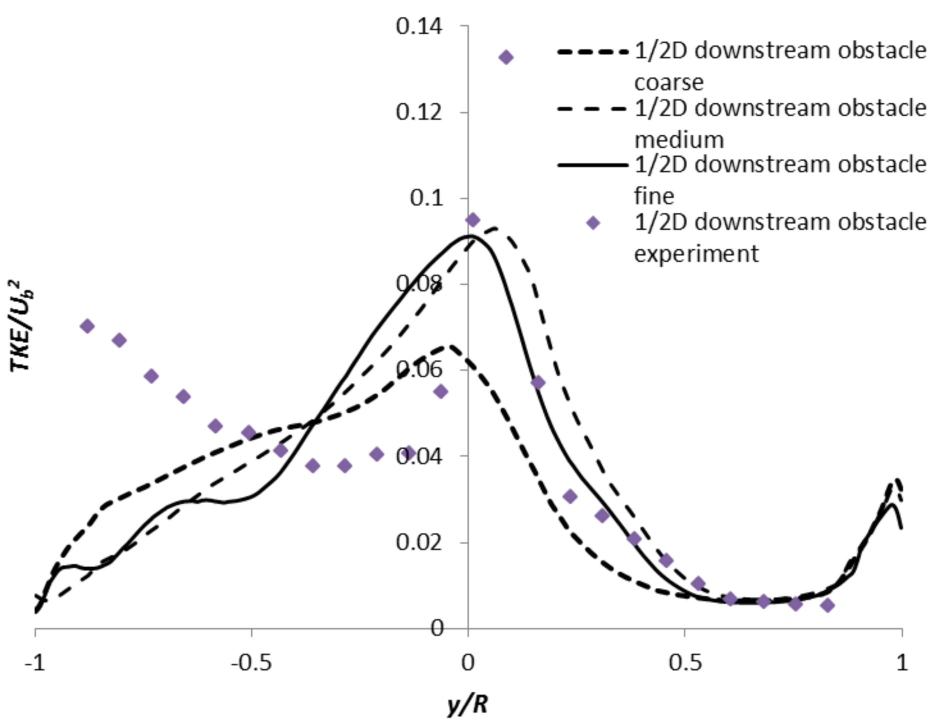

Figure D - 27 Computed normalized TKE at centerplane, at 1/2D downstream 30B obstacle, Re=35,000.

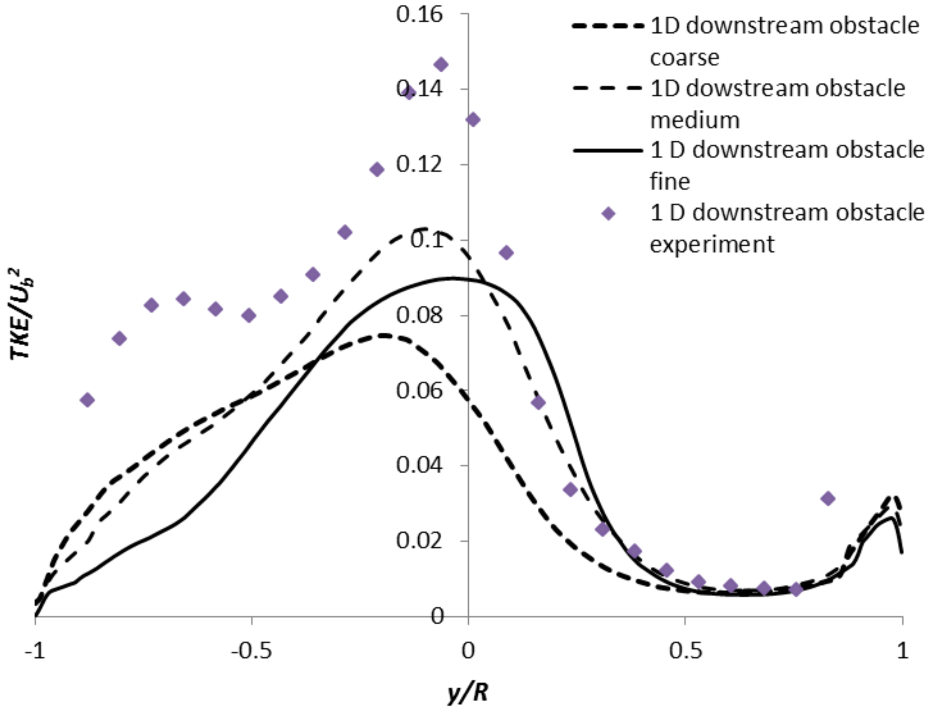

Figure D - 28 Computed normalized TKE at centerplane, at 1D downstream 30B obstacle, Re=35,000.

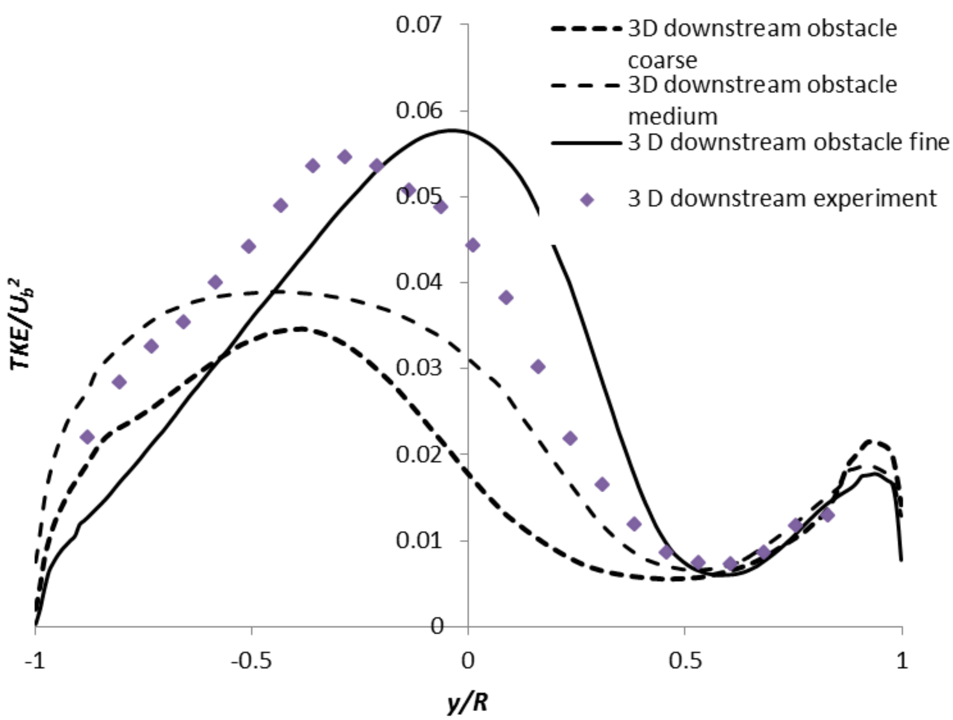

Figure D - 29 Computed normalized TKE at centerplane, at 3D downstream 30B obstacle, Re=35,000.

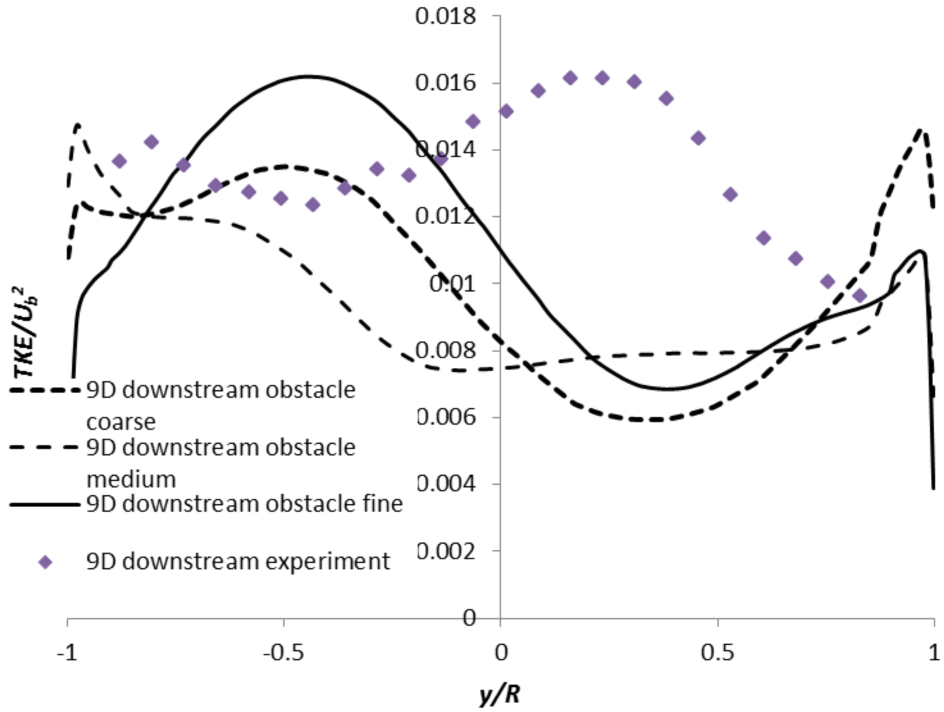

Figure D - 30 Computed normalized TKE at centerplane, at 9D downstream 30B obstacle, Re=35,000.

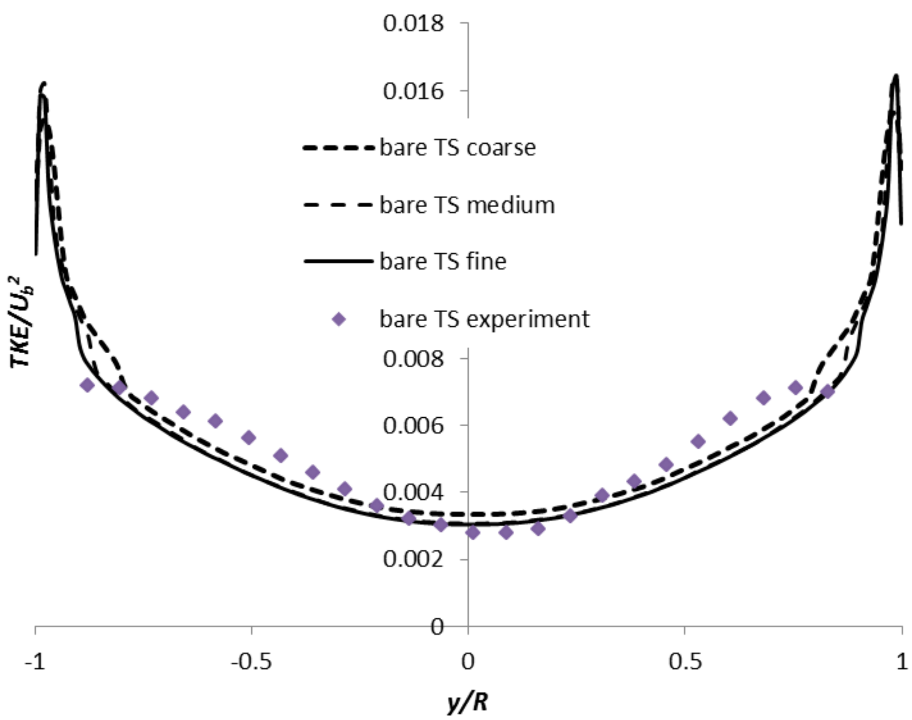

Figure D - 31 Computed normalized TKE at centerplane, fully developed flow bare test section, Re=35,000.

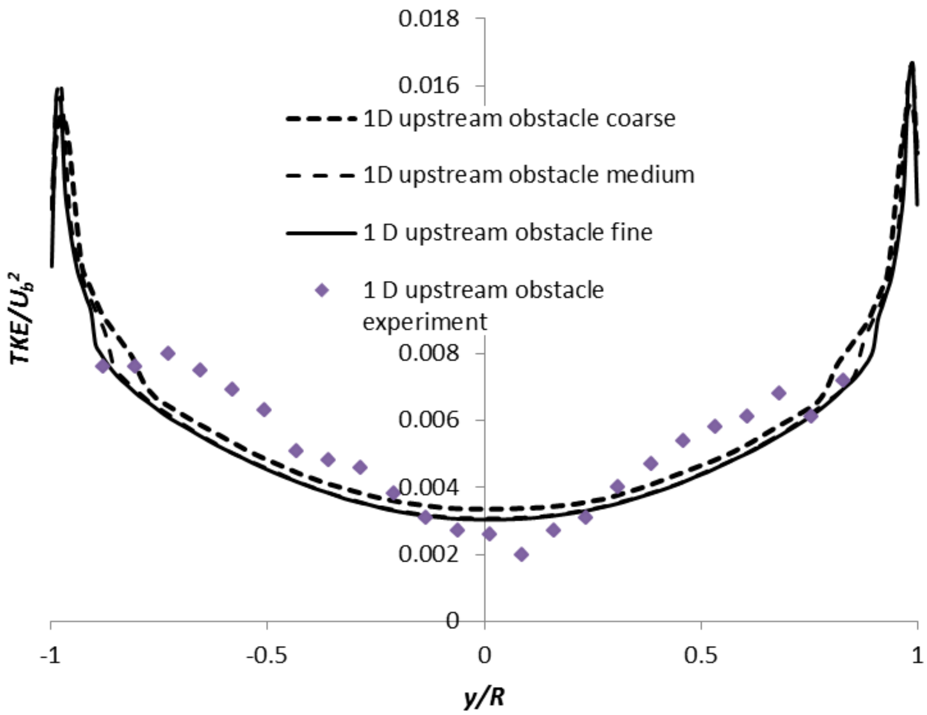

Figure D - 32 Computed normalized TKE at centerplane, at 1D upstream 30R obstacle, Re=35,000.

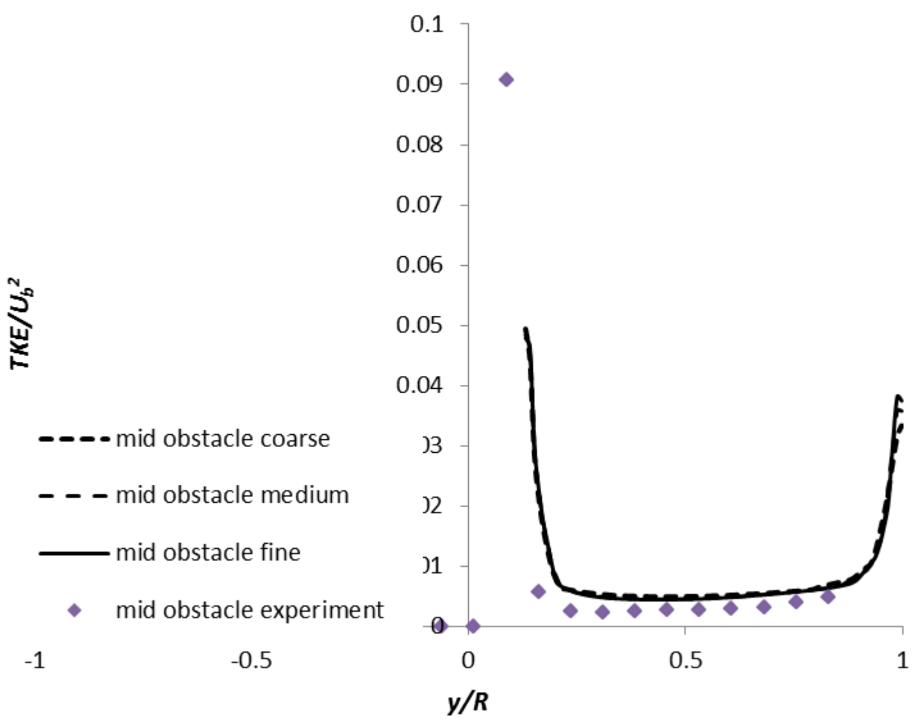

Figure D - 33 Computed normalized TKE at centerplane, mid 30R obstacle, Re=35,000.

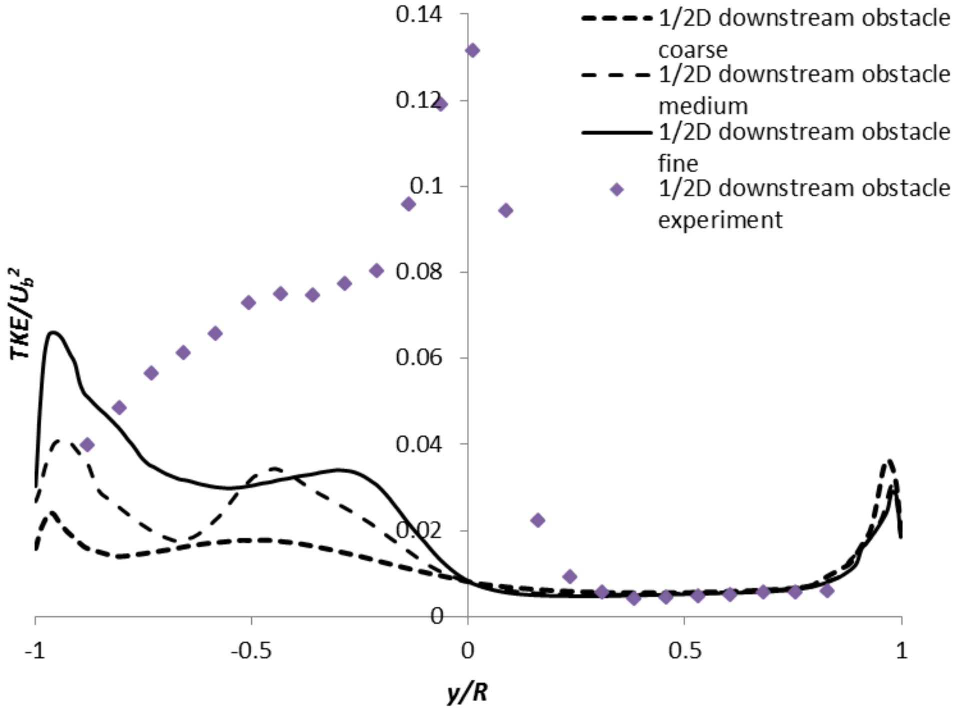

Figure D - 34 Computed normalized TKE at centerplane, at 1/2D downstream 30R obstacle, Re=35,000.

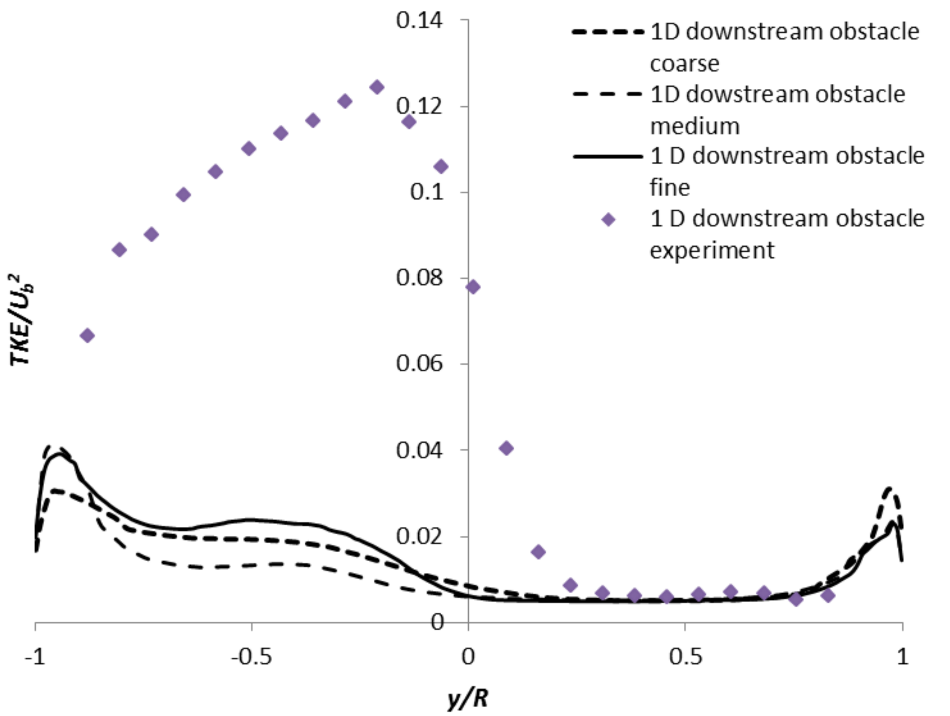

Figure D - 35 Computed normalized TKE at centerplane, at 1D downstream 30R obstacle, Re=35,000.

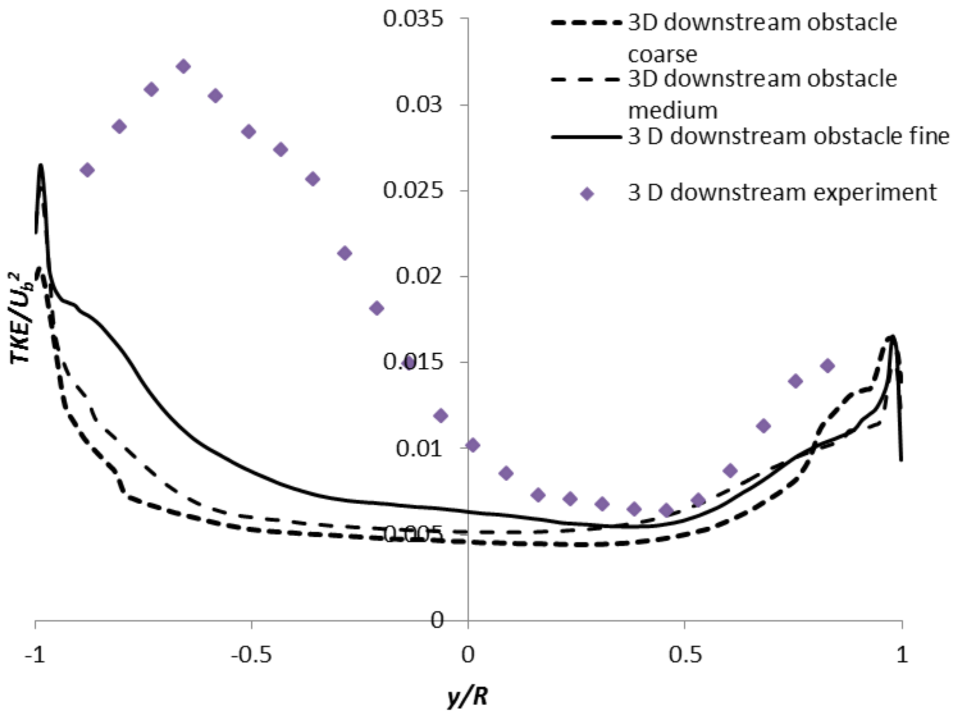

Figure D - 36 Computed normalized TKE at centerplane, at 3D downstream 30R obstacle, Re=35,000.

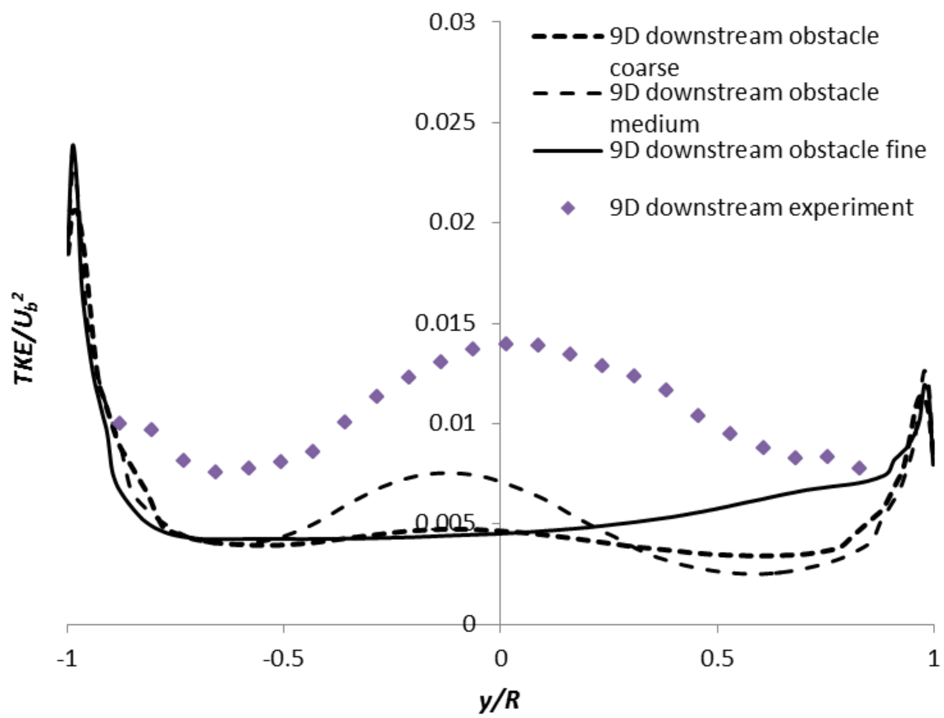

Figure D - 37 Computed normalized TKE at centerplane, at 9D downstream 30R obstacle, Re=35,000.

Mesh convergence issues and inconsistency with the experimental data

During the development of meshes for numerical simulations, in order to confirm the convergence of results provided by the meshes and demonstrate sufficiency of the number of nodes selected, three meshes were generated for each geometry investigated: coarse, medium and fine meshes. This approach is consistent with general practices used in performing numerical simulations. In the initial stage, the modelled geometry included the 3 m development length, prior the test section, which was an accurate representation of the experimental loop. The reason for the long development section in the experimental loop was that the loop was previously used for two-phase flow experiments (i.e. mixtures of air-water) for which the development length is significantly longer, of the order of 100*D*. Contrary to expectations, the initial results of simulations showed convergence issues. In order to mitigate this issue, we decided to change the modelled geometry by shortening the development section from 3 m to 1 m, based on the observation from the initial set of simulations that in the development section the flow required approximately 20*D* to reach the fully developed profile, which means that keeping a much longer development section was not necessary. For single phase pipe flow, the 20D value obtained from the numerical simulations was also consistent with pipe data from textbooks. In order to ensure that flow was fully developed before entering the segment containing the obstacle, the updated geometry had a development section of 1 m, which is approximately 30*D*. Details about these meshes (e.g. size, structure) are given in the first paragraphs of Appendix D. The shorter development length allowed more nodes to be allocated in the regions containing the obstacles, thus intensifying the use of the available computational resources in the region of interest. However, the results of the new set of simulations did not show substantial improvement of convergence between meshes. Limitation of computational resources and time allocated to complete this study prevented us to further explore additional mitigation techniques, such as conducting unsteady simulations, using refined turbulence models (e.g. RSM or LES) or modelling a simplified geometry (e.g. 2D) and gradually building the complexity, which would allow a better understanding of the nature of issues (mesh, turbulence model, assumptions) encountered. It should be noted that, despite the apparent simplicity of the modelled geometry, there were challenges to accurate model the experimental setup. Modelling the area of contact between the obstacle and the inside wall of the test section introduces well-known numerical difficulties and the computation of a three-dimensional separated and recirculating flow region is also a known challenging problem.

APPENDIX E: ANALYSIS OF OPTICAL DISTORTIONS

An element of concern of the PIV investigation was that the curvature of the wall of the test section, made of acrylic glass, might have induced optical distortions which are difficult to correct for, especially in the areas close to the top and the bottom of the measurement plane, where the light scattered by the seeding particles would intersect the test section wall at high angles of incidence. In order to circumvent the above mentioned concern, a test section made of Teflon was manufactured. The reason for the selection of Teflon was that its refractive index is 1.33, thus practically identical to the refractive index of water. Nevertheless, the relatively low transparency of Teflon required a very thin Teflon test section wall. A wall thickness of 0.3 mm was the minimum achievable in the machine shop, in order to ensure mechanical integrity during manufacturing and to be able to withstand the hydrostatic pressure during loop operation. Subsequent testing with the PIV system showed that the transparency of the Teflon test section was insufficient to ensure adequate visibility of the seeding particles (only a small fraction of particles were visible) and showed very poor signal to noise ratio of the captured images, hence this path was not pursued further. The test section wall was made of acrylic glass and had a thickness of 3.5 mm. In order to minimize the distortion caused by the curved surface of the tube, an external prismatic tank filled with water was used. Quantification of the errors caused by light refraction and geometric distortions complement the uncertainty analysis of PIV measurement. It should be noted, however, that the PIV software had calibration routines designed to correct for optical and perspective distortions, thus the current analysis was performed to assess their magnitude and improve our understanding. Two types of distortions have been identified:

1) Perspective distortions

2) Optical distortions

Two representative cases have been analyzed:

1) Distortions in the axial direction

In the center of the measurement window, incident light is normal to all interfaces, thus the image is not distorted. The highest distortions occur at the boundaries of the image. Fig E-1 shows a schematic of the light path starting from a light source P (e.g. illuminated particle) located near the axial boundary of the measurement window. The light crosses water/acrylic or acrylic/air interfaces and is subject to successive refractions, until it reaches the camera's objective, C. The virtual image is found at the intersection of incident light extension with an undistorted light ray, P'.

Estimation of "displacement" of particle P was performed by applying Snell's law at all boundaries crossed by light and solving the triangles formed by the light path.

Snell's law applied at each interface between two different light propagation media

$$\frac{\sin\alpha_{12}}{\sin\alpha_{21}} = \frac{n_2}{n_1} \quad (1)$$

$$\frac{\sin\alpha_{23}}{\sin\alpha_{32}} = \frac{n_3}{n_2} \quad (2)$$

$$\frac{\sin\alpha_{34}}{\sin\alpha_{43}} = \frac{n_4}{n_3} \quad (3)$$

$$\frac{\sin\alpha_{45}}{\sin\alpha_{54}} = \frac{n_5}{n_4} \quad (4)$$

The acrylic walls of the test section and the tank are assumed parallel, thus:

$$\alpha_{21} = \alpha_{23} \quad (5)$$

$$\alpha_{32} = \alpha_{34} \quad (6)$$

$$\alpha_{12} = \alpha_{34} \quad (7)$$

In the square triangle PA'A: $\tan\alpha_{12} = \dfrac{y_1}{\delta_1}$ (8)

Similarly, $\tan\alpha_{23} = \dfrac{y_2}{\delta_2}$ (9)

$$\tan\alpha_{34} = \frac{y_3}{\delta_3} \quad (10)$$

$$\tan\alpha_{45} = \frac{y_4}{\delta_4} \quad (11)$$

$$\tan\alpha_{54} = \frac{y_5}{\delta_5} \quad (12)$$

$$y_P = \sum_{i=1}^{5} y_i \quad (13)$$

The equations (1) to (13) are a system of equations with 13 unknown, that is, eight angles and five distances y_i (i=1..5). The system has been solved numerically for the given geometry and the most significant results are presented in Table E-1.

The results indicate that the optical distortion consists mainly in modification of the apparent "depth" of the particle. The axial displacement of particles during two successive images is of the order of few millimeters, thus the "depth" optical distortion is negligible. A more significant distortion is the perspective distortion, which is the apparent size of particle displacement caused by the angle of view of camera relative to the particles located at the boundaries of the measurement window. The perspective distortion is caused mainly by i) the distance between the camera and the particle and ii) the viewing angle relative to the plane of motion, which is smaller than 90 deg, causing an apparent reduction of the axial velocity

The above mentioned distortion, if uncorrected affects only the axial (e.g. streamwise) velocity component; a table containing estimates of errors caused by this is provided below:

Table E - 1 Estimates of errors caused by perspective distortions

y_P (mm)	1	2	5	10	20	50	75
$\delta_{PP'}$(mm)	5.8	5.8	8.4	8.5	9.3	9.4	9.4
Incident angle (deg)	0.1	0.19	0.48	0.97	1.9	4.8	7.2
Perspective distortion (%)	~0	~0	-0.007	-0.03	-0.11	-0.7	-1.6

2) Distortions caused by the tube curvature

Distortions caused by tube curvature have been estimated by tracking the light ray emitted by a particle located in the proximity of the test section wall (see Figure E-2).

Similar to the previous analysis, estimation of "displacement" of particle P was performed by applying Snell's law to all boundaries crossed by light:

$$\frac{\sin\alpha_{12}}{\sin\alpha_{21}} = \frac{n_2}{n_1} \tag{1}$$

$$\frac{\sin\alpha_{23}}{\sin\alpha_{32}} = \frac{n_3}{n_2} \tag{2}$$

$$\frac{\sin\alpha_{34}}{\sin\alpha_{43}} = \frac{n_4}{n_3} \tag{3}$$

$$\frac{\sin\alpha_{45}}{\sin\alpha_{54}} = \frac{n_5}{n_4} \tag{4}$$

$$\alpha_{34} = \alpha_{54} \tag{5}$$

Sine law in Δ AOP:

$$\frac{AP}{\sin\alpha} = \frac{y_P}{\sin\alpha_{12}} = \frac{r_i}{\sin\beta} \tag{6}$$

$$\alpha_{12} + \alpha + \beta = 180° \tag{7}$$

Cosine law in Δ AOB:

$$AB = \sqrt{r_i^2 + r_o^2 - 2r_i r_o \cos\gamma} \tag{8}$$

$$\angle D'BD = 180° - (\alpha + \gamma + \alpha_{23}) \tag{9}$$

$$\alpha_{32} = 90° - \angle D'BD \tag{10}$$

$$\gamma = \alpha_{21} - \alpha_{23} \tag{11}$$

It is noted that the perspective distortion in the transverse direction is negligible and the main component is given by the tube curvature optical distortion, which impacts the transverse velocity component only, according to the estimates given in Table E-2:

Table E- 1 Estimates of errors caused by test section curvature

y_P (mm)	1	2	5	10	12	13	15
Apparent length of 1mm segment centered at P	1.025	1.023	1.02	1.014	1.01	1.004	0.91
Optical distortion (%)	2.5	2.3	2.0	1.4	1.0	0.4	-9.2

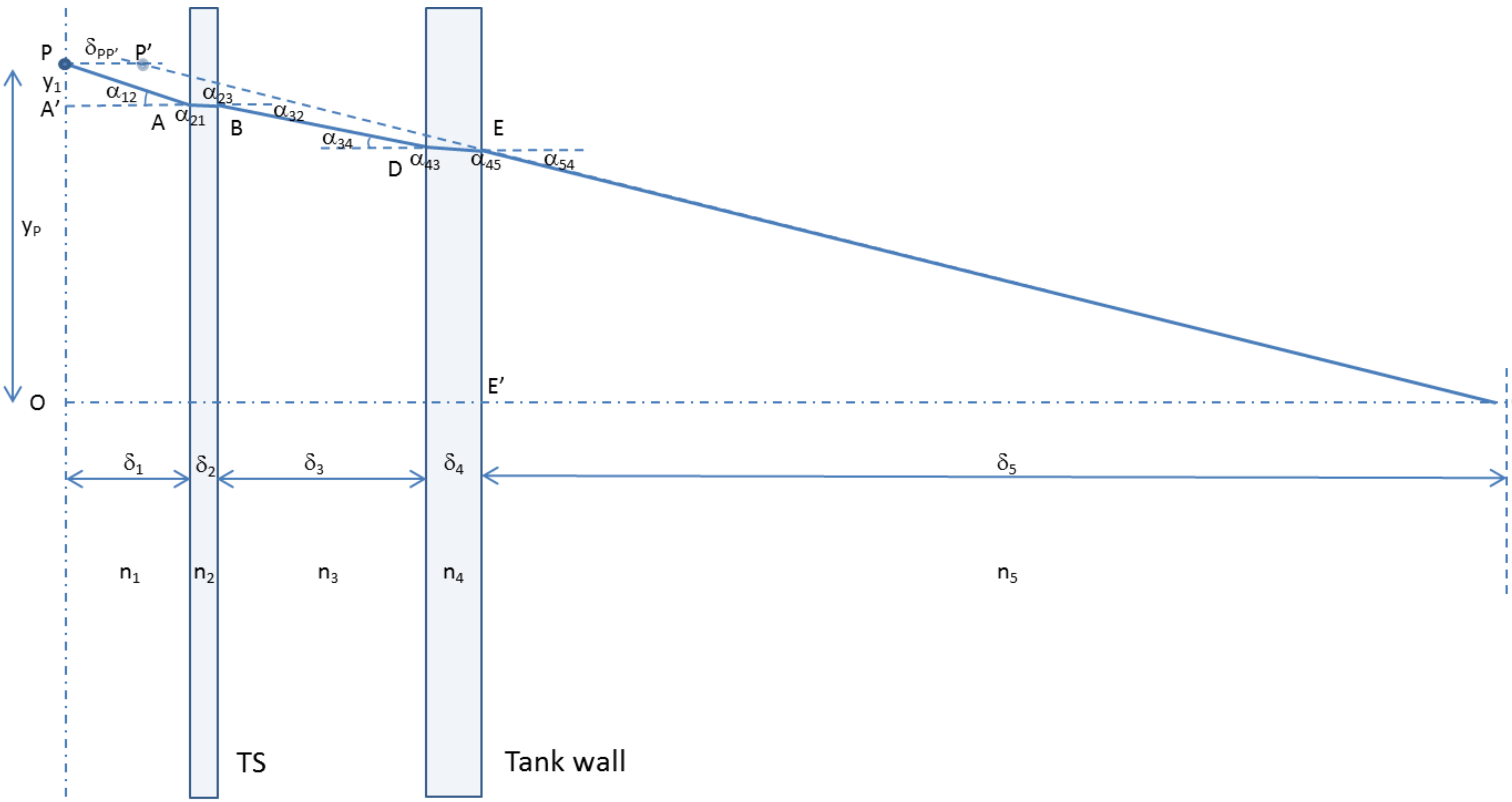

Figure E - 1 Schematic diagram of top view of the measurement tank.

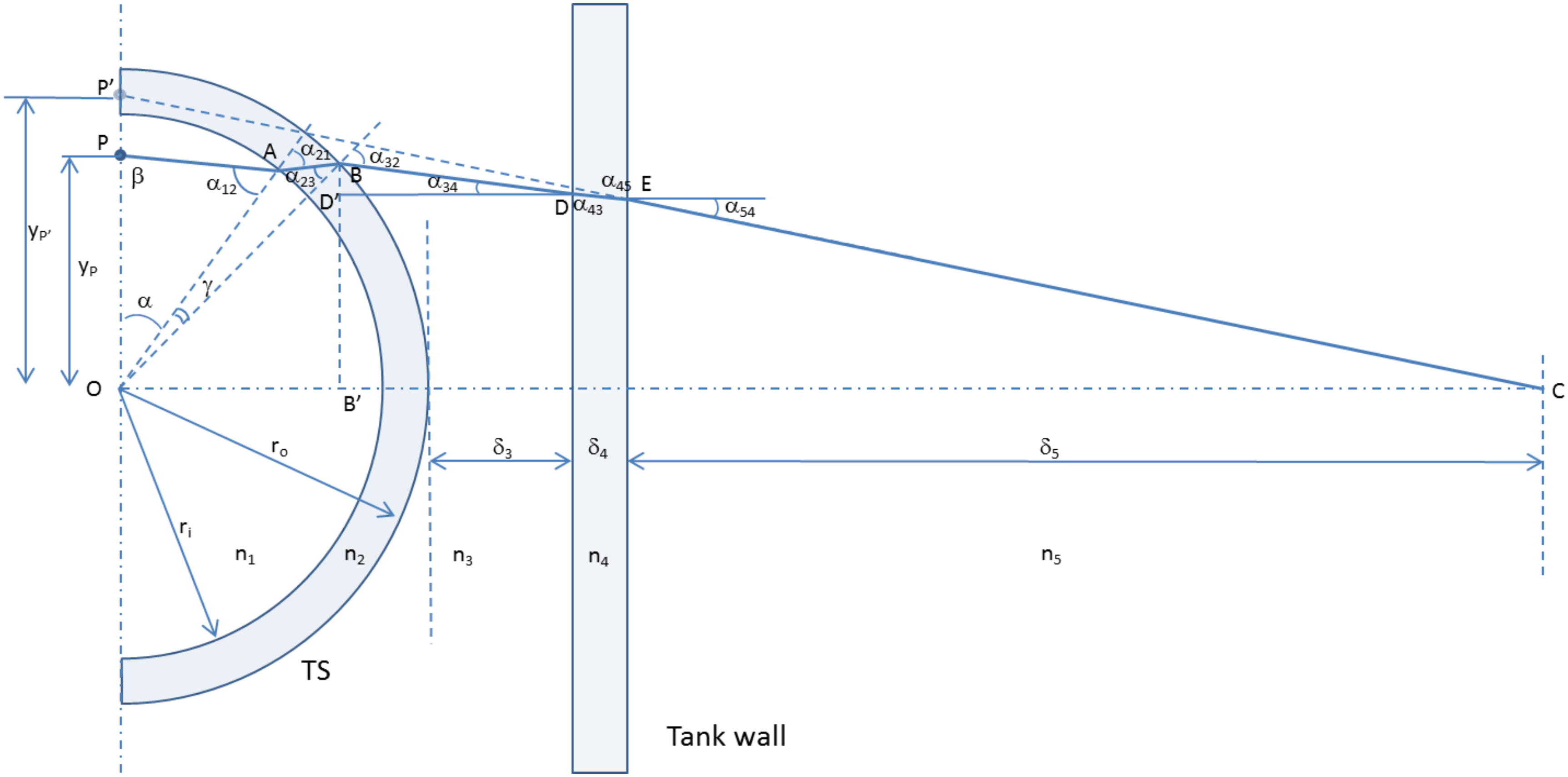

Figure E - 2 Schematic diagram of the side view of the measurement test section and the water tank.

APPENDIX F: ANALYSIS OF PIV CONVERGENCE

In order to assess the sufficiency of the number of frames (N=500) selected for the PIV experiments, a convergence analysis was performed. Thus, two case studies have been selected. The selection criteria required that they should include diverse obstacle types and different Re numbers. The cases, denoted as Case A and Case B are described in the following paragraphs.

The following quantities were computed and plotted using samples of PIV frames containing N=50, 100, 200, 300 and 500 images, respectively:

a) time averaged streamwise planar velocity component ($\overline{U}$), normalized by U_b
b) root mean square of streamwise velocity fluctuations u', normalized by U_b
c) root mean square of spanwise velocity fluctuations v', normalized by U_b
d) Reynolds stress $\overline{uv}$ normalized by U_b^2

Case A: 30B, Re=11,000 in the bare test section

Figures F-1 to F-4 indicate that convergence was achieved for all samples for the time averaged streamwise velocity component, whilst the rest of selected quantities require a sample of at least 200 frames to achieve convergence.

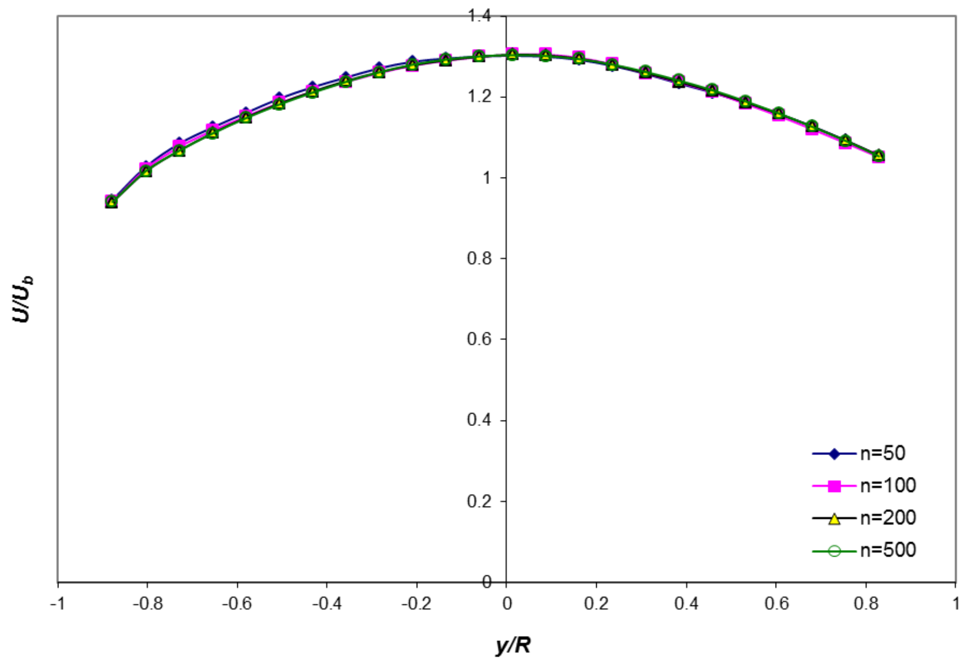

Figure F - 1 Normalized time averaged streamwise planar velocity component, case A.

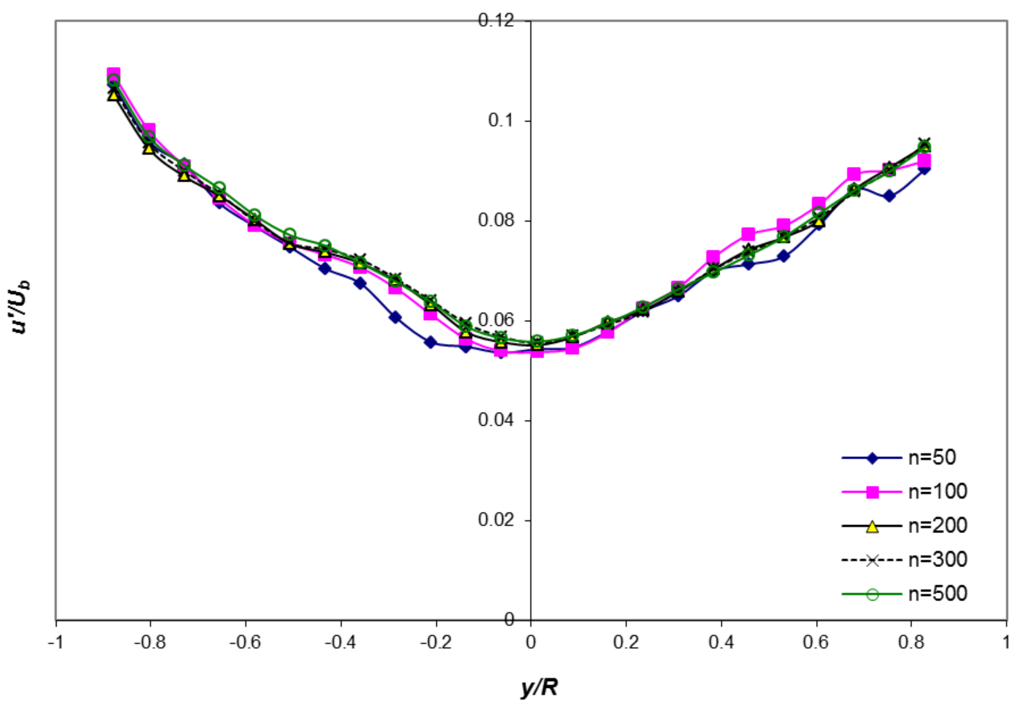

Figure F - 2 Normalized rms of streamwise velocity fluctuations, case A.

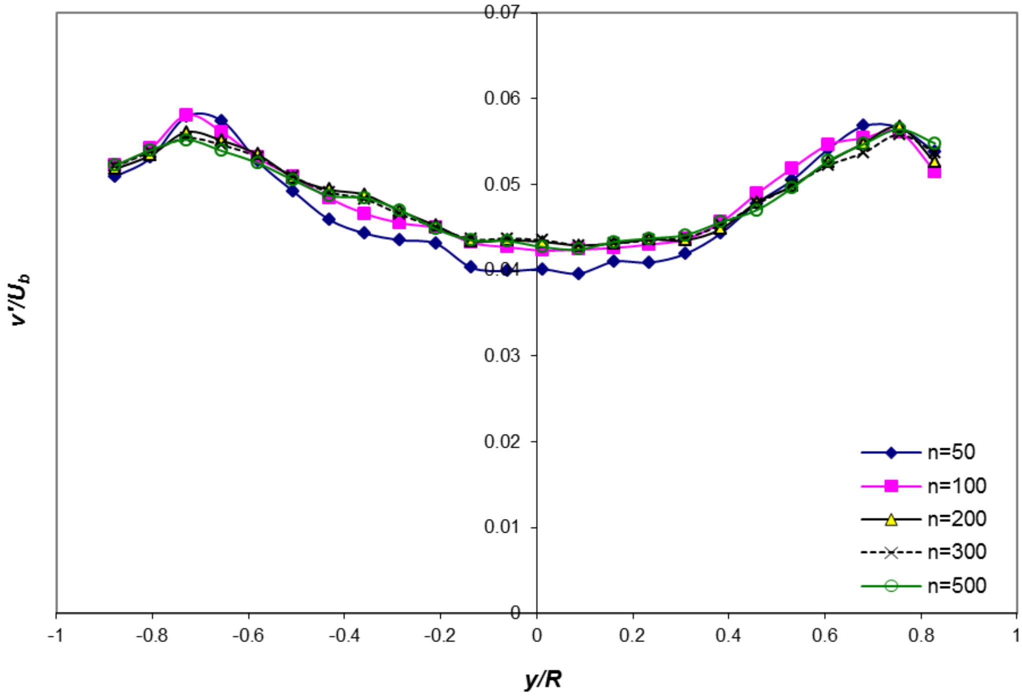

Figure F - 3 Normalized rms of spanwise velocity fluctuations, case A.

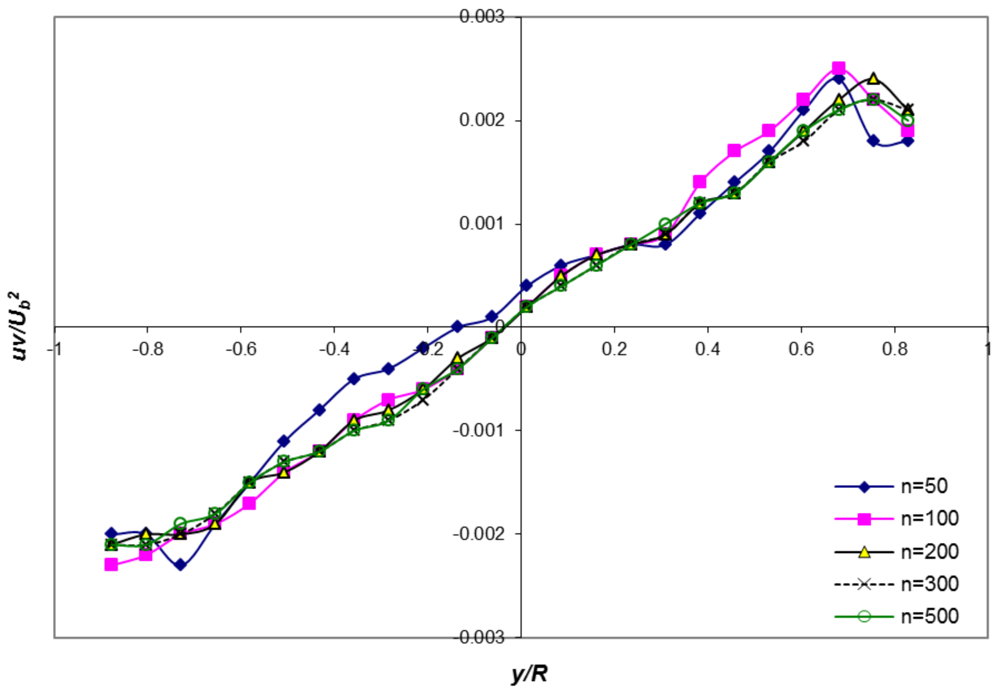

Figure F - 4 Normalized Reynolds stress, case A.

To substantiate further the convergence analysis, the standard deviation of errors was plotted against the size of a sample. For a data point *i* obtained from a sample of size *N*, the error was defined as the difference between the quantity $X_{N=500}$ and X_N:

$$error_i = X_{i,N=500} - X_{i,N}$$

$$st\_devX = \sqrt{\frac{\sum_{i=1}^{M} error_i^2}{M}}$$

As expected, as the size of a sample increases, the standard deviation of errors decreases, as illustrated by the plots from Figures F – 9 and F-10.

Case B includes data measured at 1D downstream from the trailing edge of 30R at Re=35,000 thus in the separation region. The plots from Figures F-5 to F-8 indicate that, proper convergence can be achieved for the time-averaged streamwise velocity for a sample of at least 100 frames, however, the sample size for Reynolds stress seems to be larger, at least 300 frames.

Case B: 30R, Re=35,000 at 1D downstream trailing edge

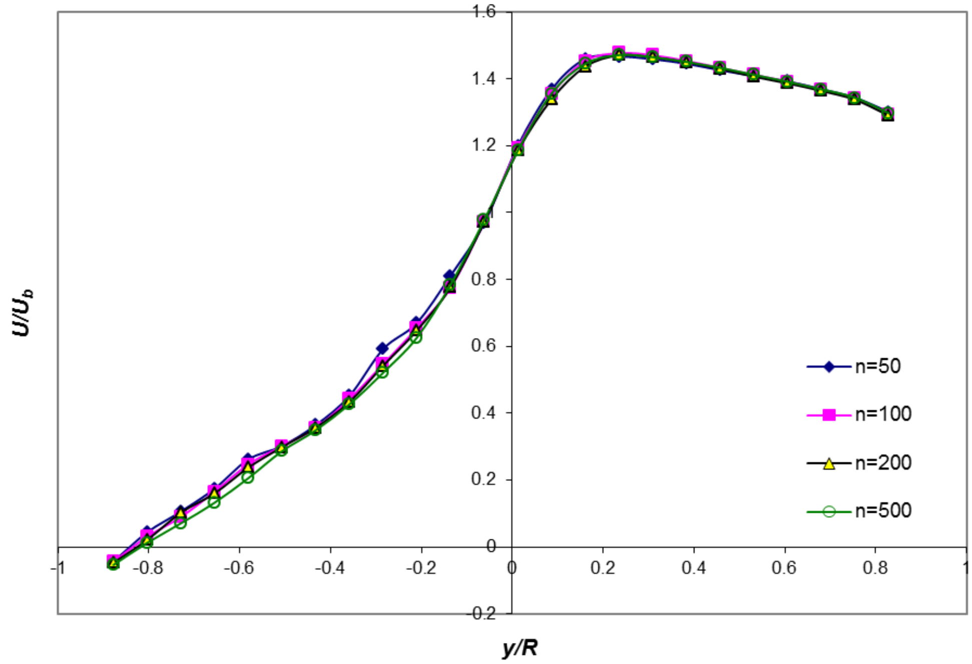

Figure F - 5 Normalized time averaged streamwise planar velocity component, case B.

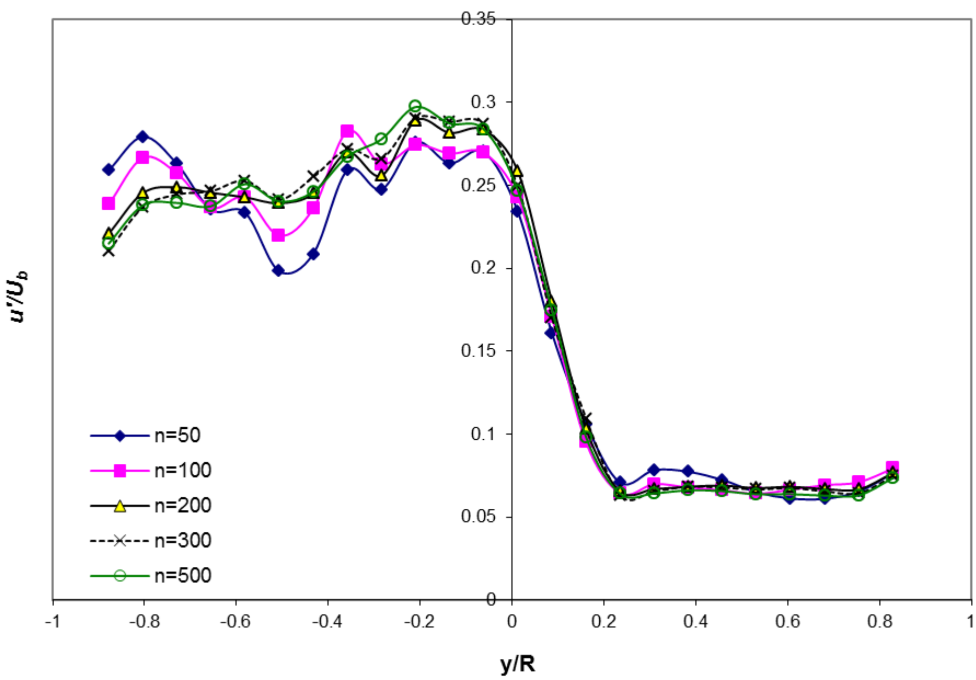

Figure F - 6 Normalized streamwise rms of velocity fluctuations, case B.

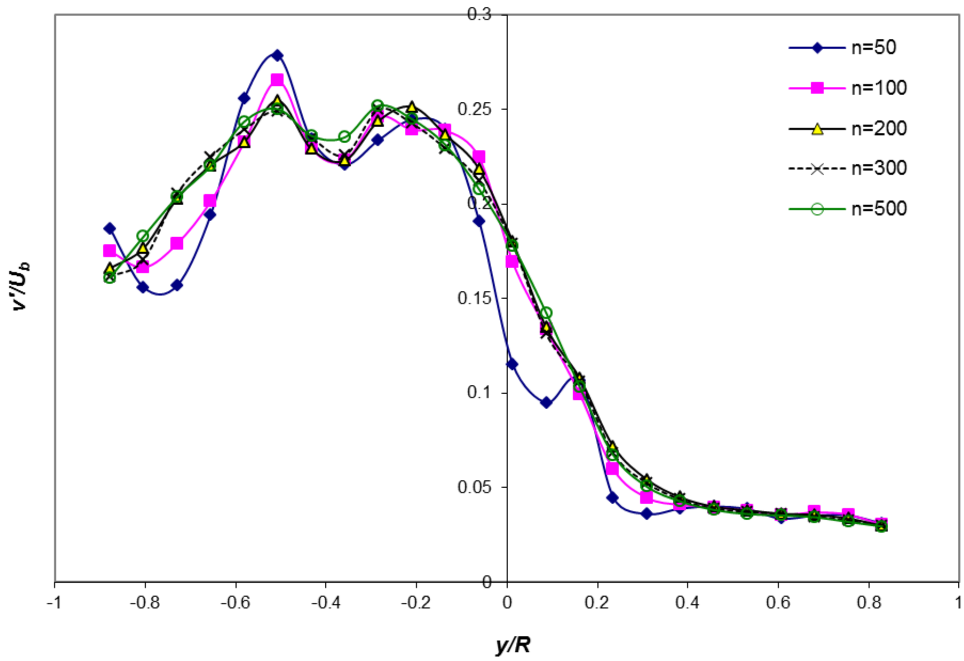

Figure F - 7 Normalized rms of spanwise velocity fluctuations, case A.

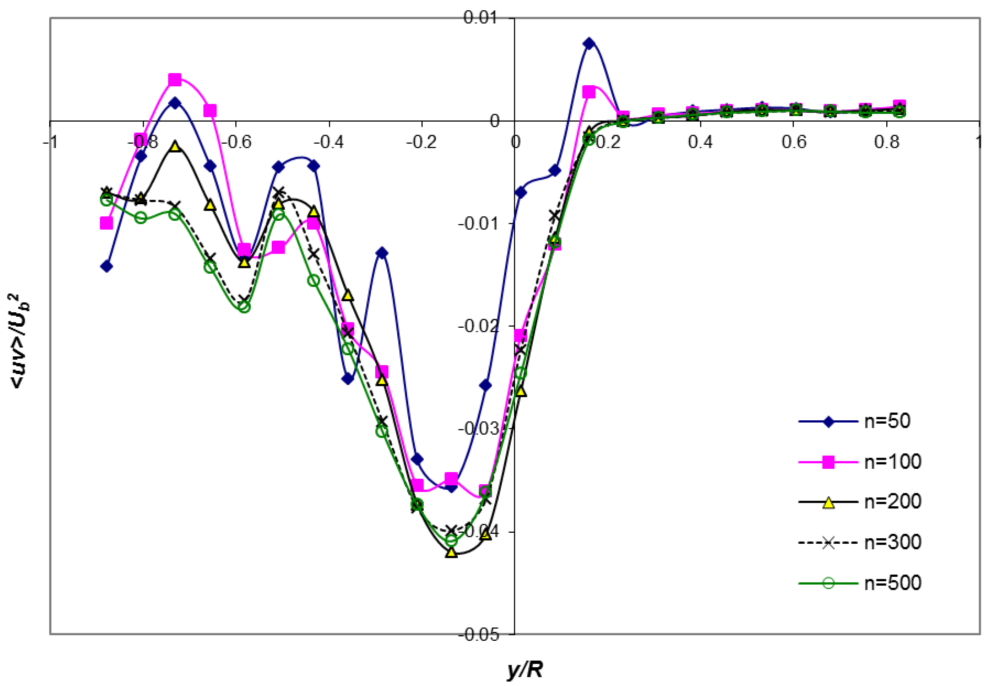

Figure F - 8 Normalized Reynolds stress, case B.

It can be concluded that:

a) The minimum number of frames required to achieve convergence for PIV data post processing seems dependent on the parameter of interest and the flow conditions.
b) As such, time averaged velocities seem to converge for samples larger than 100 frames, regardless the flow conditions;
c) Other parameters of interest (e.g. rms of velocity fluctuations, Reynolds stresses) seem to converge for samples larger than 300 frames for flows that undergo separation/recirculation, and 200 frames otherwise.

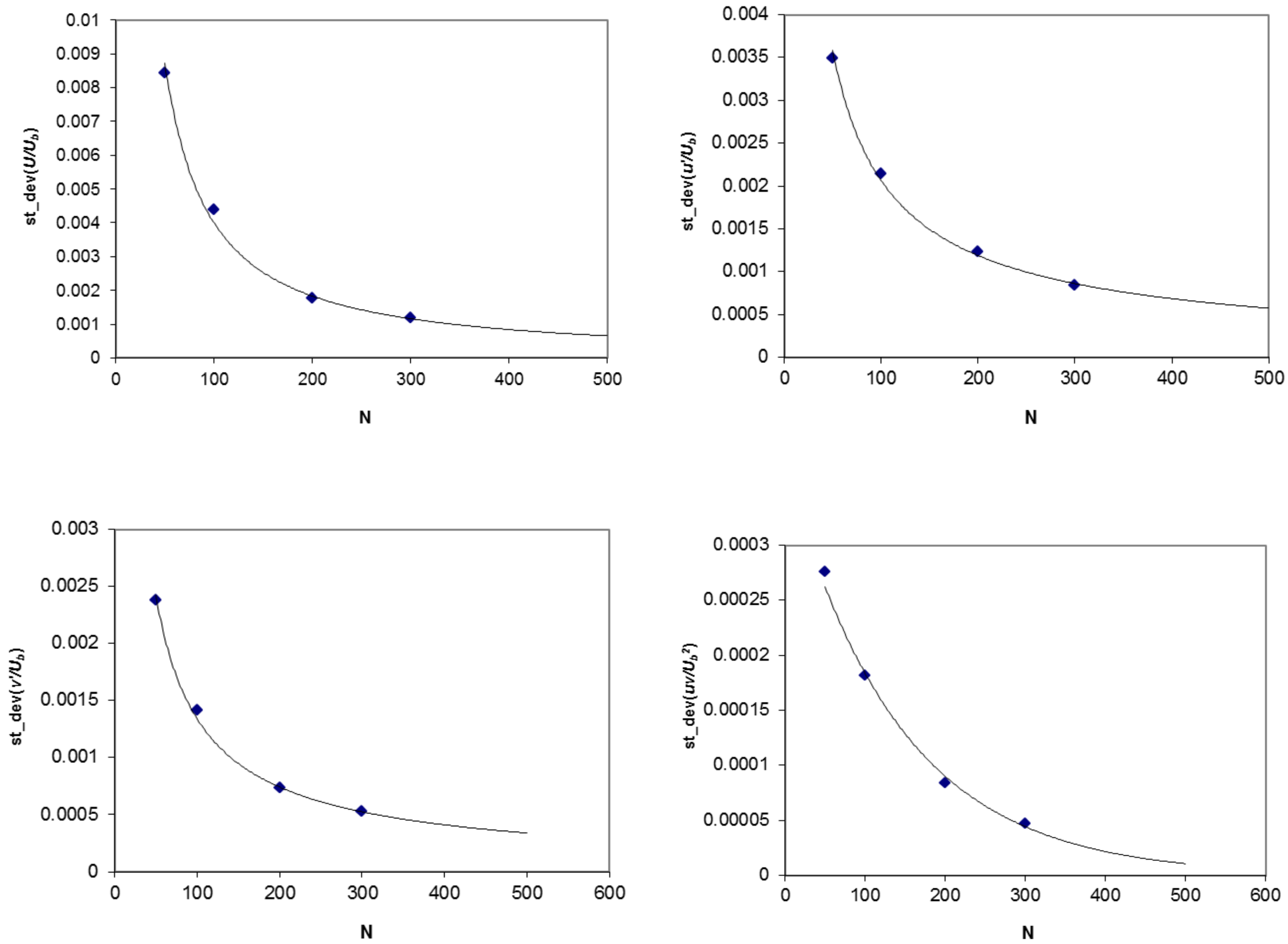

Figure F - 9 Standard deviations of errors vs the size of samples, case A.

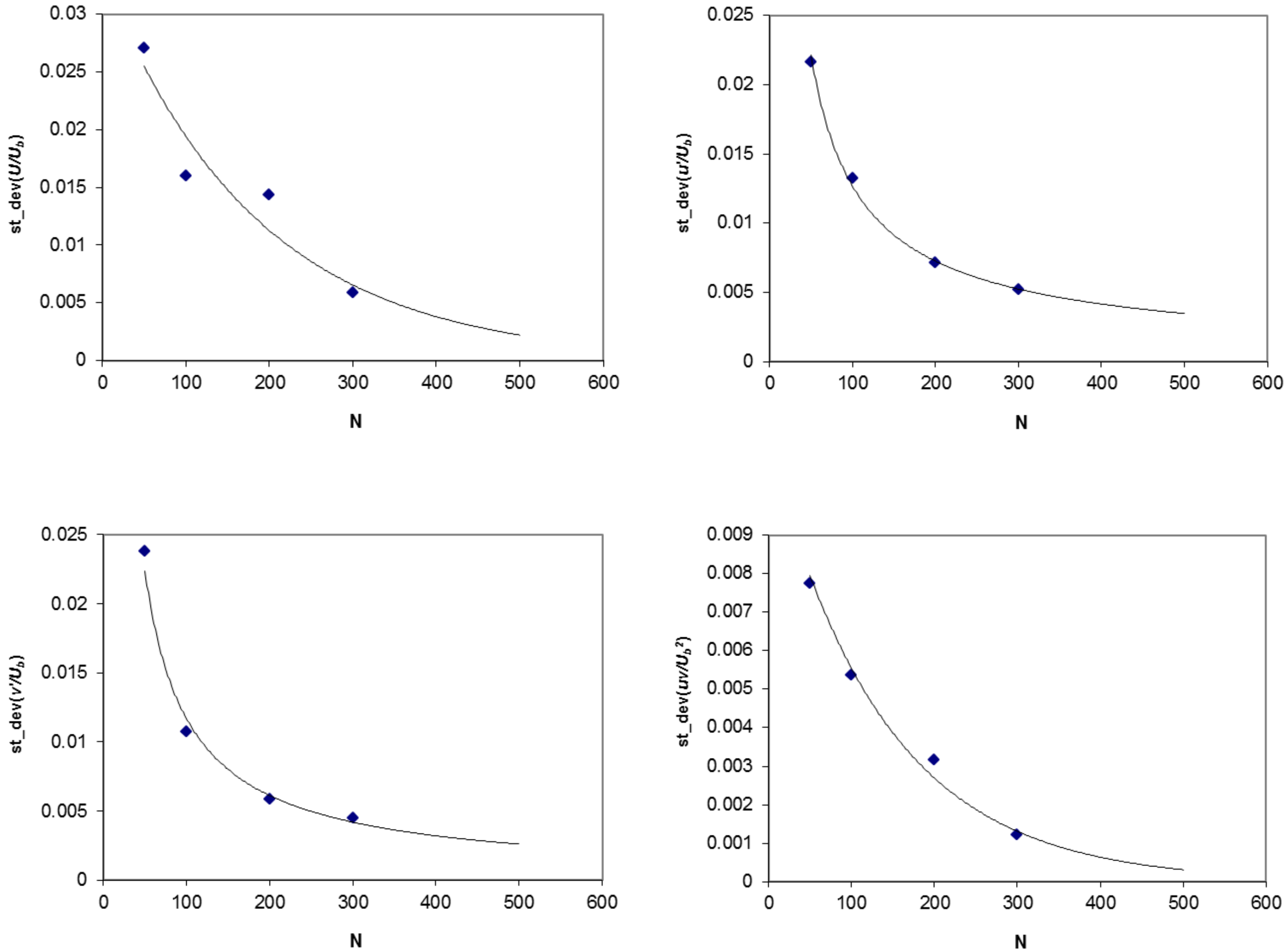

Figure F - 10 Standard deviations of errors vs the size of samples for case B.